Radio Science Bulletin

ISSN 1024-4530

INTERNATIONAL
UNION OF
RADIO SCIENCE

UNION
RADIO-SCIENTIFIQUE
INTERNATIONALE

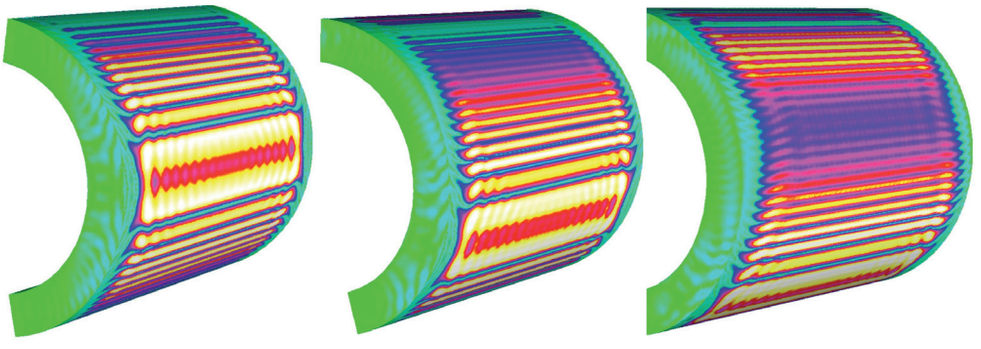

No 336
March 2011

URSI, c/o Ghent University (INTEC)
St.-Pietersnieuwstraat 41, B-9000 Gent (Belgium)

Contents

Front cover: "The near fields for a 41x41 patch array on a finite cylindrical grounded dielectric for scan angles of (l-r) 0ø, 30ø, and 60ø. These were computed using the non-conformal, non-overlapping finite-element domain-decomposition method presented in the paper by M. Vavoukis and J. F. Lee, in the special section on "Computational Electromagnetics for Large Antenna Arrays."

For information, please contact :
The URSI Secretariat
c/o Ghent University (INTEC)
Sint-Pietersnieuwstraat 41, B-9000 Gent, Belgium
Tel.: (32) 9-264 33 20, Fax: (32) 9-264 42 88
E-mail: info@ursi.org

The International Union of Radio Science (URSI) is a foundation Union (1919) of the International Council of Scientific Unions as direct and immediate successor of the Commission Internationale de Télégraphie Sans Fil which dates from 1913.

Editorial

Special Section on Computational Electromagnetics for Large Array Antennas

In this issue, we are most fortunate to have a special section on "Computational Electromagnetics for Large Array Antennas." The Guest Editor for this section is Jin-Fa Lee of the ElectroScience Laboratory, The Ohio State University (1320 Kinnear Rd., Columbus, OH 43212 USA; Tel: +1-614-292-7270; Fax: +1-614-292-7297; E-mail: jinlee@esl.eng.ohio-state.edu). The *Radio Science Bulletin* is most grateful for his efforts in preparing this special section.

Large (but finite) array antennas present special challenges for computational electromagnetics. Because they are electrically large, the number of unknowns necessary to accurately model their behavior can quickly become very large. Using classical or general-purpose simulation approaches for such problems can be very challenging. It is not unusual to have problems involving matrices with millions to hundreds of millions of unknowns. Because the arrays are finite, the effects of the edges that truncate the arrays are important, and methods based on infinite arrays (often taking advantage of the periodicity of the infinite array) do not give sufficiently accurate results. It is therefore necessary to use approaches that divide the problem into manageable "sub-problems," while still allowing accurate simulation of the edge effects when the results of these "sub-problems" are combined to give the results for the whole array. The three papers in this special section describe different approaches to doing this.

While the papers in this special section specifically treat the important and interesting problem of large array antennas, many of the methods they describe have been used for a wide variety of other computational electromagnetics problems involving electrically large scatterers or radiators. This special section thus provides a very readable introduction to some of the most modern techniques used for such electrically large computational problems.

The first of the special-section papers is by R. W. Kindt, K. Sertel, and J. L. Volakis. They describe techniques for solving the large array antenna problem using decomposition methods involving the Finite-Element Method or integral-equation approaches. This is an excellent paper to read first, because the authors make a conscious attempt to introduce the concepts of the problem and the solution approaches presented using language that should be readily understandable by most radio scientists. They begin with a discussion of the use of commercially available general-purpose electromagnetic simulators for solving large array problems. This provides an introduction to the various techniques used in such simulators, as well as a review of the operation counts and memory requirements of such techniques. The authors then review the techniques available for modeling *infinite* arrays, and discuss the problems associated with applying such techniques to large *finite* arrays. The use of domain-decomposition techniques with the Finite-Element Method for solving large finite array problems is introduced and explained. This is followed by a description of the Array-Decomposition Method, based on the use of integral equations to solve the problem. Part of the advantage of this method is that the periodicity of the array and the resulting many identical coupling paths in the array can be exploited to yield a block-Toeplitz structure for the matrices involved. The authors then describe how array decomposition can be combined with the Fast Multipole Method as another approach to solving the large array problem. It is shown that one of the benefits of this approach is that the matrix-storage requirements remain the same regardless of the size of the array. The issues of modeling the interaction of the array with the structure on which it is mounted are addressed. As noted, this paper provides a particularly nice introduction to the special section.

The second special-section paper, by Rob Maaskant, Raj Mittra, and Anton Tijhuis, describes the use of a multi-level version of the Characteristic Basis Function Method. The authors describe how this approach has been used to model various aspects of the Square Kilometre Array project. The Characteristic Basis Function Method is an enhancement to the widely used Method of Moments. It uses special "macro" basis functions – the characteristic basis functions – that have the effect of compressing the moment matrix such that no iteration is necessary to solve it. It can solved simultaneously for multiple right-hand sides. The authors begin with a very nice review of the various methods used for treating large array problems. They then illustrate how the matrix equation can be reduced by using a simple example. The description of the process is summarized with a simple step-by-step recipe. This is followed by showing how the far-field pattern and the input-impedance matrix of the array can be computed using the Multi-Level Characteristic Basis Function Method. They demonstrate the method by applying it to several large-array problems involving tapered-slot antenna elements. The largest of these involved 25 subarrays composed of 64 elements each. Using the method described, it was possible to solve this problem on a notebook computer.

The third special-section paper is by M. Vavoukis and J. F. Lee. It describes a different approach to the large-array problem. While it is again based on a combination of domain decomposition

and the Finite-Element Method, it also uses a finite-element tearing and interconnecting algorithm to take advantage of the repetition within the array. Furthermore, the domain-decomposition methods employed have an important distinction: they are non-conformal and non-overlapping. This means that once the computational domain is decomposed into subdomains, the mesh on either side of the interface between two of the subdomains can be totally different. As explained by the authors, this has significant advantages. The paper begins with an important discussion of why domain-decomposition methods are used in electromagnetic problems. The authors then summarize the main elements of the solution approach they present. A comprehensive review of the literature on domain-decomposition methods is presented. This is followed by sections describing each of the three main elements of the solution approach. The notation is explained. The boundary-value problem is described. This includes a discussion of how domain decomposition can be applied to Maxwell's equations, and an analysis of the convergence of the method. Two different simple approximations to key quantities are introduced. A new, non-conforming Finite-Element Method is then presented. This is followed by an explanation of how key quantities are discretized, and the introduction of the finite-element tearing and interconnecting algorithm. Having explained the solution method in detail, the authors present a variety of numerical examples. All computations were carried out on a desktop computer. The examples include a radar array, and a series of finite cylindrical conformal arrays ranging in size from 11×11 to 41×41 elements. Comparisons are made between the planar and conformal versions of the arrays to illustrate the effect curvature has on the performance of the arrays.

Our Other Papers

Commission C has done an outstanding job of providing us with *Reviews of Radio Science* during this triennium. The invited paper in this issue by J. Pérez-Romero, D. Noguet, M. López-Benítez, and F. Casadevall is our fourth such review. It discusses the important topic of how cognitive radio can be used together with the concept of dynamic-spectrum-access networks to significantly improve utilization of the radio spectrum. The paper begins with a description of how cognitive-radio techniques can be used to provide dynamic spectrum access. The techniques that have to be developed to implement this are described. These include the ability to sense spectrum (and particularly, unused spectrum); spectrum management, involving the best choice of available spectrum considering other users' requirements; spectrum mobility, which involves the ability to sense when the primary user of a range of spectrum becomes active, and the ability to shift spectral use to accommodate that user's needs; and spectrum sharing, which enables multiple secondary spectrum users to share available spectrum. The techniques for sensing spectrum are examined in detail. This is followed by a survey of standardization activities for dynamic-spectrum-access networks. Methods of measuring spectrum to identify available spectrum are discussed. This includes techniques and equipment for measuring spectrum, various measurements of spectrum occupancy, and other spectrum metrics. The ways of applying all of these measures to cognitive radio are explained. The paper ends with a most interesting set of measurements demonstrating how all of these techniques can be applied, made in an urban area of Barcelona, Spain. The measurements showed duty cycles ranging from a few percent to less than 20% for a very large range of frequencies. The results suggested that there was a very significant amount of spectrum that could be potentially used if cognitive radio and dynamic-spectrum-access techniques were employed.

The efforts of M. Luise, Associate Editor for Commission C, and Phil Wilkinson in bringing us this *Review* are gratefully acknowledged.

Gordon James has provided us with a most interesting Commission H *Review of Radio Science*. In his invited paper, he reviews the major developments in our understanding of electric antennas in space plasmas. He begins with an overview of research in this area. He then looks at active dipoles as probes. He presents the linear theory for such dipoles, and reviews the dispersion relations and their radiation properties. He looks at radiation in a cold magnetoplasma, and the radiation and resistance of a dipole in a plasma. Other topics covered for active dipoles include the effects of a hot plasma, the full EM theory, and radiation and measurements at VLF and in the transition domain. Observations and theory related to nonlinear phenomena are then explored. The passive dipole as a probe is introduced. The importance of the accurate determination of the effective length of such a dipole in a plasma is explained, and the challenges of making such a determination are examined. Related results from computer modeling and laboratory measurements are reviewed. The paper concludes with a summary of open questions that need to be answered in order to advance the use of dipole probes and our understanding of space plasmas.

The efforts of Ondrej Santolik, Associate Editor for Commission H, and Phil Wilkinson in bringing us this *Review* are greatly appreciated.

Our Other Contributions

We have two book reviews in this issue, brought to us by Kristian Schlegel. The books deal with dusty plasmas, and with measurements made using RF and optical waves.

Jim Lin's "Radio-Frequency Radiation Safety and Health" column looks at the role of the International Non-Ionizing Radiation Protection Commission (ICNIRP) in setting exposure guidelines for radio-frequency fields. In particular, the guidelines for magnetic resonance imaging are examined.

Register and Make Reservations!

Now is the time to make your reservations and travel plans to attend the XXX URSI General Assembly and Scientific Symposium, to be held August 13-20, 2011, in Istanbul, Turkey. Early registration ends May 16, 2011. You can view the scientific program and register at http://www.ursigass2011.org. I urge you plan on attending, and I look forward to seeing you there.

URSI Accounts 2010

The world is changing fast and the success of scientific organizations such as URSI is highly dependent on the flexibility to adapt to these changing environments. The economic situation in many countries has put stress on the funds available for scientific and long-term research, however up till now, with a rather limited impact on the URSI accounts themselves. The URSI accounts for 2010 show a positive result which is normal for a year preceding the GASS and also contributions from Member Committees are varying which is also usual. The continuous effort to reduce the administrative costs has resulted in keeping the spending well under control and the current status of the assets allow us to take a few initiatives. These initiatives are however an investment in the future of URSI and target Young Scientists and young researchers to stimulate them to participate at URSI events through Student Paper Competitions and Young Scientists awards. Their involvement in URSI, their commitment and their research results are both a basis for the future existence of URSI but will also be of benefit for our society as a whole.

Paul Lagasse
Secretary General

BALANCE SHEET: 31 DECEMBER 2010

	EURO	EURO
ASSETS		
Dollars		
Merrill Lynch WCMA	0.00	
Fortis	4,566.00	
Smith Barney Shearson	4,882.55	
		9,448.55
Euros		
Banque Degroof	86.20	
Fortis zichtrekening	58,473.93	
Fortis spaarrekening	378,340.74	
		536,900.87
Investments		
Demeter Sicav Shares	22,681.79	
Rorento Units	111,414.88	
Aqua Sicav	63,785.56	
Merrill-Lynch Low Duration (304 units)	0.00	
Massachusetts Investor Fund	251,965.13	
Provision for (not realised) less value	(8,631.61)	
Provision for (not realised) currency differences	(60,253.45)	
	380,962.30	
684 Rorento units on behalf of van der Pol Fund	12,414.34	
		393,376.64
Short Term Deposito		0.00
Petty Cash		1,776.83
Total Assets		941,502.89
Less Creditors		
IUCAF	12,850.45	
ISES	5,078.63	
		(17,929.08)
Balthasar van der Pol Medal Fund		(12,414.34)
NET TOTAL OF URSI ASSETS		**911,159.47**

The net URSI Assets are represented by:	EURO	EURO
Closure of Secretariat		
Provision for Closure of Secretariat		90,000.00
Scientific Activities Fund		
Scientific Activities in 2011	75,000.00	
Publications in 2011	20,000.00	
Young Scientists in 2011	40,000.00	
Administration Fund in 2011	85,000.00	
Scientific paper submission software in 2011	0.00	
I.C.S.U. Dues in 2012	5,000.00	
		225,000.00
XXIX General Assembly 2008/2011 Fund:		
During 2011 (GA 2008)		0.00
During 2009 - 2010 - 2011 (GA 2011)		160,000.00
Total allocated URSI Assets		475,000.00
Unallocated Reserve Fund		436,159.47
		911,159.47

Statement of Income and expenditure for the year ended 31 December 2010

I. INCOME		
Grant from ICSU Fund and US National Academy of Sciences	0.00	
Allocation from UNESCO to ISCU Grants Programme	0.00	
UNESCO Contracts	0.00	
Contributions from National Members (year -1)	5,744.00	
Contributions from National Members (year)	192,296.00	
Contributions from National Members (year +1)	42,627.00	
Contributions from Other Members	0.00	
Special Contributions	0.00	
Contracts	0.00	
Sales of Publications, Royalties	1,050.00	
Sales of scientfic materials	0.00	
Bank Interest	4,319.83	
Other Income	4,158.00	
Total Income		**250,194.83**
II. EXPENDITURE		
A1) Scientific Activities		65,015.31
General Assembly 2005/2008/2011	29,202.94	
Scientific meetings: symposia/colloqiua	33,750.00	
Working groups/Training courses	0.00	
Representation at scientific meetings	2,062.37	
Data Gather/Processing	0.00	
Research Projects	0.00	
Grants to Individuals/Organisations	0.00	
Other	0.00	
Loss covered by UNESCO Contracts	0.00	
A2) Routine Meetings		14,857.80
Bureau/Executive committee	14,857.80	
Other	0.00	

A3) Publications		13,676.45
B) Other Activities		2,000.00
Contribution to ICSU	0.00	
Contribution to other ICSU bodies	2,000.00	
Activities covered by UNESCO Contracts	0.00	
C) Administrative Expenses		92,920.25
Salaries, Related Charges	80,380.14	
General Office Expenses	13,421.10	
Travel and representation	7,030.38	
Office Equipment	2,701.50	
Accountancy/Audit Fees	5,178.26	
Bank Charges/Taxes	2,277.51	
Loss on Investments (realised/unrealised)	(18,068.64)	
Total Expenditure:		**188,469.81**
Excess of Expenditure over Income		61,725.02
Currency translation diff. (USD => EURO) - Bank Accounts		844.29
Currency translation diff. (USD => EURO) - Investments		18,238.29
Currency translation diff. (USD => EURO) - Others		127.25
Accumulated Balance at 1 January 2009		830,224.62
		911,159.47

Rates of exchange

January 1, 2010	1 $ = 0.6930 EUR
December 31, 2010	1 $ = 0.7610 EUR

Balthasar van der Pol Fund

684 Rorento Shares : market value on December 31 (Aquisition Value: USD 12.476,17/EUR 12.414,34)	32,654.16
Book Value on December 31, 2010/2009/2008/2007	12,414.34

Market Value of investments on December 31, 2010-2007

Demeter Sicav	69,135.00
Rorento Units (1)	620,620.00
Aqua-Sicav	89,044.52
M-L Low Duration	0.00
Massachusetts Investor Fund	183,080.07
	961,879.59
Book Value on December 31, 2010/2009/2008/2007	393,376.64

(1) Including the 684 Rorento Shares of v d Pol Fund

APPENDIX : Detail of Income and Expenditure

I. INCOME		
Other Income		
Income General Assembly 2005	0.00	
Income General Assembly 2008	0.00	
Young scientist support (Japan)	4,158.00	
Support Kogamidal	0.00	
Closure Radio Science Press	0.00	
Commission B+C	0.00	
Mass investtors growth stock Fund	0.00	
Other	0.00	
		4,158.00
II . EXPENDITURE		
General Assembly 2008		
Organisation	0.00	
Vanderpol Medal	0.00	
Young scientists	0.00	
Expenses officials	0.00	
Student support	0.00	
General Assembly 2011		
Organisation	29,202.94	
		29,202.94
Symposia/Colloquia/Working Groups		
Commission A	0.00	
Commission B	9,000.00	
Commission C	2,000.00	
Commission D	3,000.00	
Commission E	0.00	
Commission F	7,800.00	
Commission G	3,000.00	
Commission H	2,000.00	
Commission J	750.00	
Commission K	1,200.00	
Central Fund	5,000.00	
		33,750.00
Contribution to other ICSU bodies		
FAGS	0.00	
IUCAF	2,000.00	
		2,000.00
Publications		
Printing ‘The Radio Science Bulletin’	6,129.84	
Mailing ‘The Radio Science Bulletin’	7,546.61	
		13,676.45

IUCAF Annual Report for 2010

1. Introduction

The Scientific Committee on Frequency Allocations for Radio Astronomy and Space Science, IUCAF, was formed in 1960 by its sponsoring Scientific Unions, COSPAR, the IAU, and URSI. Its brief is to study and coordinate the requirements of radio frequency allocations for passive (i.e., non-emitting or receive-only) radio sciences, such as radio astronomy, space research and remote sensing, in order to make these requirements known to the national administrations and international bodies that allocate frequencies. IUCAF operates as a standing inter-disciplinary committee under the auspices of ICSU, the International Council for Science. IUCAF is a Sector Member of the International Telecommunication Union (ITU).

2. Membership

At the end of 2010 the membership for IUCAF was:

URSI	S. Ananthakrishnan (Comm J)	India
	S. Reising (Comm F)	USA
	I. Häggström (Comm G)	Sweden
	A. Tzioumis (Comm J)	Australia
	W. van Driel (Comm J)	France
IAU	H. Chung	Korea (Republic of)
	H.S. Liszt (Vice Chair)	USA
	M. Ohishi (Chair)	Japan
	K.F. Tapping	Canada
	A. Tiplady	South Africa
COSPAR	Y. Murata	Japan
at large:	W.A. Baan	the Netherlands
	D.T. Emerson	USA

Dr. Harvey Liszt of the United States of America was appointed vice chairman of IUCAF in February 2010. IUCAF also has a group of Correspondents, in order to improve its global geographic representation and for issues on spectrum regulation concerning astronomical observations in the optical and infrared domains.

3. International Meetings

During the period of January to December 2010, its Members and Correspondents represented IUCAF in the following international meetings:

January-February	ITU-R Working Party 1A (spectrum management), Geneva, Switzerland
May - June	The 3rd IUCAF Summer School on Spectrum Management, Tokyo, Japan
June	ITU-R Working Party 7D (radio astronomy), Geneva, Switzerland
June	ITU-R Working Party 1A (spectrum management) Geneva, Switzerland
July	Space Frequency Coordination Group meeting (SFCG-30), Palm Cove, Australia
September	AP-RASC'10 (2010 Asia-Pacific Radio Science Conference), Toyama, Japan
October	ITU-R Study Group 7 (Science services) and Working Party 7D (radio astronomy), Geneva, Switzerland

Additionally, many IUCAF members and Correspondents participated in numerous national or regional meetings (including CORF, CRAF, RAFCAP, the FCC etc.), dealing with spectrum management issues, such as the preparation of input documents to various ITU forums.

4. IUCAF Business Meetings

During 2010 IUCAF had face-to-face committee meetings before each of the ITU-R WP 7D meetings and the IUCAF Summer School listed above. During these ITU sessions ad-hoc meetings of IUCAF were held to discuss further its meeting strategy, financial issues, recruitment of new members, initiatives and future contributions to international spectrum management meetings and so on.

Although such face-to-face meetings have been convenient and effective, throughout the year much IUCAF business is undertaken via e-mail communications between the members and correspondents.

5. The 3rd IUCAF-Summer School

The 3rd IUCAF summer school on spectrum management for radio astronomy was held between May 31st and June 4th, 2010, at the Mitaka campus of the National Astronomical Observatory of Japan (NAOJ), located about 20 km from central Tokyo. There were 44 participants from 13 countries: Japan (21), Germany (3), UK (2), Denmark (1), the Netherlands (2), Portugal (2), USA (5), China (2), South Korea (2), Australia (2), Malaysia (1) and Nigeria (1). There were about 10 young (under 35 years old) people that were new to the spectrum management and seven regulators from Japan, China and Europe.

The summer school program covered introductions to radio astronomy and Earth observations, radio science and related technologies and procedures on how to use (allocate) frequency resources. This includes the structure and role of the International Telecommunication Union

Figure 1. The participants in the third IUCAF Summer School in Tokyo

(ITU) and regional telecommunities (CEPT, CITEL, APT); the roles of science bodies to protect radio astronomy and Earth observations (IUCAF, CRAF, CORF, RAFCAP); interference mitigation techniques; and radio interference topics such as Power Line Telecommunications (PLT), RFID, Ultrawideband (UWB) devices, Software-Defined Radio (SDR), Cognitive Radio Systems (CRS), and others. There was also a lecture on the SKA project and radio quiet zones for future radio astronomy. The summer school program and the presentation files used at the summer school are available from the IUCAF's web page at http://www.iucaf.org/SSS2010/presentations/SS2010_presentations.htm .

It should be noted that the summer school was supported financially by IUCAF, CRAF, CORF and RAFCAP.

The summer school was run in a very friendly atmosphere and excellent weather, and the participants, especially young students, actively asked questions. In the middle of the summer school, the participants enjoyed a half-day tour to the Nobeyama Radio Observatory of NAOJ, where the 45-m millimetre-wave telescope, the Nobeyama Millimeter Array, and the Nobeyama Radio Heliograph are located.

It can be concluded that the 3rd IUCAF summer school was quite successful, and that the participants were able to learn many topics to be utilized to ensure the protection of radio astronomy and Earth observations towards better understanding of the Earth and the Universe.

6. Potecting the Passive Radio Science Services

At the ITU, the work in the various Working Parties of interest to IUCAF was focused on the relevant agenda items that were adopted in 2007 for WRC-12 of ITU, the World Radiocommunication Conference in 2012, as well as on the creation and maintenance of various ITU-R Recommendations and ITU-R Reports.

A WRC-12 agenda item which is most relevant to radio astronomy concerns is the use of the radio spectrum between 275 and 3 000 GHz. This frequency range is used for radio astronomy observations of important spectral lines and continuum bands used in studies to understand the Universe. New receiver technology and new instruments (both ground-based and space based) being used in the 275 – 1 000 GHz region are helping to refine the results of radio astronomy observations in this spectrum range, while similar developments in the 1 000-3 000 GHz range are leading to a better understanding of specific spectral lines and atmospheric windows that are of interest to radio astronomers. Significant infrastructure investments are being made under international collaboration for the use of these bands between 275 and 3 000 GHz. For example, the Atacama Large Millimeter/submillimeter Array (ALMA), a facility currently under construction in northern Chile, will provide new insights on the structure of the universe through observations in the 30 - 1 000 GHz range. Space-based highly sensitive telescopes observe spectral lines from a variety of molecules and atoms and continuum thermal radiation from very small particles (cosmic dust).

No frequency allocations for the use of this frequency range will be made at WRC-12, but the radio astronomy community has to identify a list of specific bands of interest. This list was established in close collaboration with the IAU Working Group on Important Spectral Lines, and a new ITU-R Recommendation RA.1860 (Preferred frequency bands for radio astronomical measurements in the range 1-3 THz) was published on February, 2010. Terrestrial use of frequencies in this range is strongly constrained by the Earth's atmosphere. This is especially true above 1 000 GHz, where atmospheric absorption at sea level sites can exceed thousands of dB per km due to the effects of water vapour and oxygen. A new Report ITU-R RA.2189, which was published in 2010, utilized these physical conditions and reports that this frequency range can be used both by the passive (receive-only) and active (transmitting) radio services with little possibility of interference. IUCAF members actively participated in the drafting and approval process of these important Recommendations and Reports.

The work towards a new ITU-R Report on "The essential role and global importance of radio spectrum use for Earth observations and for other related science applications", which contains a description of benefits from spectrum use by radio astronomy and space research, has been completed, and the Report (RS. 2178) was published in October, 2010.

Power Line Communications (PLC) utilizing the 2-30 MHz frequency range is a technology to send electrical signals through power lines for communication purposes. This technology enables broadband Internet access and home LAN by means of "existing" power lines. Since the power lines are designed and installed to carry current at 50/60Hz only, there has been serious concern that the electromagnetic field radiated by the power lines may cause harmful interferences to the radio communication services such as broadcasting, communication, and radio astronomy observations. In this regard IUCAF members submitted to ITU-R Working Party 1A (spectrum management) several contribution papers containing measurement results of actual harmful interference from PLC and theoretical analyses. These study results were welcomed by the ITU-R Working Party 1A, and were adopted as a part of the ITU-R Report SM.2158 (Impact of power line telecommunication systems on radiocommunication systems operating in the LF, MF, HF and VHF bands below 80 MHz). The new Report was updated in 2010, by incorporating new IUCAF contributions.

IUCAF member, A. Tzioumis, is the Chair of ITU-R Working Party 7D (radio astronomy), and IUCAF member, H. Chung, is the vice-chairman of ITU-R Study Group 7 (Science Services). IUCAF member S. Ananthakrishnan is the Chair of URSI Commission J (radio astronomy).

7. Contact with the Sponsoring Unions and ICSU

IUCAF maintains regular contact with its supporting Scientific Unions and with ICSU. The Unions play a strong supporting role for IUCAF and the membership is greatly encouraged by their support.

Pursuing its brief, IUCAF continued its activities towards strengthening its links with other passive radio science communities, in particular in space science, and defining a concerted strategy in common spectrum management issues.

IUCAF member W. van Driel has been appointed president of IAU Commission 50 (Protection of existing and potential observatory sites). Two IUCAF members, A. Tzioumis and M. Ohishi, have joined the Organising Committee of IAU Commission 50. IUCAF member, A. Tzioumis, was Chair of the Working Group on Radio Frequency Interference of IAU Division X (radio astronomy) until August 2009, and IUCAF member, W.A. Baan, has been appointed as the new chair of this Working Group. IUCAF chair, M. Ohishi, chairs the Working Group on Astrophysically Important Spectral Lines of Division X. The IUCAF chair, M. Ohishi, has also been appointed the president of IAU Commission 5 on Documentation and Astronomical Data. He is also appointed the official liaison between the IAU and the ITU.

The preparation towards the next URSI General Assembly and Scientific Symposium (GASS), to be held in August 2011 in Istanbul, is ongoing, led by the Chair of URSI Commission J (radio astronomy), S. Ananthakrishnan, who is also an IUCAF member. Several session proposals were submitted, and a session on spectrum allocation and use issues (session J08) will be held during the URSI GASS. Many IUCAF members have already submitted papers to be presented at this GASS. IUCAF members also actively participated in national URSI meetings, such as AP-RASC 2010 held in Toyama, Japan and the USNC-URSI National Radio Science Meeting in Boulder, CO, USA.

The scientific assembly of the COSPAR was held in July, 2010, in Bremen, Germany. Some IUCAF members attended the COSPAR meeting.

8. Publications and Reports

IUCAF has a permanent web address, http://www.iucaf.org, where the latest updates on the organization's activities are made available. All contributions to IUCAF-sponsored meetings are made available on this website.

IUCAF produced a White Paper discussing extensive ITU-R items of concern to radio astronomy on the agenda of the upcoming World Radiocommunication Conference 2012 (WRC12), which is available at http://www.cv.nrao.edu/~hliszt/RFI/CPM/IUCAFWhitePaper.pdf .

9. Conclusion

IUCAF interests and activities range from preserving what has been achieved through regulatory measures or mitigation techniques, to looking far into the future of high frequency use, giant radio telescope use and large-scale distributed radio telescopes. Current priorities, which will certainly keep us busy through the next years, include the use of powerful radars and satellite down-links close in frequency to the radio astronomy bands, the coordination of the operation in shared bands of radio observatories and powerful transmissions from downward-looking satellite radars, the possible detrimental effects of ultra-wide band (UWB) transmissions at around 24/79 GHz regions and high-frequency power line communications (HF-PLC) on all passive services, the scientific use of the 275 to 3 000 GHz frequency range, and studies on the operational conditions that will allow the successful operation of future giant radio telescopes.

IUCAF is grateful for the moral and financial support that has been given for these continuing efforts by ICSU, COSPAR, the IAU, and URSI during the recent years. IUCAF also recognizes the support given by radio astronomy observatories, universities and national funding agencies to individual members in order to participate in the work of IUCAF.

Masatoshi Ohishi, IUCAF Chair
IUCAF website : http://www.iucaf.org
IUCAF contact : iucafchair@ iucaf.org

Special Section on Computational Electromagnetics for Large Antenna Arrays

A Review of Finite Array Modeling via Finite-Element- and Integral-Equation-Based Decomposition Methods

R.W. Kindt
K. Sertel
J.L. Volakis

Abstract

There are many techniques available for the design and analysis of finite array structures. For the reader trying to decide what computational method is best suited for the array-design problem at hand, this article will help clarify what factors are important in receiving an expedient and accurate answer. Without getting too technical or exhaustive, this article details some of the relevant aspects of existing computational electromagnetic techniques, explaining some advantages and disadvantages of less-accurate methods compared to the most-accurate methods. This partial review covers several options for finite array design, including approximate methods based on infinite array analysis, brute-force generalized approaches, moderately accurate FEM-based (Finite-Element-Method-based) decomposition techniques, and concludes with a review of efficient and rigorous integral-equation-based methods. Finite array methods based on integral-equation formulations, while the most computationally intense, achieve the most accurate solutions available. When formulated to specifically address finite array problems, these techniques can be highly efficient without compromising generality.

1. Introduction

There are many commercial software packages on the market for computational electromagnetic (CEM) simulation (e.g., *HFSS*, *FEKO*, *CST*, *TICRA*). However, for the engineer intending to design finite antenna arrays, these tools are best suited for general-purpose design, and are not optimized for modeling array-type structures. While one can make the argument that general-purpose codes are more robust than those specialized for solving a particular type of problem, i.e., finite arrays, it is also true that a generalized approach is simply not as fast or as efficient for tackling a specific type of problem. Specialized design tools for modeling finite arrays can be fast, efficient, and arguably just as robust as the general-purpose tools if the techniques reduce to a generalized approach in the limiting case of a single array element.

Many engineers are not aware that sophisticated and mature tools exist for the accurate analysis of finite array structures. The purpose of this article is to describe some of these array tools, using simpler language intended for a wider audience. This partial review begins with a look at computational electromagnetic techniques for various types of arrays based on either finite-element formulations, integral-equation formulations, or a combination of the two. Without getting too technical, this article explains some of the advantages and disadvantages of the various techniques, with details on their capabilities and limitations. Several options for finite array design are covered, including simple approximate methods (based on infinite array analysis), brute-force generalized approaches, and moderately accurate Finite-Element-Method-based decomposition techniques. It concludes with a review of highly efficient and rigorous integral-equation-based methods, ideal for the analysis of finite arrays. Although these integral-equation-

R. W. Kindt is with the Naval Research Laboratory, 4555 Overlook Ave. SW, Washington, DC 20375 USA; e-mail: rick.kindt@nrl.navy.mil. K. Sertel and J. L. Volakis are with the ElectroScience Lab, The Ohio State University, 1320 Kinnear Rd, Columbus, OH 43212 USA; e-mail: sertel.1@osu.edu, volakis.1@osu.edu.

based methods are the most computationally intense, they also guarantee the most accurate and expedient solutions available. The techniques covered here can be formulated as a part of any antenna software design suite for fast, efficient, and accurate solutions of array design problems. They can also lead to a robust and generalized solution approach to general-purpose analysis of individual antennas (i.e., a single array element), or other electromagnetic structures.

2. General-Purpose Electromagnetic Simulators

For electromagnetic design, it is advantageous to start with a general-purpose simulator tool, many being available commercially. These tools are valuable for design because they are suitable for a wide range of problems. Over the years, general-purpose computational electromagnetic tools have become increasingly powerful, and to some degree they can be used to model small finite arrays. However, it is important to understand the limitations of the general-purpose simulators, and to understand that even with unlimited resources (i.e., supercomputing facilities), there are practical limits to the maximum size of solvable problems.

This review focuses on full-wave numerical techniques that solve Maxwell's equations in the frequency domain. The Finite-Element Method is a popular solver that uses partial differential equations to model electromagnetic-wave phenomena. The Method of Moments (MoM), an analysis technique based on integral-equation formulations, is also popular for solving electromagnetic problems. Details on these two formulation types – Finite-Element Method and MoM – can be found in a number of popular electromagnetic texts [1-4]. Both approaches, the Finite-Element Method and the MoM, involve solving linear systems of equations of the form $[A]\{x\} = \{b\}$, where $\{x\}$ is the solution to the problem, viz., $\{x\} = [A]^{-1}\{b\}$. Matrix storage is a significant factor limiting the maximum-solvable problem size, as geometries that increase in size linearly often require storage that grows nonlinearly. In practical terms, a problem twice as large will typically require significantly more than double the storage. It will also take much longer than twice the time to solve. Because of this, the past two decades have focused on decreasing storage and increasing speed for solving large-scale computational electromagnetic problems.

The MoM has a dense system of equations $[A]$, requiring $O\left(N^2\right)$ storage, where N denotes the length of the solution vector $\{x\}$, which requires $O(N)$ storage. For the Finite-Element Method, the system of equations is sparsely populated, such that $[A]$ requires only $O(N)$ storage. Although the Finite-Element Method's matrix storage is relatively insignificant, factorization can still require up to $O\left(N^2\right)$ storage. To put this comparison in practical terms, let us consider a problem having a million degrees of freedom, with each number needing four bytes of storage. The Finite-Element Method, with $O(N)$ storage, requires only several megabytes (MB) to store the matrix, whereas the MoM, having $O\left(N^2\right)$ storage, requires several *terabytes* (TB) for the entire matrix. While this could make the MoM appear less attractive as a computational method, there are other critical factors to consider in the success of a computational electromagnetic tool. For the MoM, it is generally possible to use compression techniques to reduce the matrix-storage burden.

The reader may also be familiar with some popular techniques for reducing matrix storage/accelerating solutions, such as the Fast Multipole Method (FMM), the Multi-Level Fast Multipole Algorithm (MLFMA), the Adaptive Integral Method (AIM), and the Adaptive Cross-Approximation (ACA) Method, to name a few [5-10]. Using these so-called fast methods, it is possible to reduce the matrix storage of the MoM such that it is on par with the ordinary Finite-Element Method, or $O(N)$.

This is difficult to achieve without sacrificing accuracy, as compression techniques typically lead to a loss of information, and usually apply best to special problems. Further, although $O(N)$ storage may be achieved with fast methods, the actual value may be $4N$, $10N$, etc. Typically, the Fast Multipole Method has $O\left(N^{1.5}\right)$ matrix storage, and the Multi-Level Fast Multipole Algorithm has $O(N \log N)$. For the same problem with a million degrees of freedom considered earlier, this equates to matrix storage of several gigabytes (GB) and tens of megabytes, respectively, for the Fast Multipole Method and the Multi-Level Fast Multipole Algorithm. Hence, matrix compression as achieved by these can make the MoM competitive with the Finite-Element Method.

The more costly operation in terms of storage is due to the factorization/computation of $[A]^{-1}$, required to solve the system of equations. To avoid costly matrix factorization, it is possible to solve the system of equations iteratively by successively (intelligently) guessing at $\{x\}$ [11]. Iterative operations require only $O(N)$ storage, but the success of solution methods depends on the conditioning of the matrix, and convergence (achieving the correct solution) is not guaranteed. As N increases (i.e., for larger arrays), the matrix $[A]$'s condition number also increases, implying large numerical round-off errors that accumulate and may prevent convergence. Therefore, simply improving the storage of a computational electromagnetic method is not sufficient to guarantee a solvable problem. Finite-Element Method systems can have relatively poor condition numbers to begin with, making their iterative solution slow. While some commercial simulation packages support iterative solution methods on demand, they are therefore primarily not employed for this reason. Although convergence is typically better for the MoM, the same is generally true for problems with a large system matrix. In practice, for iterative methods, it is generally necessary to use some level of direct matrix factorization to partially solve the system of equations. This process is typically referred to as matrix

preconditioning, and has the effect of reducing the matrix system's condition number [11]. Standard matrix preconditioning techniques can dramatically help improve the solution of the matrix system. However, in recent years, major advances have been made in direct solvers for linear systems of equations [12-14]. These techniques have significantly improved the speed and utility of general-purpose EM solvers.

Nevertheless, the resources required by standard factorization methods increase nonlinearly as the systems of equations grow linearly. That is, a problem twice as large in matrix size would require resources much greater than a factor of two. Although general-purpose computational electromagnetic tools may thus be useful for design, the brute-force approach to solving problems is not suitable for modeling large finite array problems. At best, for large finite array problems, the solution process of general-purpose computational electromagnetic tools would be slow and inefficient, a limitation that cannot be alleviated, even with unlimited computational resources (i.e., supercomputing facilities). For general-purpose computational electromagnetic tools, the absolute best-case matrix storage will of course be $O(N)$, but even with the best factorization/solution scheme, the storage required for factorization/solution will likely be significantly more. Fortunately, specialized decomposition methods for array analysis can lead to considerably faster solutions and require significantly less than $O(N)$ matrix storage and factorization.

3. Infinite Array Analysis

Rather than jumping straight into a full finite array analysis, we start by considering the simpler case of infinite array modeling. Efficient techniques exist to characterize periodic array structures using a single, infinitely repeating cell [15-17]. With this approach, a quick and useful answer can be derived from solving a comparably small problem,

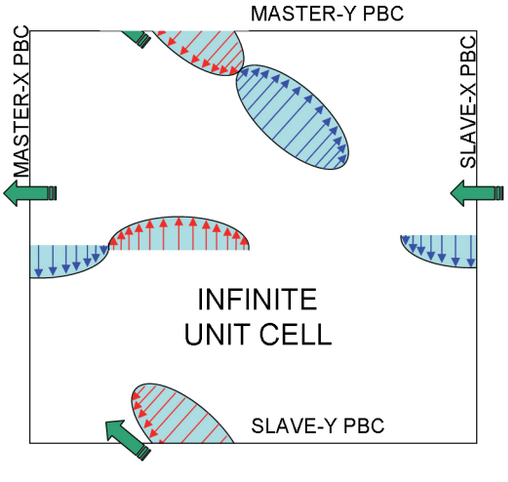

Figure 1. Periodic boundary conditions exactly continue the phase and amplitude of electromagnetic waves/fields from one side of the unit cell to the other, and are more accurate than waveguide simulators.

i.e., a single identical array element in the infinite array. Ultimately, the design engineer intends to build a finite array, but the assumption (for better or worse) is that a large finite array will behave similarly to an infinite array. Although this analysis ignores edge effects, the infinite array design is a reasonable place to start. Most commercial simulation packages include support for some type of infinite cell modeling.

The accuracy of the infinite array simulation depends on several important factors that must be fully understood. First, accuracy depends strongly on the periodic boundary conditions of the unit cell forming the array, as shown in Figure 1. A popular option for modeling the infinite array cell is the waveguide-simulator approach [18]. In the waveguide simulator, a single array element is modeled using perfect electric conductor (PEC) and perfect magnetic conductor (PMC) walls to truncate the electric and magnetic fields of the unit cell. This technique is relatively simple to implement in both the Finite-Element Method and the MoM. The advantage of the waveguide-simulator technique is simplicity, and a quick and roughly accurate answer at the initial stage of the finite array design. However, this approach assumes field symmetry within the unit cell of the array, and also cannot be used to predict scan performance. If the element of the array is not geometrically symmetric, the answer is only roughly accurate, at best. The preferred approach is to therefore enforce periodic boundary conditions on the sidewalls of the unit cell. With this approach, the phase/magnitude of the vector fields at the master boundary continue seamlessly as they enter the slave boundary on the opposite side of the cell [19]. This technique can be implemented in both the Finite-Element Method and the MoM, and, more importantly, it makes no assumptions about field or geometric symmetry within the unit cell. Further, it is possible to model the phased-array scan performance for predicting scan anomalies, cross-polarization purity, and other antenna-performance metrics. Although this approach breaks the symmetry of the Finite-Element Method's system of equations, it is not much slower than the waveguide simulator, making infinite array analysis with periodic boundary conditions an invaluable approach to obtaining preliminary array design and optimization results. Some good examples of techniques utilizing this approach were given in [15-20].

For infinite array analysis (and for all computational electromagnetic modeling tools), the boundary condition used to truncate the mesh at the radiating aperture of the unit cell is of significant importance. In the Finite-Element Method, the simplest truncation approach is to use an absorbing boundary condition (ABC) or perfectly matched layer (PML) [2, 3, 21]. In their simplest form, these boundary conditions absorb the outwardly-radiating waves as if they were plane waves traveling out of the domain. This can be a reasonable approximation for radiating antenna elements. Further, the absorbing boundary conditions can be easily implemented without significantly increasing matrix storage. However, waves that are not incident perpendicularly to the

boundary (such as with array scanning) can reflect internally, and the assumption of only outwardly traveling waves may not capture all the physics of the environment – both issues causing inaccurate solutions.

Although perfectly matched layers are significantly more effective than absorbing boundary conditions in this regard, the most robust and accurate approach is to employ integral equations to truncate the radiation boundary. In this approach, a periodic Green's function rigorously models the exact radiating conditions [20]. In the Finite-Element Method, the fields at the cell's boundary are matched with radiating currents of the integral equations to give an accurate answer both inside and outside the unit cell. The combined use of the Finite-Element Method with integral equations is typically referred to as the Finite-Element-Boundary-Integral (FE-BI) Method in the electromagnetics community [2, 3, 22, 23]. While the main benefit of integral equations is their accuracy, drawbacks are speed and storage, as pointed out in the previous section. However, the combination of the Finite-Element Method to model the interior regions of a problem and integral equations to enforce radiation conditions on the boundary provides for accuracy and efficiency, leading to one of the most-successful simulators available today.

For finite array modeling, a popular but crude method is to employ the field solution of the infinite array obtained as described here and multiply it by a finite array factor. Many finite array simulation tools do little more than this approximation. While this approach can give a rough estimate of the radiation pattern (main-lobe level and number of lobes), it fails to capture the significant truncation effects of the finite array. Relying on this type of analysis is thus not advisable. A better strategy is to use the unit-cell model as a building block for a complete finite array design, analyzed using one of the more-powerful analysis techniques described below.

4. Domain Decomposition – Finite-Element Method

A new class of domain-decomposition techniques was recently proposed to solve Finite-Element-Method problems in electromagnetics. This is referred to as the Domain-Decomposition-Finite-Element Method, or DD-FEM [24, 25]. The technique uses special boundary conditions to partition large and intractable problems into smaller coupled problems that are more easily solvable. By doing so, these methods improve scalability to allow for large-scale problem solutions.

While DD-FEM has improved the capability of general-purpose solvers, it has also enabled the fast analysis and design of finite array problems [24, 26-33]. For finite arrays, rather than treating the structure as a general problem, the unit cell of the array is modeled only once and repeated, to save significant storage. To explain this, let us consider an array of n elements, each having an individual system of equations of size m, such that $nm = N$. No matter how large the array size n gets, the unique element matrix storage is only $O(m)$, with factorization cost at most $O(m^2)$. This results in significantly less than $O(N)$ matrix storage for large n. That is, the DD-FEM requires approximately the same matrix storage for finite arrays as was required for infinite arrays (i.e., a single unit cell). However, in the end, it is necessary to store the fields for the entire finite array, implying that the *total* storage will still be at least $O(N)$. Further, solution times will be relative to the size of the finite array.

The DD-FEM is one of the more-promising computational developments in recent years. Although it has been implemented in commercial codes, such tools are mainly available through a few research groups that specialize in this type of analysis. Because most DD-FEM tools employ absorbing boundary conditions and perfectly matched layers for mesh truncation, it is important to understand the limitations of this approach. When most of the energy is radiated outwards from the array structure, it is a reasonably safe approximation to use absorbing boundary conditions or perfectly matched layers to truncate the problem domain. However, these boundary conditions tend to be less accurate for large scan angles and/or scattering applications. When accuracy is important, it may be necessary to employ more-rigorous truncation schemes, such as those based on integral equations. Although integral-equation methods can be employed in a generalized way, efficient truncation methods exist for finite-array-type problems, some examples of which are addressed in the following sections [34].

5. The Array-Decomposition Method

One of the first specialized integral-equation approaches for analyzing finite array structures is the Array-Decomposition Method (ADM) [35]. The Array-Decomposition Method reduces the computational burden of integral equations while maintaining full solution accuracy. For array-type problems, the Array-Decomposition Method exploits the repeatable nature of the array geometry to achieve significantly reduced matrix storage. By taking advantage of the fact that there are many identical coupling paths within the regular finite array lattice, the system of equations is organized to benefit from block-Toeplitz properties, further reducing matrix storage. This provides the basis for a scalable FFT-accelerated solution of the system of equations. In some sense, the Array-Decomposition Method pre-solves the fields within the individual array elements, and iteratively solves for the mutual coupling within the array. This intuitive solution approach, based on the array physics, in combination with a reorganized system of equations, is efficient and highly effective for expedient analysis. For the antenna array engineer, this means an Array-Decomposition-Method-based code can

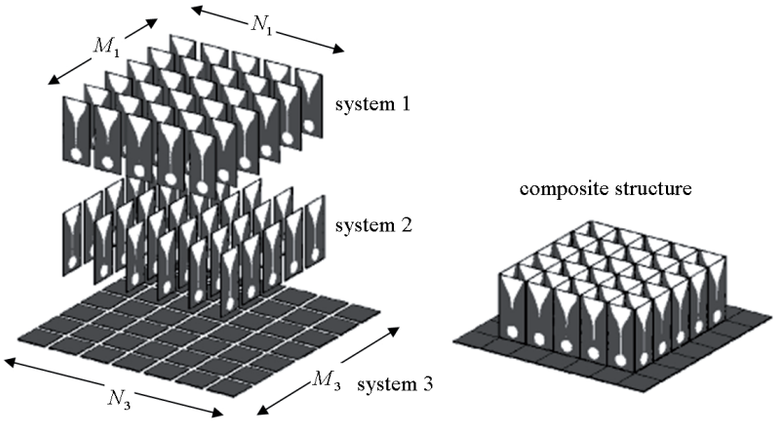

Figure 2. An example composite array geometry, decomposed using the Array-Decomposition Method.

accurately model very large finite array structures in reduced time. In the limiting case of a single antenna, the formulation reduces to the underlying generalized solution approach. Hence, the Array-Decomposition Method can be implemented into any code without a loss of generality, providing an efficient solution to the special case of the finite array without restricting the versatility of the modeling tool. The Array-Decomposition Method is intended to work with integral equations such as the MoM, and with hybrid methods such as the Finite-Element-Boundary-Integral Method. The latter has the benefit of modeling arbitrary materials within the Finite-Element-Method domain. More details are given below.

Consider a linear array of n identical antenna elements on a regular grid, with each of these antennas discretized using m unique current coefficients to model currents on the surface of the structure. The complete impedance matrix, $[Z]_{coupled}$, for the array system is then of size mn, and can be organized into n^2 blocks of size m^2. In an array of identical elements, with fixed spacing between elements (and hence translational symmetry), this system will have a block-Toeplitz property, i.e., $Z_{pq} = Z_{p-q}$. Hence, of the original n^2 terms in the $[Z]_{coupled}$ matrix, it is only necessary to store $2n-1$ of them without loss of information. The reduced storage format of the impedance matrix then takes the form

$$[Z]^{Toeplitz} = \begin{bmatrix} Z_{q-p} & \cdots & Z_{-1} & Z_0 & Z_1 & \cdots & Z_{p-q} \end{bmatrix}. \quad (5.1)$$

This "near-zone decomposition" generates a pronounced reduction in storage. If we consider that a single array element has a system of equations of size m, then the Array-Decomposition Method has $O\left(nm^2\right)$ matrix memory requirements, for a total system size $N = nm$. By comparison, a brute-force approach to modeling the problem using the MoM requires $O\left(N^2\right) = O\left(n^2m^2\right)$ matrix storage. Therefore, for large arrays (i.e., large n), the $O\left(nm^2\right)$ storage of the Array-Decomposition Method is considerably less than a general integral-equation approach. In [35], an example of a 30 × 30 finite array of tapered-slot antennas was analyzed. It was shown that the conventional MoM required almost four terabytes of storage, whereas the Array-Decomposition Method only needed 16 gigabytes. Further, $[Z_0]^{-1}$ can be used as a highly-effective block-diagonal matrix preconditioner to accelerate iterative solution of the system of equations.

Many common structures can be partitioned mathematically using higher-dimensional array descriptions, and the Array-Decomposition Method does this efficiently and automatically with *N*-dimensional FFT acceleration. The algorithm is not limited to one-dimensional, two-dimensional, or even three-dimensional arrays. Indeed, many structures, such as the structure in Figure 2, can be modeled more efficiently by identifying them as multiple arrays with different periodicities. The approach can be used for rectangular and also triangular lattices. Because of this, the Array-Decomposition Method has been used in applications beyond the usual linear and planar arrays. It has also been used for arrays that are conformal to curved surfaces of aircraft [36].

The disadvantage of the Array-Decomposition Method is that the matrix storage is not fixed. That is, as the array size increases, matrix storage also increases. A possible solution to decreasing matrix storage is to compute only the dominant mutual-coupling terms within the array, and to ignore the weak coupling between far-separated elements [37]. This truncated-coupling moving-window approach results in the same matrix storage for an array of any size. This technique can be tuned to make a tradeoff between storage and accuracy, and can be suitable for some applications. A more-robust solution is to combine the Array-Decomposition Method with another technique that rapidly computes distant-element coupling without compromising accuracy. This approach is discussed in the following section, where the Array-Decomposition Method is combined with the Fast Multipole Method.

6. The Array Decomposition-Fast Multipole Method

The Array-Decomposition Method can be readily combined with the Fast Multipole Method to treat distant interactions using a faster plane-wave expansion, without appreciably decreasing solution accuracy. The Fast-Multipole-Method expansion is applied to the element interactions using the same decomposition framework as the Array-Decomposition Method. This technique is referred to as the Array-Decomposition-Fast Multipole Method (AD-FMM) [38]. As with the Array-Decomposition Method, there is a significant reduction in storage for array-type problems, and a concurrent increase in solution speeds. As already noted, the AD-FMM has fixed matrix storage for an array of any size, which is on par with that required for a single array element, or roughly $O\left(m^2\right)$. In other words, *it has the same matrix storage requirement regardless of the array size*. To the average engineer, this means that very large arrays can be modeled using a basic desktop computer. As would be expected, for the limiting case of a single array element, the AD-FMM reduces to the Fast-Multipole-Method-accelerated general-purpose code.

Consider the interaction of distant elements within the array environment. Rather than using a Green's function to evaluate the interaction of distant and weakly coupled array elements, a plane-wave expansion can be used. In its simplest implementation, the AD-FMM computes the far-zone representation of the identical array element via the Fourier transform of the near-zone currents about the element's phase center. This spectral representation, commonly referred to as the signature function, requires a minimum number of unique directions, k, to adequately represent the element's coupling information in the far zone. In the same way that smaller arrays have fewer sidelobes, smaller elements have a simpler far-zone signature. Even for an antenna with a high amount of detail, the storage cost of the signature function will be much smaller than the cost of the equivalent near-zone interactions of the conventional MoM, or $O(k) \ll O\left(m^2\right)$.

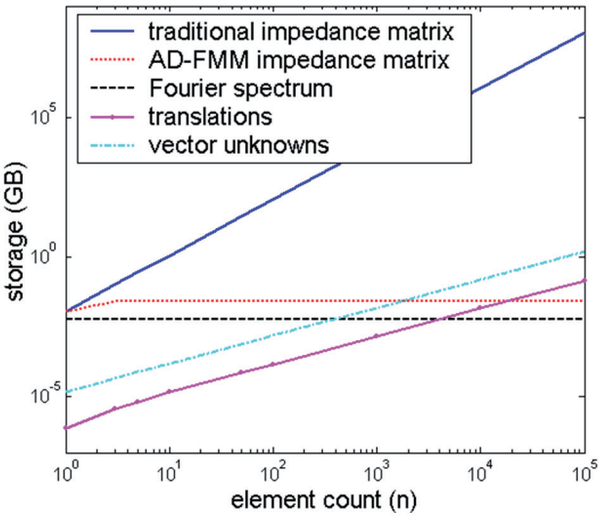

Figure 3. Storage trends for the AD-FMM.

To evaluate the interaction of the array elements in the far zone, the spectra of any two elements of the array must be aligned by computing a scalar translation from one array element to another. For the array, this translation factor must be computed for each of the k directions of the far-zone signature, and for each unique element interaction within the array. Because the far-zone translation operation for the array features the same translational symmetry found in the near-zone interactions (i.e., it is also based on the array grid), there are only $O(n)$ unique element-to-element interactions, reducing the cost of the far-zone translations to a mere $O(kn)$. Much like the reduced storage of the near-zone impedance matrix, the far-zone translations can be stored in reduced Toeplitz form as

$$[\mathrm{T}]^{Toeplitz} = \left[\mathrm{T}_{q-p} \quad \cdots \quad \mathrm{T}_{-1} \quad \mathrm{T}_0 \quad \mathrm{T}_1 \quad \cdots \quad \mathrm{T}_{p-q}\right], \quad (1)$$

with each T_{pq} having k entries. Only the near-element interactions are carried out in the near zone, including the self-element interaction $p-q=0$, along with (most likely) some portion of the adjacent element interactions $|p-q|=1$, or up to some near-zone threshold $|p-q|=n_{max}$. Beyond this threshold, coupling is treated as a far-zone interaction computed via the Fast-Multipole-Method expansion. Hence, the AD-FMM has two complementary storage structures:

$$[Z]^{Toeplitz}$$

$$= \left[0 \quad \cdots \quad 0 \quad Z_{-nmax} \quad \cdots \quad Z_0 \quad \cdots \quad Z_{nmax} \quad 0 \quad \cdots \quad 0\right] \quad (2)$$

and

$$[\mathrm{T}]^{Toeplitz}$$

$$= \left[\mathrm{T}_{q-p} \quad \cdots \quad \mathrm{T}_{1-nmax} \quad 0 \quad \cdots \quad 0 \quad \mathrm{T}_{nmax+1} \quad \cdots \quad \mathrm{T}_{p-q}\right] \quad (3)$$

As the zero entries in the matrix structures are not stored, the near-zone matrix will remain fixed for any array of size $n \geq n_{max}$ (i.e., all arrays beyond a given size have the same limited impedance-matrix storage).

Figure 3 shows the trends of the various storage components of the AD-FMM as compared to the traditional MoM approach for a generic linear antenna array of n elements, each with $m = 1000$ (unique current coefficients), and an electrical size proportional to half a wavelength. From Figure 3, we observed that the AD-FMM's storage is dominated by the vector current coefficients (the dashed

Method	FE-BI	MLFMA	ADM	AD-FMM
Matrix storage requirements	217 PB	88 GB	121 GB	192 MB
Matrix fill-time	10 years*	5 days*	3 days*	7 minutes
Solution iterations	–	–	100*	100
Solution time	–	–	25 hours*	2 days
Total storage cost	217 PB	94 GB	121 GB	432 MB
Total solution time	–	–	4 d*	2 d

** estimated results*

Table 1. A comparison of a 64 ×64 finite array problem, with approximately 7,000,000 degrees of free

cyan line) for large arrays ($O(N)$ storage). In contrast, the traditional MoM is bounded by the impedance matrix's storage (the solid blue line), which grows at a much faster rate. In [39], the details of the AD-FMM algorithm were presented, with significant further improvements and results given in [34].

As a practical example of the AD-FMM's performance, consider a 64 × 64 array of small flared-notch elements requiring approximately 1700 degrees of freedom to represent the radiating currents on the array-element boundary, and approximately 7,000,000 degrees of freedom for the full array. Table 1 gives a summary of the approximate storage requirements for several of the rigorous algorithms already mentioned in this article. Of the exact/rigorous methods given, it is clear that the AD-FMM is the only viable choice for this analysis when storage and solution time are the main considerations.

As another practical example, in [34] we considered the coupled arrays shown in Figure 4. The arrays consisted of horizontal and vertical ultra-wideband flared-notch

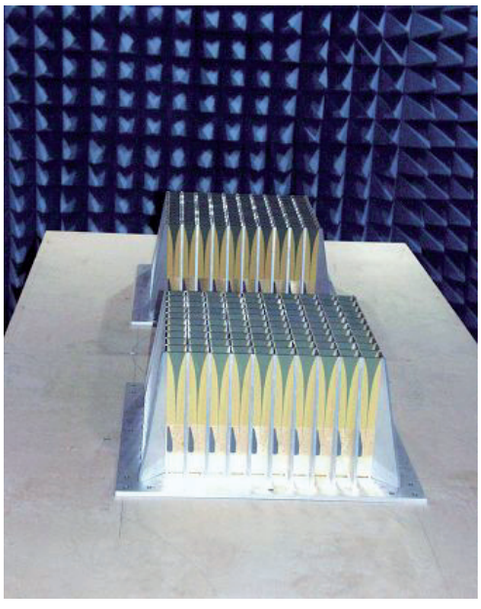

Figure 4. The AD-FMM was used to model the coupling between two wideband antenna arrays on a platform. The array design and measurements were performed at NRL [40].

elements a few wavelengths long at the highest frequency of operation. Element design information was given in [40]. For the analysis here, the task is to model the coupling between the two 10 × 10 finite arrays. It is important to note that these elements are highly detailed, consuming significant modeling resources even for a single element. It is not a stretch to suggest that modeling one of the finite arrays with existing general-purpose electromagnetic simulators on a personal computer is not feasible. For the conventional Finite-Element Method, the problem would take too many resources, unless DD-FEM was employed. Even so, to capture the coupling in the two-array problem, it would be necessary to model all the space between the arrays. Creating a large-enough computational domain to capture all the physics of the coupling environment could be difficult, depending on the array separation distance, thus calling the accuracy of the solution into question. In contrast, with the appropriate Green's function and the AD-FMM, it is possible to model these two array structures sitting on a large (assumed infinite) ground plate with considerable accuracy and relatively few resources. Table 2 gives the storage requirements for various solution methods for modeling this problem with integral equations. Each element in the model requires on the order of 4000 degrees of freedom for the radiating currents on the cell boundary, depending on the solution frequency. The resulting storage requirements are given in the table. Note that as is often the case when analyzing complex structures such as these, a general implementation of the Multi-Level Fast Multipole Algorithm will require significantly more storage than the purported $O(N \log N)$, due to the high sub-wavelength detail of the antenna elements.

Like the Array-Decomposition Method, the AD-FMM can be applied to arrays with any number of dimensions, as well as to the interaction of multiple array structures sharing common dimensions. Over the years, this approach to array analysis has been applied very successfully. The AD-FMM

Solution Method	Matrix Storage
FE-BI	6,940 GB
MLFMA	90 GB
ADM	126 GB
AD-FMM	0.25 GB

Table 2. The storage required for the array coupling problem of Figure 4.

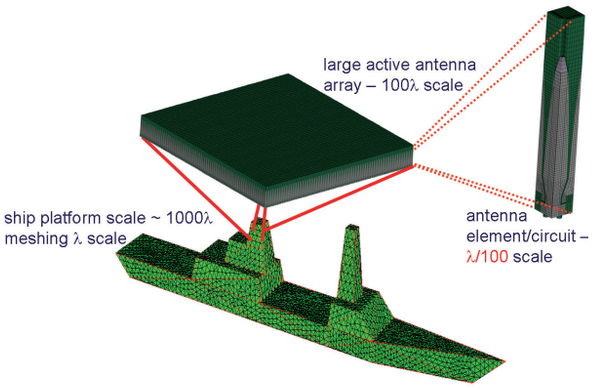

Figure 5. Array modeling needs to include some degree of platform interaction to properly account for co-site interference. This typically requires a hybrid solution approach, involving full-wave finite array methods plus high-frequency techniques.

has also been applied to characterizing propagation channels in buildings and rooms, where parts of the environment can be treated as array-type structures, such as wall structures, chairs, etc. [41].

In summary, the AD-FMM gives highly accurate answers to finite array design problems. The final storage for the AD-FMM is at most $O(m^2)$ for the near-zone impedance-matrix storage (on par with a single array element, and the same for an array of any size); km for the array element far-zone spectrum; and an additional $O(kn)$ for the block-Toeplitz translation matrix. For finite array problems, these storage factors are typically much less than the $O(nm)$ storage required for the unique array element current coefficients. Suffice it to say that the storage for the AD-FMM will be significantly less than that of a general solution approach. The AD-FMM maintains the fast and effective preconditioning of the Array-Decomposition Method, combined with very low and fixed matrix-storage requirements for finite arrays of any size. In addition, while the solution speeds of the generalized Multi-Level Fast Multipole Algorithm and the AD-FMM are both technically $O(N \log N)$, in practice, the AD-FMM is always considerably faster for array-type problems, particularly those with significant sub-wavelength features. The efficient (low-overhead) and scalable nature of the AD-FMM algorithm, the highly-effective matrix preconditioning, and the explicit exploitation of highly optimized system routines for computing FFTs all contribute to the successful application of the AD-FMM for the special case of finite arrays. The storage requirements and solution speeds are on a par with the DD-FEM technique considered earlier. The main difference is that the DD-FEM only considers array coupling locally (i.e., only through adjacent array elements), whereas the AD-FMM captures the coupling globally, i.e., throughout the entire array via the efficient use of an integral-equation formulation.

7. Hybrid Array/Platform Interactions

In practice, it is not sufficient to model a finite array as a standalone structure. That is to say, most often the environment within which the array is mounted has a significant effect on the performance of the array. For example, if the array is mounted within a recessed cavity, or if the array is terminated in some amount of material treatment, it could be critical to model the effects at the edge of the array. When these effects are tightly coupled, it becomes critical to perform a simultaneous solution of the coupled problem. For example, if the array structure resides in a cavity, it is not possible to perform the solution of the array and the cavity independently and to attempt to superimpose the solution in post-processing. When interfering systems are not tightly coupled, it may be sufficient to model the interactions indirectly, using a hybrid approach of rigorous methods for the arrays and high-frequency asymptotic methods for capturing indirect platform effects. This is a useful approach for computing the coupling among multiple antenna arrays mounted on ships or aircraft, where EMI/EMC is a significant issue, but the arrays are separated by reasonable distances. Multi-scale problems, such as the platform shown in Figure 5, are difficult to address, as there is not a single computational method that is well-suited to the entire analysis. Researchers at the US Naval Research Laboratory (NRL) and the ElectroScience Laboratory (ESL) of The Ohio State University (OSU) share a common vision of the importance of modeling finite array structures within their actual operating environment (i.e., as mounted in the platform conditions). At the Naval Research Laboratory, codes based on the AD-FMM algorithms are routinely used in combination with the Navy Radar Target Signature (RTS) code [42] to model (1) the performance of large finite arrays embedded into Navy platforms, and (2) to predict the coupling and interference between multiple radar/communication systems, including reflections from ship structures and various sea-scattering conditions in the analysis. Similarly, at ESL, the AD-FMM has been used in combination with the Ohio State University Basic Scattering Code (*OSU-BSC*) for evaluating the relevant dominant UTD (Uniform Theory of Diffraction) ray-field interactions between ship structures and embedded arrays [43]. The ability to model the interaction of sensitive systems and predict co-site interference is of tremendous interest to the Navy community.

As a general rule, fast array methods (e.g., the AD-FMM, the DD-FEM) are used to model the intricate array structures, and general Finite-Element Method/MoM solvers can be used to best approximate the edge conditions of the embedded arrays. At lower frequencies, the Multi-Level Fast Multipole Algorithm-type algorithms can be used to model platform structures as well. However, above 1 GHz, asymptotic methods typically must be used, prompting the necessity for some form of hybrid solution.

8. Conclusion

General-purpose electromagnetic design tools have become increasingly powerful over the years. It is therefore to some degree possible to model finite array configurations with these commercial tools. Certainly, a design engineer will always benefit from a good general-purpose electromagnetic simulator. However, as explained in this article, there are inherent limitations in a brute-force approach to solving array-type problems with general-purpose tools. For finite array analysis, it makes sense to take a more-intelligent design approach that exploits redundancies within the array geometry. Specialized techniques can be significantly more expedient and require considerably fewer resources. The hallmark of a truly efficient array technique is that it should have matrix storage that is the same for an array of any size, total storage of $O(N)$, with a linearly-scalable solution at a speed of $O(N \log N)$. The techniques addressed in this article have these characteristics. Although they were not covered in this article, there are many other noteworthy methods specialized for array analysis: some examples are listed in [44-47]. As with any specialized techniques, the proper use and limitations of the methods must be understood.

The DD-FEM (Domain-Decomposition-Finite-Element Method) is a particularly effective tool when specialized for finite array problems. However, there are limitations in the accuracy of the boundary conditions that need to understood and accounted for. If a more accurate solution is required, the integral-equation-based array-decomposition methods (the Array-Decomposition Method and the AD-FMM: Array-Decomposition-Fast Multipole Method) are very expedient and fast techniques to use. As with any problem, there is never a single correct way to solve a finite array problem. The important thing is to understand the conditions at hand well enough that the most-appropriate tool can be selected, based on the quality of the answer desired. As much as we tend to desire the most automatic solution possible – i.e., finite array design with the push of a single button – there is simply not the equivalent of a "finite array wizard" that instantly completes a finite array design with the speed and ease of spreadsheet computations. Finite array design is a difficult task, and to handle it appropriately requires some rather sophisticated tools.

As a final note, if the design engineer is limited to using a 32-bit operating system or a 32-bit processor, it is important to keep in mind that all rigorous/exact methods are limited by the required $O(N)$ storage. When a code uses four bytes to store each variable, the solution to a 100-million-unknown problem will require nearly 1 GB of memory, not including storage for the system of equations that must be solved. As one can imagine, this places significant stress on the current generation of computing facilities. Further, such problems may affect the scalability of algorithms for clustered networks in the case when the system vectors cannot be fully stored in the memory of a single machine. Although this is less of an issue with 64-bit technology, the dominance of vector storage should not be discounted.

9. References

1. C. A. Balanis, *Antenna Theory, Analysis,and Design, Second Edition*, 1997.

2. J. M. Jin, *The Finite Element Method in Electromagnetics*, New York, J. Wiley & Sons, 1993.

3. J. L. Volakis, A. Chatterjee, and L. C. Kempel, *Finite Element Method for Electromagnetics*, New York, IEEE Press, 1998.

4. A. F. Peterson, S. L. Ray, and R. Mittra, *Computational Methods for Electromagnetics*, New York, Wiley-IEEE Press, 1997.

5. R. Coifman, V. Rokhlin, and S. Wandzura, "The Fast Multipole Method for the Wave Equation: A Pedestrian Prescription," *IEEE Antennas Propagation Magazine*, **35**, 1993, pp. 7-12.

6. K. Sertel, *Multilevel Fast Multipole Method for Modeling Permeable Structures Using Conformal Finite Elements*, PhD dissertation, University of Michigan, Ann Arbor, 2003.

7. S. Bindiganavali and J. L. Volakis, "Scattering from Plates Containing Small Features Using the Adaptive Integral Method (AIM)," *IEEE Transactions on Antennas and Propagation*, December 1998, pp. 1867-1878.

8. E. Bleszynski, M. Bleszynski, and T. Jaroszewicz, "AIM: Adaptive Integral Method for Solving Large Scale Electromagnetic Scattering and Radiation Problems," *Radio Science*, **31**, 1996, pp. 1225-1251.

9. W. C. Chew, J. M. Jin, C. C. Lu, E. Michielssen, and J. M. Song, "Fast Solution Methods in Electromagnetics," *IEEE Transactions on Antennas and Propagation*, **AP-45**, 3, March 1997, pp. 533-543.

10. K. Zhao, M. N. Vouvakis, and J.-F. Lee, "The Adaptive Cross Approximation Algorithm for Accelerated Method of Moments Computations of EMC Problems," *IEEE Transactions on Electromagnetic Compatibility*, **47**, 4, November 2005, pp. 763-773.

11. Y. Saad, *Iterative Methods for Sparse Linear Systems*, New York, PWS Publishing, 1996.

12. O. Schenk and K. Gärtner, "Solving Unsymmetric Sparse Systems of Linear Equations with PARDISO," *Journal of Future Generation Computer Systems*, **20**, 2004, pp. 475-487.

13. P. R. Amestoy, I. S. Duff, and J.-Y. L'Excellent, "Multifrontal Parallel Distributed Symmetric and Unsymmetric Solvers," *Comput. Methods in Appl. Mech. Eng.*, **184**, 2000, pp. 501-520.

14. Y. Zhu and A. C. Cangellaris, *Multigrid Finite Element Methods for Electromagnetic Field Modeling*, New York, John Wiley, 2006.

15. E. W. Lucas and T. P. Fontana, "A 3-D Hybrid Finite Element/ Boundary Element Method for the Unified Radiation and Scattering Analysis of General Infinite Periodic Arrays," *IEEE Transactions on Antennas and Propagation*, **AP-43**, 2, February 1995, pp. 145-153.

16. D. T. McGrath and Pyati, V. P., "Phased Array Antenna Analysis with Hybrid Finite Element Method," *IEEE Transactions on Antennas and Propagation*, **AP-42**, 12, December 1994, pp. 1625-1630.

17. T. F. Eibert, J. L. Volakis, D. Wilton, and D. Jackson, "Hybrid FE/BI Modeling of 3D Doubly Periodic Structures Using Triangular Prismatic Elements and a MFIE Accelerated by the Ewald Transformation," *IEEE Transactions on Antennas and Propagation*, **AP-47**, 5, May 1999, pp. 843-850.

18. P. W. Hannan and M. A. Balfour, "Simulation of Phased-Array Antennas in Waveguides," *IEEE Transactions on Antennas and Propagation*, **AP-13**, 1965, pp. 342-353.

19. S. D. Gedney, J.-F. Lee, and R. Mittra, "A Combined FEM/ Mom Approach to Analyze the Plane Wave Diffraction by Arbitrary Gratings," *IEEE Transactions on Microwave Theory and Techniques*, **40**, February 1992, pp. 363-370.

20. S. Singh, W. F. Richards, J. R. Zinecker, and D. R. Wilton, "Accelerating the Convergence of Series Representing the Free Space Green's Function," *IEEE Transactions on Antennas and Propagation*, **AP-38**, 12, December 1990, pp. 1958-1962.

21. D. M. Kingsland, J. Gong, J. L. Volakis, and J. F. Lee, "Performance of an Anisotropic Artificial Absorber for Truncating Finite-Element Meshes," *IEEE Transactions on Antennas and Propagation*, **AP-44**, 7, July 1996, pp. 975-982.

22. J.-M. Jin and J. L. Volakis, "A Finite Element-Boundary Integral Formulation for Scattering by Three-Dimensional Cavity-Backed Apertures," *IEEE Transactions on Antennas and Propagation*, **AP-39**, 1, January 1991, pp. 97-104.

23. J.-M. Jin and J. L. Volakis, "A Hybrid Finite Element Method for Scattering and Radiation by Microstrip Patch Antennas and Arrays Residing in a Cavity," *IEEE Transactions on Antennas and Propagation*, **AP-39**, 11, November 1991, pp. 1598-1604.

24. S. C. Lee, M. Vouvakis, and J.-F. Lee, "A Non-Overlapping Domain Decomposition Method with Non-Matching Grids for Modeling Large Finite Antenna Arrays," *Journal of Computational Physics*, **203**, 1, February 2005, pp. 1-21.

25. M. N. Vouvakis, *A Non-Conformal Domain Decomposition Method for Solving Large Electromagnetic Wave Problems*, PhD Dissertation, Ohio State University, Columbus, OH, 2005.

26. S. S. Holland, W. Wang, R. Kindt, D. H. Schaubert, and M. N. Vouvakis, "A Wavelength Scaled Array of Doubly-Mirrored Balanced Antipodal Vivaldi Antennas (Dm-BAVAs)," IEEE International Symposium on Antennas and Propagation, 2009.

27. R. Kindt and M. Kragalott, "A Wavelength-Scaled Ultra-Wide Bandwidth Array," IEEE International Symposium on Antennas and Propagation *Digest*, June 1-5, 2009, pp. 1-4.

28. R. W. Kindt and R. Pickles, "12-to-1 Bandwidth All-Metal Vivaldi Array Element," IEEE International Symposium on Antennas and Propagation *Digest*, June 1-5, 2009, pp. 1-4.

29. G. N. Paraschos, R. Kindt, D. H. Schaubert, and M. N. Vouvakis, "Radiation and Coupling Studies of Finite-Size Dual Polarized Vivaldi Arrays Using a Domain Decomposition FEM," IEEE International Symposium on Antennas and Propagation *Digest*, June 1-5, 2008, pp. 1-4.

30. M. N. Vouvakis, R. Kindt, and J.-F. Lee, "A Coupled DD-FEM and ADM/CG-FFT BEM for Antenna Arrays," IEEE International Symposium on Antennas and Propagation, Albuquerque, NM, 2006.

31] R. Kindt and M. Vouvakis, "Analysis of Wavelength-Scaled Array Architectures via Domain Decomposition Techniques for Finite Arrays," International Conference on Electromagnetics in Advanced Applications, ICEAA '09, September 14-18, 2009, pp. 196-199.

32. R. W. Kindt and M. N. Vouvakis, "Analysis of a Wavelength-Scaled Array (WSA) Architecture," *IEEE Transactions on Antennas and Propagation*, **AP-58**, 9, September 2010, pp. 2866-2874.

33. R. W. Kindt and W. R. Pickles, "Ultrawideband All-Metal Flared-Notch Array Radiator," *IEEE Transactions on Antennas and Propagation*, **AP-58**, 11, November 2010.

34. R. W. Kindt, *Rigorous Analysis of Composite Finite Array Structures*, PhD dissertation, EECS Dept., University of Michigan, Ann Arbor, 2004.

35. R. W. Kindt, K. Sertel, E. Topsakal, and J. L. Volakis, "Array Decomposition Method for the Accurate Analysis of Finite Arrays," *IEEE Transactions on Antennas and Propagation*, **AP-51**, 6, June 2003, pp. 1364-1372.

36. R. W. Kindt, P. Janpugdee, P. H. Pathak, and J. L. Volakis, "Analysis of Large Finite Arrays Integrated into Curved Platforms," IEEE International Symposium on Antennas and Propagation, Washington, DC, 2005.

37. R. Kindt, K. Sertel, E. Topsakal, and J. L. Volakis, "An Extension of the Array Decomposition Method for Large Finite-Array Analysis," *Microwave and Optical Technology Letters*, **38**, 4, August 20, 2003, pp. 323-328.

38. R. W. Kindt and J. L. Volakis, "Array Decomposition-Fast Multipole Method for Finite Array Analysis," *Radio Science*, **39**, 2, April 2004.

39. R. Kindt and J. L. Volakis, "The Array Decomposition-Fast Multipole Method," IEEE International Symposium on Antennas and Propagation *Digest*, **4**, June 22-27, 2003, pp. 3 - 6.

40. M. Kragalott, W. R. Pickles, and M. S. Kluskens, "Design of a 5:1 Bandwidth Stripline Notch Array from FDTD Analysis," *IEEE Transactions on Antennas and Propagation*, **AP-48**, 11, November 2000, pp. 1733-1741.

41. C.-P. Lim, J. L. Volakis, K. Sertel, R. W. Kindt, and A. Anastasopoulos, "Indoor Propagation Models Based on Rigorous Methods for Site-Specific Multipath Environments,"

IEEE Transactions on Antennas and Propagation, **AP-54**, 6, June 2006, pp. 1718-1725.

42. M. Busse, H. L. Toothman, and D. Zolnick, "Radar Target Signature User Manual – Version 10.0," Naval Research Laboratory, Washington, DC, Report NRL/PU/5310-98-370, 1998.

43. E. H. Newman and R. J. Marhefka, "Overview of MM and UTD Methods at the Ohio State University (Radar Target Scattering)," *Proc. IEEE*, **77**, 5, May 1989, pp. 700-708.

44. D. J. Bekers, S. J. L. van Eijndhoven, A. A. F. van de Ven, P.-P. Borsboom, and A. G. Tijhuis, "Eigencurrent Analysis of Resonant Behavior in Finite Antenna Arrays," *IEEE Transactions on Microwave Theory and Techniques*, **54**, 6, June 2006, pp. 2821-2829.

45. H.-T. H. Chou, P. H. Pathak, P. Nepa, and O. A. Civi, "Efficient Hybrid Discrete Fourier Transform-Moment Method for Fast Analysis of Large Rectangular Arrays," *IEE Proceedings on Microwaves, Antennas and Propagation*, **149**, 2002, pp. 1-6.

46. R. Maaskant, R. Mittra, and A. Tijhuis, "Fast Analysis of Large Antenna Arrays Using the Characteristic Basis Function Method and the Adaptive Cross Approximation Algorithm," *IEEE Transactions on Antennas and Propagation*, **AP-56**, 11, November 2008, pp. 3440-3451.

47. P. Pirinoli, L. Matekovits, F. Vipiana, G. Vecchi, and M. Orefice, "Multi-Grid SFX-MR Approach for the Analysis of Large Arrays," 18th International Conference on Applied Electromagnetics and Communications (ICECom), October 12-14, 2005, pp. 1-4.

Multilevel Characteristic Basis Function Method (MLCBFM) for the Analysis of Large Antenna Arrays

Rob Maaskant
Raj Mittra
Anton Tijhuis

Abstract

A multi-level version of the Characteristic Basis Function Method (CBFM) is presented for computing the input impedance matrix and radiation patterns of very large antenna arrays. Specifically, we consider the challenging problem of an electrically large subarray that is surrounded by (many) other disjoint subarrays, and solve this problem by employing a two-level Characteristic Basis Function Method. At level zero, Rao-Wilton-Glisson (RWG) basis functions are employed to locally synthesis the surface current. Next, the number of degrees of freedom (DoFs) for the current is reduced at level one by employing the characteristic basis functions (CBFs), each of which is a macro basis function supported by an antenna element, and is a fixed combination of RWG basis functions. Moreover, the characteristic basis functions at level two are supported by subarrays to further reduce the degrees of freedom. This multilevel approach is memory efficient and generates a final reduced matrix equation that can be solved directly, i.e., in-core through standard Gaussian elimination techniques, even though the conventional MoM (Method of Moments) formulation of the same problem may require more than one million RWG basis functions. Numerical examples are presented for various array sizes, including a 25 subarray problem comprised of 64 tapered-slot antennas (TSAs) each. The proposed method demonstrates very good accuracy, numerical efficiency, and a reduced memory storage requirement.

1. Introduction

The numerical method presented in this paper has been developed within the framework of the Square Kilometre Array (SKA) project. This is a worldwide endeavor to design and construct a revolutionary new radio telescope with a collecting area which is on the order of one million square meters, in the wavelength range from 3 m to 1 cm [1-3]. Within this context, the potentials of various array technologies are evaluated by analyzing the impedance as well as the radiation characteristics through electromagnetic-field analyses. In some of these studies, it is vitally important to accurately analyze electrically large – but finite – array antennas and associated truncation effects. Given the electrical size and geometrical complexity of such structures, the numerical analysis presents a severe computational burden, especially when only limited computing resources are available [4, 5].

A wide variety of numerically efficient techniques has been developed over the last few decades to alleviate the above problem. However, in this work we will only consider the class of iteration-free integral-equation techniques, and focus specifically on a recently developed method called the Characteristic Basis Function Method (CBFM). It enhances the conventional Method of Moments by compressing the moment matrix such that the resultant reduced matrix equation can be solved in an iterative-free manner - simultaneously for multiple right-hand sides (MRHS) [6, 7]. The matrix compression is achieved by employing macro basis functions (characteristic basis functions, or CBFs). These are constructed as fixed combinations (aggregations) of subdomain basis functions, each of which is defined over a much smaller support [8, 9]. An even higher compression of the final reduced matrix is achieved through the use of a multilevel version of the Characteristic Basis Function Method. Toward this end, the concept of basis-function aggregation is repeated, such that higher-order characteristic basis functions are expressed in terms of lower-order characteristic basis functions. At the lowest level, the (subdomain) basis functions are chosen to have a simple analytic form, and to conform to arbitrarily shaped geometries, so that the higher-order characteristic basis functions will also satisfy this advantageous geometrical property. An inherent advantage of using these

Rob Maaskant is with the Netherlands Institute for Radio Astronomy (ASTRON), PO Box 2, 7990 AA Dwingeloo, The Netherlands; e-mail: (maaskant@astron.nl). Raj Mittra is with the Electromagnetic Communication Laboratories, Pennsylvania State University, University Park, PA 16802, USA; e-mail: mittra@engr.psu.edu. Anton Tijhuis is with the Faculty of Electrical Engineering, Eindhoven University of Technology, PO Box 513, 5600 MB Eindhoven, The Netherlands; e-mail: a.g.tijhuis@tue.nl.

macro basis functions is that existing computer codes that employ sub-sectional basis functions can be reused with only minor modifications.

Furthermore, in the Characteristic Basis Function Method, the entire computational domain is subdivided into smaller subdomains, each of which supports a set of numerically generated macro basis functions. Such a domain-decomposition technique is advantageous, since many algorithmic steps involved can be carried out in parallel on supercomputers or on platforms with multiple processors [10, 11]. Furthermore, the modular setting of a domain-decomposition technique enables one to analyze/optimize the entire structure at minimal cost by only reconsidering the domains that need to be altered [12].

The concept of reducing the size of the matrix equation by employing numerically generated macro basis functions, and decomposing the problem into smaller problems, has also been widely exploited in other recently developed iterative-free methods for solving large-scale problems. Examples include the Synthetic-Functions Approach (SFX) [13, 14], the Sub-Entire-Domain Basis Function Method (SED) [15], the eigencurrent approach [16], and a subdomain multilevel approach [17]. These methods can be distinguished from each other by the way they generate the macro basis functions, and also by the methods they use to synthesize a junction current between electrically connected subdomains. We note that one can employ a special type of junction basis functions, or an overlapping domain-decomposition technique in which adjacent sets of macro basis functions partially overlap [13, 18].

For electrically large problems, the overall solution time of the Characteristic Basis Function Method is governed by the time it takes to construct the reduced matrix equation, as opposed to solving it. Various acceleration techniques have been proposed to reduce the matrix construction time, including multipole approaches [29, 20]; the Adaptive Cross Approximation (ACA) technique [21]; a multi-level decomposition approach [22]; and the Adaptive Integration Method (AIM) [23]. These methods all rely on the fact that the electric field generated by a macro basis function is a relatively smoothly varying function over the support of the macro test function. This is particularly true if the macro basis and test functions are well separated. Hence, for electrically large antenna and scattering problems, many of the reduced-matrix entries (characteristic basis function reaction integrals) can be rapidly computed.

The reciprocity theorem is often used to compute only the upper-triangular part of the reduced matrix, and this saves approximately a factor of two in the total filling time. More importantly, many reactions between (groups of) characteristic basis functions are replicated elsewhere in the array, because of translation symmetry. Even though the moment matrix may not have a full block-Toeplitz symmetry, many entries (even blocks) of the reduced matrix are thus identical and, hence, can simply be copied during the matrix-construction process.

This paper focuses on the challenging case of large arrays of strongly coupled tapered-slot antennas (TSAs). The radiation and scattering characteristics of such arrays have been considered by others, as well. Much work has been performed on the edge-truncation effects, and the efficient computation of embedded element patterns and element impedances by the authors of [24], both in the time and the frequency domain. In [25], the Finite Element Method was combined with an Integral-Equation technique (FEM-IE) to iteratively solve for the fields in tapered-slot-antenna arrays that involve dielectric materials.

One of the major problems arising in the SKA project is the analysis of large arrays comprising of disjoint phased-array tiles. These structures exhibit multi-scale (quasi-periodic) features, both at the antenna-element level and at the subarray level. To handle these problems, an approximately infinite array approach at the subarray level was developed in [26]. There, the infinite sum was truncated in the spatial domain to compute the scan impedance of antenna elements that were located within an electrically large subarray surrounded by (many) other actively phase-steered subarrays. Basically, the Characteristic Basis Function Method is used here at the antenna-element level, whereas an infinite-array approach is used at the subarray level. Although the method represents a viable alternative to a full-fledged Characteristic Basis Function Method solution, it does not directly yield for us the (passive) input-impedance matrix and embedded element patterns of the antenna array. As a remedy, we propose in this paper to use the Multilevel Characteristic Basis Function Method, since this overcomes the associated memory problems and directly provides us with the impedance and radiation characteristics of all tapered-slot-antenna elements. Note that the capabilities of the Multilevel Characteristic Basis Function Method were already demonstrated for scattering problems in [27].

The paper is organized as follows. First, we provide a brief description of the Multilevel Characteristic Basis Function Method. We describe the steps that are involved in the process of constructing a reduced-matrix equation at all levels, as well as the generation of characteristic basis functions for antenna-type problems. The computation of the input-impedance matrix and radiation patterns are also discussed. Second, the Multilevel Characteristic Basis Function Method is used to compute the radiation patterns and impedances of a 576 tapered-slot-antenna-element array (nine subarrays of 64 tapered-slot antennas each). The results are then compared to those obtained from a mono-level Characteristic Basis Function Method. Third, the problem is enlarged to incorporate 25 subarrays of 64 tapered-slot antennas each. Since the size of this problem exceeds one million RWG basis functions, it renders the problem unmanageable, even when a mono-level Characteristic Basis Function Method approach is used to reduce the size of the associated matrix. However, it will be demonstrated below that the memory requirements can be relaxed when it is solved through a Multilevel Characteristic Basis Function Method approach.

2. Outline of the Multi-Level Characteristic Basis Function Method

2.1 Matrix-Equation Reduction

To understand how the Multilevel Characteristic Basis Function Method achieves its matrix compression, it is instructive to consider the specific example in Figure 1. This depicts an array of two subarrays of two electrically interconnected tapered-slot antennas each. Level-0 in Figure 1 corresponds to the case where the currents are synthesized by M_0 Rao-Wilton-Glisson (RWG) basis functions [28]. The associated matrix equation that needs to be solved reads

$$\mathbf{Z}^{[0]}\mathbf{I}^{[0]} = \mathbf{V}^{[0]}, \tag{1}$$

where the (uncompressed) moment matrix, $\mathbf{Z}^{[0]}$, is of size $M_0 \times M_0$, and where the RWG expansion-coefficient vector is $\mathbf{I}^{[0]} = \left[I_1^{[0]}, I_2^{[0]}, \ldots, I_{M_0}^{[0]} \right]^T$. The superscript T denotes the transpose, and $\mathbf{V}^{[0]}$ is the excitation vector. In the following, we will assume that the matrix equation is very large and cannot be solved through standard Gaussian-elimination techniques.

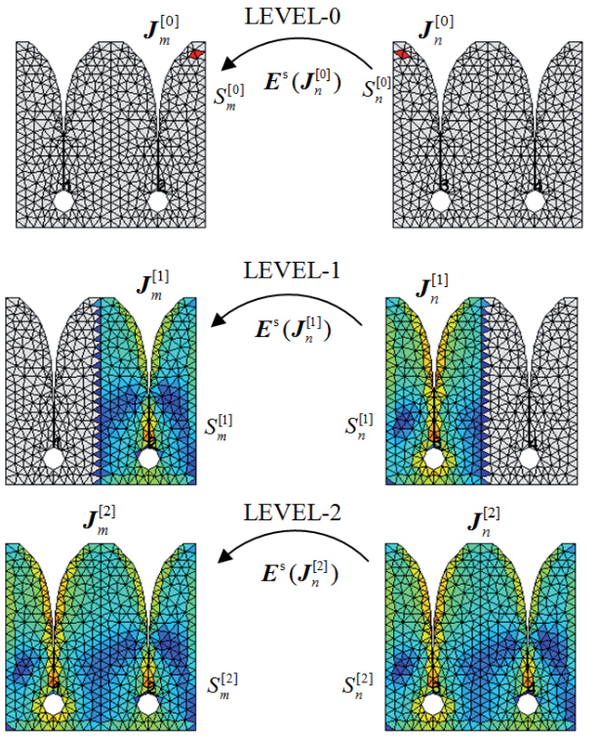

Figure 1. A methodology to compress the moment matrix through a Multilevel Characteristic Basis Function Method approach. Level-1: reactions between RWG basis functions. Level-2: reactions between characteristic basis functions supported by antenna elements (plus a single-cell extension). Level-3: reactions between characteristic basis functions supported by subarrays

For perfectly conducting sheets, and when Galerkin's scheme is used for testing the electric-field integral equation through a symmetric product, the moment matrix in Equation (1) is symmetric and the elements are recognized as reaction integrals. The matrix element $Z_{mn}^{[0]}$ thus denotes the radiated electric field, $\mathbf{E}^s$, generated by the nth RWG basis function $\mathbf{J}_n^{[0]}$, which is tested over the support, $S_m^{[0]}$ of basis function $\mathbf{J}_m^{[0]}$ (see also Figure 1). The matrix element can be written as

$$Z_{mn}^{[0]} = \int_{S_m^{[0]}} \mathbf{J}_m^{[0]} \bullet \mathbf{E}^s\left(\mathbf{J}_n^{[0]}\right) dS, \tag{2}$$

with $m, n \in \{1, 2, \ldots, M_0\}$. Furthermore, the mth element of the excitation vector $\mathbf{V}^{[0]}$ is expressed in terms of the incident electric field $\mathbf{E}^{inc}$ as

$$V_m^{[0]} = -\int_{S_m^{[0]}} \mathbf{J}_m^{[0]} \bullet \mathbf{E}^{inc} dS. \tag{3}$$

It is pointed out that the matrix Equation (1) is significantly smaller when we employ a set of M_1 *macro*-domain basis functions, $\left\{\mathrm{J}_m^{[1]}\right\}_{m=1}^{M_1}$, with $M_1 \ll M_0$. One then needs to solve the relatively small-size matrix equation $\mathbf{Z}^{[1]}\mathbf{I}^{[1]} = \mathbf{V}^{[1]}$, where the matrix $\mathbf{Z}^{[1]}$ is of size $M_1 \times M_1$ The elements of $\mathbf{Z}^{[1]}$ and $\mathbf{V}^{[1]}$ are defined through Equations (2) and (3), respectively, where the 0 index is replaced by 1. In the Characteristic Basis Function Method, the macro basis functions are called characteristic basis functions (CBFs), and are expressed in terms of a fixed combination of lower-level basis functions. For instance, at level-1 (see Figure 1), the mth characteristic basis function $\mathbf{J}_m^{[1]}$ is expressed in terms of the M_0 RWG basis functions $\left\{\mathrm{J}_m^{[0]}\right\}$ at level-0 as

$$\mathbf{J}_m^{[1]} = \sum_{m=1}^{M_0} I_m^{\mathrm{CBF};[0]} \mathbf{J}_m^{[0]}, \tag{4}$$

where the $I_m^{\mathrm{CBF};[0]}$ are predetermined RWG expansion coefficients describing the "shape" of the mth characteristic basis function $\mathbf{J}_m^{[1]}$. Note that for antenna problems, it is natural to take the support of the level-1 characteristic basis functions to be equal to the size of a single antenna element (as in Figure 1), particularly because the degree of translation symmetry for array antennas is largest at the antenna-element level. Hence, the characteristic basis functions have a local support, and many RWG expansion coefficients in Equation (4) will be zero. The determination of the expansion

coefficients in Equation (4) will be described in Section 2.3, where we also explain the single-cell extension in the overlapping region, as shown in Figure 1.

Once the level-1 characteristic basis functions have been generated, the elements of the reduced matrix $\mathbf{Z}^{[1]}$ can be computed. For instance, and with reference to Equation (2), the matrix element $Z_{mn}^{[1]}$ (with $m,n \in \{1,2,\ldots,M_1\}$) is computed as

$$Z_{mn}^{[1]} = \int\limits_{S_m^{[1]}} \mathbf{J}_m^{[1]} \bullet \mathbf{E}^s\left(\mathbf{J}_n^{[1]}\right) dS$$

$$= \sum_{m=1}^{M_0}\sum_{n=1}^{M_0} I_m^{\mathrm{CBF};[0]} \left[\int\limits_{S_m^{[0]}} \mathbf{J}_m^{[0]} \bullet \mathbf{E}^s\left(\mathbf{J}_n^{[0]}\right) dS \right] I_n^{\mathrm{CBF};[0]} \quad (5)$$

$$= \left(\mathbf{I}^{\mathrm{CBF}m;[0]}\right)^T \mathbf{Z}^{[0]} \mathbf{I}^{\mathrm{CBF}n;[0]},$$

where we have made use of Equation (4) and the linearity of the operators in computing the scattered field, $\mathbf{E}^s$. The column vector $\mathbf{I}^{\mathrm{CBF}n;[0]}$ holds the RWG expansion coefficients of the nth characteristic basis function $\mathbf{J}_n^{[1]}$ at level-1. Because the vectors $\mathbf{I}^{\mathrm{CBF}m;[0]}$ and $\mathbf{I}^{\mathrm{CBF}n;[0]}$ contain many zero entries, effectively, only the matrix block $\mathbf{Z}_{mn}^{[0]}$ of $\mathbf{Z}^{[0]}$ in Equation (5) is required, namely the matrix that corresponds to the RWG basis functions on the observation and the source domains $S_m^{[1]}$ and $S_n^{[1]}$ (see Figure 1, level-1), respectively. In the following, we will therefore discard the zeros in the expansion-coefficient vectors, and instead work with the much-smaller matrix block $\mathbf{Z}_{mn}^{[0]}$, and the expansion-coefficient vectors $\mathbf{I}_m^{\mathrm{CBF};[0]}$ and $\mathbf{I}_n^{\mathrm{CBF};[0]}$ that are associated with the local supports $S_m^{[1]}$ and $S_n^{[1]}$, respectively.

Following the above methodology, we move to the next higher level (level-2) and increase the support of the characteristic basis functions, as shown in Figure 1, where a characteristic basis function occupies an entire subarray. From Equation (5), it is then evident that an element of the reduced matrix $\mathbf{Z}^{[2]}$ can be expressed in terms of the elements of $\mathbf{Z}^{[1]}$ in conjunction with the characteristic-basis-function expansion coefficients at level-1.

In general, at the ith level ($i = 1,2,\ldots$), one observes that

$$Z_{mn}^{[i]} = \left(\mathbf{I}_m^{\mathrm{CBF};[i-1]}\right)^T \mathbf{Z}_{mn}^{[i\text{-}1]} \mathbf{I}_n^{\mathrm{CBF};[i-1]}. \quad (6)$$

For an element $V_m^{[i]}$ of the excitation vector $\mathbf{V}^{[i]}$,

$$V_m^{[i]} = \left(\mathbf{I}_m^{\mathrm{CBF};[i-1]}\right)^T \mathbf{V}_m^{[i\text{-}1]}, \quad (7)$$

where one observes that Equations (6) and (7) are both written in terms of a recursive formula [27].

It is assumed that the matrix equation at the highest level can be solved directly, after which the expansion coefficients for the current can be computed at any lower level through the recursive version of Equation (4).

According to the above-described Multilevel Characteristic Basis Function Method, the general procedure for solving the large matrix Equation (1) consists of the following steps:

1. Generate characteristic basis functions at level-1 by extracting small subarrays from the fully meshed antenna array (equipped with RWG basis functions), and subsequently excite them to generate primary and secondary characteristic basis functions (see Section 2.3). If the final radiation pattern is of interest, then also compute the far-field patterns of the characteristic basis functions at level-1. Superimpose these to form the total radiation pattern, once the characteristic-basis-function expansion coefficients at level-1 are known (see Step 3).

2. Rapidly construct $\mathbf{Z}^{[1]}$ through the Adaptive Cross Approximation (ACA) algorithm, as was described in [21]. In addition, exploit reciprocity and take advantage of the fact that many rank-deficient block matrices associated with group pairs of characteristic basis functions at level-1 are identical, and, hence, can be simply copied during the construction of the matrix $\mathbf{Z}^{[1]}$ [26].

3. Generate characteristic basis functions at level-2 by extracting larger subarrays from the fully meshed antenna array, and subsequently excite them to generate primary and secondary characteristic basis functions at level-2. To be able to solve for the excitations of each of these larger subarray problems, we make use of the Characteristic Basis Function Method at the lower level, i.e., level-1. The level-2 characteristic basis functions are thus expressed in terms of the level-1 characteristic basis functions by using their expansion coefficients (see Equation (4)). These coefficients are also used to determine the level-2 characteristic-basis-function far-field patterns, because each of these is a superposition of level-1 characteristic-basis-function patterns (see Section 2.2).

4. Continue by generating characteristic basis functions at level i with the aid of a the Characteristic Basis Function Method approach at the level $i-1$ (for $i = 3,4,\ldots$), and compute a new set of characteristic-basis-function patterns.

5. Construct and solve the reduced matrix equation for the full problem only at the highest level for a certain (reduced) set of excitation vectors. Afterwards, the antenna input-impedance matrix is computed from the expansion-coefficient vector and the reduced matrix at the highest level (*cf.* Section 2.2). The total radiation pattern is computed directly with the aid of this characteristic-basis-function expansion-coefficient vector and the last-determined set of characteristic-basis-function patterns. If required – for example, to visualize the surface-current distribution – the solution at the lowest level (for the RWG basis) can be recovered through the recursive version of Equation (4).

2.2 Computation of the Far-Field Pattern and Input Impedance Matrix through the Multilevel Characteristic Basis Function Method

The mth characteristic-basis-function far-field function $\mathbf{f}_m^{\mathrm{CBF};[i]}$ at the level i can be expanded in terms of the M_{i-1} characteristic-basis-function far-field patterns $\left\{\mathbf{f}_m^{\mathrm{CBF};[i-1]}\right\}$ at the lower level $i-1$ as follows:

$$\mathbf{f}_m^{\mathrm{CBF};[i]}(\theta,\phi)=\sum_{m=1}^{M_{i-1}} I_m^{\mathrm{CBF};[i-1]}\mathbf{f}_m^{\mathrm{CBF};[i-1]}(\theta,\phi), \quad (8)$$

where $I_m^{\mathrm{CBF};[i-1]}$ is the mth expansion coefficient for the mth characteristic basis function at the level $i-1$. The coefficient vector $\mathbf{I}^{CBF;[i-1]}$ is computed via the Characteristic Basis Function Method for a certain array excitation. In the process of computing the characteristic-basis-function patterns at each level, one should realize that many of the subdomains support the same set of characteristic basis functions, so that the respective characteristic-basis-function patterns are identical as well, apart from a phase correction due to their translated position. For instance, we can write

$$\mathbf{f}_p^{\mathrm{CBF};[i]}=\mathbf{f}_q^{\mathrm{CBF};[i]}\exp\left[-jk\,\mathbf{r}_{pq}\bullet\hat{\mathbf{r}}(\theta,\phi)\right], \quad (9)$$

where the pth characteristic-basis-function pattern at the level i is derived from the qth pattern by accounting for the translation vector, $\mathbf{r}_{pq}$. The unit vector $\hat{\mathbf{r}}(\theta,\phi)$ denotes the direction of observation, and k is the free-space wavenumber of the medium. Finally, it is obvious that the total array far-field pattern, $\mathbf{f}^{[i]}$, which is the quantity of interest at the highest level, can also be expanded in terms of the characteristic basis functions and associated expansion coefficients at the lower level $i-1$.

In the solution of the electric-field integral equation, it is straightforward to use voltage generators and to short circuit the other terminals, so that the antenna input-admittance matrix is obtained naturally. The mutual admittance, Y_{ab}^{ant}, between two accessible ports a and b, can be computed in terms of a reaction integral, which is of a variational form. Suppose that $\mathbf{J}_a$ is the array surface-current distribution that results from exciting terminal a with a voltage source of amplitude V_a, while all other terminals are short-circuited. Likewise, $\mathbf{J}_b$ is a result of exciting terminal b with V_b, while all other terminals are short-circuited. A stationary formula for the mutual antenna admittance, Y_{ab}^{ant}, was been in [29] with the aid of the Lorentz reciprocity theorem. The resulting expression is

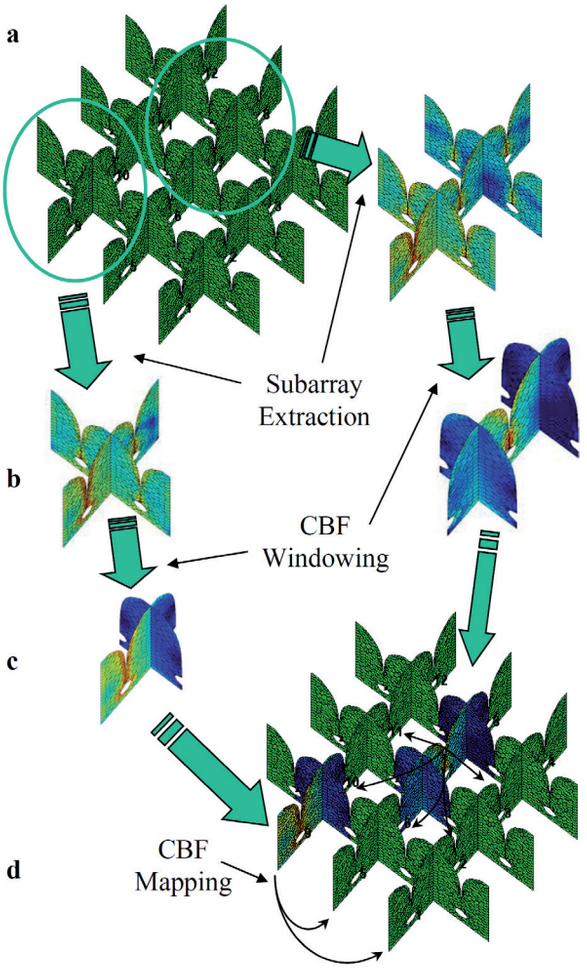

Figure 2. An approach to generate and window primary characteristic basis functions for the transmitting case: (i) Subarray extraction and generation of primary characteristic basis functions; (ii) Trapezoidal post-windowing of characteristic basis functions; (iii) One-to-one mapping of characteristic basis functions throughout the array lattice.

$$Y_{ab}^{\text{ant}} = -\frac{1}{V_a V_b} \int_{S_a} \mathbf{J}_a \bullet \mathbf{E}^s(\mathbf{J}_b)\, dS \qquad (10)$$

$$= -\frac{1}{V_a V_b} \left(\mathbf{I}_a^{CBF;[i-1]}\right)^T \mathbf{Z}^{[i-1]} \mathbf{I}_b^{CBF;[i-1]},$$

where the solutions at the level i for the currents $\mathbf{J}_a$ and $\mathbf{J}_b$ have been substituted in terms of the characteristic-basis-function expansion-coefficient vectors at the lower level $i-1$ (*cf.* Equation (5)). It is important to note that a minus sign appears in front of Equation (10), which is contrary to the plus sign presented earlier in [21] and in [30, p. 109].

2.3 Generation and Windowing of Characteristic Basis Functions at all Levels

A rather attractive feature of the Characteristic Basis Function Method is the way the physics-based characteristic basis functions are generated. We will briefly describe this procedure at level-1 for an overlapping domain-decomposition approach, applied to antenna-array problems for transmitting. The details can be found in several previously published works [18, 21] and [26].

For large antenna-array problems, we first extract several distinct and relatively small subarrays from the fully meshed array, typically from the center, corners, and edges of the array. The subarray sizes are chosen such that the direct electromagnetic environment for the center, corner, and edge elements of the corresponding subarrays closely resemble their original electromagnetic-array environment. For instance, Figure 2b illustrates two subarrays that are extracted from a 4 x 3 x 2 dual-polarized Vivaldi array (four elements in the E plane, three elements in the H plane, and two polarizations). These two subarrays represent a corner and center element, along with their interconnected neighboring elements, respectively.

Next, we solve for a set of surface currents induced in each of the subarrays by sequentially exciting the antenna terminals of the corresponding subarray (Figure 1b). Hence, for this example, four primary characteristic basis functions are generated for the subarray comprising the corner element, and seven primary characteristic basis functions are generated for the subarray comprising the center element.

We next apply a (trapezoidal) post-windowing function to the sets of primary characteristic basis functions (in Figure 1b) to suppress the undesired edge-truncation effects by reducing the support of the so-generated primary characteristic basis functions (Figure 1c). In essence, the RWG expansion coefficients making up the characteristic basis functions are post-multiplied with suitable weights. Note that the partially overlapping windowing functions have to add up to unity, so that the tapered characteristic basis functions add up in a correct manner as well, particularly in the overlapping regions.

In our specific example (Figure 1), the support covers half of the neighboring elements, although this can be changed in a manner discussed in [18]. For instance, in [21], very good accuracy was realized with only a single-cell overlap.

Finally, the set of characteristic basis functions are mapped, one-to-one, onto the corresponding edge and center elements, so that each array-element/subdomain will have its own set of characteristic basis functions (Figure 1d). Note that for this example, six subarrays have to be extracted in total to accommodate characteristic basis functions on all the array elements (three subarrays per polarization, i.e., two subarrays for the opposite-edge elements, and one for a center element).

The number of characteristic basis functions on array elements can be enlarged in order to model surface currents on array elements that can have a large number of degrees of freedom. This can be done by appending a set of secondarily generated characteristic basis functions to the already existing set of primary characteristic basis functions [7]. This is accomplished by taking the primary characteristic basis functions as distant current sources irradiating the subarrays. The thus generated currents then induce extra surface currents on these subarrays, after which these newly generated currents are truncated/windowed again, and added to the primary set of characteristic basis functions. Finally, one needs to ortho-normalize the characteristic basis functions, and retain only a minimal number of them. Both of these steps can be accomplished with the aid of a singular-value decomposition (SVD), and a thresholding procedure on the singular values [31, 32].

The above procedure is repeated to generate the characteristic basis functions for the higher levels. The only difference is that we will have to employ a lower-level Characteristic Basis Function Method to be able to solve for the subarray currents.

A rigorous full-wave analysis of phased-array antennas, each of which is surrounded by a number of other disjoint antenna arrays, becomes computationally prohibitive whenever we consider a large number of electrically large subarrays. A mono-level Characteristic Basis Function Method employs a relatively small number of characteristic basis functions, thereby reducing the computational complexity of solving the matrix equation by a large factor. However, beyond a certain point, the numerical analysis of a much-larger array of subarrays will inevitably pose a computational burden, which is caused by an increase in the number of unknowns.

To alleviate the associated memory problems, we propose to use the two-level Characteristic Basis Function Method, as outlined in Figure 1. This first generates characteristic basis functions at the antenna-element level, after which the characteristic basis functions are generated for each of the subarrays. The accuracy and computational efficiency is demonstrated below for various antenna array sizes.

All the computations were carried out by using double-precision arithmetic on a Dell Inspiron 9300 notebook, equipped with an Intel Pentium-M processor operating at 1.73 GHz, and 2.0 GB of RAM.

The tapered-slot antenna-element geometry was adopted from [18] and [21], and serves here as a reference case for further study.

2.4 An Array of Two Subarrays of Two Tapered-Slot Antenna Elements Each

We will first examine the accuracy of the Multilevel Characteristic Basis Function Method for a relatively small antenna-array problem, so that the direct MoM solution can be used as a reference for the purpose of validation. Specifically, the antenna subarray problem in Figure 1 is solved, for which we disable the Adaptive Cross Approximation algorithm, and set the singular-value-decomposition threshold in the Characteristic Basis Function Method to zero. This implies that we will employ all the primary and secondary characteristic basis functions that have been generated. The radius for generating the secondary basis functions is set large enough so as to include all the neighboring antenna-array elements at level-1, and all the neighboring subarrays at level-2. The relative error in the computed antenna input-impedance matrix is defined as

$$Error_{\%} = \frac{\left\| \mathbf{Z}_{\mathrm{MoM}}^{\mathrm{ant}} - \mathbf{Z}_{\mathrm{CBFM}}^{\mathrm{ant}} \right\|_F}{\left\| \mathbf{Z}_{\mathrm{MoM}}^{\mathrm{ant}} \right\|_F} \times 100\% , \qquad (11)$$

where $\|\cdot\|_F$ denotes the Frobenius norm, which takes the square root of the sum of the absolute squares of the matrix elements.

Table 1 illustrates that the number of basis functions was reduced from 2534 RWG basis functions for a direct MoM to only 12 characteristic basis functions (the matrix compression was 99.998%) for a level-2 Characteristic Basis Function Method. Furthermore, the relative error of a level-2 Characteristic Basis Function Method is much smaller than one percent and is – remarkably enough for this specific example – almost equal to the accuracy of a level-1 Characteristic Basis Function Method. Not unexpectedly, the total execution time was smallest for a direct MoM approach, particularly because the Characteristic Basis Function Method requires an additional amount of time to generate the characteristic basis functions and to construct a reduced matrix equation. On the contrary, in a classical MoM approach, the total execution time is governed by the time to solve the matrix equation, as it scales with the cube of the number of independent basis functions: consequently, it is advantageous to reduce the number of independent basis functions. Once this reduction has been achieved – for instance, through the use of the Multilevel Characteristic Basis Function Method – then the upper limit of the solution time is determined by the largest matrix equation that can still be solved in-core (typically, the matrix size must remain smaller than 7000 × 7000).

Figures 3 and 4 illustrate the E- and H-plane cuts of the computed embedded element patterns (150 ohm port termination) in the case where element 1 and, subsequently, element 2 was excited. One observes that the numerical results, as computed by a direct MoM approach, a level-1 Characteristic Basis Function Method, and a level-2 Characteristic Basis Function Method, were visually indistinguishable from each other. This was also confirmed by the low relative error in the numerically computed input-impedance matrix of the antenna (see Table 1).

2.5 Nine Subarrays Composed of 64 Tapered-Slot-Antenna Elements Each

The numerical accuracy and efficiency of a two-level Characteristic Basis Function Method approach, relative to a mono-level Characteristic Basis Function Method approach, will be evaluated in this section, for an array of nine disjoint subarrays of 64 tapered-slot-antenna elements each.

Quantity	Level-0 (Direct MoM)	Level-1 CBFM	Level-2 MLCBFM
#RWGs	2534	2534	2534
#CBFs (Level-1)	–	40	40
#CBFs (Level-2)	–	–	12
Generation time CBFs	0 min 0 sec	2 min 28 sec	2 min 41 sec
Total execution time	1 min 20 sec	5 min 48 sec	5 min 57 sec
Relative error $\mathbf{Z}^{\mathrm{ant}}$	0%	0.0267%	0.0266%

Table 1. A comparison between a direct MoM approach, a mono-level, and a level-2 Multilevel Characteristic Basis Function Method in reducing the number of independent basis functions, the generation time of basis functions, and the total solution time (at 900 MH).

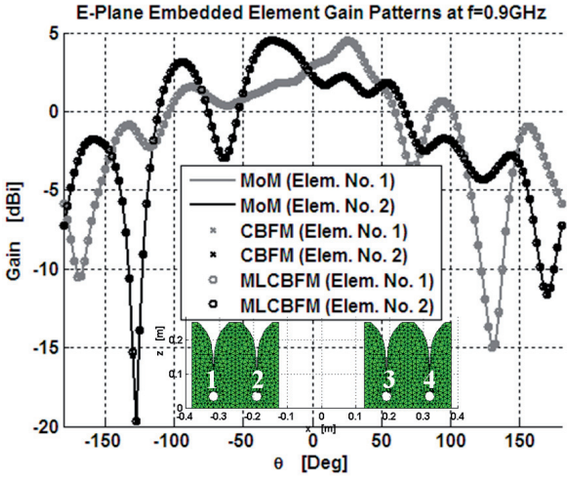

Figure 3. The computed E-plane element-gain patterns at 900 MHz. The results were computed through a direct MoM approach, a 1-level Characteristic Basis Function Method, and a 2-level Characteristic Basis Function Method.

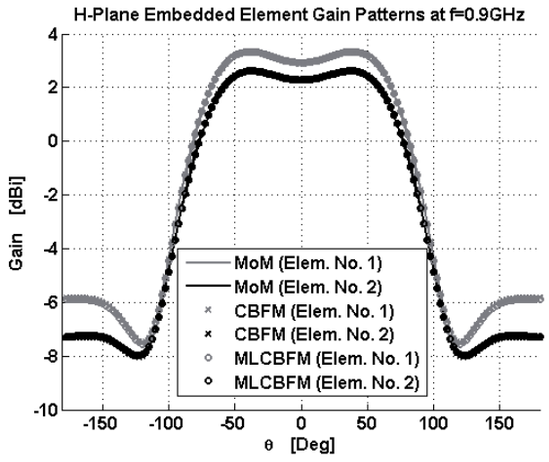

Figure 4. The computed H-plane element-gain patterns at 900 MHz. The results were computed through a direct MoM approach, a 1-level Characteristic Basis Function Method, and a 2-level Characteristic Basis Function Method.

The anomalous antenna-impedance effects, associated with the (resonant) gaps/slots between disjoint subarray tiles, were reported in [33, 34], and will therefore not be discussed in this paper. These gaps may need to be introduced for servicing purposes, so that, e.g., individual subarrays can be installed and/or removed as modular units. Furthermore, the transport and manufacturability of relatively small units may be advantageous.

The numerical computations were performed for a singular-value-decomposition threshold level of 10^{-2} (used to reduce and retain a minimal set of basis function at each level of the Multilevel Characteristic Basis Function Method). The Adaptive Cross Approximation threshold, which was used to rapidly construct the low-rank (off-diagonal) moment-matrix blocks, was set to 10^{-3}. Numerical experiments showed that a reduced Adaptive Cross Approximation threshold level has a positive effect on the symmetry of the input-impedance matrix. Furthermore, it suppresses the spurious ripples that the element radiation patterns may exhibit, albeit at a cost of longer matrix filling time. At level-1, the radius for generating the secondary characteristic basis functions was taken equal to the width of two antenna elements, whereas it was enlarged at level-2 to incorporate all the surrounding subarrays. We also studied the case in which we bypassed the generation of secondary characteristic basis functions at level-2.

Figures 6a and 6b illustrate the E-plane cuts of the power beam pattern of two subarrays, i.e., of the central and edge tiles on the right-hand side of the central tile (secondary characteristic basis functions included). The tiles were subsequently scanned to broadside ($\theta_{scan} = 0°$), and to an off-broadside direction ($\theta_{scan} = 60°$). The level-1 and level-2 Characteristic Basis Function Method were found to yield very similar results. The agreement slightly degraded when the beam was scanned to off-broadside directions. This was expected, because the (active) mutual coupling between the tiles increased for off-broadside scan

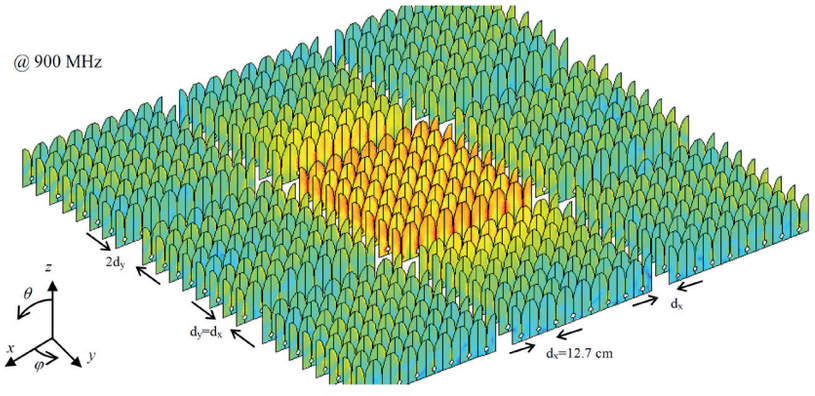

Figure 5. An array of nine subarrays (3×3) (see also [26]), each of them composed of 64 tapered-slot-antenna elements (8×8). To illustrate coupling effects, the active antennas within the central tile were excited by a voltage-gap generator placed across the slot of each tapered-slot-antenna element. The central tile scanned to broadside (end-fire direction), whereas the tapered-slot antennas of the surrounding tiles were short-circuited. The magnitude of the surface-current distribution is shown (log scale) as computed by a direct Characteristic Basis Function Method approach.

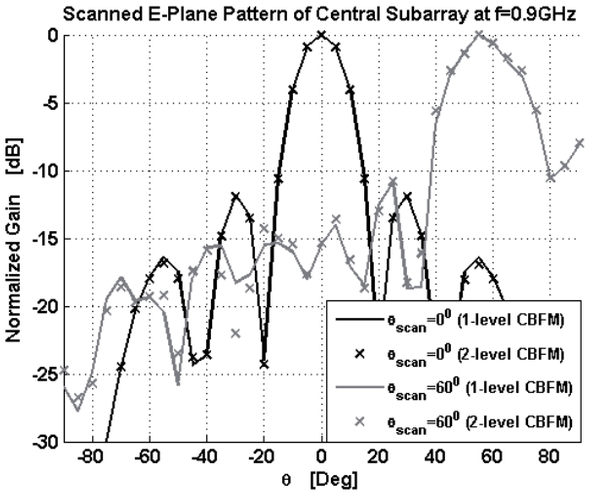

Figure 6a. E-plane cuts of the power pattern (at 900 MHz) of a subarray beam for the central tile when scanned to broadside ($\theta_{scan} = 0°$), and to an off-broadside direction ($\theta_{scan} = 60°$), for both a level-1 and level-2 Characteristic Basis Function Method.

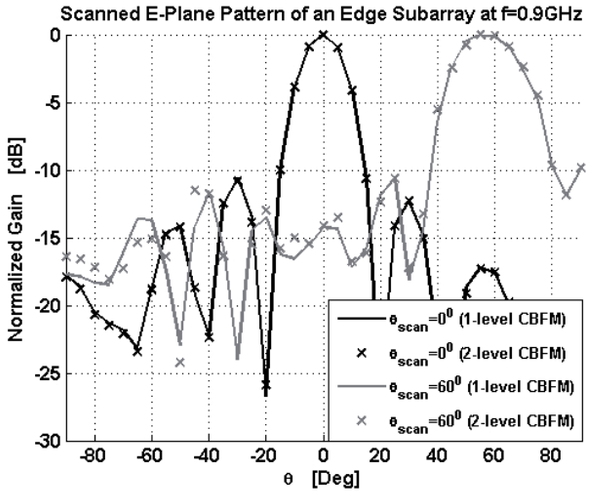

Figure 6b. E-plane cuts of the power pattern (at 900 MHz) of a subarray beam for an edge tile (to the right of the center tile: see Figure 5) when scanned to broadside ($\theta_{scan} = 0°$), and to an off-broadside direction ($\theta_{scan} = 60°$), for both a level-1 and level-2 Characteristic Basis Function Method.

directions. In these cases, the antenna tile that was excited also illuminated the neighboring tiles, so that a more-accurate numerical scheme was required than for a broadside-scanned beam.

Not surprisingly, the relative error of the numerically computed antenna input-impedance matrix in Table 2 reduced from 15.6% to 4.5% when the secondary characteristic basis functions at level-2 were included. This error reduction required almost twice the amount of characteristic basis functions, but did not lead to a much longer simulation time, because the construction of the reduced matrix was the most time-demanding element in the process.

The reduction in the number of unknowns was seen to be rather significant. The original problem (level-0) required 375,192 RWG basis functions, which was reduced to only 4320 by a level-1 Characteristic Basis Function Method approach. The degrees of freedom for the current was reduced even further at level-2, down to 1116. Since the total execution time increased only slightly, it supported the conclusion of [27], namely that the Multilevel Characteristic Basis Function Method is a memory-efficient implementation of a mono-level Characteristic Basis Function Method.

Quantity	**Level-1 CBFM**	**Level-2 CBFM (Primary CBFs at Level-2 Only)**	**Level-2 CBFM (Primary + Secondary CBFs)**
#RWGs	375192	375192	375192
Time to generate the mesh	32 min 11 sec	1 min 38 sec	1 min 38 sec
#MoM blocks to be constructed, exploiting reciprocity and translation symmetry	4770 out of 331776	4770 out of 331776	4770 out of 331776
#Primary CBFs (Level-1)	1584	1584	1584
#Primary + secondary CBFs (Level-1)	4320	4320	4320
#Primary CBFs (Level-2)	–	576	576
#Primary + secondary CBFs (Level-2)	–	576 (one CBF per antenna element)	1116
Generation time CBFs	9 min 11 sec	17 min 39 sec	23 min 58 sec
Total execution time (excludes meshing time)	151 min 46 sec	160 min 14 sec	166 min 33 sec
Relative error $\mathbf{Z}^{ant}$	0%	15.6%	4.5%

Table 2. The required computational resources and execution time for a level-1 and for two level-2 Characteristic Basis Function Method approaches (at 900 MHz).

# RWGs (level-0)	# CBFs (level-1)	# CBFs (level-2)	# MoM blocks	# MoM blocks (Exploiting Symmetry and Reciprocity)	Time to Build MoM Blocks	Total Execution Time
1042200	12000	3100	2560000	14574	323 min 55 sec	667 min 33 sec

Table 3. The required computational resources and execution time for a level-2 CBFM approach (at 900 MHz, with 25 antenna tiles).

2.6 25 Subarrays Composed of 64 Tapered-Slot-Antenna Elements Each

Next, we present the results for a very large antenna array, one that could no longer be solved by using the mono-level Characteristic Basis Function Method. We considered an antenna array consisting of 25 subarrays, each comprised of 64 tapered-slot-antenna elements (see Figure 7). The problem required more than one million RWG basis functions (at level-0), and the number of level-1 characteristic basis functions exceeded 10,000 (see Table 3). The problem was solved in-core through standard Gaussian-elimination techniques at level-2, where the number of characteristic basis functions was as low as 3100. For this simulation, we used the Characteristic Basis Function Method-Adaptive Cross Approximation settings as mentioned in the previous section. The total execution time was just over 11 hours, most of which was devoted to filling the blocks of the moment matrix. The approximate time for assembling the reduced matrix was ~176 min; for computing the reduced set of excitation vectors, ~103 min; for solving the reduced matrix at level-2 (3100 x 3100) and computing the antenna impedance matrix, ~22 min; and the remaining time was spent on the generation of the primary and secondary characteristic basis functions. It is worth pointing out that the mesh generation took only 18 min 9 sec, because advantage was taken of the fact that a large degree of translation symmetry existed at all levels for regularly-spaced antenna arrays.

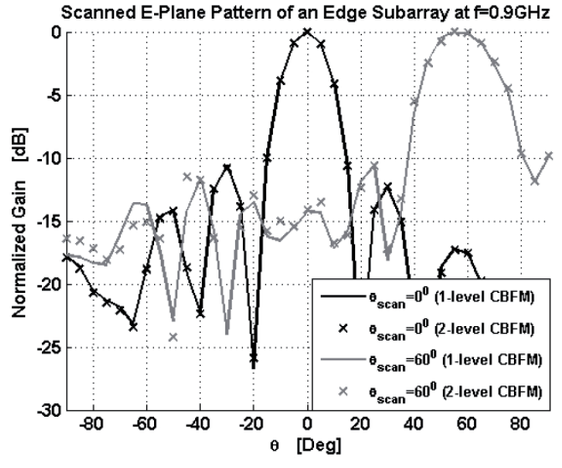

Figure 7. An array of 25 subarrays (5×5), each of them composed of 64 tapered-slot-antenna elements (8×8). To illustrate coupling effects, the active antennas within the central tile were excited by a voltage-gap generator placed over the slot of each tapered-slot-antenna element. The central tile scanned to broadside (end-fire direction), whereas the tapered-slot antennas of the surrounding tiles were short-circuited. The magnitude of the surface-current distribution is shown on a log scale (80 dB dynamic range).

3. Conclusions

In this paper, we have presented a multi-level version of the numerically efficient Characteristic Basis Function Method (CBFM) for computing the input-impedance matrix and radiation patterns of very large antenna arrays. Numerical examples have been presented for various array sizes, including a 25 subarray problem of 64 tapered-slot antennas (TSAs) each, which required more than one million RWG basis functions. The proposed method demonstrated very good accuracy, numerical efficiency, and a reduced memory-storage requirement. This led us to conclude that the Multilevel Characteristic Basis Function Method algorithm is memory efficient, and it generates a final reduced matrix equation that can be solved directly, in-core, using standard Gaussian-elimination techniques. Hence, the Multilevel Characteristic Basis Function Method extends the capabilities of the mono-level Characteristic Basis Function Method, and is useful for solving large antenna (and scattering) problems. Finally, we note that the total execution time in the Multilevel Characteristic Basis Function Method is only slightly higher, primarily because of the overhead related to the generation of characteristic basis functions.

4. Acknowledgment

This work was sponsored by the Square Kilometre Array (SKA) Aperture Array Verification Program (AAVP), and the Netherlands Organization for Scientific Research (NWO).

5. References

1. P. J. Hall, "The Square Kilometre Array: An Engineering Perspective," (reprinted from *Experimental Astronomy*, **17**, 1-3, 2004), Berlin, Springer, 2005, ISBN: 1-4020-3797-x.

2. A. B. Smolders and M. P. van Haarlem, "Perspectives on Radio Astronomy: Technologies for Large Antenna Arrays," Conference Proceedings ASTRON, April 1999, , ISBN: 90-805434-2-x.

3. http://www.skatelescope.org/.

4. R. Mittra, "A Look at Some Challenging Problems in Computational Electromagnetics," *IEEE Antennas and Propagation Magazine*, **46**, 5, October 2004, pp. 18-32.

5. R. Maaskant, M. Ivashina, R. Mittra, W. Yu, and N.-T. Huang, "Parallel FDTD Modeling of a Focal Plane Array with Vivaldi Elements on the Highly Parallel LOFAR Bluegene/L Supercomputer," IEEE International Symposium on Antennas and Propagation *Digest*, Albuquerque, New Mexico, July 2006, pp. 3861-3864.

6. V. Prakash and R. Mittra, "Characteristic Basis Function Method: A New Technique for Efficient Solution of Method of Moments Matrix Equations," *Micr. Opt. Technol.*, **36**, January 2003, pp. 95-100.

7. J. Yeo, V. Prakash, and R. Mittra, "Efficient Analysis of a Class of Microstrip Antennas Using the Characteristic Basis Function Method (CBFM)," *Micr. Opt. Technol.*, **39**, December 2003, pp. 456-464.

8. G. A. E. Vandenbosch and A. R. Van de Cappelle, "Use of Combined Expansion Scheme to Analyze Microstrip Antennas with the Method of Moments," *Radio Science*, **27**, November/December 1992, pp. 911-916.

9. J. Heinstadt, "New Approximation Technique for Current Distribution in Microstrip Array Antennas," *Micr. Opt. Technol.*, **29**, October 1993, pp. 1809-1810.

10. E. Lucente and A. Monorchio, "A Parallel Iteration-Free MoM Algorithm Based on the Characteristic Basis Function Method," International URSI Commission B EM Theory Symposium, EMTS 2007, July 26-28, 2007, Ottawa, Canada.

11. D. J. Ludick and D. B. Davidson, "Investigating Efficient Parallelization Techniques for the Characteristic Basis Function Method (CBFM)," Proceedings of the International Conference on Electromagnetics in Advanced Application (ICEAA), Torino, September 2009, pp. 400-403.

12. A. M. van de Water, B. P. de Hon, M. C. van Beurden, A. G. Tijhuis, and P. de Maagt, "Linear Embedding via Green's Operators: A Modeling Technique for Finite Electromagnetic Band-Gap Structures," *Phys. Rev. E*, **72**, 2005, 056704.

13. L. Matekovits, V. A. Laza, and G. Vecchi, "Analysis of Large Complex Structures with the Synthetic-Functions Approach," *IEEE Transactions on Antennas and Propagation*, **AP-55**, 9, September 2007, pp. 2509-2521.

14. L. Matekovits, G. Vecchi, G. Dassano, and M. Orefice, "Synthetic Function Analysis of Large Printed Structures: The Solution Space Sampling Approach," IEEE International Symposium on Antennas and Propagation, Boston, Massachusetts, July 2001, pp. 568-571.

15. W. B. Lu, T. J. Cui, Z. G. Qian, X. X. Yin, and W. Hong, "Accurate Analysis of Large-Scale Periodic Structures Using an Efficient Sub-Entire-Domain Basis Function Method," *IEEE Transactions on Antennas and Propagation*, **AP-52**, 11, November 2004, pp. 3078-3085.

16. D. J. Bekers, S. J. L. van Eijndhoven, A. A. F. van de Ven, P. Borsboom, and A. G. Tijhuis, "Eigencurrent Analysis of Resonant Behavior in Finite Antenna Arrays," *IEEE Transactions on Microwave Theory and Techniques*, **54**, 6, June 2006, pp. 2821-2829.

17. E. Suter, J. R. Mosig, "A Subdomain Multilevel Approach for the Efficient MoM Analysis of Large Planar Antennas," *Micr. Opt. Technol.*, **26**, 4, August 2000, pp. 270-277.

18. R. Maaskant, R. Mittra, and A. G. Tijhuis, "Application of Trapezoidal-Shaped Characteristic Basis Functions to Arrays of Electrically Interconnected Antenna Elements," Proceedings of the International Conference on Electromagnetics in Advanced Application (ICEAA) 2007, September 17-21, 2007, pp. 567-571.

19. C. Craeye, "A Fast Impedance and Pattern Computation Scheme for Finite Antenna Arrays," *IEEE Transactions on Antennas and Propagation*, **AP-54**, 10, October 2006, pp. 3030-3034.

20. E. Garcia, C. Delgado, F. S. de Adana, F. Cátedra, and R. Mittra, "Incorporating the Multilevel Fast Multipole Method into the Characteristic Basis Function Method to Solve Large Scattering and Radiation Problems," IEEE International Symposium on Antennas and Propagation, Honolulu, Hawaii, June 2007, pp. 1285-1288.

21. R. Maaskant, R. Mittra, and A. G. Tijhuis, "Fast Analysis of Large Antenna Arrays Using the Characteristic Basis Function Method and the Adaptive Cross Approximation Algorithm," *IEEE Transactions on Antennas and Propagation*, **AP-56**, 11, pp. 3440-3451, November 2008.

22. I. Stevanovic, and J. R. Mosig, "Subdomain Multilevel Approach with Fast MBF Interactions," IEEE International Symposium on Antennas and Propagation, Monterey, California, June 2004, pp. 367-370.

23. P. De Vita, A. Freni, L. Matekovits, P. Pirinoli, and G. Vecchi, "A Combined AIM-SFX Approach for Large Complex Arrays," IEEE International Symposium on Antennas and Propagation, Honolulu, Hawaii, June 2007, pp. 3452-3455.

24. C. Craeye, A. O. Boryssenko, and D. H. Schaubert, "Analysis of Infinite and Finite Arrays of Tapered-Slot Antennas for SKA," Proc. EUMC, Milan, Italy, 2002, pp. 1003-1006.

25. M. N. Vouvakis, S.-C. Lee, K. Zhao, and J.-F. Lee, "A Symmetric FEM-IE Formulation with a Single-Level IE-QR Algorithm for Solving Electromagnetic Radiation and Scattering Problems," *IEEE Transactions on Antennas and Propagation*, **AP-52**, 11, November 2004, pp. 3060-3070.

26. R. Maaskant, R. Mittra, and A. G. Tijhuis, "Fast Solution of Multi-Scale Antenna Problems for the Square Kilometre Array (SKA) Radio Telescope Using the Characteristic Basis Function Method (CBFM)," *Applied Computational Electromagnetics Society (ACES) Journal*, **24**, 2, April 2009, pp. 174-188.

27. J. Laviada, F. Las-Heras, M. R. Pino, and R. Mittra, "Solution of Electrically Large Problems with Multilevel Characteristic Basis Functions," *IEEE Transactions on Antennas and Propagation*, **AP-57**, 10, October 2009, pp. 3189-3198.

28. S. Rao, D. Wilton, and A. Glisson, "Electromagnetic Scattering by Surfaces of Arbitrary Shape," *IEEE Transactions on Antennas and Propagation*, **AP-30**, 3, May 1982, pp. 409-418.

29. R. Maaskant, *Analysis of Large Antenna Systems*, PhD dissertation, Eindhoven University of Technology, Eindhoven, 2010.

30. R. F. Harrington, *Field Computation by Moment Methods*, New York, Macmillan Company, 1968.

31. G. H. Golub and C. F. van Loan, *Matrix Computation*, Baltimore, MD, John Hopkins University Press, 1989.

32. C. Delgado, F. Catedra, and R. Mittra, "A Numerically Efficient Technique for Orthogonalizing the Basis Functions Arising in the Solution of Electromagnetic Scattering Problems Using CBFM," IEEE International Symposium on Antennas and Propagation, Honolulu, Hawaii, June 2007, pp. 3608-3611.

33. D. H. Schaubert, and A. O. Boryssenko, "Subarrays of Vivaldi Antennas for Very Large Apertures," Proceedings of the 34th European Microwave Conference, Amsterdam, 2004, pp. 1533-1536.

34. D. H. Schaubert, S. Kasturi, M. W. Elsallal, and W. van Cappellen, "Wide Bandwidth Vivaldi Antenna Arrays – Some Recent Developments," Proceedings of the European Conference on Antennas and Propagation, Nice, France, 2006.

Modeling Large Finite Antenna Arrays with Non-Conformal, Non-Overlapping Finite-Element Domain-Decomposition Methods

M. Vavoukis
J.F. Lee

Abstract

A non-conformal, non-overlapping domain-decomposition method is described and applied to model large finite antenna arrays. Only the first-order Robin transmission condition is employed, since it is adequate for most antenna-array radiation problems. Moreover, a finite-element tearing and interconnecting (FETI) algorithm is also discussed in detail for treating the large number of repetitions within the arrays. Furthermore, through measurements and the full-wave Finite-Element Method, we validate the accuracy of the proposed non-conformal, non-overlapping domain-decomposition method. Finally, with the aid of the domain-decomposition method, we are able to rigorously compare the performance of antenna arrays on flat and curved platforms.

1. Introduction

This paper is largely based on the PhD dissertation of Dr. M. Vavoukis [1]. The main emphasis of the paper is to discuss the use of domain decompositions (DD) for the solution of Maxwell's equations in the time-harmonic regime, particularly in solving large finite antenna arrays. The vehicle that will be used to demonstrate the power of the proposed domain-decomposition algorithms will be the Tangential Vector Finite-Element Method (TVFEM), but the methodologies can be also extend to other partial differential equation (PDE) or integral-equation-(IE) based numerical methods. All the domain-decomposition methods and algorithms described herein share one very important common characteristic: they are be non-overlapping and non-conforming in nature. That is, the original computational domain is decomposed into a set of disjoint domains, whereas the mesh on either side of a domain interface can be completely different.

1.1 Why Use Domain-Decomposition Methods to Analyze Electromagnetic Problems?

The answers to this question are four:

1. It is well known that as the electrical size of the computational domain in a partial-differential-equation- or integral-equation-based method increases, the performance of iterative solution methods dramatically deteriorates. Domain-decomposition methods try to overcome this effect using a "divide and conquer" strategy. Namely, instead of solving the original large and hard-to-solve problem in the entire computational domain, they divide it into smaller and easier-to-solve sub-problems, related to each subdomain. This strategy can be used to create effective preconditioners in a Krylov-based solver, or as a direct domain-decomposition method in a stationary iteration scheme.

2. In the quest to solve larger and larger electromagnetic (EM) problems using discretization-based methods, the amount of memory needed to set up and solve a problem scales (in the best case) as $O(N)$, where N is the number of unknowns needed to solve the problem. Naturally, this complexity poses an inherent limitation related to the size of memory utilized by a single computer. To overcome this problem, large-scale parallel processing needs to be used. Fortunately, domain-decomposition methods are inherently parallelizable. Specifically, their parallel versions are easy to implement in numerical codes, and moreover both memory and computational time are nearly linearly scalable with the number of processors.

M. Vavoukis is with the Electrical and Computer Engineering Department, University of Massachusetts at Amherst, Amherst, MA, USA; e-mail: vouvakis@ecs.umass.edu. J. F. Lee is with the Electrical and Computer Engineering Department, The Ohio State University, Columbus, OH, USA; e-mail: lee.1863@osu.edu.

3. Most of the large EM problems encountered possess certain repetitions, or symmetries of some geometrical features. For example, large antenna arrays or metamaterial structures exhibit many repetitions, whereas most of the scattering targets of interest do have at least one plane of symmetry. Domain-decomposition methods easily exploit these duplications and symmetries, which numerically translate into a tremendous reduction in computational memory and possibly CPU time.

4. Last but not the least, solving large EM problems with the Finite-Element Method or even the Boundary Element Method (BEM) requires some sort of discretization of the geometry into a mesh. In the case of the Boundary Element Method, the generation of that volume or surface mesh can be an extremely challenging task, especially when the size of the problem is large and at the same time exhibits multi-scale features. Using the proposed non-conforming domain-decomposition methods, the meshing of such geometries can be tremendously relaxed, since each domain mesh is kept relatively small, and the conformity constraints across domains are absent. Moreover, adaptive-mesh-refinement strategies become more flexible, since they can be based on subdomains alone. In addition, the non-conformity of the mesh creates new potentials for fast optimization strategies.

Antenna arrays make up a very important class of large and geometrically complicated EM problems. Arrays are used on every wireless-communication base station, on every radar system, and on nearly every satellite communication link. The proposed method is tailored to take advantage of the repetitions among array elements, leading to an extremely efficient EM analysis (see [2]). Due to this very fact of exploiting repetitions, the proposed method can be adapted for the analysis of finite photonic crystals (PC), photonic bandgap (PBG) or electromagnetic bandgap (EBG) structures, and any other type of metamaterial that is finite in extent. Since the proposed domain decomposition is built on the top of a Finite-Element Method kernel, the incorporation of lumped L and C elements used in many metamaterials is relatively easy. In addition, complex materials, such as ferrites, garnets, ferromagnetics, ferroelectrics, and other exotic materials used to form metamaterials, are easily incorporated into the proposed method. In light of the above-mentioned comments, novel microwave and antenna technologies printed on metamaterial substrates can be efficiently simulated (see [3]).

Having established the reasons and the significance for using domain-decomposition methods in solving EM problems, it is time to address the specific domain-decomposition methodologies that will be employed to accomplish this goal. The key ingredients of the proposed approach can be grouped into the following three categories:

1. The Non-Overlapping Schwarz Algorithm is a domain-decomposition algorithm wherein each subdomain does not overlap with its neighboring subdomains, but only at an interface. The Schwarz algorithm proceeds by solving each subdomain problem alternatively, and passing information across domain interfaces through an appropriate transmission condition (TC) [1, 4]. It has been repeatedly pointed out that the communication of information thought the transmission conditions is of crucial importance in obtaining a stable, optimal, and convergent domain-decomposition algorithm. The algorithm is iterative: starting from an initial guess for each domain, the subdomain solutions and communication across subdomains proceeds until a certain equilibrium in the solution of the entire domain has been achieved. The non-overlapping Schwarz algorithm has been directly used as an iterative solver, or as an additive or multiplicative preconditioner on Krylov-subspace methods. The non-overlapping variant of the Schwarz algorithm is more elegant and efficient than its overlapping counterparts; unfortunately, it poses more mathematical challenges in achieving stability, optimality, and convergence.

2. Cement Finite Elements is a methodology of solving finite-element problems with non-conforming or non-matching triangulations across an interface. In a more general setting, cement elements can be used to interface between different types of elements, for example, finite elements with spectral elements, etc. Usually, the appropriate continuity conditions on the solution across the different triangulations are weakly enforced through the use of a Lagrange multiplier set.

3. The Finite-Element Tearing and Interconnecting (FETI) algorithm is a class of iterative sub-structuring algorithms based on Lagrange multipliers. Like all sub-structuring algorithms, Finite-Element Tearing and Interconnecting tries to establish an iterative process based on a reduced number of unknowns, usually the unknowns on the domain-interface skeleton. Many different variants of the algorithm can be found in the literature, e.g., 2-level-FETI, FETI-2LM, FETI-H, FETI-DP [5-9], etc., dedicated to a specific application. The main idea among all Finite-Element Tearing and Interconnecting algorithms is to solve each subdomain problem independently (the tearing process), and to then use a set of extra Lagrange-multiplier unknowns to appropriately constrain the solutions across interfaces, in an iterative fashion (the interconnecting process). In comparison to other sub-structuring algorithms, Finite-Element Tearing and Interconnecting exhibits superior parallelization scalability. When used as a preconditioner, it can result in faster and scalable algorithms with respect to the number of domains and the size of the overall problem. The specific Finite-Element Tearing and Interconnecting algorithm that we employ here is slightly different from the algorithms proposed by Farhat [5-8]. However, the differences are minor, and thus we see no need to name it differently for the proposed tearing and connecting scheme.

2. Literature Review

Domain-decomposition methods have been among the favorite areas of research in the applied-mathematics, computational-mechanics, and fluid-dynamics communities during the last ten years. Even though domain decomposition is a relative new field, a number of specialized scientific symposiums have been organized and dedicated to domain-decomposition methods; among these, the most prominent is the annual International Conference on Domain Decomposition Methods. In the general literature, three books stand out: *Domain Decomposition, Parallel Multilevel Methods for Elliptic Partial Differential Equations* by B. Smith et al. [10]; *Domain Decomposition Methods for Partial Differential Equations* by Quarteroni and Valli [11]; and the recent book by Toselli and Widlund, *Domain Decomposition Methods – Algorithms and Theory*. Two more monographs from the Springer-Verlag series on Lecture Notes in Computational Science and Engineering have been devoted to domain-decomposition methods: *Discretization Methods and Iterative Solvers Based on Domain Decomposition* by B. Wohlmuth [8], and the edited monograph of L. Pavarino and A. Tosseli, *Recent Developments in Domain Decomposition Methods* [13]. In addition, a number of general domain-decomposition tutorial articles have been published; among them. we cite [14, 15].

The electrical-engineering community, and especially the engineering EM community, has in recent years been utilizing domain-decomposition methods in earnest to solve EM-related problems. Stupfel applied the domain-decomposition method to analyze two-dimensional scalar and three-dimensional vector wave problems in [16] and [17], respectively. In both works, a Finite-Element Method non-overlapping onion-like domain decomposition was used to analyze scattering problems. In the microwave community, domain-decomposition methods have been used to analyze interconnects and printed-circuit boards (PCBs) in the quasistatic regime using the Finite-Element Method [18-20]. Domain decomposition has also been used in the context of the Finite-Difference Time-Domain method (FDTD) on both two-dimensional and three-dimensional scattering problems [21, 22]. At this point, it is important to address the contributions of Prof. Gedney's group in [23, 24]. In the former paper, the Finite-Element Tearing and Interconnecting method was used to solve three-dimensional wave-guiding problems in the frequency domain with parallel machines. In the latter paper, the method was extended to a three-dimensional Finite-Element Time-Domain method (FETD) to solve cavity problems. In the EM literature, there have been a number of other domain-decomposition attempts. More precisely, these were domain-partitioning schemes that resulted in banded matrices solved with direct solvers [25-27]. Recently, Kindt, Sertel, and Volakis proposed a Finite-Element Boundary-Integral- (FEBI) based array-decomposition methodology (ADM) to analyze finite antenna arrays, [28, 29]. Even though this approach is generally classified into the classical domain-decomposition approaches, it is more like a domain-partitioning scheme that globally transfers information across domains, through the use of the appropriate Green's function. Certain translational symmetries (Toeplitz matrix structure) can be exploited through the use of the FFT or even the Finite Multipole Method (FMM). As the most-recent additions to the application of domain-decomposition methods for solving full-wave electromagnetic problems, we cite Prof. Jin's works [9, 33], and our own contributions [30-32].

2.1 Non-Overlapping Schwarz Domain Decomposition

The classical Schwarz alternating algorithm is over a century old. In 1896, Schwarz [34] developed the overlapping variant of the algorithm to prove the uniqueness of the Laplace problem in non-separable domains. The first to recognize the numerical implications of the algorithms was Miller in 1965 [35], and later Loins in [36] and [37]. The first non-overlapping Schwarz Algorithm was proposed by Loins in [38]. In these early studies of the Schwarz algorithms, elliptic (static) problems were considered. Apart form the non-overlapping variant of Loins, all the information communication was done though the use of a Dirichlet-to-Dirichlet or Neumann-to-Neumann or even Dirichlet-to-Neumann-type interface transmission condition. Alternatively, a Robin-type transmission condition had to be imposed, to ensure convergence for the non-overlapping variant of [38]. For that reason, the non-overlapping Schwarz algorithm with Robin transmission conditions is often called the *Lions-Schwarz Algorithm*. The first to extend and study the non-overlapping Schwarz Algorithm for Helmholtz (dynamic) problems was Despres [39, 40].

The first to tailor the non-overlapping Schwarz algorithm for Maxwell's equations and time-harmonic EM problems was Despres, Collino, and Robles in their early work [41]. The appropriate Robin transmission conditions were extended to account for the vector nature of the problem. This modified Schwarz algorithm is often termed the *Despres-Schwarz Algorithm*. Following the footsteps of Despres and Collino in [42], Rawat and Lee in [32] introduced new transmission conditions that further improved the convergence and overall efficiency of the Despres-Schwarz algorithm.

2.2 Non-Conforming Finite-Element Methods

As in the case of non-overlapping Schwarz methods, non-conforming/non-matching element techniques had their origin in the French school of applied mathematics. Almost a decade ago, Bernardi, Maday, and Patera [43, 44] proposed the mortar element to solve domain-decomposition problems with non-matching interfaces. In this original work, the

authors used the constrained-multiplier approach to enforce a weak continuity of the solution across the non-conforming interfaces. The method was applied to two-dimensional elliptic problems that led to a symmetric positive definite variational statement. Note that in this early work and all of the following work based on the constrained-multiplier space, no extra unknowns were introduced, but the finite support of the basis functions on the non-mortar interfaces was lost. The unconstrained multiplier approach of realizing mortar elements was proposed in 1999 by Ben Belgacem in [45]. The extensions of the constrained mortar-element method to the low-frequency Maxwell's problem, mainly for eddy-current applications, was done in [46-48]. In these studies, the optimality and error estimates of the mortar method were assessed.

Even though mortar-element methods have been very successful in treating non-conforming grids with Dirichlet-to-Neumann or Neumann-to-Neumann domain-decomposition algorithms, they cannot be easily used for domain-decomposition algorithms based on Robin or other transmission conditions. For such transmission conditions, a new class of non-conforming methods has been proposed: the cement element method. The method was originally proposed by Arbogast and Yotov in [49] for elliptic and parabolic problems. The term "cement" is due to Achdou et al. [50], who used the methods in the context of a finite volume. Independently, Lee, Vouvakis, and Lee developed a variant of the cement method for Maxwell's equation in [2]. The method is based on a mixed finite-element formulation that does not require the mortar and non-mortar sides. The two sides of the nonconforming triangulations are symmetric, and local adaptive-mesh-refinement techniques can be used on each side, e.g., the mortar side, without the need of modifying the non-mortar-side's mesh. Along with other advantages, Robin or other higher-order transmission conditions [31, 32] can be weakly enforced through the use of a double-valued Lagrange multiplier (on either side of the interface), representing the electric current.

2.3 Finite-Element Tearing and Interconnection (FETI) Algorithms

This method was introduced by Farhat and Roux in [5] in the early nineties. Finite-Element Tearing and Interconnecting was originally used to solve elliptic problems arising in structural mechanics. Due to its superior scalability and parallel performance over other sub-structuring methods, Finite-Element Tearing and Interconnecting quickly gained popularity in other areas of computational science, such as elasticity, acoustic scattering, the Stokes equations, and Maxwell's equations [21, 22, 9, 33]. Along with the various applications, a number of different variants of the method started to emerge. With regard to this, we refer to the Two-Level FETI-H in [6, 7], and the FETI-DP in [8, 9]. In the former case, the "H" stands for Helmholtz, and it is an adaptation of the method to account for the wave nature of Helmholtz problems. The method is used in the context of a two-level (one local, one global) preconditioner to achieve scalability and superior convergence. Note that one and two (one on either side of the interface) Lagrange multiplier sets were previously proposed in the framework of FETI-H.

3. Notation

Throughout the manuscript, boldface capital letters will represent matrices and operators, except when explicitly stated otherwise. Boldface lowercase letters will represent column/row vectors and vector fields. An over-hat, e.g., $\hat{\mathbf{a}}$ indicates a unit vector in $\mathcal{R}^3$. Position vectors $\mathbf{r}$ and $\mathbf{r}'$ refer to the observation and source, respectively. Throughout the document, the free-space wavenumber will be denoted by $k = \omega\sqrt{\mu_0\epsilon_0}$, where $\omega = 2\pi f$ is the radial frequency of operation, and ϵ_0 and μ_0 are the free-space permittivity and permeability, respectively. Note that $\epsilon_r = \frac{\epsilon}{\epsilon_0}$ and $\mu_r = \frac{\mu}{\mu_0}$ represent the relative permittivity and permeability of dielectric and magnetic materials, respectively. The free-space intrinsic impedance is represented by $\eta = \sqrt{\frac{\mu_0}{\epsilon_0}}$. The fundamental solution (Green's function) for the scalar Helmholtz equation for free space is denoted by

$$g\left(\mathbf{r}\left|\mathbf{r}'\right.\right) = \frac{e^{-jk|\mathbf{r}-\mathbf{r}'|}}{4\pi|\mathbf{r}-\mathbf{r}'|}, \quad \mathbf{r} \neq \mathbf{r}'. \tag{1}$$

Most of the definitions will be loosely presented for the sake of brevity and clarity. First, let's define the surface integral of two complex-valued vector functions as

$$\langle \mathbf{u}, \mathbf{v} \rangle_\Gamma = \int_\Gamma (\mathbf{u} \bullet \mathbf{v})\, dx^2 . \tag{2}$$

Similarly, the volume integral of two complex-valued functions in a domain Ω is denoted by

$$\langle \mathbf{u}, \mathbf{v} \rangle_\Omega = \int_\Omega (\mathbf{u} \bullet \mathbf{v})\, dx^3 . \tag{3}$$

Several spaces need to be defined beforehand. The following convention will be adopted: spaces of scalar-valued functions will be denoted by $\mathcal{H}$, whereas for spaces of vector-valued functions the boldface letter $\mathbf{H}$ will be used. One of the most important spaces in electromagnetics is that of curl-conforming functions in a subdomain Ω:

$$\mathbf{H}(curl, \Omega) = \left\{ \mathbf{u} \left| \int_\Omega \left(|\nabla \times \mathbf{u}|^2 + |\mathbf{u}|^2 \right) dx^3 < \infty \right. \right\}. \tag{4}$$

This is the space where the electric and magnetic field reside. The physical meaning of the space $\mathbf{H}(curl, \Omega)$ is that in subdomain Ω, the electric and magnetic energies

are finite. It is now time to introduce some trace operators and spaces of tangential vector fields on the surface $\Gamma = \partial\Omega$ First, let's define the *tangential surface trace*, γ^t, acting on $\mathbf{u}$ as

$$\gamma^t \mathbf{u} \coloneqq \hat{\mathbf{n}} \times \left(\mathbf{u} \times \hat{\mathbf{n}}\right), \tag{5}$$

where $\hat{\mathbf{n}}$ denotes the outward- (with respect to Ω) pointing unit vector on Γ. In other words, $\gamma^t \mathbf{u}$ contains the tangential components of the vector field $\mathbf{u}$ on the surface Γ. A second trace necessary for the definition of the integral equations is the *twisted tangential trace*, $\gamma^\times$, which is defined as

$$\gamma^\times \mathbf{u} \coloneqq \hat{\mathbf{n}} \times \mathbf{u}, \tag{6}$$

which again implies that $\gamma^\times \mathbf{u}$ contains the tangential components of $\mathbf{u}$ on surface Γ, the same as $\gamma^t \mathbf{u}$, but twisted 90° around $\hat{\mathbf{n}}$.

Of particular interest in this work will be the spaces $\mathbf{H}_{\|}^{1/2}(\Gamma)$ and $\mathbf{H}_{\perp}^{1/2}(\Gamma)$ of surface vector functions on Γ. Informally speaking, these spaces contain the tangential surface vector fields with "weak tangential continuity" and "weak normal continuity," respectively, across the edges of a faceted surface, Γ. It is important to emphasize the weak nature of the continuity, since the surface can be faceted. In that case, strong continuity along the edges and corners cannot be rigorously defined. The corresponding dual spaces of $\mathbf{H}_{\|}^{1/2}$ and $\mathbf{H}_{\perp}^{1/2}$ will be denoted by $\mathbf{H}_{\|}^{-1/2}$ and $\mathbf{H}_{\perp}^{-1/2}$, respectively. Finally, and most importantly for this work, the following two spaces need to be defined:

$$\mathbf{H}_{\|}^{-1/2}\left(div_\Gamma, \Gamma\right) = \left\{\mathbf{u} \in \mathbf{H}_{\|}^{-1/2}(\Gamma), div_\Gamma \mathbf{u} \in H^{-1/2}(\Gamma)\right\} \tag{7}$$

and

$$\mathbf{H}_{\perp}^{-1/2}\left(curl_\Gamma, \Gamma\right) = \left\{\mathbf{u} \in \mathbf{H}_{\perp}^{-1/2}(\Gamma), curl_\Gamma \mathbf{u} \in H^{-1/2}(\Gamma)\right\}, \tag{8}$$

where div_Γ and $curl_\Gamma$ are the surface divergence and curl operators. From an engineering point of view, it is sufficient to say the $\mathbf{H}_{\|}^{-1/2}\left(div_\Gamma, \Gamma\right)$ is the space that to which some of the most famous vector basis functions in the EM community, such as the RWG [51], belong. Similarly, $\mathbf{H}_{\perp}^{-1/2}\left(curl_\Gamma, \Gamma\right)$ contains the surface Whitney 1-form (or edge elements) [52]. It is very important at this point to note that $\mathbf{H}_{\perp}^{-1/2}\left(curl_\Gamma, \Gamma\right)$ and $\mathbf{H}_{\|}^{-1/2}\left(div_\Gamma, \Gamma\right)$ are *dual* to each other through a duality pairing defined in Equation (2).

4. Boundary-Value Problem and Formulation

4.1 Boundary-Value Problem Statement

The electromagnetic scattering or radiation in unbounded domains is governed by Maxwell's equations for the electric and magnetic fields $(\mathbf{E}, \mathbf{H})$, subject to the Silver-Muller radiation condition. The formal statement of such a boundary-value problem (BVP) can be found elsewhere [53]. Here, only an approximate problem will be considered for the sake of simplicity. Namely, the unbounded domain is replaced by a bounded domain Ω, with first-order absorbing boundary condition (ABC) imposed on the finite truncation boundary $\partial\Omega = \Gamma_{ext}$. Under conditions of time-harmonic excitations, and in the absence of nonlinear materials, the Maxwell's system is reduced into the following boundary-value-problem statement:

Find the electric field $\mathbf{E} \in \mathbf{H}\left(curl; \Omega\right)$ such that

$$\begin{aligned}
&\nabla \times \frac{1}{\mu_r} \nabla \times \mathbf{E} - k^2 \epsilon_r \mathbf{E} = -\jmath k \eta \mathbf{J}^{imp} && \text{in } \Omega \\
&\gamma^\times \left(\frac{1}{\mu_r} \nabla \times \mathbf{E} \right) = 0 && \text{on } \Gamma_{pmc} \\
&\gamma^\times \left(\mathbf{E} \right) = 0 && \text{on } \Gamma_{pec} \\
&\gamma^\times \left(\frac{1}{\mu_r} \nabla \times \mathbf{E} \right) - \jmath k \gamma^t \left(\mathbf{E} \right) = 0 && \text{on } \Gamma_{ext}
\end{aligned} \tag{9}$$

The excitation is assumed to be an imposed electric current, $\mathbf{J}^{imp}$, within the domain of interest. The Neumann and Dirichlet boundary conditions are imposed on perfect magnetic conductors (PMC) on surface Γ_{pmc}, and on perfect electric conductors on surface Γ_{pec}, respectively. The last boundary condition represents the first-order absorbing boundary condition imposed on the finite truncation boundary, Γ_{ext}. It should be noted that the theory and formulation in this paper is not restricted by the use of the absorbing boundary condition; this was only done for reasons of brevity and simplicity. The same formulation holds true for PML, boundary integral [53, 54], or any other boundary-truncation method.

4.2 Domain Decomposition for Maxwell's Equations

In the case of the non-overlapping domain decomposition, the computational domain, Ω, is decomposed into a number of disjoint subdomains. For the sake of brevity and simplicity and without loss of generality, only two subdomains, Ω_1 and Ω_2, will be considered. In

each subdomain, let us denote the restrictions of the unknown vector field $\mathbf{E}$ as $\mathbf{E}_1$ and $\mathbf{E}_2$ for subdomains Ω_1 and Ω_2 respectively. With respect to Figure 1, the decomposed continuous boundary-value problem reads:

Given an arbitrary initial value $\left[\mathbf{E}_1^{(0)}, \mathbf{E}_2^{(0)}\right]$, find $\left[\mathbf{E}_1^{(n)}, \mathbf{E}_2^{(n)}\right]$ through the iteration

$$\nabla \times \frac{1}{\mu_r} \nabla \times \mathbf{E}_1^{(n)} - k^2 \epsilon_r \mathbf{E}_1^{(n)} = -\jmath k \eta \mathbf{J}_1^{imp} \quad \text{in } \Omega_1 ,$$

$$\gamma^{\times}\left[\frac{1}{\mu_r} \nabla \times \mathbf{E}_1^{(n)}\right] = 0 \quad \text{on } \Gamma_{pmc} ,$$

$$\gamma^{\times}\left(\mathbf{E}_1^{(n)}\right) = 0 \quad \text{on } \Gamma_{pec} , \tag{10}$$

$$\gamma^{\times}\left[\frac{1}{\mu_r} \nabla \times \mathbf{E}_1^{(n)}\right] - \jmath k \gamma^{t}\left[\mathbf{E}_1^{(n)}\right] = 0 \quad \text{on } \partial\Omega_1 \bigcap \Gamma_{ext} ,$$

$$\gamma^{\times}\left[\frac{1}{\mu_r} \nabla \times \mathbf{E}_1^{(n)}\right]_{\Gamma_{12}^{(1)}} - \mathbf{S}_1 \left\{\gamma^{t}\left[\mathbf{E}_1^{(n)}\right]\right\}$$

$$= -\gamma^{\times}\left[\frac{1}{\mu_r} \nabla \times \mathbf{E}_2^{(n-1)}\right]_{\Gamma_{12}^{(2)}} - \mathbf{S}_1 \left\{\gamma^{t}\left[\mathbf{E}_2^{(n-1)}\right]\right\} \quad \text{on } \Gamma_{12}$$

and

$$\nabla \times \frac{1}{\mu_r} \nabla \times \mathbf{E}_2^{(n)} - k^2 \epsilon_r \mathbf{E}_2^{(n)} = -\jmath k \eta \mathbf{J}_2^{imp} \quad \text{in } \Omega_2 ,$$

$$\gamma^{\times}\left[\frac{1}{\mu_r} \nabla \times \mathbf{E}_2^{(n)}\right] = 0 \quad \text{on } \Gamma_{pmc} ,$$

$$\gamma^{t}\left[\mathbf{E}_2^{(n)}\right] = 0 \quad \text{on } \Gamma_{pec} , \tag{11}$$

$$\gamma^{\times}\left[\frac{1}{\mu_r} \nabla \times \mathbf{E}_2^{(n)}\right] - \jmath k \gamma^{t}\left[\mathbf{E}_2^{(n)}\right] = 0 \quad \text{on } \partial\Omega_2 \bigcap \Gamma_{ext} ,$$

$$\gamma^{\times}\left[\frac{1}{\mu_r} \nabla \times \mathbf{E}_2^{(n)}\right]_{\Gamma_{12}^{(2)}} - \mathbf{S}_2 \left\{\gamma^{t}\left[\mathbf{E}_2^{(n)}\right]\right\}$$

$$= -\gamma^{\times}\left[\frac{1}{\mu_r} \nabla \times \mathbf{E}_1^{(n-1)}\right]_{\Gamma_{12}^{(1)}} - \mathbf{S}_2 \left\{\gamma^{t}\left[\mathbf{E}_1^{(n-1)}\right]\right\} \text{ on } \Gamma_{12} .$$

We note that $\gamma^{\times}\left(\mathbf{u}\right)_{\Gamma_{12}^{(i)}} = \hat{\mathbf{n}}_i \times \mathbf{u}$, where $\hat{\mathbf{n}}_i$ is the unit normal on the interface boundary Γ_{12}, and pointing away from subdomain Ω_i (refer to Figure 1). Moreover $\square^{(n)}$ denotes the iteration count. Two important remarks should accompany the decomposed continuous boundary-value problem of Equation (10) and (11). It is apparent that the divergence-free condition was dropped from both subdomain boundary-value problems. This was only done due to reasons of space limitations; at this moment, the reader should assume that this condition is carried with the vector *curl-curl* equation until the definition of the discrete-problem statement. There, its enforcement will be done through a graph-partitioning (tree-co-tree) gauge. The second and most important remark refers to the "artificial" transmission condition used to communicate information across domains. As was noted by many researchers in the past [42, 32], the choice of the transmission condition has tremendous impact on the success and speed of the Domain-Decomposition algorithm. The important principles for "designing" a transmission condition are two: (1) to ultimately enforce the tangential continuity of the electric and magnetic fields across the subdomain interface; and (2) to provide a means of accelerating the convergence for the domain-decomposition iteration loop. Looking at the last equation of Equations (10) and (11), both principles have been taken into consideration. The continuity of the tangential magnetic field is imposed by the first term in each side of the two equations, whereas the continuity of the electric field is imposed through the tangential operators $\mathbf{S}_i\left(\bullet\right)$, where $i = 1, 2$. It is vital for the operator to be non-singular, and strictly positive definite; otherwise, the electric-field continuity cannot be imposed. In the next section, how to choose the tangential operators $\mathbf{S}_i\left(\bullet\right)$ such that it not only leads to the correct physics of the problem, but also accelerates the convergence, will be discussed.

4.3 Convergence Analysis

In this section, a detailed analysis of the transmission conditions used in the present domain-decomposition method will be presented. As was stated earlier, a judicious choice of the transmission conditions "artificially" imposed across subdomain interfaces not only ensures uniqueness, but also accelerates convergence in a domain-decomposition algorithm. Even though in practical domain-decomposition-method implementations transmission conditions can be imposed on completely arbitrarily shaped interfaces, the

general analysis of such situations can be very difficult or impossible. For that reason, we will restrict our analysis to only planar interfaces. Moreover, infinite lateral extent (half-space subdomains) will be assumed, in order to facilitate the mathematical apparatus provided by Fourier theory. At this point, it is important to stress that although Fourier analysis is restricted to rather idealistic geometries, it has been found that its convergence estimates very accurately predict quite complicated interface boundaries [4, 2, 32].

For reasons given in the previous paragraph, the simplified model problem of Figure 2 will be considered. The electromagnetic boundary-value problem of interest consists of the vector *curl-curl* equation in $\Omega = \mathcal{R}^3$, and the Silver-Müller radiation condition at infinity. Note that no perfect electric conductor, perfect magnetic conductor, or material inhomogeneities are present in Ω. The decomposed problem is now that of Equations (10) and (11) on $\Omega_1 = (-\infty, 0] \times \mathcal{R}^2$ and $\Omega_2 = [0, +\infty) \times \mathcal{R}^2$, respectively. The planar interface $\Gamma_{12} \equiv \Gamma = \mathcal{R}^2$ of the model problem is shown in Figure 2.

With respect to Figure 2, let us first introduce the following two-dimensional (partial) Fourier-transform pair:

$$\widehat{f}\left(k_x, k_y, z\right) = \frac{1}{2\pi} \int_{-\infty}^{+\infty} \int_{-\infty}^{+\infty} f\left(x, y, z\right) e^{\jmath(k_x x + k_y y)} dx dy \,, \tag{12}$$

$$f\left(x, y, z\right) = \frac{1}{2\pi} \int_{-\infty}^{+\infty} \int_{-\infty}^{+\infty} \widehat{f}\left(k_x, k_y, z\right) e^{-\jmath(k_x x + k_y y)} dk_x dk_y \,,$$

where k_x, k_y are the Fourier variables. In a straightforward way, the Fourier analysis of the boundary-value problem described in Equations (10) and (11) will require the application of the Fourier transform on both vector *curl-curl* equations, subject to the Silver-Müller radiation condition on each domain, and each of the transmission conditions. Even though this is a simple concept, the underlying algebraic manipulations are lengthy and require analytic evaluations of the eigenvalues and eigenvectors of a 2 x 2 matrix, which leads to rather complicated final expressions for the convergence factors.

Alternatively, a considerably easier approach will be formulated based on the concept of transverse electric (TE) or H, and transverse magnetic (TM) or E, modal decomposition of electromagnetic fields [1, [2, 4]. The validity of the approach is based on the fact that any electromagnetic field produced by an arbitrarily oriented electric or magnetic source in a "layered" environment, such as in the mode problem, can be written as a superposition of TE and TM modes with respect to the normal to the "layered" interface. The term "layered" implies geometry with multiple planar parallel interfaces that extend laterally to infinity. It is apparent that the model problem of Figure 2 belongs to the abovementioned category. The second key ingredient of the following derivation is the use of a rotational transformation of the Fourier variables k_x, k_y to the "natural" spectral coordinates u and v, which significantly simplifies the expressions of the electromagnetic fields in the Fourier domain.

The analysis starts by expressing both electric and magnetic fields in terms of scalar "wave" functions, ψ for TE and ϕ for TM. Specifically, for the TE(H) modes,

$$\mathbf{E} = -\hat{\mathbf{z}} \times \nabla \psi = \hat{\mathbf{x}} \frac{\partial \psi}{\partial y} - \hat{\mathbf{y}} \frac{\partial \psi}{\partial x} \,,$$

$$\mathbf{H} = -\frac{\eta}{\jmath k} \left(\nabla \times \nabla \times \hat{\mathbf{z}} \psi \right) \tag{13}$$

$$= -\frac{\eta}{\jmath k} \left[\hat{\mathbf{x}} \frac{\partial^2 \psi}{\partial x \partial z} + \hat{\mathbf{y}} \frac{\partial^2 \psi}{\partial y \partial z} - \hat{\mathbf{z}} \left(\frac{\partial^2 \psi}{\partial x^2} + \frac{\partial^2 \psi}{\partial y^2} \right) \right] .$$

For TM(E) modes,

$$\mathbf{E} = \nabla \times \nabla \times \hat{\mathbf{z}} \phi = \left[\hat{\mathbf{x}} \frac{\partial^2 \phi}{\partial x \partial z} + \hat{\mathbf{y}} \frac{\partial^2 \phi}{\partial y \partial z} - \hat{\mathbf{z}} \left(\frac{\partial^2 \phi}{\partial x^2} + \frac{\partial^2 \phi}{\partial y^2} \right) \right], \tag{14}$$

$$\mathbf{H} = -\frac{\jmath k}{\eta} \left(\hat{\mathbf{z}} \times \nabla \phi \right) = -\frac{\jmath k}{\eta} \left(\hat{\mathbf{x}} \frac{\partial \psi}{\partial y} - \hat{\mathbf{y}} \frac{\partial \psi}{\partial x} \right),$$

where ψ and ϕ are scalar and satisfy the Helmholtz equation:

$$\left(\frac{\partial^2}{\partial x^2} + \frac{\partial^2}{\partial y^2} + \frac{\partial^2}{\partial z^2} + k^2 \right) f\left(x, y, z\right) = 0 \,, \quad f = \psi, \phi \,. \tag{15}$$

The goal now is to express all fields in the Fourier (spectral) domain. Taking the Fourier transform of Equations (15) leads to

$$\left[\frac{d^2}{dz^2} + \left(k^2 - \beta^2 \right) \right] \widehat{f}\left(k_x, k_y, z\right) = 0 \,, \quad f = \psi, \phi \tag{16}$$

where $\beta^2 = k_x^2 + k_y^2$ is the radial Fourier variable. It is convenient to further define the z-directed wavenumber as

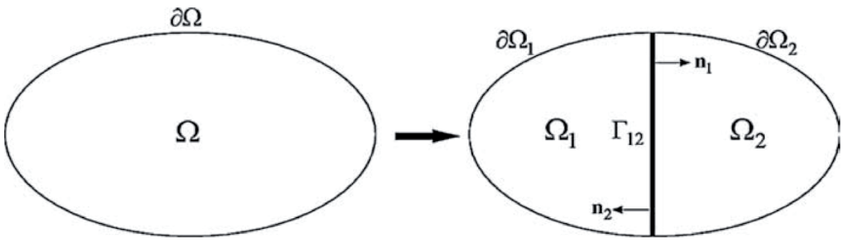

Figure 1. The decomposition of the computational domain into two non-overlapping domains.

$$k_z^2 = \beta^2 - k^2$$

$$\Rightarrow k_z = \begin{cases} \jmath\sqrt{k^2-\beta^2} & k > |\beta|, \text{ propagating modes} \\ \sqrt{\beta^2-k^2} & k < |\beta|, \text{ evanescent modes} \end{cases} \quad (17)$$

Before starting to simplify Equations (13) and (14) by applying the Fourier transform, it would be useful to introduce the following transformation to the "natural" Fourier coordinate system $(k_x, k_y) \rightarrow (k_u, k_v)$, since it will significantly simplify the field representations. The transformation is

$$\begin{bmatrix} u \\ v \end{bmatrix} = \begin{bmatrix} \sin\alpha & -\cos\alpha \\ \cos\alpha & \sin\alpha \end{bmatrix} \begin{bmatrix} x \\ y \end{bmatrix}, \quad (18)$$

where the rotation angle is given by $\cos\alpha = \frac{k_x}{\beta}$ or $\sin\alpha = \frac{k_y}{\beta}$, which more importantly leads to

$$k_u = k_x \sin\alpha - k_y \cos\alpha = 0, \quad (19)$$

$$k_v = k_x \cos\alpha + k_y \sin\alpha = \beta.$$

It should be noted here that the abovementioned transformation can be also viewed as a transformation to the polar Fourier domain, with radial variable β and angular Fourier angle α. This is a fairly standard approach in dealing with the derivation of "layered" Green's functions in electromagnetics.

Having defined the auxiliary Fourier wave functions $\tilde{\psi}$ and $\tilde{\phi}$ and the rotation transformation, it is now time to apply the Fourier transform to the TE and TM modal fields of Equations (13) and (14). In doing so, the following expressions are obtained for the TE modes:

$$\tilde{\mathbf{E}} = -\jmath\left[\hat{\mathbf{x}} k_y \tilde{\psi} - \hat{\mathbf{y}} k_x \tilde{\psi}\right], \quad (20)$$

$$\tilde{\mathbf{H}} = \frac{\eta}{\jmath k}\left[\hat{\mathbf{x}}\jmath k_x \frac{d\tilde{\psi}}{dz} + \hat{\mathbf{y}}\jmath k_y \frac{d\tilde{\psi}}{dz} - \hat{\mathbf{z}}\beta^2\tilde{\psi}\right].$$

Applying the rotational transformation of Equation (18), the Fourier fields for the TE modes are further simplified to

$$\tilde{\mathbf{E}} = -\hat{\mathbf{u}}\jmath\beta\tilde{\psi}, \quad (21)$$

$$\tilde{\mathbf{H}} = \frac{\eta}{\jmath k}\left[\hat{\mathbf{v}}\jmath\beta\frac{d\tilde{\psi}}{dz} - \hat{\mathbf{z}}\beta^2\tilde{\psi}\right].$$

In a similar fashion, the TM Fourier fields in the rotated system become

$$\tilde{\mathbf{E}} = -\hat{\mathbf{v}}\jmath\beta\frac{d\tilde{\phi}}{dz} + \hat{\mathbf{z}}\beta^2\tilde{\phi}, \quad (22)$$

$$\tilde{\mathbf{H}} = \hat{\mathbf{u}}\frac{k}{\eta}\beta\tilde{\phi},$$

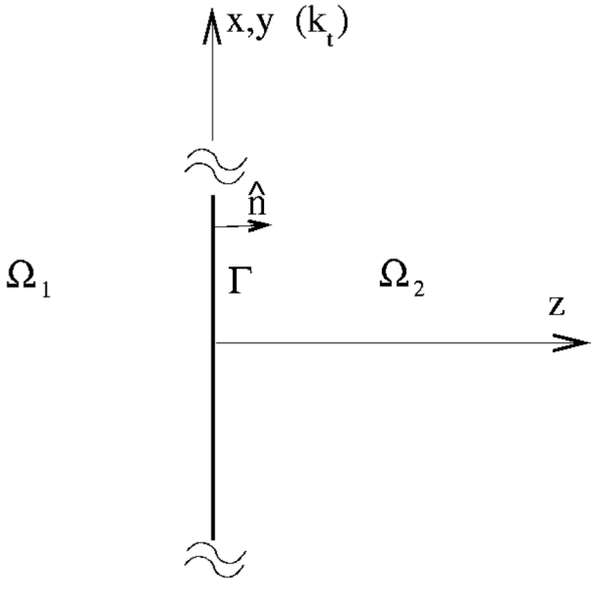

Figure 2. An idealized domain decomposition used in the Fourier analysis.

Ω_1		Ω_2	
$\widehat{\mathbf{E}}^{(n)}$	$\widehat{\mathbf{H}}^{(n)}$	$\widehat{\mathbf{E}}^{(n)}$	$\widehat{\mathbf{H}}^{(n)}$
$\hat{\mathbf{u}}\left[-\jmath\beta\mathcal{B}_1^{(n)}e^{+k_z z}\right]$	$\mathcal{B}_1^{(n)}\frac{1}{\jmath k\eta}\left(\hat{\mathbf{v}}\jmath k_z-\hat{z}\beta\right)\beta e^{+k_z z}$	$\hat{\mathbf{u}}\left[-\jmath\beta\mathcal{B}_2^{(n)}e^{-k_z z}\right]$	$-\mathcal{B}_2^{(n)}\frac{1}{\jmath k\eta}\left(\hat{\mathbf{v}}\jmath k_z+\hat{\mathbf{z}}\beta\right)\beta e^{-k_z z}$
$\mathcal{A}_1^{(n)}\left(-\hat{\mathbf{v}}\jmath k_z+\hat{\mathbf{z}}\beta\right)\beta e^{+k_z z}$	$\hat{\mathbf{u}}\left[\mathcal{A}_1^{(n)}\frac{k}{\eta}\beta e^{+k_z z}\right]$	$\mathcal{A}_2^{(n)}\left(\hat{\mathbf{v}}\jmath k_z+\hat{\mathbf{z}}\beta\right)\beta e^{-k_z z}$	$\hat{\mathbf{u}}\left(\mathcal{A}_2^{(n)}\frac{k}{\eta}\beta e^{-k_z z}\right)$

Table 1. The TE and TM Fourier field representations on the two subdomains.

where both $\hat{\psi}$ and $\hat{\phi}$ satisfy the one-dimensional homogeneous wave equation

$$\frac{d\hat{f}}{dz}-k_z^2\hat{f}=0,\quad f=\psi,\phi. \tag{23}$$

The general solutions of the ordinary differential equation in Equation (23) are of the form

$$\hat{f}=\mathcal{A}^{+}e^{-k_z z}+\mathcal{A}^{-}e^{+k_z z}. \tag{24}$$

Referring to the interface problem of Figure 2 subject to the Silver-Müller radiation on each appropriate side of Ω_1 and Ω_2, only outgoing waves ought to be considered. The solutions in each subdomain thus become

$$\hat{f}_1\left(k_x,k_y,z\right)=\mathcal{F}_1^{-}\left(k_x,k_y,0\right)e^{k_z z}\quad\text{in }\Omega_1, \tag{25}$$

$$\hat{f}_2\left(k_x,k_y,z\right)=\mathcal{F}_2^{+}\left(k_x,k_y,0\right)e^{-k_z z}\quad\text{in }\Omega_2,$$

where $\mathcal{F}_1^{-}$ and $\mathcal{F}_2^{+}$ are the Fourier modal excitation coefficients to be determined by the enforcement of the transmission condition across interface Γ_{12}. Note that in the following part of the section, $\mathcal{F}_1^{-}$ and $\mathcal{F}_2^{+}$ will be replaced with $\mathcal{A}_1$ and $\mathcal{A}_2$, respectively, when referring to TM modes, and with $\mathcal{B}_1$ and $\mathcal{B}_2$ when referring to TE modes.

Putting together Equations (21), (22), and (23), the Fourier field representations of Table 1 are obtained.

The objective of this section is to find the convergence rates, ρ^{TE} and ρ^{TM}, of the TE and TM modes, respectively, as functions of k_z. To achieve that, it is necessary to find a relationship between the excitation coefficients, $\mathcal{A}^{(n)}$ and $\mathcal{A}^{(n-2)}$, for the TM modes, along with $\mathcal{B}^{(n)}$ and $\mathcal{B}^{(n-2)}$ for the TE modes. This is done through the enforcement of the transmission condition on both domains, namely through the last equations in Equations (10) and (11):

$$\begin{aligned}&\hat{\mathbf{j}}_1^{(n)}-\hat{\mathbf{S}}_1\left[\hat{\mathbf{e}}_1^{(n)}\right]=-\hat{\mathbf{j}}_2^{(n-1)}-\hat{\mathbf{S}}_1\left[\hat{\mathbf{e}}_2^{(n-1)}\right]\ \text{at } z=0^{-}\\&\hat{\mathbf{j}}_2^{(n)}-\hat{\mathbf{S}}_2\left[\hat{\mathbf{e}}_2^{(n)}\right]=-\hat{\mathbf{j}}_1^{(n-1)}-\hat{\mathbf{S}}_2\left[\hat{\mathbf{e}}_1^{(n-1)}\right]\ \text{at } z=0^{+}\end{aligned} \tag{26}$$

The analysis proceeds by finding $\hat{\mathbf{j}}_i$ and $\hat{\mathbf{e}}_i$, $i=1,2$, with the use of Table 1. After some very simple and short algebraic manipulations, the tangential Fourier fields of Table 2 are obtained. Note that with the use of the rotational transformation in the Fourier domain, the tangential TE and TM fields are completely decoupled. This is something that is

	Ω_1		Ω_2	
	$\hat{\mathbf{e}}^{(n)}\left(z=0^{-}\right)$	$\hat{\mathbf{j}}^{(n)}\left(z=0^{-}\right)$	$\hat{\mathbf{e}}^{(n)}\left(z=0^{+}\right)$	$\hat{\mathbf{j}}^{(n)}\left(z=0^{+}\right)$
TE	$\hat{\mathbf{u}}\left[-\jmath\beta\mathcal{B}_1^{(n)}\right]$	$\hat{\mathbf{u}}\left[\mathcal{B}_1^{(n)}\jmath\beta k_z\right]$	$\hat{\mathbf{u}}\left[-\jmath\beta\mathcal{B}_2^{(n)}\right]$	$\hat{\mathbf{u}}\left[\mathcal{B}_2^{(n)}\jmath\beta k_z\right]$
TM	$\hat{\mathbf{v}}\left[-\mathcal{A}_1^{(n)}\jmath k_z\beta\right]$	$\hat{\mathbf{v}}\left[-\mathcal{A}_1^{(n)}\jmath k^2\beta\right]$	$\hat{\mathbf{v}}\left[\mathcal{A}_2^{(n)}\jmath k_z\beta\right]$	$\hat{\mathbf{v}}\left[\mathcal{A}_2^{(n)}\jmath k^2\beta\right]$

Table 2. TE and TM Fourier tangential field representations on the domain interface.

reflected in Table 2, since the TE representation involves only the **u** coordinate, whereas the TM representation involves only the **v** coordinate.

With this observation in mind, it is now straightforward to substitute the values of Table 2 in Equation (26) and to obtain the following convergence factors:

$$\rho^{TE}\left(k_z\right)=\frac{\left|\mathcal{B}_1^{(n)}\right|}{\left|\mathcal{B}_1^{(n-2)}\right|}=\left|\frac{k_z-\hat{S}_{2u}}{k_z+\hat{S}_{1u}}\frac{k_z-\hat{S}_{1u}}{k_z+\hat{S}_{2u}}\right|, \quad (27)$$

for TE modes and

$$\rho^{TM}\left(k_z\right)=\frac{\left|\mathcal{A}_1^{(n)}\right|}{\left|\mathcal{A}_1^{(n-2)}\right|}=\left|\frac{k^2+\hat{S}_{2v}k_z}{k^2-\hat{S}_{1v}k_z}\frac{k^2+\hat{S}_{1v}k_z}{k^2-\hat{S}_{2v}k_z}\right|, \quad (28)$$

for TM modes. $\hat{S}_{iu}$ and $\hat{S}_{iv}$ are the two orthogonal Fourier components of the operator $\hat{\mathbf{S}}$. From Equations (27) and (28), it is apparent that in the Fourier domain, choosing

$$\hat{S}_{1u}=\hat{S}_{2u}=k_z \quad (29)$$

and

$$\hat{S}_{1v}=\hat{S}_{2v}=-\frac{k^2}{k_z} \quad (30)$$

will lead to $\rho^{TE}\left(k_z\right)=\rho^{TM}\left(k_z\right)=0$. Therefore, a stationary iteration-based domain-decomposition algorithm will converge in two iterations. In practice, an algorithm with such a transmission condition would require the inverse Fourier transform of k_z and $\frac{1}{k_z}$. This task requires the inverse Fourier transform of the square root, which would lead to a non-local vector function in the *xyz* domain. This is similar to the two-dimensional Helmholtz equation, but in the case of Maxwell's equations, matters are more complicated, due to Equation (30). Rather that trying to invert the square root and its reciprocal, several local (sparse) approximations of Equations (29) and (30) can be found. In this paper, only two will be presented.

4.4 First-Order (Robin) Transmission Condition

This is the simplest approximation, easy to implement and to theoretically analyze. The operator **S** is chosen as

$$\mathbf{S}=\gamma, \quad \gamma\in\mathbb{C}. \quad (31)$$

It is the goal of this section to find if the choice of Equation (31) can potentially lead to a convergent stationary iteration domain-decomposition algorithm. It is easy to see that $\hat{S}_{1u}=\hat{S}_{1v}=\hat{S}_{2u}=\hat{S}_{2v}=\gamma$; thus, Equations (29) and (30) simplify to

$$\rho^{TE}\left(k_z\right)=\frac{\left|\mathcal{B}_1^{(n)}\right|}{\left|\mathcal{B}_1^{(n-2)}\right|}=\left|\frac{k_z-\gamma}{k_z+\gamma}\right|^2, \quad (32)$$

and

$$\rho^{TM}\left(k_z\right)=\frac{\left|\mathcal{A}_1^{(n)}\right|}{\left|\mathcal{A}_1^{(n-2)}\right|}=\left|\frac{k^2+\gamma k_z}{k^2-\gamma k_z}\right|^2. \quad (33)$$

In a more convenient way, the convergence estimates of Equations (32) and (33) can be written in terms of the transverse spectral variable β, with the aid of Equation (17). Therefore, for each mode set, two subsets of modes need to be defined, the propagating and the evanescent, identified as

$$\rho^{TE}\left(\beta\right)=\begin{cases}\left|\dfrac{\jmath\sqrt{k^2-\beta^2}-\gamma}{\jmath\sqrt{k^2-\beta^2}+\gamma}\right|^2 & k>|\beta|, \text{ propagating modes}\\ \left|\dfrac{\sqrt{\beta^2-k^2}-\gamma}{\sqrt{\beta^2-k^2}+\gamma}\right|^2 & k<|\beta|, \text{ evanescent modes}\end{cases} \quad (34)$$

and

$$\rho^{TM}\left(\beta\right)=\begin{cases}\left|\dfrac{k^2+\jmath\gamma\sqrt{k^2-\beta^2}}{k^2+\jmath\gamma\sqrt{k^2-\beta^2}}\right|^2 & k>|\beta|, \text{ propagating modes}\\ \left|\dfrac{k^2+\gamma\sqrt{\beta^2-k^2}}{k^2+\gamma\sqrt{\beta^2-k^2}}\right|^2 & k<|\beta|, \text{ evanescent modes}\end{cases} \quad (35)$$

In a convergent domain-decomposition scheme that employs a stationary outer-loop iteration, all four modes in Equations (34) and (35) should have $\rho<1$. This implies that our analysis and convergence rates are valid for both Jacobi and Gauss-Seidel iteration schemes, or in terms of the Schwarz theory, both additive and multiplicative Schwarz. On the other hand, if each of the above schemes is used as a preconditioning accelerator on a Krylov-type method, a spectral radius $\rho>1$ does not necessarily imply that the method diverges.

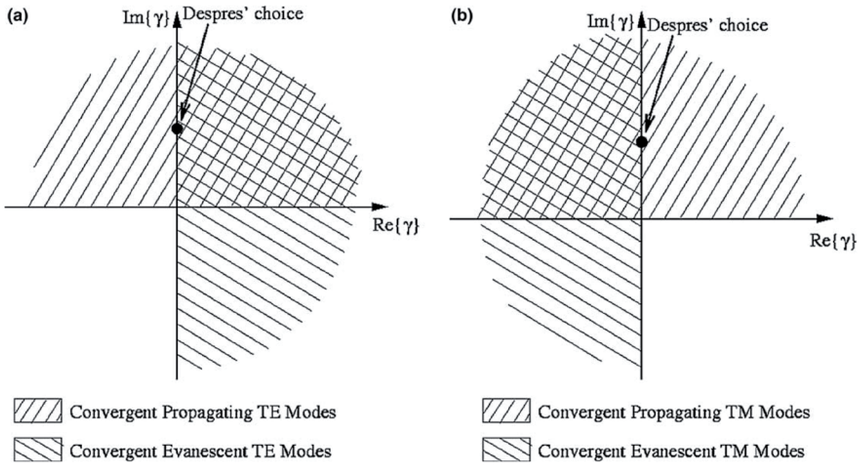

Figure 3a. Regions of convergence of the propagation and evanescent modes for the TE modes for the first-order (Robin) transmission conditions.

Figure 3b. Regions of convergence of the propagation and evanescent modes for the TM modes for the first-order (Robin) transmission conditions.

In light of Equations (34), (35), and the comments of the previous paragraph, a number of convergent regions can be identified for each set of modes, based on the choice of the Robin constant γ. From Equation (34), it is clear that choosing $\mathrm{Im}\{\gamma\} > 0$ will lead to convergent TE propagation modes, whereas the $\mathrm{Re}\{\gamma\} > 0$ would lead to convergent TE evanescent modes. These convergence regions for the TE modes are depicted in Figure 3a in the complex γ plane. It is clear that the first quadrant will be the preferred choice, since both evanescent and propagation modes converge. Furthermore, as in the Helmholtz case, even if γ is chosen in the appropriate quadrant, the cutoff mode $\beta = k$ (plane wave incidence parallel to the interface) will never converge, since that choice makes $\rho^{TE}(\beta = k) = 1$. On the other hand, the situation for the TM modes is quite different. From Equation (35), the propagating TM modes will converge in the region where $\mathrm{Im}\{\gamma\} > 0$, but the evanescent modes will converge in the region $\mathrm{Re}\{\gamma\} < 0$ which is complementary to the evanescent TE-mode case.

Again, the regions of convergence for the TM modes are plotted in the complex γ plane in Figure 3b. This is a situation unique to Maxwell's equations. Unfortunately, this complicates the convergence behavior of a stationary iteration domain decomposition. As is apparent from Figure 2, there is no region where all four different modes are convergent. In the first quadrant, all TE modes together with the propagating TM modes are convergent, but the evanescent TM modes are divergent, $\rho_{evan}^{TM} > 1$; this situation is depicted in Figure 3a. Similarly, in the second quadrant, all TM and propagating TE modes are convergent, but the evanescent TE mode diverges, $\rho_{evan}^{TE} > 1$, as shown in Figure 3b. The situation becomes more severe in the other two quadrants, where new two sets of modes do not converge at the same time. It is interesting to observe the duality among TE and TM as we switch quadrants; this is true wherever the locations of γ are symmetrically positioned with respect to the imaginary axis.

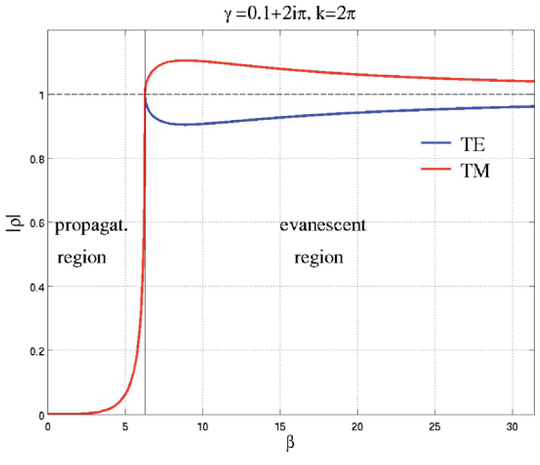

Figure 4a. The convergence rates as a function of the spectral variable of the TE and TM modes for the first-order transmission condition, when γ is located in the first complex quadrant.

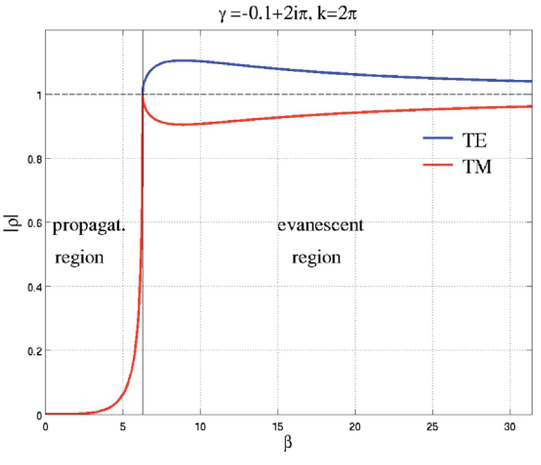

Figure 4b. The convergence rates as a function of the spectral variable of the TE and TM modes for the first-order transmission condition, when γ is located in the second complex quadrant.

	Ω_1			Ω_2		
	$\hat{\mathbf{e}}^{(n)}\left(z=0^-\right)$	$\hat{\mathbf{j}}^{(n)}\left(z=0^-\right)$	$\mathbf{curl}curl\left[\hat{e}^{(n)}\left(z=0^-\right)\right]$	$\hat{\mathbf{e}}^{(n)}\left(z=0^+\right)$	$\hat{\mathbf{j}}^{(n)}\left(z=0^+\right)$	$\mathbf{curl}curl\left[\hat{e}^{(n)}\left(z=0^-\right)\right]$
TE	$\hat{\mathbf{u}}\left[-\mathcal{B}_1^{(n)}\jmath\beta\right]$	$\hat{\mathbf{u}}\left[\mathcal{B}_1^{(n)}\jmath\beta k_z\right]$	$\hat{\mathbf{u}}\left[\mathcal{B}_1^{(n)}\jmath\beta\beta^2\right]$	$\hat{\mathbf{u}}\left[-\mathcal{B}_2^{(n)}\jmath\beta\right]$	$\hat{\mathbf{u}}\left[\mathcal{B}_2^{(n)}\jmath\beta k_z\right]$	$\hat{\mathbf{u}}\left[\mathcal{B}_2^{(n)}\jmath\beta\beta^2\right]$
TM	$\hat{\mathbf{v}}\left[-\mathcal{A}_1^{(n)}\jmath k_z\beta\right]$	$\hat{\mathbf{v}}\left[-\mathcal{A}_1^{(n)}\jmath k^2\beta\right]$	0	$\hat{\mathbf{v}}\left[\mathcal{A}_2^{(n)}\jmath k_z\beta\right]$	$\hat{\mathbf{v}}\left[\mathcal{A}_2^{(n)}\jmath k^2\beta\right]$	0

Table 3. TE and TM Fourier tangential field representations on the domain interface.

Fortunately, for the case of the present paper, our primary concern is radiating applications, such as antenna arrays, where the primary quantities of interest are quantities related to the propagating modes. In this case, the choice where all the propagating modes converge and $\rho_{evan}^{TE}=\rho_{evan}^{TM}=1$ will be sufficient. Such a choice was provided by Després et al. in the original paper [39]. In that work, $\gamma=\jmath k$ was used. In this paper, the same $\gamma=\jmath k$ has been used.

4.5 Second-Order Transmission Condition

In this section, the transmission condition proposed by Collino et al. [42] is considered. The technical details of a true second-order transmission condition can be found in Rawat's PhD dissertation [4]. The operator now is approximated by

$$\mathbf{S}=\gamma\mathbf{I}\left(\bullet\right)+\delta\mathbf{curl}_\Gamma curl_\Gamma\left(\bullet\right),\quad \gamma,\delta\in\mathbb{C}, \qquad (36)$$

where $\mathbf{I}$ denotes the identity operator and $\mathbf{curl}_\Gamma$ and $curl_\Gamma$ denote the vector and scalar tangential rotational operators. With this choice, Table 3 is the result.

With the use of Equation (36), Equation (26) becomes

$$\hat{\mathbf{j}}_1^{(n)}-\gamma\hat{\mathbf{e}}_1^{(n)}-\delta\mathbf{curl}curl\left[\hat{\mathbf{e}}_1^{(n)}\right]$$

$$=-\hat{\mathbf{j}}_2^{(n-1)}-\gamma\hat{\mathbf{e}}_2^{(n-1)}-\delta\mathbf{curl}curl\left[\hat{\mathbf{e}}_2^{(n)}\right]\ \text{at } z=0^-, \qquad (37)$$

$$\hat{\mathbf{j}}_2^{(n)}-\gamma\hat{\mathbf{e}}_2^{(n)}-\delta\mathbf{curl}curl\left[\hat{\mathbf{e}}_1^{(n)}\right]$$

$$=-\hat{\mathbf{j}}_1^{(n-1)}-\gamma\hat{\mathbf{e}}_1^{(n-1)}-\delta\mathbf{curl}curl\left[\hat{\mathbf{e}}_1^{(n)}\right]\ \text{at } z=0^+.$$

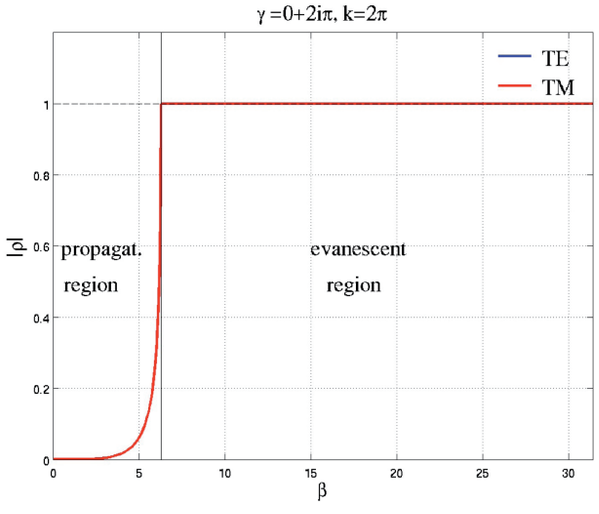

Figure 5a. The convergence rates as a function of the spectral variable (incident field angle) of the TE and TM modes for $\gamma=\jmath k$ (Despres' choice)

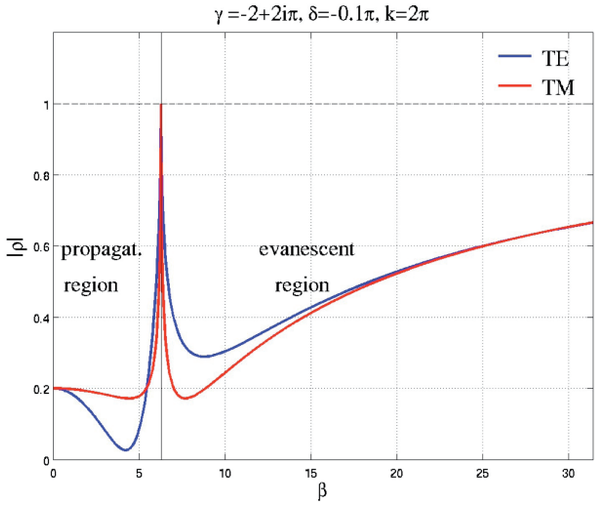

.Figure 5b. The convergence rates as a function of the spectral variable (incident field angle) of the TE and TM modes for the second-order transmission condition by Collino et al. [42].

Again, after simple algebraic manipulations, the following result is obtained:

$$\rho^{TE}\left(k_z\right)=\left|\frac{k_z-\gamma+\delta\beta^2}{k_z+\gamma-\delta\beta^2}\right|^2 \tag{38}$$

for the TE modes, whereas the TM modes remain the same as in the first-order case, namely given by Equations (33) or (35). The TE convergence rate can further be written as

$$\rho^{TE}\left(k_z\right)=\left|\frac{k_z+\delta k_z^2-\left(\gamma-\delta k^2\right)}{k_z-\delta k_z^2+\left(\gamma-\delta k^2\right)}\right|^2, \tag{39}$$

or as a function of the transverse spectral variable as

$$\rho^{TE}\left(\beta\right)$$

$$=\begin{cases}\left|\dfrac{\jmath\sqrt{k^2-\beta^2}+\delta\beta^2-\gamma}{\jmath\sqrt{k^2-\beta^2}-\delta\beta^2+\gamma}\right| & k>|\beta|, \text{ propagating modes}\\ \left|\dfrac{\sqrt{\beta^2-k^2}+\delta\beta^2-\gamma}{\sqrt{\beta^2-k^2}-\delta\beta^2+\gamma}\right|^2 & k<|\beta|, \text{ evanescent modes}\end{cases} \tag{40}$$

Even though it is not easily recognizable, Equation (35) for the TM modes and Equation (40) for the TE modes can lead to a convergent stationary iteration algorithm, if, of course, $k\neq\beta$. The idea is to choose the Robin constant, γ, in such a way that the TM modes converge for both propagating and evanescent modes. This was done in the previous section by choosing $\mathrm{Im}\{\gamma\}>0$, $\mathrm{Re}\{\gamma\}<0$ (refer to Figure 4). In the next step, it is easy to see that with this Robin constant that both propagating and evanescent TE modes would converge if $\mathrm{Re}\{\delta\}<1$. Additionally, this choice of γ and δ makes the operator $\mathbf{S}$ positive definite, and it thus preserves the continuity of the tangential electric fields across the interface. At this point, no optimization has been tried for the second-order parameter, but as is shown in Figure 5b, both propagating and evanescent modes favorably converge. In contrast, the Robin transmission condition with Després' choice, shown in Figure 5a, fails to converge the evanescent modes. However, we note that for these two non-optimized examples, the Robin transmission condition has superior convergence for propagating modes. As was mentioned previously, in this paper we are primarily interested in open radiating structures (large finite antenna arrays). Therefore, only the Robin condition with Després' choice was used in the numerical results.

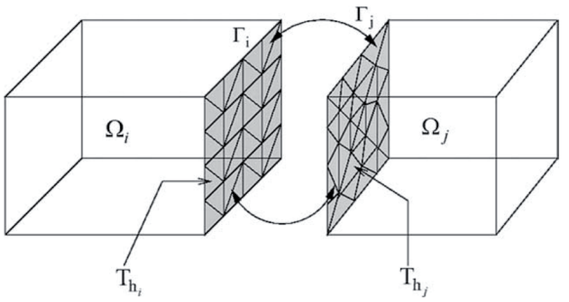

Figure 6. Non-conforming triangulation on either side of an inter-domain interface.

4.6 Non-Conforming (Cement) Finite-Element Method

The domain-decomposition method suggested by Equations (10) and (11) requires a matching grid between subdomains Ω_1 and Ω_2. Practically, this requirement can significantly tax the numerical analyst when he or she tries to analyze large finite antenna arrays, or any other large and geometrically complicated structure. In this paper, we propose a novel approach, similar to the mortar techniques employed in the literature, for a domain-decomposition method with non-matching grids. With the proposed technique, each subdomain can be meshed independently, without considerations of conformity with adjacent subdomains.

With the introduction of a Lagrange multiplier representing the dual (electric current) variable,

$$\mathbf{j}_i=\gamma_i^t\left(\frac{1}{\mu_{ri}}\nabla\times\mathbf{E}_i\right)\in\mathbf{H}_{\|}^{-1/2}\left(div_\Gamma,\Gamma_i\right) \tag{41}$$

at interfaces Γ_1 and Γ_2, the two-subdomain problem of Figure 6 decouples into two independent problems. The decomposed boundary-value problem is now compactly written as

$$\nabla\times\frac{1}{\mu_{ri}}\nabla\times\mathbf{E}_i^{(n)}-k^2\epsilon_{ri}\mathbf{E}_i^{(n)}=-\jmath k\eta\mathbf{J}_i^{imp} \text{ in } \Omega_i,$$

$$\gamma^t\left[\mathbf{E}_i^{(n)}\right]=0 \text{ on } \Gamma_{pec},$$

$$\gamma^\times\left[\frac{1}{\mu_{ri}}\nabla\times\mathbf{E}_i^{(n)}\right]=0 \text{ on } \Gamma_{pmc}, \tag{42}$$

$$\mathbf{j}_i^{(n)} - \gamma \mathbf{e}_i^{(n)} = -\mathbf{g}_i^{(n-1)} \quad \text{on } \Gamma_i ,$$

$$\gamma^{\times}\left[\frac{1}{\mu_{ri}}\nabla \times \mathbf{E}_i^{(n)}\right] - \jmath k \gamma^t \left[\mathbf{E}_i^{(n)}\right] = 0 \quad \text{on } \Gamma_{ext} \qquad ,$$

for $i = 1,2$, where $\mathbf{e}_i = \gamma^t(\mathbf{E}_i) \in \mathbf{H}_{\perp}^{-1/2}(curl_{\Gamma}, \Gamma_i)$ is the tangential component of the electric field on interface Γ_i In addition, $\mathbf{g}_i^{(n-1)} = \mathbf{j}_{neig(i)}^{(n-1)} - \gamma \mathbf{e}_{neigh(i)}^{(n-1)}$, with $neig(i)$ indicating the neighboring domains of domain i. Although in principle the triangulations in $\tilde{A}_i$ and $\tilde{A}_j$ can be drastically different, the rule of thumb is that the spatial resolutions h_i (the characteristic element size in triangulation T_{h_i}) and h_j (the characteristic element size in triangulation T_{h_j}) should be of the same order to assure accuracy. We cite the work of Chen et al. [55] for the rigorous analysis of such situations, as well as for the discontinuous-coefficient case. The proposed method of treating non-conforming meshes differs from other approaches in two important aspects. First, the Lagrange-multiplier unknowns carry significant physical meaning, namely, they are proportional to the electric current density on the surfaces. Second, the proposed cement technique will not result in any zero diagonal blocks in the final matrix equations, thus regularizing the resulting mixed problem.

4.7 Galerkin Statement

To implement the domain-decomposition iteration described by Equation (42), we need to employ finite-dimensional descriptions for Ω_1 and Ω_2. In the current implementation, we have chosen to discretize Ω_1 and Ω_2 into unions of tetrahedrons. The corresponding spaces for the fields and the cement variables are

$$\mathbf{E}_i \in \mathbf{S}_i^h \subset \mathbf{H}_0(curl; \Omega_i), \qquad (43)$$

$$\mathbf{j}_i \in \Lambda_i^h \subset \mathbf{H}_{|\perp}^{-\frac{1}{2}}(curl_{\Gamma}; \Gamma_i).$$

Specifically, the basis functions for $\mathbf{E}_1$, $\mathbf{E}_2$ within each tetrahedron are the second-order $(p=2)$, first kind of mixed $\mathbf{H}(curl)$ conforming vector elements [52]. Moreover, for the cement variables, $\mathbf{j}_1$, $\mathbf{j}_2$, the basis functions are the discontinuous second-order, mixed-surface $\mathbf{H}(curl)$ conforming vector elements. The function spaces for the cement variables are a bit unusual, and we refer interested readers to references [4, 31, 32] for in-depth discussions on the choice of the function spaces. It suffices to say that the incorporation of the proper function spaces is essential to the robust convergence in the domain-decomposition algorithm.

Consequently, the corresponding Galerkin weak statements for Equation (42) can now be formerly stated as

Seek

$$\left[\mathbf{E}_1^{(n)}, \mathbf{E}_2^{(n)}\right] \in \mathbf{S}_1^h \times \mathbf{S}_2^h \text{ and } \left[\mathbf{j}_1{}^{(n)}, \mathbf{j}_2{}^{(n)}\right] \in \Lambda_1^h \times \Lambda_2^h$$

such that

$$a_1\left[\mathbf{v}_1^h, \mathbf{E}_1^{(n)}\right]_{\Omega_1} + \jmath k \left\langle \gamma^t \mathbf{v}_1^h, \mathbf{e}_1^{(n)} \right\rangle_{\partial\Omega_1 \cap \Gamma_{ext}} + \left\langle \gamma^t \mathbf{v}_1^h, \mathbf{j}_1^{(n)} \right\rangle_{\Gamma_1}$$

$$= -\jmath k \eta \left(\mathbf{v}_1^h, \mathbf{J}_1^{imp}\right)_{\Omega_1},$$

$$a_2\left[\mathbf{v}_2^h, \mathbf{E}_2^{(n)}\right]_{\Omega_2} + \jmath k \left\langle \gamma^t \mathbf{v}_2^h, \mathbf{e}_2^{(n)} \right\rangle_{\partial\Omega_2 \cap \Gamma_{ext}} + \left\langle \gamma^t \mathbf{v}_2^h, \mathbf{j}_2^{(n)} \right\rangle_{\Gamma_2}$$

$$= -\jmath k \eta \left(\mathbf{v}_2^h, \mathbf{J}_2^{imp}\right)_{\Omega_2}, \qquad (44)$$

$$\left\langle \lambda_1^h, \mathbf{e}_1^{(n)} \right\rangle_{\Gamma_1} + \frac{1}{\gamma}\left\langle \lambda_1^h, \mathbf{j}_1^{(n)} \right\rangle_{\Gamma_1}$$

$$= \left\langle \lambda_1^h, \mathbf{e}_2^{(n-1)} \right\rangle_{\Gamma_1} - \frac{1}{\gamma}\left\langle \lambda_1^h, \mathbf{j}_2^{(n-1)} \right\rangle_{\Gamma_1},$$

$$\left\langle \lambda_2^h, \mathbf{e}_2^{(n)} \right\rangle_{\Gamma_2} + \frac{1}{\gamma}\left\langle \lambda_2^h, \mathbf{j}_2^{(n)} \right\rangle_{\Gamma_2}$$

$$= \left\langle \lambda_2^h, \mathbf{e}_1^{(n-1)} \right\rangle_{\Gamma_2} - \frac{1}{\gamma}\left\langle \lambda_2^h, \mathbf{j}_1^{(n-1)} \right\rangle_{\Gamma_2},$$

$$\forall \left(\mathbf{v}_1^h, \mathbf{v}_2^h\right) \in \mathbf{S}_1^h \times \mathbf{S}_2^h \text{ and } \left(\lambda_1^h, \lambda_2^h\right) \in \Lambda_1^h \times \Lambda_2^h,$$

where the bilinear form $a_i(\mathbf{v}, \mathbf{u})_{\Omega_i}$ is defined by

$$a_i(\mathbf{v}, \mathbf{u})_{\Omega_i} = \int_{\Omega_i} \left(\nabla \times \mathbf{v} \bullet \frac{1}{\mu_r} \nabla \times \mathbf{u} - k^2 \mathbf{v} \bullet \epsilon_r \mathbf{u}\right) dx^3 ,$$

and $\langle \mathbf{v}, \mathbf{u} \rangle_{\Gamma} = \int \mathbf{v} \bullet \mathbf{u} dx^2$. Notice that the communication or coupling between domains comes through the interfaces, and, more precisely, through the right-hand-side term $\mathbf{g}_{neig(i)}^{(n-1)} = \mathbf{j}_{neig(i)}^{(n-1)} + \gamma \mathbf{e}_{neigh(i)}^{(n-1)}$. This relates the solution of the neighboring subdomains at the previous domain-decomposition iteration to the *i*th domain in the present domain-decomposition iteration. The statement in Equation (44) was obtained through the standard Galerkin treatment, together with the scaling of the constraint equation in Equation (42) by $-\frac{1}{\gamma}$. Notice that with these modifications, the symmetry of each subdomain problem is retained.

As a result of using a Robin-type transmission condition, the resulting mixed formulation of Equation (44) is a generalized formulation that avoids zero diagonal blocks on the dual unknowns. After finite-dimensional discretization, the final linear system of equations is of the form

$$\mathbf{K}_i \mathbf{u}_i^{(n)} = \mathbf{y}_i + \mathbf{g}_i^{(n-1)}, \quad \forall i = 1, \cdots I , \tag{45}$$

where $\mathbf{K}_i, \mathbf{u}_i, \mathbf{y}_i$ and $\mathbf{g}_i$ are

$$\mathbf{K}_i = \begin{pmatrix} \mathbf{A}_i^{\mathrm{II}} & \mathbf{A}_i^{\mathrm{I}\Gamma} & \mathbf{0} \\ \mathbf{A}_i^{\Gamma\mathrm{I}} & \mathbf{A}_i^{\Gamma\Gamma} & \mathbf{T}_i \\ \mathbf{0} & \mathbf{T}_i^T & \mathbf{T}_i \end{pmatrix}, \tag{46}$$

$$\mathbf{y}_i = \begin{pmatrix} \tilde{\mathbf{b}}_i \\ \mathbf{0} \\ \mathbf{0} \end{pmatrix},$$

$$\mathbf{u}_i^{(n)} = \begin{pmatrix} \tilde{\mathbf{E}}_i^{(n)} \\ \tilde{\mathbf{e}}_i^{(n)} \\ \tilde{\mathbf{j}}_i^{(n)} \end{pmatrix}, \tag{47}$$

$$\mathbf{v}_i^{(n)} = \begin{pmatrix} \tilde{\mathbf{e}}_i^{(n)} \\ \tilde{\mathbf{j}}_i^{(n)} \end{pmatrix},$$

$$\mathbf{g}_i^{(n)} = \begin{pmatrix} \mathbf{0} & \mathbf{0} & \mathbf{0} \\ \mathbf{0} & \mathbf{0} & \mathbf{0} \\ \mathbf{0} & \mathbf{T}_{ij}^T & \mathbf{T}_{ij} \end{pmatrix} \bullet \begin{pmatrix} \mathbf{0} \\ \mathbf{0} \\ \tilde{\mathbf{j}}_j^{(n)} \end{pmatrix}. \tag{48}$$

Note that all matrices involved in Equations (46)-(48) are sparse. Note also that the $\mathbf{A}$ matrices are finite-element matrices with first-order absorbing boundary conditions on the exterior surfaces, Γ_{ext} , and can be found in standard Finite-Element Method books for EM. Moreover, the $\mathbf{T}$ matrices are given by

$$\left(\mathbf{T}_{ij}\right)_{mn} = \int_{\Gamma_i \bigcap \Gamma_j} \left(\hat{\mathbf{n}}_i \times \mathbf{w}_m \bullet \hat{\mathbf{n}}_j \times \mathbf{w}_n \right) dx^2 , \tag{49}$$

$$\left(\mathbf{T}_i\right)_{mn} = \int_{\Gamma_i} \left(\hat{\mathbf{n}}_i \times \mathbf{w}_m \bullet \hat{\mathbf{n}}_j \times \mathbf{w}_n \right) dx^2 . \tag{50}$$

4.8 Finite-Element Tearing and Interconnecting Iterative Sub-Structuring Algorithm

As was pointed out earlier, the class of problems (large finite antenna arrays) that we consider herein has a large number of repeated domains. The solution of Equation (45) in a straightforward manner would require the solution of every subdomain problem on each iteration step. An elegant way to overcome this is to rewrite Equation (45) as

$$\mathbf{u}_i^{(n)} = \mathbf{K}_i^{-1} \mathbf{y}_i + \mathbf{K}_i^{-1} \mathbf{g}_i^{(n)}, \ \forall i = 1, \cdots I . \tag{51}$$

Before proceeding with the rest of the derivation, let us first define two useful restriction operators: one that restricts the solution vector on inter-domain interface unknowns,

$$\mathbf{v} = \mathbf{R}_{DP} \mathbf{u} = \begin{pmatrix} \mathbf{0} & \mathbf{0} & \mathbf{0} \\ \mathbf{0} & \mathbf{I} & \mathbf{0} \\ \mathbf{0} & \mathbf{0} & \mathbf{I} \end{pmatrix} \bullet \begin{pmatrix} \tilde{\mathbf{E}}_i^{(n)} \\ \tilde{\mathbf{e}}_i^{(n)} \\ \tilde{\mathbf{j}}_i^{(n)} \end{pmatrix}, \tag{52}$$

and another that restricts just the dual part of the solution,

$$\tilde{\mathbf{j}}_i^{(n)} = \mathbf{R}_D \mathbf{u} = \begin{pmatrix} \mathbf{0} & \mathbf{0} & \mathbf{0} \\ \mathbf{0} & \mathbf{0} & \mathbf{0} \\ \mathbf{0} & \mathbf{0} & \mathbf{I} \end{pmatrix} \bullet \begin{pmatrix} \tilde{\mathbf{E}}_i^{(n)} \\ \tilde{\mathbf{e}}_i^{(n)} \\ \tilde{\mathbf{j}}_i^{(n)} \end{pmatrix}. \tag{53}$$

Applying the surface restriction on both sides of Equation (51) results in

$$\mathbf{R}_{DP}\mathbf{u}_i^{(n)} = \mathbf{R}_{DP}\mathbf{K}_i^{-1}\mathbf{y}_i + \mathbf{R}_{DP}\mathbf{K}_i^{-1}\mathbf{g}_i^{(n-1)}. \quad (54)$$

Furthermore, we utilize a trivial property of the restriction matrix,

$$\mathbf{R}_D^T\mathbf{R}_D = \begin{pmatrix} \mathbf{0} & \mathbf{0} & \mathbf{0} \\ \mathbf{0} & \mathbf{0} & \mathbf{0} \\ \mathbf{0} & \mathbf{0} & \mathbf{I} \end{pmatrix}, \quad (55)$$

and the following equation is obtained:

$$\mathbf{R}_{DP}\mathbf{u}_i^{(n)} = \mathbf{R}_{DP}\mathbf{K}_i^{-1}\mathbf{y}_i + \mathbf{R}_{DP}\mathbf{K}_i^{-1}\mathbf{R}_D^T\mathbf{R}_D\mathbf{g}_i^{(n-1)} . (56)$$

Equation (56) can be compactly written as

$$\mathbf{v}_i^{(n)} = \mathbf{x}_i^0 + \mathbf{Z}_i\tilde{\mathbf{g}}_i^{(n-1)}, \quad \forall i = 1,\cdots I, \quad (57)$$

where

$$\mathbf{x}_i^0 = \mathbf{R}_{DP}\mathbf{K}_i^{-1}\mathbf{y},$$

$$\mathbf{Z}_i = \mathbf{R}_{DP}\mathbf{K}_i^{-1}\mathbf{R}_D, \quad (58)$$

$$\mathbf{g}_i = \mathbf{R}_{DP}\tilde{\mathbf{g}}_i .$$

The iteration scheme of Equation (58) can be solved with a Jacobi or Gauss-Seidel stationary iteration method, or with the Krylov-based iterative-matrix solutions. Moreover, we note that the iteration matrix is a dense matrix, and its construction requires the solution of the subdomain as many times as the dual unknown's space kernel. However, the construction of $\mathbf{Z}_i$ is independent of the iteration. It can thus be done once in the preprocessing step. For general domain decomposition, this may not be an efficient way to proceed. However, in the case of many repeating subdomains, the computational cost can be greatly decreased.

5. Numerical Results

In this section, we present applications of the proposed Finite-Element-Method-based domain-decomposition method to large finite antenna arrays. Most of the examples examined are real-life industrial problems that involve large electrical size as well as geometric and material complexities. Their full-wave analysis is thus fairly challenging even today, particularly on a personal computer without parallelization. The purpose of this section is to demonstrate the validity, accuracy, performance, and versatility of the proposed method. For that reason, comparisons with measurements and other already validated methods and codes will be given. For example, in Section 5.1, comparisons with measurements and full Finite-Element-Method results will be given for radiating problems. Both near- and far-field quantities are considered. A large part of the section will be devoted to analyzing conformal arrays and printed antennas. Even though such finite antenna arrays have been previously analyzed with spectral or spatial-domain Method of Moments (e.g., for cylindrical dipoles, see [56], or for planar patches, see [57, 58]), in both cases an infinite dielectric substrate was considered. Here, the real-

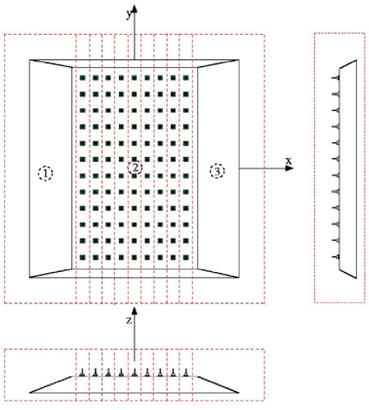

Figure 7a. The geometry and domain partitioning of a 9 x 12 monopole antenna array mounted on a wedge-tail ground plane.

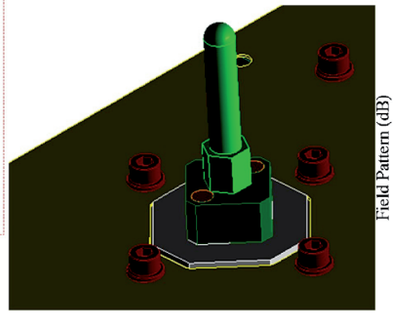

Figure 7b. The detail of the radiating monopole of the antenna array of Figure 7a.

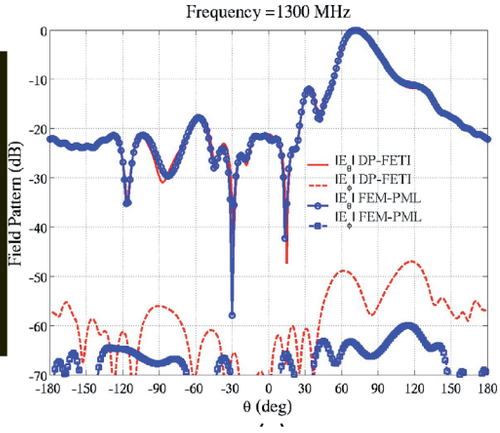

Figure 7c. A comparison of the azimuth far-field radiation pattern with the full Finite-Element Method for the antenna array of Figure 7a.

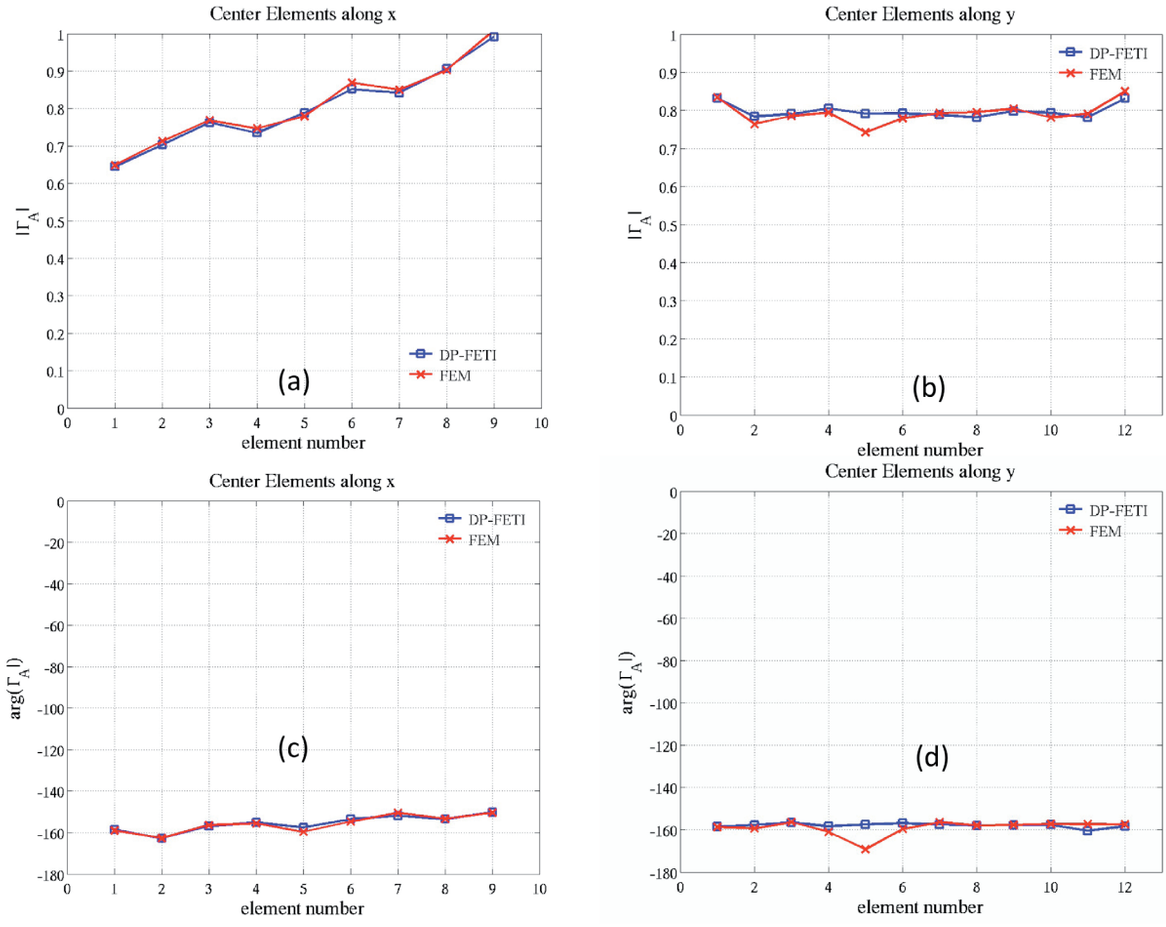

Figure 8a. Comparisons of the active reflection coefficient computed with the full Finite-Element Method and the domain-decomposition Finite-Element Tearing and Interconnecting algorithm. The magnitude across center elements in the scanning direction is shown.

Figure 8b. Comparisons of the active reflection coefficient computed with the full Finite-Element Method and the domain-decomposition Finite-Element Tearing and Interconnecting algorithm. The magnitude across center elements in the non-scanning direction is shown.

Figure 8c. Comparisons of the active reflection coefficient computed with the full Finite-Element Method and the domain-decomposition Finite-Element Tearing and Interconnecting algorithm. The phase across center elements in the scanning direction is shown.

Figure 8d. Comparisons of the active reflection coefficient computed with the full Finite-Element Method and the domain-decomposition Finite-Element Tearing and Interconnecting algorithm. The phase across center elements in the non-scanning direction is shown.

life problem of a finite array on a finite mounting platform will be considered.

All computations were performed on a PC with a single 2.4 GHz Intel Xeon processor with 512 KB L2 cache and 2 GB RAM. Double-precision complex arithmetic was assumed. The computational codes were implemented in object-oriented *C++* using the GNU *g++* compiler with optimization level –O9.

5.1 Radar Arrays

The first antenna radiation considered is shown in Figure 7a. It consisted of an array of 9 x 12 monopole radiators excited by a coaxial feeder at their base. The details of each monopole and its coax-like feed are shown in Figure 7b. The array resided on a finite perfect electrically conducting (PEC) plate, connected into four wedges on each side. The array was excited with constant amplitude and linear-progressive phase along the *x* direction. This excitation ideally resulted in a radiation peak at the elevation angle $\theta = 90°$, $\phi = 90°$, where (θ, ϕ) are the polar angles with respect to the $\hat{\mathbf{z}}$ and $\hat{\mathbf{x}}$ axes. The frequency of operation was assumed to be $f = 1.3$ GHz.

The configuration was simulated with both the proposed method and a full Finite-Element Method. In both cases, the boundaries of the computational domain were placed $\lambda/2$ away from the structure, where $\lambda = c/f$ is the wavelength in free space. The two main parameters of interest were the shape of the radiation pattern and the directivity of the antenna, which is the ratio of the peak over the total radiated power of the antenna. The *x*-*y* cut of

	DD with FETI	Full FEM
Meshing Time	32 sec	38 min 12 sec
Total Solution Time	5 h 20 sec	19 h 32 sec
Memory (GB)	1.5	1.8
Directivity (dBi)	22.01	22.02

Table 4. The computational statistics of domain decomposition with Finite-Element Tearing and Interconnecting compared to the full Finite-Element Method for the 9×12 monopole array. The computations were performed with double-precision arithmetic on an Intel Xeon 2.4 GHz processor with 512 KB L2 cache and 2 GB RAM.

the radiation pattern is shown in Figure 7c. In the same plot, the solid lines represent the full Finite-Element-Method results, while the circle/solid line curves represent the proposed method's results. Much of the dominant component field agreed favorably with the full Finite-Element Method. At this point, it should be noted that the reference full Finite-Element Method result was obtained using an h-adaptive mesh refinement process. As can be seen in Figure 7c, only minor discrepancies were present at low field levels. It should be also noted that both the full Finite-Element Method and the domain-decomposition method subdomain solvers' accuracies were set to 10^{-3}, whereas the outer loop for the domain-decomposition method was set to 10^{-2}. For that residual, the domain-decomposition method converged in 32 outer-loop iterations. In Figure 8, the active reflection coefficients of each array element are considered. It is well known that the computation of near-field quantities such as input impedance and active reflection coefficient for the case of arrays is more sensitive to errors in a simulation. As is shown in Figure 8, both the magnitude and phase agreed favorably with the full Finite-Element-Method results. Finally, a summary of both the domain-decomposition with Finite-Element Tearing and Interconnecting and the full Finite-Element-Method computational statistics and other important items of merit are summarized in Table 4. Here, it should be noted (as will become evident form later examples) that for a small number of repetitions as in the present array problem, domain-decomposition without Finite-Element Tearing and Interconnecting would outperform the Finite-Element Tearing and Interconnecting in terms of memory savings. Despite that fact, the Finite-Element Tearing and Interconnecting algorithm was chosen because larger arrays of the same geometry were of interest.

The second array considered consisted of a 24 x12 monopole array on a flat ground plane. For this experiment, the proposed domain-decomposition method was compared with measured data. The measured configuration is shown in Figure 9a, and the monopole and coax feeder are shown in Figure 9b. The challenge in this simulation was to accurately represent the *thin* flat ground plane. Even though the ground plane was thin enough, it could not be modeled as infinitely thin. As can be shown in Figure 9c, the far-field patterns agreed very well with measurements. Note that the gain and directivity were predicted with 0.05 dB accuracy. Before closing this section, it is interesting to stress that the full Finite-Element-Method model was

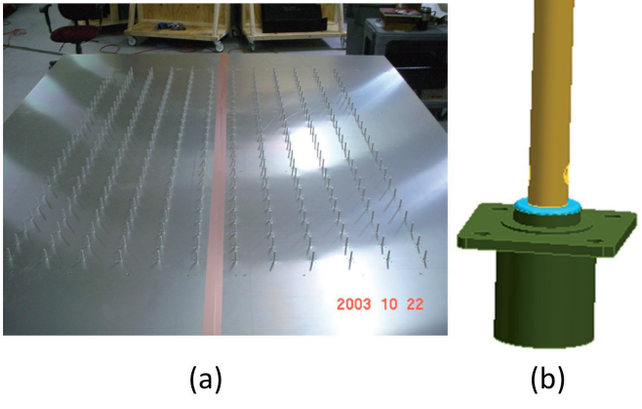

Figure 9a. A photo of the measured configuration for a 24×12 monopole array on a flat finite ground plane.

Figure 9b. A detailed drawing of the monopole radiator for the array in Figure 9a.

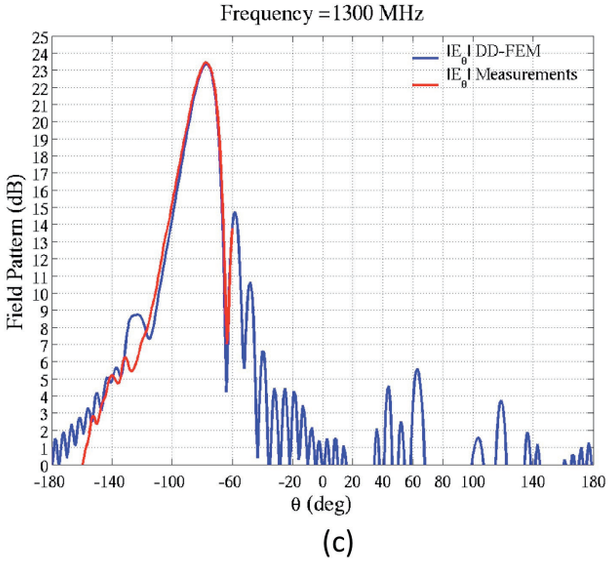

Figure 9c. The domain-decomposition method compared to measurements of the elevation far-field pattern for the array in Figure 9a.

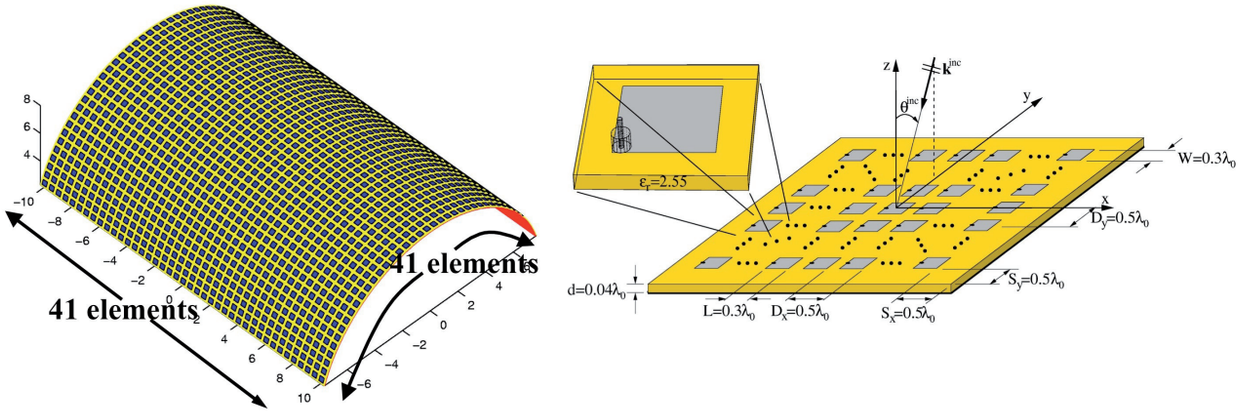

Figure 10. A 41x41 patch antenna array conformally mounted on a finite cylinder and its planar counterpart.

impossible to fit in a PC with 2 GB RAM, whereas the domain-decomposition method used only 550 MB. Moreover, the domain-decomposition method did not utilize the Finite-Element Tearing and Interconnecting sub-structuring algorithm, and it converged to a residual of 10^{-2} within 26 outer-loop iterations. Here and in all computations, the residual was defined as

$$\delta = \frac{\left\| \mathbf{x}^{(n)} - \mathbf{x}^{(n-1)} \right\|_2}{\left\| \mathbf{x}^{(n)} \right\|_2}, \qquad (59)$$

where $\mathbf{x}$ is the solution vector. For the case of domain decomposition, this involves the entire primal (volume) unknowns of the problem. For the case of the Finite-Element Tearing and Interconnecting, this refers to only the dual unknowns. The total solution time for this problem was less than 1 h 42 m, and the computations involved four million total Finite-Element-Method unknowns.

5.2 Finite Conformal Arrays

Conformal antenna arrays are of vital importance, since the large majority of the arrays mounted on aircraft, spacecraft, ships, and missiles have to conform to the body of the platform because of aerodynamics. Despite the common use of conformal antennas, little has been done for the development of analysis and design tools. A majority of the conformal designs are based on planar approximations, experimental or empirical intuition, and a handful of existing analysis methods based on rigorous Green's function approaches that use the layered cylindrical Green's function [59]. Among others, it is worth mentioning the work of Da Silva et al. [60], and the more-resent and rigorous work of Erturk et al. [56]. In [56], the authors rigorously analyzed finite arrays of axially printed diploes on a large cylinder using a hybrid spatial/spectral-domain Green's function representation in conjunction with the Method of Moments and an element-by-element approach that rigorously incorporated the mutual-coupling effects.

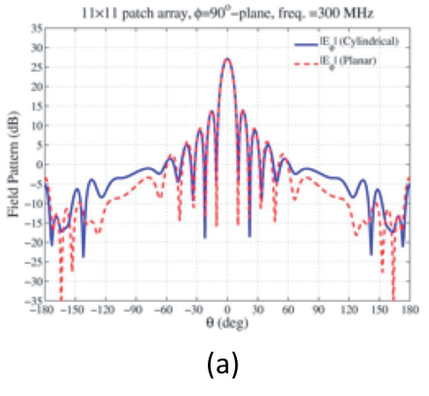

(a)

Figure 11a. The far-field patterns for 11×11 patch arrays printed on finite planar and cylindrical grounded dielectrics: 0° scan.

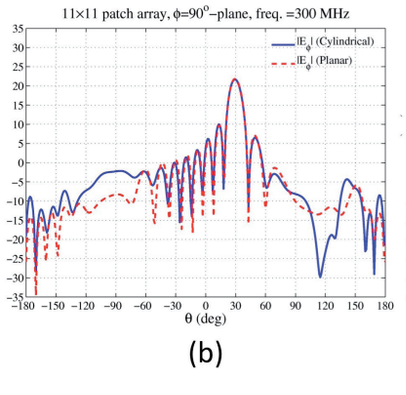

(b)

Figure 11b. The far-field patterns for 11×11 patch arrays printed on finite planar and cylindrical grounded dielectrics: 30° scan

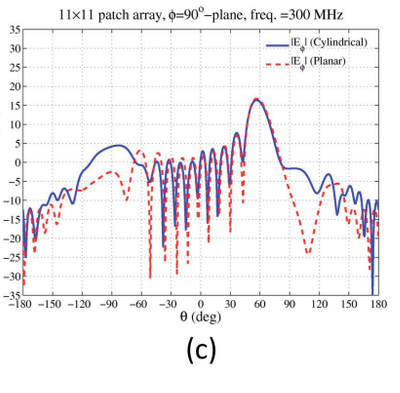

(c)

Figure 11c. The far-field patterns for 11×11 patch arrays printed on finite planar and cylindrical grounded dielectrics: 60° scan.

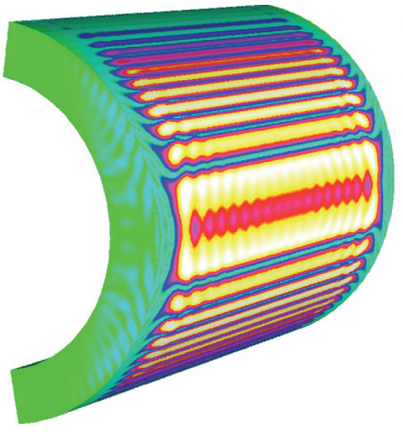

Figure 12a. The near fields for a 41×41 patch array on a finite cylindrical grounded dielectric: 0° scan.

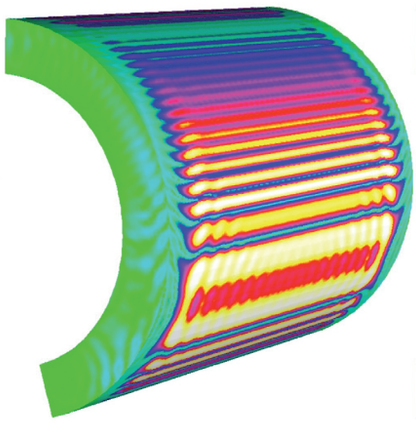

Figure 12b. The near fields for a 41×41 patch array on a finite cylindrical grounded dielectric: 30° scan.

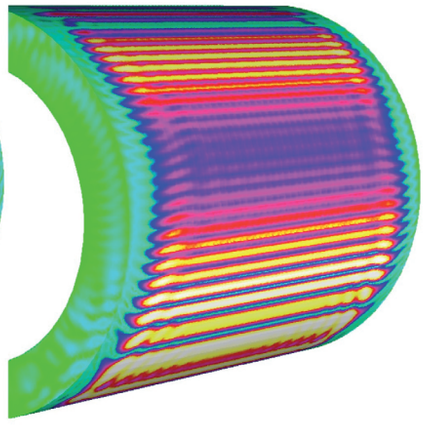

Figure 12c. The near fields for a 41×41 patch array on a finite cylindrical grounded dielectric: 60° scan.

Unlike most of the existing approaches, the proposed domain-decomposition method is based on the Finite-Element-Method approach. It thus is able to analyze complex antenna elements with complex feeding and excitations. More importantly, because the method is not based on knowledge of the Green's function, it works equally well for large and small cylindrical curvature. Effects of a finite cylindrical mounting platform or substrate can be accurately accounted for.

The conformal patch arrays considered here were coaxially fed rectangular patch arrays. The geometry of the elements can be found in Figure 10. They were arranged in a rectangular periodic lattice with a period of $0.5\lambda_0 \times 0.5\lambda_0$ The radius of the cylindrical sector on which the array was printed was chosen to be $8\lambda_0$, where λ_0 is the free-space wavelength. In this study, a series of arrays was analyzed, in order to further understand the effects of curvature. Four arrays with 11×11, 21×21, 31×31, and 41×41 elements were considered, keeping the same cylinder radius, and increasing the cylinder's coverage by adding elements in both the axial and circumferential directions. For illustration, we plot the 41×41 cylindrical array arrangement in Figure 10. Each array and its planar counterpart were analyzed in the radiating mode for various scan angles. The near fields at a boxed surface $1.5\lambda_0$ around the antenna are shown in Figure 11 for the 41×41 patch array for 0°, 30°, and 60° scans in the circumferential H plane.

It was more interesting to make a comparison between the present cylindrical patch arrays with their planar counterparts. In Figure 12, the H-plane far-field patterns of an 11×11 array are considered. Both planar (blue line) and cylindrical (red line) arrays were plotted together for 0°, 30°, and 60° H-plane scans. In both the planar and cylindrical arrays, a simple uniform amplitude and appropriate phasing was employed. Under all four excitations, the effect of the curvature was predominately apparent in the sidelobes, especially around $\theta = 90°$. For broadside excitation, the main-beam region was mainly unaffected, even though a close look revealed a 0.16 dB peak directivity reduction due to the curvature beam

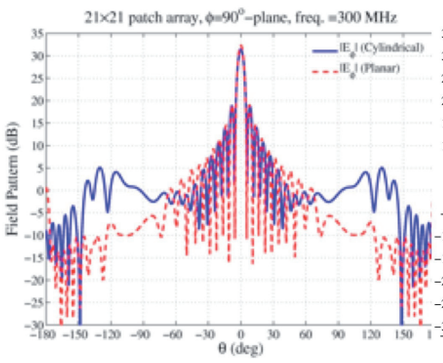

Figure 13a. The far-field patterns for 21×21 patch arrays printed on finite planar and cylindrical grounded dielectrics: 0° scan.

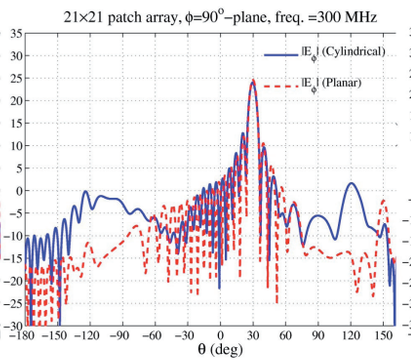

Figure 13b. The far-field patterns for 21×21 patch arrays printed on finite planar and cylindrical grounded dielectrics: 30° scan

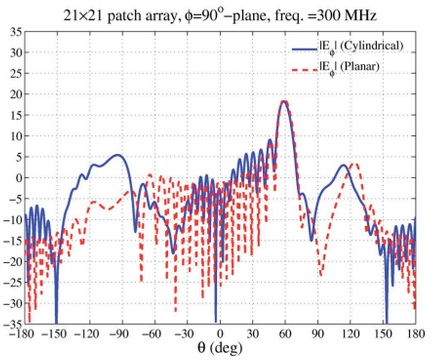

Figure 13c. The far-field patterns for 21×21 patch arrays printed on finite planar and cylindrical grounded dielectrics: 60° scan.

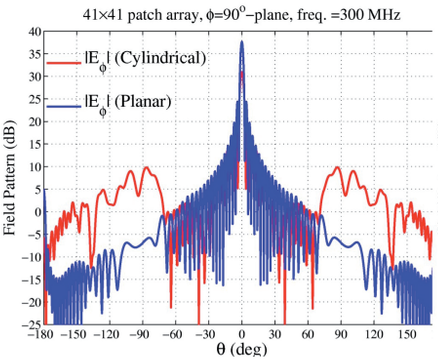

Figure 14a. The far-field patterns for 41×41 patch arrays printed on finite planar and cylindrical grounded dielectrics: 0° scan.

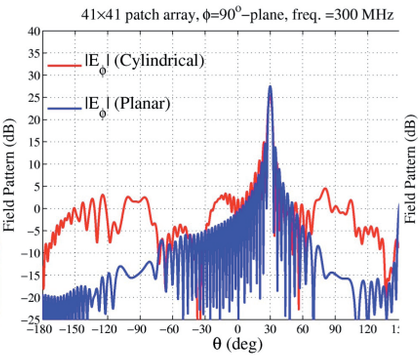

Figure 14b. The far-field patterns for 41×41 patch arrays printed on finite planar and cylindrical grounded dielectrics: 30° scan.

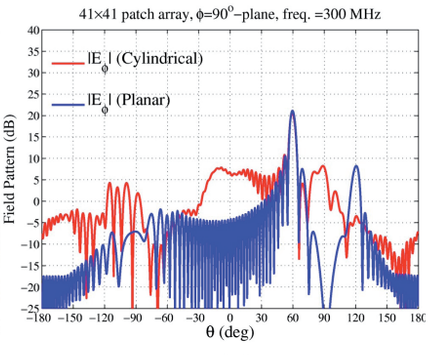

Figure 14c. The far-field patterns for 41×41 patch arrays printed on finite planar and cylindrical grounded dielectrics: 60° scan.

spreading. This effect became apparent for larger arrays. Notice that there was a slight shift in the location of the sidelobe peaks and nulls between the planar and cylindrical arrays. These effects should be expected, since each element in the cylindrical array had peak radiation at an angle normal to the cylinder's tangent plane at that location, which led to a different location for the sidelobe peaks. This could explain the 0.16 dB directivity reduction, which directly translated to spreading of the main bean. Notice that in order to compensate for this spreading effect, elaborate pattern-synthesis algorithms would have to be developed, which would incorporate the mutual coupling and the element orientation. The broadside and H-plane scanned far-field patterns of the 21×21 array configurations are shown in Figure 13, while the 41×41 array is plotted in Figure 14. In all cases, it was apparent that as the size of the array increased, the peak directivity of the cylindrical array decreased compared to the peak directivity of the planar counterpart, predominately for close-to-broadside scan angles. In all three figure clusters, the effects of the edge diffraction from the finite platform were visible at the close-to-grazing angles, in the form of high oscillating ripples. We also noted another interesting observation, concerning the directivity's front-to-back ratio at broadside excitation. In every arrangement, the front-to-back ratio of the planar configuration was of the order of 32 dB, and was always less that the equivalent of the cylindrical configuration's ratio. Specifically, the ratios were 32.3, 40.5, 37.2, and 36.8 for the cylindrical arrays.

In order to further quantify and understand the trends, differences, and similarities between planar and cylindrical arrays, a table with the peak directivities and angle of maxima is given in Table 5. The first and most prominent observation concerns the differences between the peak directivities of planar and cylindrical arrays as the size increased. The planar arrays almost always had better directivity (except at 90° for the 31×31 and 41×41 arrays), and, more importantly, as the size increased, the difference became larger. This behavior can be explained using the array effective-aperture concept. It is known that the directivity is directly proportional to the electrical area of the antenna from the angle of interest (scan angle). In the planar arrangement, the effective aperture doubles every time the array size doubles. This effect was observed if one compared the broadside directivity difference between the 21×21 and 11×11 arrays, from Table 5. In theory, this should be double – thus, 6 dB – whereas in practice, it was 5.11 dB. For the case of the 21×21 and 41×41 arrays, the computed number was 5.29 dB. Both numbers were close to the ideal 6 dB, but slightly smaller, since mutual-coupling effects and edge diffraction from the arrays and dielectric edges were not taken into account in the simple effective-aperture approximations. Using the same

		0° scan	30° scan	60° scan	90° scan
11×11	Planar	27.29dB (0°)	21.78 (30°)	16.72 (57°)	10.89 (71°)
	Cylindrical	27.13 (0°)	21.67 (29°)	16.36 (57°)	10.77 (71°)
	Difference	0.16	0.11	0.36	0.12
21×21	Planar	32.34 (0°)	24.60 (30°)	18.76 (59°)	11.10 (75°)
	Cylindrical	31.47 (0°)	24.00 (29°)	18.27 (58.5°)	10.91 (82°)
	Difference	0.87	0.6	0.49	0.19
31×31	Planar	35.42 (0°)	26.31 (30°)	20.11 (595°)	10.35 (78°)
	Cylindrical	32.70 (0°)	24.86 (30°)	19.76 (59°)	12.39 (87.5°)
	Difference	2.72	1.45	0.35	–2.04
41×41	Planar	37.63 (0°)	27.51 (30°)	21.13 (59.7°)	8.08 (76.3°)
	Cylindrical	30.97 (0°)	25.33 (29.7°)	20.56 (59.7°)	13.89 (87.7°)
	Difference	6.66	2.18	0.57	–5.81

Table 5. The peak directivity in dB as a function of scan angle for both of the planar and cylindrical arrays examined. The number inside the parenthesis indicates the angle where the peak directivity occurred.

Array Size	# Unknowns Cylindrical	# Unknowns Planar	Memory (MB)	#Iteration (tol = 10^{-1})
11×11	6.3 million	6.9 million	680	56
21×21	23.9 million	25.3 million	731	62
31×31	50.2 million	55.0 million	794	65
41×41	87.8 million	96.2 million	853	68

Table 6. A summary of the computational requirements of the conformal-array radiation simulations using the domain decomposition with Finite-Element Tearing and Interconnecting. All computations were performed in double-precision arithmetic.

effective-aperture principle, it could be concluded that the projected area of the cylinder will not double every time the elements are doubled in each direction. From Figure 10 and some elementary calculations involving the ratio of the projected areas of the 11×11 and 21×21 arrays, the result was that the directivity of the 21×21 array should have been 32.9 dB, whereas the calculations predicted 31.47 dB. This difference can be attributed to diffraction and mutual coupling. However, if the same calculation was done for the 41×41 array, the approximation led to 36.1 dB, which was almost 6 dB more that the full-wave computations. To explain these discrepancies, the effective aperture theory has to be compensated for the misalignment of the element radiation pattern, which leads to the extra beam-spreading factor, as discussed above. On the other hand, for grazing angles, the cylindrical arrays should radiate, better since the effective area is larger than that of the planar arrays. This effect was clearly observed in the last row of Table 5.

Before closing this section, it is useful to demonstrate the efficiency and versatility of the domain-decomposition method with Finite-Element Tearing and Interconnecting. In these runs, only one element block and one air block were independently discretized for each array configuration: planar and cylindrical. The meshing and creation of the Finite-Element Tearing and Interconnecting "transfer-function" matrix Z was created only once in the preprocessing, and it took a total of approximately 2.6 h to assemble for each configuration. The mesh of each antenna element was discretized with an initial mesh of $h = \lambda_0/4$ and nine h-adaptive mesh refinements with 0.038 error, based on the indicators and adaptive process described in [61]. The total number of unknowns, the amount of memory, and the domain-decomposition outer-loop iterations are documented in Table 6 for the various configurations and array sizes. Among all the different excitations, the maximum solution time was 2.9 h for the 11×11, 8.1 h for the 21×21, 36.4 h for the 31×31, and 33.6 h for the 41×41 cylindrical configurations. Note that in these simulations, simple Gauss-Siedel stationary iterations were employed. No Krylov-matrix solution techniques were adopted in these simulations. The improvements through the use of Krylov matrix solutions were reported in references [3, 4, 30-32].

6. Conclusions

This paper described a successful application of the domain-decomposition method in time-harmonic electromagnetic problems, particularly for modeling large finite antenna arrays. In all, very impressive results and computational statistics were produced. This makes the domain-decomposition methods a valuable alternative for future state-of-the-art computational engines. A variety of real-life industrial problems were successfully solved.

This first attempt to use domain-decomposition methods for electromagnetic computations revealed a number of issues and challenges. As was concluded from the convergence analysis, the present Robin transmission condition works very well for radiating problems and problems with a significant propagating mode spectrum, but tends to saturate for evanescent modes. The cement element method is a very promising mixed variational method of imposing various constraints, such as non-conforming meshes. It appears to work surprisingly well for complicated meshes, as long as the mesh ratios on either side of the interface are of compatible order. The proposed Finite-Element Tearing and Interconnecting algorithm was conceived and understood in a much different framework from the framework of the mechanical or mathematics communities. It was understood as a systematic method for obtaining "numerical" Green's/EM transfer functions of domains. Even though a direct factorization could achieve that goal, in this work, an iterative process more in line with the abovementioned insight was utilized. It turned out to be very efficient. In particular, it was found that for problems with a large number of identical repetitions, the Finite-Element Tearing and Interconnecting method outperformed the other alternatives. Furthermore, the Finite-Element Tearing and Interconnecting algorithm provides a great vehicle for modular optimization.

7. References

1. M. Vavoukis, *A Non-conformal Domain Decomposition Method for Solving Large Electromagnetic Wave Problems*, PhD dissertation, Electrical and Computer Engineering Department, The Ohio State University, 2005.

2. S. C. Lee, M. Vouvakis, and J. F. Lee, "A Non-Overlapping Domain Decomposition Method with Non-Matching Grids for Modeling Large Finite Antenna Arrays," *J. Comput. Phys.*, **203**, February 2005, pp. 1-21.

3. M. Vouvakis, Z. Cendes, and J. F. Lee, "A FEM Domain Decomposition Method for Photonic and Electromagnetic Band Gap Structures," *IEEE Transactions on Antennas and Propagation*, **AP-54**, 2, February 2006.

4. V. Rawat, *Finite Element Domain Decomposition with Second Order Transmission Conditions for Time Harmonic Electromagnetic Problems*, PhD dissertation, Electrical and Computer Engineering Department, The Ohio State University, 2009.

5. C. Farhat and F.-X. Raux, "A Method of Finite Element Tearing and Interconnecting and its Parallel Solution Algorithms," *Internat. J. Numer. Methods Engrg.*, **32**, 1991, pp. 1205-1227.

6. C. Farhat, A. Macedo, M. Lesoinne, F.-X. Roux, F. Magoules, and A. de La Bourdonnaie, "Two-level Domain Decomposition Methods with Lagrange Multipliers for the Fast Iterative Solution of Acoustic Scattering Problems," *Comput. Methods Appl. Mech. Engrg.*, **184**, 2000, pp. 213-239.

7. C. Farhat, A. Macedo, and M. Lesoinne, "A Two-Level Domain Decomposition Method for the Iterative Solution of High Frequency Exterior Helmholtz Problems," *Numer. Math.*, **85**, 2000, pp. 283-308.

8. C. Farhat, M. Lesoinne, P. LeTallec, K. Pierson, and D. Rixen, "FETI-DP: A Dual-Primal Unified FETI Method – Part I: A Faster Alternative to the Two-Level FETI Method," *Int. J. Numer. Meth. Engng.*, **50**, 2001, pp. 1523-1544.

9. Y. J. Li and J. M. Jin, "A Vector Dual-Primal Finite Element Tearing and Interconnecting Method for Solving 3D Large-Scale Electromagnetic Problems," *IEEE Transactions on Antennas and Propagation*, **AP-54**, 10, October 2006, pp. 3000-3009.

10. B. Smith, P. Bjorstad, and W. Gropp, *Domain Decomposition Parallel Multilevel Methods for Elliptic Partial Differential Equations*, New York, NY, Cambridge University Press, 1996.

11. A. Quarteroni and A. Valli, *Domain Decomposition Methods for Partial Differential Equations*, New York, NY, Oxford University Press, 1999.

12. A. Toselli and O. Widlund, *Domain Decomposition Methods - Algorithms and Theory*, **34**, Berlin, Springer, 2005.

13. L. F. Pavarino and A. Toselli, *Recent Developments in Domain Decomposition Methods*, **23**, Berlin, Springer, 2002.

14. T. F. Chan and T. P. Mathew, "Domain Decomposition Algorithms," *Acta Numerica*, 1994, pp. 61-143.

15. J. Xu, "Iterative Methods by Space Decomposition and Sub Space Correction," *SIAM Review*, **34**, 1992, pp. 581-613.

16. B. Stupfel, "A Fast-Domain Decomposition Method for the Solution of Electromagnetic Scattering by Large Objects," *IEEE Transactions on Antennas and Propagation*, **AP-44**, 1996, pp. 1375-1385.

17. B. Stupfel and M. Magnot, "A Domain Decomposition Method for the Vector Wave Equation," *IEEE Transactions on Antennas and Propagation*, **AP-48**, 2000, pp. 653-660.

18. Z. Zhu, H. Ji, and W. Hong, "An Efficient Algorithm for the Parametric Extraction of 3-D Interconnect Structures in the VLSI Circuits: Domain-Decomposition Method," *IEEE Trans. Micro. Theory Tech.*, **45**, 1997, pp. 1179-1184.

19. V. V. Veremey and R. Mittra, "Domain Decomposition Approach for Capacitance Computation of Nonorthogonal Interconnect Structures," *IEEE Trans. Micro. Theory Tech.*, **48**, 2000, pp. 1428-1434.

20. V. V. Veremey and R. Mittra, "Efficient Computation of Interconnect Capacitances Using the Domain Decomposition Approach," *IEEE Trans. Advanced Packaging*, **22**, 1999, pp. 348-355.

21. L. Yin and W. Hong, "A Fast Algorithm Based on the Domain Decomposition Method for Scattering Analysis of Electrically Large Objects," *Radio Science*, **37**, 2002, pp. 1-9.

22. L. Yin and W. Hong, "A Novel Algorithm Based on the Domain-Decomposition Method for the Full-Wave Analysis of 3-D Electromagnetic Problems," *IEEE Trans. Micro. Theory Tech.*, **50**, 2002, pp. 2011-2017.

23. U. Navsariwala and S. D. Gedney, "An Efficient Implementation of the Finite-Element Time-Domain Algorithms on Parallel Computers Using a Finite-Element Tearing and Interconnecting Algorithm," *Micro. Opt. Tech. Lett.*, **16**, 1997, pp. 204-208.

24. C. T. Wolfe, U. Navsariwala, and S. D. Gedney, "A Parallel Finite-Element Tearing and Interconnecting Algorithm for Solution of the Vector Wave Equation with PML Absorbing Medium," *IEEE Transactions on Antennas and Propagation*, **AP-48**, 2000, pp. 278-284.

25. R. Lee and V. Chupongstimun, "A Partitioning Technique for the Finite Element Solution of Electromagnetic Scattering from Electrically Large Dielectric Cylinders," *IEEE Transactions on Antennas and Propagation*, **AP-42**, 1994, pp. 737-741.

26. Y. S. Choi-Grogan, K. Eswar, P. Sadayappan, and R. Lee, "Sequential and Parallel Implementations of the Partitioning Finite-Element Method," *IEEE Transactions on Antennas and Propagation*, **AP-44**, 1996, pp. 1609-1616.

27. P. Liu and Y.-Q. Jin, "The Finite-Element Method with Domain Decomposition for Electromagnetic Bistatic Scattering from the Comprehensive Model of a Ship on and a Target Above a Large-Scale Rough Sea Surface," *IEEE Trans. Geosci. Remote Sensing*, **42**, pp. 950-956, 2004.

28. R. W. Kindt, K. Sertel, E. Topsakal, and J. L. Volakis, "Array Decomposition Method for the Accurate Analysis of Finite Arrays," *IEEE Transactions on Antennas and Propagation*, **AP-51**, 2003, pp. 1364-1372.

29. R. W. Kindt, K. Sertel, and J. L. Volakis, "Array Decomposition-Fast Multipole Method for Finite Array Analysis," *Radio Science*, **39**, 2004.

30. K. Zhao, V. Rawat, S.-C. Lee, and J.-F. Lee, "A Domain Decomposition Method with Non-Conformal Meshes for Finite Periodic and Semi-Periodic Structures," *IEEE Transactions on Antennas and Propagation*, **AP-55**, 9, September 2007, pp. 2559-2570.

31. Z. Peng and J. F. Lee, "Non-Conformal Domain Decomposition Method with Second Order Transmission Conditions for Time-Harmonic Electromagnetics," *Journal of Computational Physics*, **229**, 16, August 2010, pp. 5615-5629.

32. V. Rawat and J. F. Lee, "Non-Overlapping Domain Decomposition with Second Order Transmission Condition for Time-Harmonic Maxwell's Equations," *SIAM Journal on Scientific Computing*, **32**, 6, December 2010, pp. 3584-3603.

33. Y. J. Li and J. M. Jin, "A New Dual-Primal Domain Decomposition Simulation of 3D Large-Scale Electromagnetic Problems," *IEEE Transactions on Antennas and Propagation*, **AP-55**, 10, October 2007, pp. 2803-2810.

34. H. Schwarz, "Uber Einige Abbidungsaufgaben," *Ges. Math. Abh.*, **11**, 1896, pp. 65-83.

35. K. Miller, "Numerical Analogs to the Schwarz Alternating Procedure," *Numer. Math.*, **7**, 2965, pp. 91-103.

36. P.-L. Lions, "On the Schwarz Alternating Method I," in T. Chan, R. Blowinski, J. Peraux, and O. Widlund (eds.), *First International Symposium on Domain Decomposition Methods*, Paris, France Philadelphia, PA, SIAM, 1987, pp. 1-42.

37. P.-L. Lions, "On the Schwarz Alternating Method II: Stochastic Interpretation and Order Properties," in T. Chan, R. Blowinski, J. Peraux, and O. Widlund (eds.), *Second International Symposium on Domain Decomposition Methods*, Paris, France, Philadelphia, PA, SIAM, 1988, pp. 47-70.

38. P.-L. Lions, "On the Schwarz Alternating Method III: A Variant for Nonoverlapping Subdomains," in T. Chan, R. Blowinski, J. Peraux, and O. Widlund (eds.), *Third International Symposium on Domain Decomposition Methods*, Houston, TX, SIAM, Philadelphia, PA, 1989, pp. 202-223.

39. B. Despres, "Domain Decomposition Method and the Helmholtz Problem," First International Conference on Mathematical and Numerical Aspects of Wave Propagation Phenomena, Strasbourg, Philadelphia, PA, SIAM, 1991, pp. 44-52.

40. B. Despres, "Domain Decomposition Method and the Helmholtz Problem. II," Second International Conference on Mathematical and Numerical Aspects of Wave Propagation Phenomena, Newark, DE, Philadelphia, PA, SIAM, 1993, pp. 4197-206.

41. B. Despres, P. Joly, and J. E. Roberts, "A Domain Decomposition Method for the Harmonic Maxwell Equations," Iterative Methods in Linear Algebra, Amsterdam, Holland, North-Holland, 1992, pp. 245-252.

42. F. Collino, G. Delbue, P. Joly, and A. Piacentini, "A New Interface Condition in the Non-Overlapping Domain Decomposition Methods for the Maxwell Equations," *Comput. Methods Appl. Mech. Engrg.*, **148**, 1997, pp. 195-207.

43. C. Bernardi, Y. Maday, and A. Patera, "Domain Decomposition by the Mortar Element Method," in H. Kaper (ed.), *Asymptotic and Numerical Methods for Partial Differential Equations with Critical Parameters*, Reidel, Pitman, 1993, pp. 269-286.

44. C. Bernardi, Y. Maday, and A. Patera, "A New Nonconforming Approach to Domain Decomposition the Mortar Element Method," in H. Brezis and J. Lions (eds.), *Nonlinear Partial Differential Equations and their Applications*, Paris, Pitman, 1994, pp. 13-51.

45. F. Ben Belgacem, "The Mortar Finite Element Method with Lagrange Multipliers," *Numer. Math.*, **84**, 1999, pp. 173-197.

46. F. Ben Belgacem, A. Buffa, and Y. Maday, "The Mortar Finite Element Methods for 3D Maxwell Equations: First Results," *SIAM J. Numer. Anal, 39, 2001, pp. 880-901.*

47. R. H. W. Hoppe, "Mortar Edge Element Methods in R^3," *East West J. Num. Math.*, **7**, 1999, pp. 159-173.

48. F. Rapetti, "The Mortar Edge Element Method on Non-Matching Grids for Eddy Current Calculations on Moving Structures," *Int. J. Num. Model.*, **14**, 2001, pp. 457-477.

49. T. Arbogast and I. Yotov, "A Non-Mortar Mixed Finite Element Method for Elliptic Problems on Non-Matching Multiblock Grids," *Comput. Methods Appl. Mech. Engrg.*, **149**, 1997, pp. 255-265.

50. Y. Achdou, C. Japhet, Y. Maday, and F. Nataf, "A New Cement to Glue Non-Conforming Grids with Robin Interface Conditions: The Finite Volume Case," *Numer. Math.*, **92**, 2002, pp. 593-620.

51. S. M. Rao, D. R. Wilton, and A. W. Glisson, "Electromagnetic Scattering by Surfaces of Arbitrary Shape," *IEEE Transactions on Antennas and Propagation*, **AP-30**, May, 1982, pp. 409-418.

52. J.-C. Nedelec, "Mixed Finite Elements in R^3," *Numer. Math.*, **35**, 1980, pp. 315-341.

53. K. Zhao, V. Rawat, and J. F. Lee, A Domain Decomposition Method for Electromagnetic Radiation and Scattering Analysis of Multi-Target Problems, *IEEE Transactions on Antennas and Propagation*, **AP-56**, 2008, pp 2211-2221.

54. K. Zhao, *A Domain Decomposition Method for Solving Electrically Large Electromagnetic Problems*, PhD dissertation, Electrical and Computer Engineering Department, The Ohio State University, 2007.

55. Z. Chen, Q. Du, and J. Zou, "Finite Element Methods with Matching and Nonmatching Meshes for Maxwell Equations with Discontinuous Coefficients," *SIAM J. Numer. Anal.*, **37**, 2000, pp. 1542-1570.

56. V. B. Erturk, R. Rojas, and K. W. Lee, "Analysis of Finite Arrays of Axially Directed Printed Dipoles on Electrically Large Circular Cylinders," *IEEE Transactions on Antennas and Propagation*, **AP-52**, 2004, pp. 2586-2595.

57. D. M. Pozar, "Finite Phased Arrays of Rectangular Microstrip Patches," *IEEE Transactions on Antennas and Propagation*, **AP-34**, 1986, pp. 658-665.

58. V. Jandhyala, E. Michielssen, B. Shanker, and W. C. Chew, "A Fast Algorithm for the Analysis of Radiation and Scattering from Microstrip Arrays of Finite Substrates," *Micro. Opt. Tech. Lett.*, **23**, 1999, pp. 306-310.

59. J. Wait, *Electromagnetic Radiation from Cylindrical Structures*, New York, NY, Pergamon Press, 1959.

60. C. M. Da Silva, F. Lumini, J. C. S. Lakova, and F. P. Richards, "Analysis of Cylindrical Arrays of Microstrip Rectangular Patches," *Electron. Lett.*, **27**, 1991, pp. 778-780.

61. D. K. Sun, Z. Cendes, and J.-F. Lee, "Adaptive Mesh Refinement, h-Version, for Solving Multiport Microwave Devices in Three Dimensions," *IEEE Trans. Magn.*, **36**, 2000, pp. 1596-1599.

Towards More-Efficient Spectrum Usage : Spectrum-Sensing and Cognitive-Radio Techniques

J. Pérez-Romero
D. Noguet
M. López-Benítez
F. Casadevall

Abstract

The traditional approach of dealing with spectrum management in wireless communications has been through the definition of a licensed user granted exclusive exploitation rights for a specific frequency. While interference is easily avoided, this approach is unlikely to achieve the objective of maximizing the value of the spectrum. In fact, spectrum measurements carried out worldwide have revealed significant spectrum underutilization. As a result, the so-called dynamic-spectrum-access networks (DSANs) are one of the current research trends in the wireless area. In such networks, unlicensed radios (secondary users) are allowed to operate in licensed bands provided that no harmful interference is caused to the licensees (primary users). One of the key enabling technologies for this paradigm is cognitive radio (CR). This envisages a radio able to sense and be aware of its operational environment so as to dynamically and autonomously adjust its parameters to adapt to different situations. Spectrum sensing, enabling the detection of unused spectrum bands, then becomes one of the key elements of cognitive-radio technologies. Within this framework, on the one hand this paper provides insight into the different spectrum-sensing techniques and associated standardization activities. On the other hand, the paper also presents some spectrum-occupation measurement activities, targeting the characterization of how the spectrum is being used in the different bands, in order to extract the relevant parameters for cognitive-radio design. These are presented from a general methodological perspective, and also include the results obtained in a particular case study.

1. Introduction: Cognitive-Radio Techniques for Dynamic Spectrum Access

The current spectrum-management situation was inherited from the early deployment of radio broadcasting channels, in the early 1920s. At that time, no spectrum-regulation management was in place, and broadcasters competed by increasing their power levels to drown out their competitors. This situation led to high interference levels, and led to the creation of independent regulatory entities to ensure fairness amongst competitors, and better signal quality to end users. Frequencies were then assigned to broadcasters, along with transmitted-power bounds. On the other hand, licenses for exclusive rights guaranteed low interference levels and good coexistence among incumbents. The deployment of wireless fixed or mobile communication systems followed the same philosophy of a low-interference-driven regulation strategy, administratively ruled by the regulators.

In spite of better interference control, spectrum measurements carried out worldwide have revealed that the exclusive-rights spectrum-management approach exhibits significant spectrum underutilization in some bands, even if spectrum scarcity is claimed when trying to find bands to be allocated for new systems. This observation supports a measurement-driven flexible regulation strategy, rather than a static administrative command and control scheme. As a result of this fact, in order to improve efficiency through smarter spectrum management, one of the current trends is the development of so-called dynamic-spectrum-access networks (DSANs). In these networks, unlicensed radios – denoted secondary users (SU) in this context – are allowed to operate in licensed bands provided that no harmful interference is caused to the licensees, denoted primary users (PU) in this context. The proposition of the TV-band Notice of Proposed Rule Making (NPRM) in the USA [1], allowing this secondary operation in the TV broadcast bands if no interference is caused to TV receivers, was a first milestone in this direction. In this approach, secondary users will be required to properly detect the existence of the transmissions of primary user, and should be able to adapt to the varying spectrum conditions, ensuring that the primary rights are preserved. These events culminated in the creation of the IEEE 802.22 standard. This developed a cognitive-

J. Pérez-Romero, M. López-Benítez, and F. Casadevall are with the Department of Signal Theory and Communications, Universitat Politècnica de Catalunya (UPC), Barcelona, Spain ; e-mail : jorperez@tsc.upc.edu. D. Noguet is with CEA-LETI, MINATEC, 17 rue des Martyrs, 38054 Grenoble cedex 9, France ; e-mail : dominique.noguet@cea.fr.

This is an invited *Review of Radio Science* from Commission C.

radio-based physical and medium access control layer for use by license-exempt devices on a non-interfering basis in spectrum portions allocated to the TV broadcast services.

Primary-secondary (P-S) spectrum sharing can take the form of cooperation or coexistence. Cooperation involves explicit communication and coordination between primary and secondary systems. Coexistence means that both systems are operated independently. When sharing is based on coexistence, secondary devices are essentially invisible to the primary. All the complexity of sharing is thus borne by the secondary, and no changes to the primary system are needed. There can be different forms of coexistence, such as spectrum underlay (e.g., UWB) or spectrum overlay (e.g., opportunistic exploitation of white spaces in the spatial-temporal domain sustained by spectrum sensing, coordination with peers, and fast spectrum handover). As for cooperation, different forms of primary-secondary interactions are again possible. For example, spatial-temporal white spaces that can be exploited by secondary users can be signaled through appropriate channels or beacons. In addition, the interaction between primary users and secondary users provides an opportunity for the license-holder to demand payment according to the different quality-of-service grades offered to secondary users.

One of the key enabling technologies for dynamic-spectrum-access network development is cognitive radio (CR). This has been claimed to be an adequate solution to the existing conflicts between spectrum-demand growth and spectrum underutilization. The term cognitive radio was originally coined by J. Mitola III in [2, 3]. It envisaged a radio able to sense and be aware of its operational environment, so that it can dynamically and autonomously adjust its radio operating parameters accordingly to adapt to the different situations. The cognitive-radio concept was in turn built upon the software-defined radio (SDR) concept. This can be understood as a multi-band radio supporting multiple air interfaces and protocols, and being reconfigurable by software running on a digital signal processor (DSP) or a general-purpose microprocessor. Consequently, the software-defined radio constituted the basis for the physical implementation of cognitive-radio concepts.

Thanks to this capability of being aware of actual transmissions across a wide bandwidth, and of adapting their own transmissions to the characteristics of the spectrum, cognitive radios offer great potential for bringing dynamic-spectrum-access networks to reality. In fact, dynamic-spectrum-access networks are usually referred to as cognitive-radio networks (CRNs). The operating principle of a cognitive radio in the context of a dynamic-spectrum-access network is to identify spatial and temporal spectrum gaps not occupied by primary/licensed users. These are usually referred to as *spectrum holes* or *white spaces*. The cognitive radio must place secondary/unlicensed transmissions in such spaces, and vacate the channel as soon as the primary users return. The cognitive-radio concept therefore implicitly relies on two basic premises: the existence of enough white spaces caused by primary spectrum underutilization, and the ability of secondary users to effectively detect and identify the presence of licensed technologies in order not to cause harmful interference.

From a general operational perspective, a cognitive radio follows the so-called *cognition cycle* to enable interaction with the environment and the corresponding adaptation. It consists in the *observation* of the environment, the *orientation* and *planning* that leads to making the appropriate *decisions* pursuing specific operational goals, and finally *acting* over the environment. On the other hand, decisions can be reinforced by *learning* procedures, based on the analysis of prior observations and on the corresponding results of prior actuations. When particularizing the cognition cycle to the dynamic spectrum access for a secondary user, the observation then turns out to be the spectrum sensing in order to identify the potential white spaces. The orientation and planning steps are associated with the analysis of the available white spaces. Finally, the acting step is in charge of selecting adequate white space to make the secondary transmission, together with the setting of the appropriate radio parameters such as transmitted power, modulation formats, etc.

There are a number of techniques to be developed for implementation of efficient secondary-spectrum usage through cognitive-radio networks. These were classified in [4] as spectrum sensing, spectrum management, spectrum mobility, and spectrum sharing mechanisms. These techniques are briefly discussed in the following.

1.1 Spectrum Sensing

This consists of detecting the unused spectrum bands that can be potentially exploited for secondary communications. A lot of different spectrum-sensing techniques have been studied in recent years. These include the energy detector, which does not include any specific knowledge about the primary signal to be detected; matched-filter detection, which requires knowledge of the specific primary signal formats; and cyclostationarity feature detection. The possibility of combining sensing measurements from different sensors through appropriate fusion schemes has also been considered in so-called cooperative sensing. Even from a more-general perspective, the possibility that the network provides knowledge about the current spectrum bands available through some control channel has also been considered. This was the case for the development of the so-called cognitive pilot channel (CPC) in [5], for example. From this perspective, and having in mind the possibility of combining the knowledge provided by the network with the knowledge acquired by the sensing process, the spectrum-sensing concept can be generalized to the concept of spectrum awareness.

1.2 Spectrum Management

This refers to the selection of the most adequate spectrum band to carry out the transmission in accordance with the secondary user's requirements. This selection should be made based on the characteristics of the channel in terms of the maximum capacity that can be obtained by the secondary users, for example, and also taking into consideration the maximum interference that can be tolerated by primary receivers. The decision-making process here can benefit from the application of learning strategies, which, based on experience acquired from prior decisions, can orient the decisions towards the selection of some channels in front of others. For example, when the primary user activity is high in some channels, it is more likely that primary users will force the secondary transmitter to free the channel. Thus, if a primary user's activity characterization was known by the secondary users, it could prevent the secondary network from selecting these channels.

1.3 Spectrum Mobility

This functionality consists of establishing appropriate mechanisms to insure that ongoing secondary communication can be continued whenever a primary user appears in the occupied bandwidth. This will thus involve the ability to detect the appearance of this primary user, which requires some continuous monitoring of the channel, e.g., through sensing mechanisms. When the primary user then appears, the occupied channel has to be freed. An alternative channel has to be found where the communication can be continued, which is usually called *spectrum handover*. Handover has therefore a broadened meaning, compared to the *horizontal handover* typically implemented in cellular systems to enable space mobility. In the case of spectrum handover, the band and also the communication standard may change during the handover procedure, implying a so-called *vertical handover*. When both spatial and spectrum handover are considered in a dynamic-spectrum-access network, the term generalized handover is used [6].

1.4 Spectrum Sharing

This function targets the provision of an efficient mechanism so that coexisting secondary users can share the available spectrum holes. Adequate medium access control (MAC) protocols and scheduling mechanisms are needed, and they are very much dependant on how the secondary network is deployed, e.g., if it is infrastructure or infrastructure-less based, etc.

Although all the above functions have become hot research topics during the last few years, there is still a lot of work to do before cognitive-radio networks become a reality in the fullest extent. This will involve not only technical aspects, but significant regulatory changes will also be needed. In addition, this will also have implications from the technological and economical perspectives, with the appearance of new business models to exploit the capabilities offered by cognitive-radio networks. This involves different possibilities, ranging from secondary cellular operators that could offer services at cheaper prices at the expense of somehow reduced quality, to the deployment of infrastructure-less secondary networks that would enable communication of short range devices.

Based on the above context, this paper focuses on the applicability of measurement techniques to the development of cognitive-radio networks. In particular, Section 0 addresses the spectrum sensing techniques as one of the key procedures for the operation of cognitive-radio networks. Section 3 then focuses on the different standardization initiatives that have been carried out. Section 4 addresses particular aspects of spectrum-measurement techniques, and how the results from measurement campaigns can be used in cognitive-radio-network design. This is followed by the results of a real case study of spectral measurements, obtained in the area of Barcelona, in Section 5. Finally, conclusions are summarized in Section 6.

2. Spectrum-Sensing Techniques

There has been a growing interest in signal detection in the context of cognitive radio [3]. More specifically, there is interest in opportunistic radio (or overlay systems), where secondary cognitive-radio networks can be operated over frequency bands allocated to some primary system in so far as this primary system is absent (free band detection) or, in a more general case, whenever harmful interference with primary systems can be avoided. In most cases, the presence of the primary system is assessed through direct detection of its communication signal, although beaconing is sometimes considered [7]. In many situations, the primary system-detection problem is thus transposed into the problem of detecting a communication signal in the presence of noise.

Signal detection is a very old and thought-after signal-processing issue. In the context of cognitive-radio networks, the detection of primary users by the secondary system is critical in a cognitive-radio environment. Indeed, misdetection would lead to harmful interference to the primary users, while a high false-alarm probability would make actual holes unavailable to secondary usage. However, detection of primary users is made difficult due to the challenges of accurate and reliable sensing of the wireless environment. Secondary users might experience losses due to multipath fading, shadowing, and building penetration. These can result in an incorrect estimation of the wireless environment, which can in turn cause misdetection or false alarm at the secondary users. This brings the necessity for the cognitive radio to be highly robust to channel impairments, and to also be able to detect extremely low power signals.

These stringent requirements lead to important challenges for the deployment of cognitive-radio networks. Surveys of these techniques in the context of spectrum sensing have been proposed (for instance, in [8, 9]).

Although some simple detectors can be achieved directly based on the RF signal (e.g., energy detection), most of the time, the detection is processed based on the baseband digital signal, to allow for more algorithmic options. In this case, the free band detector can be illustrated as in Figure 1. The radio signal, $y(t)$, received at the antenna is first filtered with a bandwidth, *B*, which is the band under consideration. The signal is then down-converted to baseband, and digitized (at a sampling frequency of $1/T_s$) before being sent to the detector. The function that the detector has to perform is that of detecting signals in the presence of noise, which can be stated as the following hypothesis:

$$H_0: r(t) = n(t), \tag{1}$$

$$H_1: r(t) = hs(t) + n(t),$$

where H_0 is verified when the band, *B*, is signal free, and H_1 corresponds to *B* being occupied. $n(t)$ is noise, and $s(t)$ is a telecommunication signal.

Many detection techniques may be considered, depending on the detection performance and the implementation cost. Typically, detectors are categorized based on the knowledge required of the secondary users about the waveform of the primary users. Among these, we describe below the three most important options: the matched filter, energy or power detection, and the feature detector, which often exploits the cyclostationarity nature of the primary user's signal.

Using a matched filter is the optimal solution to signal detection in the presence of noise, as it maximizes the received signal-to-noise ratio (SNR) [10]. It is a coherent detection method, which necessitates the demodulation of the signal. This means that cognitive-radio equipment has *a priori* knowledge of the received signal(s), e.g., the modulation type, the pulse shaping filter, the data-packet format, etc. Most often, telecommunication signals have well-defined characteristics, e.g., the presence of a pilot, preamble, synchronization words, etc., which permit the use of these detection techniques. Based on a coherent approach, a matched filter has the advantage of only requiring a reduced set of samples, a function of the $O(1/\mathrm{SNR})$, in order to reach a convenient detection probability [11]. If $X[n]$ is completely known to the receiver, then the optimal detector for this case is

$$T(Y) = \sum_{n=0}^{N-1} Y[n]X[n] \underset{H0}{\overset{H1}{\lessgtr}} \gamma. \tag{2}$$

The matched filter lacks generality, as it can be applied to only one specific waveform. One approach to make the detector independent of the waveform is to perform non-coherent detection through energy detection [12]. This suboptimal technique has been extensively used in radiometry. Energy detection or the radiometer method relies on a stationary and deterministic model of the signal, mixed with stationary white Gaussian noise. The basic functional method involves a squaring device, an integrator, and a comparator (Figure 2). The SNR can be calculated as in the figure, so that the threshold, *K*, directly relates to some SNR value. If *V* is higher than the threshold *K*, then the presence hypothesis (H_1) is considered fulfilled. Otherwise, the band is considered to be signal free (H_0). However, in many practical implementations, the signal energy is computed on the one hand (integrator), and the threshold is computed after some calibration of the radiometer in the absence of the signal. In this case, σ_0 is omitted in the calculation of *V* (Figure 2).

This can be implemented in either the time domain or in the frequency domain. Time-domain implementation requires front-end filtering before the squaring operation. In the frequency-domain implementation, after front-end bandpass filtering, the received signal samples are converted to frequency-domain samples using the Fourier transform. Signal detection is then effected by comparing the energy of the signal samples falling within a certain frequency band with that of a threshold value. The performance of the energy detector directly depends on the integration time, which is usually limited in telecommunication systems.

An interesting alternative to energy detection consists of considering a cyclostationary model of the signal, instead of a stationary model [13]. Indeed, telecommunication signals are modulated by sine-wave carriers, pulse trains, repeated spreading, hopping sequences, or exhibit cyclic prefixes. This results in built-in periodicity, which, of course, is not present in the noise. These modulated signals are characterized as cyclostationary because their momentum (mean, autocorrelation, etc.) exhibits periodicity, thereby enabling differentiation of the modulated signal from the noise. This is due to the fact that the noise is a wide-sense stationary signal with null auto correlation (except at lag 0).

If $x(t)$ is a random process of null mean, $x(t)$ is cyclostationary of order *n* if and only if its statistic properties at order *n* are a periodic function of time. In particular, for $n = 2$, a process is cyclostationary in the large sense and respects

$$c_{xx}(t,\tau) = E[(\ )] = c_{xx}(t+T,\tau), \tag{3}$$

where *T* represents a cyclic period.

When the primary user's signal is completely unknown, it is theoretically possible to explore the

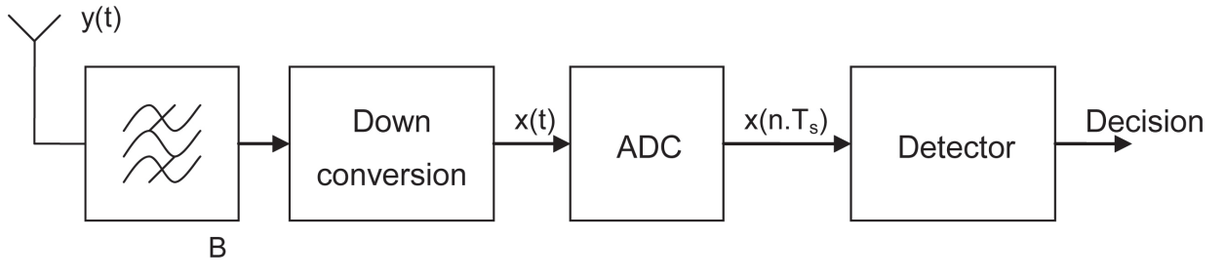

Figure 1. The architecture of the digital free-band detector.

presence of cyclic frequencies for any autocorrelation lag at any frequency. This approach is referred to as the cyclostationary spectrum density (CSD) (this is also referred to as the two-dimensional cyclostationary spectrum density) [14, 15]. However, the comprehensive two-dimensional cyclostationary spectrum density is never implemented in practice, due to its huge implementation cost. To sort out this issue, one-dimensional cyclostationary spectrum densities are preferred to limit implementation cost. The cyclostationary spectrum density can be performed using the time-domain autocorrelation [16], or through the analysis of signal periodicity redundancy in the frequency domain [17]. However, in both cases a large FFT operation (512 to 2048) needs to be implemented, leading to significant hardware complexity. When additional knowledge of the primary user's signal is exploited by the secondary users, the FFT can be avoided, and only specific known cyclic frequencies are explored, as in [18, 19]. This can lead to significant complexity reduction, as highlighted in the Wi-Fi- and DVB-T-specific implementations presented in [20]. Besides, it was shown that restricting the modulation search space (i.e., shrinking the two-dimensional cyclostationary spectrum density to a small subset of samples) also reduces the convergence of the algorithm, thereby enabling the exploitation of short-duration opportunities [21].

3. Standardization Activities in the Area of Dynamic-Spectrum-Access Networks

The trend towards dynamic-spectrum-access networks has motivated standardization bodies to propose technologies to rationalize cognitive-radio operation. These standards tackle cognitive radio from various angles. The first angle relates to the amendment of existing standards to operate under certain regulatory conditions that require dynamic-spectrum-access network features. For instance, this is the case in the TV white space. The second angle suggests analyzing dynamic-spectrum-access networks from a broader viewpoint, in order to come up with a coherent and more-general framework. In both cases, there is a need to guarantee interference-free operation to prioritize systems (e.g., TV systems in the TV white space context), or for coexistence among peers (e.g., with other unlicensed systems).

These non-interference or coexistence techniques can be divided into two categories: overlay and underlay. In the underlay case, the secondary system operates with a very low power spectral density, in order not to impact the primary (or other) users. The underlay system is thereby seen as low-power additive noise by the primary systems. This is the case of ultra-wideband (UWB) systems, which operate over a wide bandwidth. The IEEE 802.15.4a standard [22], within the IEEE 802.15 group for wireless personal area networks, can thus be considered a first attempt to enable spectrum sharing between unlicensed secondary systems and primary (licensed) systems.

However, despite the strong restrictions on spectrum density for such systems (–41.3 dBm/MHz), UWB systems operating in the low band (3-5 GHz) have been forced to include detect-and-avoid (DA) features, to insure that they are switched off whenever a WIMAX system operates within the band (typically, at 3.5 GHz). This causes the UWB system (at least in the low band) to operate in an overlay mode, where the secondary system can operate only when the band is vacant of any primary spectrum usage. The overlay approach implies that sensing (in a broad sense) and cognitive techniques are used to detect the presence of incumbents, in order to decide whether communication can be initiated and to accordingly adapt the transceiver.

This overlay approach, with a listen-before-talk strategy, was at the heart of the IEEE 802.22 group on WRANs (wireless regional area networks), launched in 2005. This standard aims at exploiting the TV white-space spectrum with a cognitive-radio approach [23, 24]. The physical and MAC layers of IEEE 802.22 are similar to IEEE 802.16, with some modifications related to the identification of the primary systems. This standard was given more prominence after the decision of the FCC to enable unlicensed access to cognitive-radio networks in the TV bands [25].

Within the IEEE, the dynamic-spectrum-access network rationalization effort came in 2005, with the creation of a set of standardization projects related to cognitive-radio networks. It was numbered IEEE 1900, which evolved in 2006 into IEEE Standards Coordinating Committee 41 (IEEE SCC41) on "Dynamic Spectrum Access Networks" [26]. The scope of IEEE SCC41 is to facilitate the development of research ideas into standards for transferring

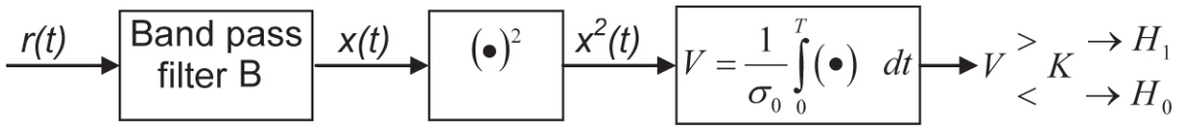

Figure 2. A block diagram of the energy detector.

the use of research results for public use. Very recently, the committee was transferred to the IEEE Communication Society (ComSoc) standards effort, and was renamed the IEEE ComSoc DYnamic SPectrum Access Networks (DYSPAN) committee. Because the dynamic-spectrum-access network was a new area in wireless communication, it was found useful to precisely define the terminology, to enable a common understanding. This was the scope of the 1900.1-2008 standard [27]. As mentioned above, coexistence among systems is of paramount importance for a cognitive-radio network. This was the scope of 1900.2-2008, which was issued the same year [28]. Similarly, the IEEE 802.19 standard defined general coexistence metrics for all IEEE 802 networks, but with a focus on operation in the unlicensed bands. Although focusing on IEEE 802 networks, the guidelines of the standard can be applicable to other unlicensed wireless systems.

In the 1900 series, the 1900.4 group is the one developing a complete framework for cognitive-radio networks. The 1900-2009 standard considers the architectural building blocks enabling network-device distributed decision making for optimized radio-resource usage in heterogeneous wireless access networks [29]. The standard includes entities comprising network and device resource managers, as well as the information to be exchanged between these entities. The aim of this framework is to optimize radio-resource usage in a cognitive-driven environment. Two projects are currently active within this group. The first is P1900.4.1, which addresses "Interfaces and Protocols Enabling Distributed Decision Making for Optimized Radio Resource Usage in Heterogeneous Wireless Networks." The second is P1900.4a, on "Architecture and Interfaces for Dynamic Spectrum Access Networks in White Space Frequency Bands." The first project focuses on the interfaces between the architectural entities defined in [29]. The latter project is an amendment of [29], to enable mobile wireless access for any radio technology. Finally, P1900.5 is developing a standard on "Policy Language and Policy Architectures for Managing Cognitive Radio for DSAN."

Compared to classical wireless networks, determining the presence of other systems is a key feature. This can be done through spectrum sensing, or by querying a data archive. How these entities are interfaced to the communication systems is being analyzed by the P1900.6 Working Group. The standard project specifies a functional interface, comprising a number of logical entities (service access points) attached to sensing, communication, and application.

Outside the IEEE Standards Association and ComSoc standards, other standardization organizations have shown significant interest in cognitive-radio networks. This is the case of ECMA, with standard 392 [30]. This standard defines a MAC and physical layer for cognitive use of TVWS (TV white space) in WLAN-like scenarios. It was released by ECMA international at the end of 2009. In addition to MAC and physical layer, ECMA-392 also includes specifications for the MUX sub-layer for higher-layer protocols. ECMA-392 was developed by technical committee TC48, task group TG1, and it is therefore also known as the ECMA TC48-TG1 standard. The standard is based on the contribution of the Cognitive Networking Alliance (CogNeA) [31], formed at the end of 2008 and composed of ETRI, Hewlett-Packard, Philips, and Samsung, the board; and Georgia Institute of Technology and Motorola, contributors. Texas Instruments was previously indicated as a member.

With similar scenarios and applications to ECMA, project IEEE P802.11.af was launched more recently, in December 2009 [32]. It is aimed at creating an amendment to IEEE 802.11 by modifying both the physical layer and MAC to meet the regulatory requirements for channel access and coexistence in the TV white space (TVWS). The group suggested the use of OFDM physical layers focused on 5 MHz channel width to comply with the 6, 7, or 8 MHz TV channels, depending on countries. Because this standard aims at operating outside the ISM band, no backward compatibility is required with former versions of IEEE 802.11, but it is not intended to go beyond 802.11a/g capacity in terms of achievable data rate. The main benefit of 802.11 WLANs in the TV white space is seen in the wider applicability of 802.11 to newly available spectrum portions, and the resulting increased commercial relevance. This project considers geo-location-based systems without sensing capabilities. This will be a significant difference from other TV-white-space-oriented standards (e.g., IEEE 802.22 or ECMA 392). This geo-location-based operation was made possible in the US by the second memorandum on TV white space "Super WiFi" operation [33].

With a wider application in mind, DYSPAN has suggested a new project to define physical layer and MAC for white spaces. These would be defined for a white-space dynamic-spectrum-access network, but do not build upon an existing standard. This project was submitted to NesCom as P1900.7. Approval is expected in early 2011.

In Europe, the ETSI Technical Committee on Reconfigurable Radio Systems (RRS) has defined a "Functional Architecture for the Management and Control of Reconfigurable Radio Systems" [34, 35], in order to

improve the utilization of spectrum and radio-resource usage. Different functional entities have been identified in the functional architecture (FA), including the dynamic spectrum management entity; the dynamic, self-organizing network-planning and management block; the joint radio-resource management entity;, and finally, the configuration-control module (CCM). This effort relates to the same objective as the objective of IEEE 1900.4, to define a global framework for cognitive-radio networks.

It can be understood from this list that standardization activity related to dynamic-spectrum-access networks is rather recent. It has evolved along with the decisions or trends at the regulation level, which is at the moment focused on TV white space operation [35, 36]. New groups are being created at a sustained pace, showing a very strong interest of stakeholders in this topic. Another interesting point that can be noticed concerns the organizations that express interest in dynamic-spectrum-access networks. Whereas classical telecommunication standardization bodies mainly gather telecom operators and vendors, dynamic-spectrum-access networks open the door to organizations that see dynamic-spectrum-access networks as a means to grant spectrum access with a non-traditional telecommunications business model. The members of the TV white-space coalition give a clear snapshot of this trend, with members such as Microsoft, Google, Dell, HP, Intel, Philips, Earthlink, and Samsung [37].

4. Measurements for the Identification of Spectrum Availability

Measurements of the radio environment can provide valuable insights into current spectrum usage. A proper understanding of spectrum-usage patterns can be very useful for defining adequate dynamic spectrum policies, and to identify appropriate frequency bands for the deployment of future cognitive-radio networks. Similarly, the identification of usage patterns can be exploited in the development of useful spectrum-usage models and more-efficient cognitive-radio techniques. Several measurement campaigns, covering both wide frequency ranges [38-43] as well as some specific licensed bands [44-48], have been performed in diverse locations and scenarios, in order to determine the degree to which allocated spectrum bands are occupied in real wireless-communication systems. This section provides a summary of the different spectrum-measurement methodologies, equipment, and metrics that are typically considered in such campaigns. Finally, it provides some hints on the applicability of measurement-based methodologies to the design of cognitive-radio networks.

4.1 Spectrum-Measurement Methodologies and Equipment

There are many factors that need to be considered when defining a strategy to meet a particular radio-spectrum occupancy-measurement need. Some basic dimensions to specify are [49] frequency (frequency span and frequency points to be measured), location (measurement-site selection), direction (antenna pointing angle), polarization (receiving antenna polarization), and time (sampling rate and measurement period). The measurement setup employed in the evaluation of spectrum occupancy should be designed by taking into account the previous factors, since they play a key role in the accuracy of the results obtained. The measurement setup should be able to detect a large number of transmitters of the most diverse nature over a wide range of frequencies, from narrowband to wideband systems, and from weak signals received near the noise floor to strong signals that may overload the receiving system.

Depending on the purposes of each specific study (e.g., broadband measurement campaigns, measurements over specific bands, temporal resolution targeted by the measurements, etc.), different configurations have been used in previous spectrum measurements. These have ranged from simple setups with a single antenna directly connected to a spectrum analyzer [47] to more-sophisticated designs [38, 40]. Different configurations between both extreme points may determine various tradeoffs between complexity and measurement capabilities.

Spectrum analyzers are one of the most commonly used pieces of equipment in the different measurement campaigns. This is because they usually allow measuring large bandwidths, although at the expense of limited time resolution, typically of the order of seconds, which might not be appropriate for certain levels of modeling. When higher time resolutions are required, other measurement platforms can be used. Examples include vector signal analyzers, or more-specific platforms, such as the universal software radio peripheral (USRP) and the GNU radio architecture. This measurement platform is able to perform spectrum measurements over bandwidths narrower than a spectrum analyzer, but with much higher time resolution, of the order of microseconds or nanoseconds. This provides not only power spectrum measurements, as it is the case with a spectrum analyzer, but true signal samples, from which the signal's phase information can be extracted. If only power measurements of the spectrum utilization are available – as in the case of spectrum-analyzer-based measurements – the energy-detection method, as described in Section 2, is the only possibility left.

With respect to the antenna equipment, when covering small frequency ranges or specific licensed bands, a single antenna may suffice. However, in broadband spectrum measurements, from a few MHz up to several GHz, two or more broadband antennas are required in order to cover the whole frequency range. Most spectrum-measurement campaigns are based on omnidirectional measurements, in order to detect primary signals coming from any direction. To this end, omnidirectional vertically polarized antennas are the most common choice.

4.2 Spectrum Occupancy Metrics

Another important methodological aspect in a measurement campaign is the specification of adequate metrics for evaluating and quantifying the level of spectral occupancy. While some of these metrics are directly provided by the measurement equipment, some others are obtained by post-processing the measured data. Some examples of metrics that have been typically used are the following.

4.2.1 Power Spectral Density

It is well known from Fourier theory that any time-domain electrical phenomenon can be expressed as the sum of one or more sine waves of appropriate frequency, amplitude, and phase. The power spectral density (PSD) of a signal is the graphical representation of its frequency content, with the abscissa being the frequency and the ordinate being the amplitude (the phase information is not captured by a spectrum analyzer). Power spectral density can be measured in different ways in order to obtain different power-spectral-density graphs; the main values used are the average power spectral density, the maximum power spectral density, and the minimum power spectral density. When considered together, the average, maximum and minimum power spectral densities provide a simple characterization of the temporal behavior of a channel. For example, if the results are quite similar, this would suggest a single transmitter that is always on and is experiencing a low level of fading, and so is also probably not moving. At the other extreme, a large difference among average, maximum, and minimum power spectral densities suggests more intermittent use of the spectrum, and therefore indicates a potential opportunity for cognitive-radio networks.

4.2.2 Spectral-Occupancy Percentage or Duty Cycle

The relevant metric for determining the degree to which spectrum is used in the temporal dimension is the spectral-occupancy percentage (or simply, the spectral occupancy), also referred to as the duty cycle. It is defined as the fraction of time that a given channel or frequency band is determined to be occupied by a licensed signal. Cognitive-radio networks may take advantage of idle-time periods to opportunistically access the available spectrum. Frequency bands with low duty cycles therefore offer an interesting opportunity for the deployment of cognitive-radio networks. When computing the duty cycle, an overall value for a given frequency band can be determined in order to quantify the degree to which spectrum is used by a certain licensed system, and hence identify the most interesting bands for the deployment of cognitive-radio networks. Nevertheless, the temporal evolution of this metric (e.g., averaged over one-hour periods or days) can also provide interesting information about the temporal utilization of the spectrum. Note that the detection of whether a frequency band is being used by a licensed user can be carried out by different sensing methods, providing different tradeoffs among required sensing time, complexity, and detection capabilities, as explained in Section 2.

4.2.3 Amplitude Probability Distribution (APD)

Key characteristics of the licensed system, such as signal bandwidth, transmitter mobility, and number of transmitters, can be easily estimated by evaluating the histogram of the received amplitude samples. This is known as the amplitude-probability-distribution (APD) analysis method [42]. The amplitude probability distribution is a three-dimensional histogram, with one axis being the amplitude, one axis being the frequency span, and the third axis being the probability of each amplitude value throughout the whole measurement period. The underlying principle of amplitude-probability-distribution analysis is that different equipment and devices show distinct behaviors in terms of power spectral density and signal characteristics. These transmitter characteristics can therefore be inferred from the statistical distribution of the amplitude probability. As an example, a single peak with narrow and sharp shape and large amplitude is associated with a fixed transmitter with rather constant power. The height and the width of the peak jointly describe the stability of the transmitted power. The higher and the narrower the peak, the more constant is the transmitted power. On the other hand, a single wide peak with large amplitude could represent a transmitter applying amplitude-modulation techniques or having mobility. A wider distribution with many peaks but small maximum amplitudes is associated with many devices received from different distances, or with a congregation of various services with distinct power regulations. Finally, in some cases the received power allows inferring the rough operating power of the transmitter directly from the amplitude-probability-distribution histogram.

4.3 Applicability to the Design of Cognitive Radio Systems

Empirical data derived from spectrum-occupancy measurement campaigns exhibit a wide set of useful applications for the design of cognitive-radio systems. These range from the simplification of analytical studies, up to the development of new techniques and algorithms for dynamic spectrum access, or simulation tools based on these models. Real field-measurement data could then be used as the support for the evaluation of different cognitive-radio mechanisms proposed in the literature, which in most cases have addressed only a system-level approach.

Cognitive-radio network operation can be optimized by making use of databases capturing the knowledge about the radio environment of a given geographical area, including elements such as geographical aspects, available

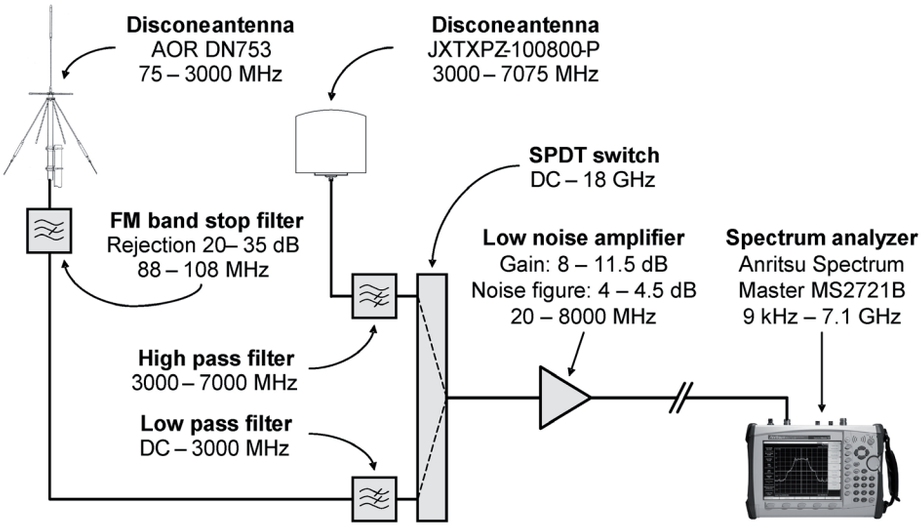

Figure 3. The measurement setup employed in this study (complete schematic).

services, spectral regulations, positioning of transmitters, transmitter profiles, primary user activity patterns, etc. The term radio-environment map (REM) was used in [50] to refer to such a database, used as the support of a cognitive-radio network. It can be clearly envisaged that through adequate feeding of the radio-environment map through results coming from measurements, it could be possible to improve the accuracy of its information. With the corresponding dissemination procedures to make this information available to cognitive-radio nodes (which could eventually combine the information with their own spectrum-sensing results), it would be possible to improve the performance of the decision-making procedures in a cognitive-radio network.

Similarly, measurements can be used for the characterization of the level of spectral occupation in the frequency, time, and space dimensions. This can enable the formulation of models to describe the utilization and activity patterns of the different frequency bands with a high level of accuracy. When addressing the definition of spectrum-occupation models, there are three main elements to define. The first element is the set of parameters, characteristics, or properties of the spectrum occupation to be represented and reproduced through the model. This can be the duration of the activity/inactivity periods of the different channels as well as their corresponding probability distributions, the fraction of time that the channels remain occupied, the distribution of occupation among channels of the same band, the distribution of the occupation in a given geographical area and the corresponding spatial correlations, the evolution of the power level present in the different channels of a given band, etc. The formulation of a new spectrum-occupation model should also identify the set of tools used to carry out the modeling. It is then possible to distinguish among models based on Markov chains, or based on fitting curves to specific parameterized analytical expressions, or based on probability density functions, stochastic processes, random fields, time series, etc. Finally, another important aspect to take into account is the information provided by this model, which refers either to the behavior of the abovementioned parameters or to other system level aspects, such as the time evolution of the instantaneous spectrum occupation for different frequency channels or geographical areas.

One of the simplest and most widely used temporal spectrum-occupation models is the first-order Markov model with idle and busy states [51-53]. It can be easily parameterized by means of empirical measurements, as was done in [52] for the ISM band of 2.4 GHz using a vector signal analyzer over specific types of traffic, or in [53] using a spectrum analyzer. In the latter case, the target was to find out the statistical distributions that best fit the idle and busy periods for different technologies, and it was shown that a geometrical distribution can fit the actual measurements in a quite acceptable way for many of the considered technologies. It was also shown that in some cases, there exists a correlation between the durations of the idle and busy periods. Works such as [54] and [55] tried to qualitatively reproduce this. One of the aspects identified in current empirical models is that distributions usually depend strongly on the time resolution of the measurements. In that sense, the extension of existing models to reproduce at least two different levels of time resolution can be envisaged, one level for an instantaneous channel occupation using high-time-resolution models (e.g., using vector analyzers), and a second level able to reproduce the load variations in a longer-term time scale (e.g., using spectrum analyzers). The modeling in this case could be based on Markov models, but also on other techniques, such as random walks [56] or time series [57]. Similarly, in [58], Fourier analysis was used to identify periodicities in the spectral-occupation patterns that could be used to decide the appropriate sensing instants.

As for the modeling of spectral occupation in the frequency dimension, one of the first models was the Laycock-Gött model [59], which tried to capture the duty cycle of different channels in the HF band. While this

model was acceptable for the large coverage areas existing in the HF band and thus the observed pattern could fit large geographical areas, the generalization to other bands with smaller coverage areas and more variability in the occupation depending on the position was hardly feasible. In that sense, another model in the context of cognitive radio was developed in [60] and further extended in [53]. It analyzed the statistical distribution of the duty cycle among channels belonging to the same band, and proposing to model it through a modified beta function, which also showed a good fit when applied to bands assigned to different technologies.

Finally, in the area of spatial-dimension modeling in [56], the spatial distribution of the spectral occupation in a real cellular system was analyzed based on monitoring the call-arrival rates and making use of variograms to obtain the variability of the spectrum spatial occupation among sectors of a given cell. In [61], the spatial characterization of the spectrum occupancy through power-spectral-density measurements was carried out by making use of the random field theory. The procedure makes use of empirical power-spectral-density measurements at different points to adjust a semi-variogram model, which reproduces the statistical properties of the average power-spectral-density values observed in a certain geographical area.

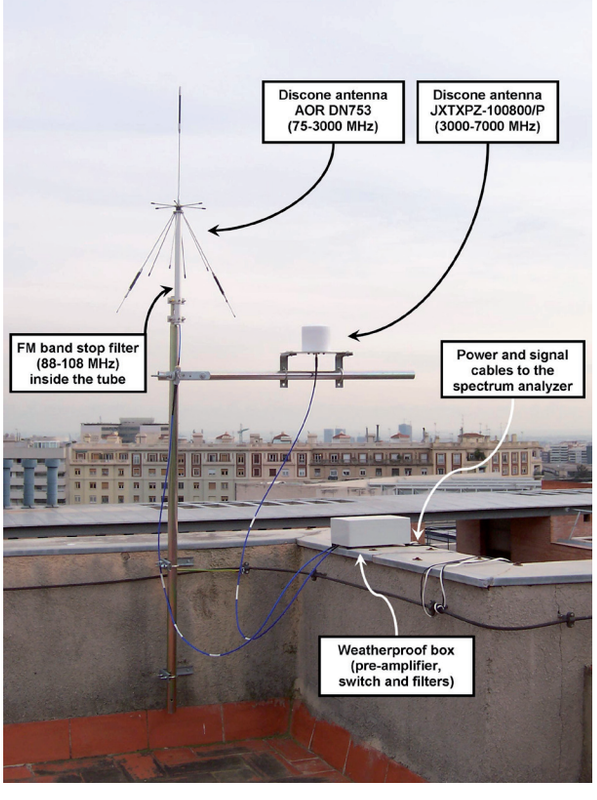

Figure 4. The measurement setup employed in this study (antenna subsystem).

5. Measurement Case Study in the Urban Area of Barcelona

This section presents a case study of spectral-occupation measurements in the urban area of Barcelona, with the objective of illustrating the methodologies described in the previous section with real measurements.

5.1 Measurement Setup and Configuration

The measurement configuration employed relied on a spectrum analyzer, to which various external devices were attached in order to improve the detection capabilities of the system, and hence to obtain more-accurate and reliable results. The design was composed of two broadband antennas that covered the frequency range from 75 to 7075 MHz, a switch to select the desired antenna, several filters to remove undesired signals, a low-noise preamplifier to enhance the overall sensitivity and thus the ability to detect weak signals, and a high-performance spectrum analyzer to record the spectral activity. A simplified schematic with all the devices and their main technical features is shown in Figure 3.

The antenna subsystem is shown in Figure 4. Two wideband discone-type antennas were used to cover the frequency range from 75 to 3000 MHz (AOR DN753) and 3000 to 7075 MHz (A-INFO JXTXPZ-100800/P). Discone antennas are wideband antennas with vertical polarization and an omnidirectional receiving pattern in the horizontal plane. Even though some transmitters are horizontally polarized, they usually are high-power stations (e.g., TV stations) that can be detected even with vertically polarized antennas. The exceptionally wideband coverage (allowing a reduced number of antennas in broadband spectrum studies) and the omnidirectional feature (allowing the detection of primary signals coming for any direction) make discone antennas attractive in radio-scanning and monitoring applications. They have been a preferred option for many spectrum studies.

The radio-frequency (RF) subsystem performed antenna selection, filtering, and amplification. The desired antenna was selected by means of a single-pole double-throw (SPDT) switch, which enabled high isolation (90-100 dB) and low insertion loss (0.1-0.2 dB). In order to remove undesired signals, three filters were included. A band-stop filter blocked signals in the frequency range of frequency-modulation (FM) broadcast stations (87.5-108 MHz). Usually, such stations are high-power transmitters that may induce overload in the receiver, thus degrading the receiver's performance by an increased noise floor or by the presence of spurious signals, which inhibits the receiver's ability to detect the presence of weak signals. Since the FM band is of presumably low interest for secondary use, due to its usually high transmission power and expected high occupancy rate, an FM band-stop filter was employed in order to remove

Parameter	Value	
Frequency range	75-3000 MHz	3000-7075 MHz
Frequency span	45-600 MHz	
Frequency bin	81.8-1090.9 kHz	
Resolution BW	10 kHz	
Video BW	10 kHz	

Table 1a. The spectrum analyzer configuration: frequency.

Parameter	Value	
Built-in pre-amp	Deactivated	Activated
Reference level	– 20 dBm	– 50 dBm
Reference level offset	0 dB	– 20 dB
Scale	10 dB/division	
Input attenuation	0 dB	
Detection type	Average (rms) detector	

Table 1c. The spectrum analyzer configuration: amplitude.

FM signals and to avoid overload problems, improving the detection of weak signals at other frequencies. Low-pass and high-pass filters were used to remove out-of-band signals, and to reduce the potential creation of intermodulation products. To compensate for device and cable losses and increase the system's sensitivity, a low-noise preamplifier was included. The selected mid-gain amplifier provided significant sensitivity improvement, while guaranteeing the spurious-free dynamic range (SFDR) required by the measured signals.

An Anritsu Spectrum Master MS2721B high-performance handheld spectrum analyzer was used to provide power-spectrum measurements, and to record the spectral activity over the complete frequency range. It provided a measurement range from 9 kHz to 7.1 GHz, a low noise level, a built-in preamplifier that facilitated the detection of weak signals, an automatically adjusted fast sweep speed, and the possibility of connecting an external USB storage device to save measurements for later data post-processing.

Since the different operating modes of spectrum analyzers can significantly alter the results of the measurement, proper parameter selection is crucial to produce valid and meaningful results. The different parameters of the spectrum analyzer were set according to the basic principles of spectrum analysis, as well as some particular considerations specific to cognitive radio. Table 1 shows the main spectrum-analyzer configuration parameters.

The measured frequency range (75-7075 MHz) was divided into 25 blocks, with variable sizes ranging from 45 MHz up to 600 MHz. The division was performed following the local Spanish governmental spectrum allocations [63], and taking into account the transmitted signal bandwidth for each band (for example, frequency bins

Parameter	Value
Measurement period	24 hours
Sweep time	Auto

Table 1b. The spectrum analyzer configuration: time.

of 81.8 kHz were used to measure 200 kHz GSM channels, while 745.5 kHz and 727.3 kHz bins were employed for 8 MHz TV and 5 MHz UMTS channels, respectively).

The resolution bandwidth (RBW) played an important role in the measurements obtained. Narrowing the resolution bandwidth increased the ability to resolve signals in frequency and reduced the noise floor (increasing the sensitivity), at the cost of an increased sweep time and, hence, a longer measurement period. Based on the results presented in [62], a 10 kHz resolution bandwidth was selected as an adequate tradeoff between detection capabilities and required measurement time. The video bandwidth (VBW) is a smoothing function that dates to analog spectrum analyzers, but is now nearly obsolete. To eliminate this analog form of averaging, the video bandwidth was set equal to the resolution bandwidth.

Each one of the 25 subbands considered in this work was measured during 24 hours. The number of recorded traces/sweeps during such a measurement period is a function of the sampling rate (i.e., the sweep time), which was automatically adjusted by the spectrum analyzer according to various configuration parameters, including the frequency span. For example, for the configuration parameters shown in Table 1, the spectrum analyzer employed swept at an approximate average speed of 25 ms/MHz. This led to average sweep times ranging from around one second for a 45 MHz span to around 15 seconds for a 600 MHz span.

For measurements below 3 GHz, where some overloading signals might have been present, only the external amplifier was used. For measurements above 3 GHz, where the received powers were lower, both the external and the spectrum analyzer's internal amplifier were employed, resulting in a noise-floor reduction of 20 dB. To simplify the data post-processing, the noise-floor values in the 75-3000 MHz and 3000-7075 MHz bands were equalized by adding a 20 dB offset to the power levels measured between 3000-7075 MHz (reference-level offset). The reference level (the maximum power of a signal that entered the spectrum analyzer and could be measured accurately) was then been adjusted according to the maximum power observed in each region, while the scale was adjusted according to the minimum signal level. No input attenuation was employed. An average-type detector was used. This detector averaged all the power levels sensed in one frequency bin, in order to provide a representative power level for each measured frequency bin.

5.2 Measurement Scenario

Most of the existing spectrum-occupancy studies were based on measurements performed in outdoor environments and, more particularly, on outdoor high points, such as building roofs, balconies, and towers. The main advantage of high points is that they provide direct line-of-sight to many kinds of primary transmitters, and therefore enable a more-accurate measurement of their actual spectral activity. Nevertheless, this scenario may not be representative of the spectrum occupancy that would be perceived by a cognitive-radio terminal in many other interesting practical situations where the secondary user is not placed on a static high point (e.g., a mobile cognitive-radio user communicating inside a building, or while walking in the street between buildings). The measurement of real network activities in additional scenarios of practical significance is therefore necessary for an adequate and full understanding of the dynamic use of spectrum.

The different geographical locations considered in this case study are illustrated in Figure 5. For outdoor high-point measurements (location 1), the equipment was placed on the roof of a three-floor urban building, belonging to the Department of Signal Theory and Communications of the Universitat Politècnica de Catalunya (UPC), Barcelona, Spain (latitude 41° 23' 20" north; longitude 2° 6' 43" east; altitude, 175 m). The selected place was a strategic location, with direct line-of-sight to several transmitting stations located a few tens or hundreds of meters away from the antenna, and without buildings blocking the radio propagation. This strategic location enabled us to accurately measure the spectral activity of (among others) TV broadcast stations, several nearby base stations for cellular mobile communications, and a military headquarters, as well as some maritime and aeronautical transmitters, due to the relative proximity to the harbor and the airport. For indoor experiments, the measurement equipment was placed inside the same building (location 2), on the middle floor. For measurements in narrow streets (locations 3 to 7), between buildings (locations 8 to 10), and open areas (locations 11 and 12), the measurement equipment was moved within the UPC's campus.

5.3 Spectrum-Occupancy Results

The measurement results obtained are summarized in Table 2. As can be appreciated for the results of location 1, the spectrum experienced relatively moderate usage below 1 GHz and low usage between 1 GHz and 2 GHz, while remaining mostly underutilized between 2 and 7 GHz. In fact, while the average duty cycle between 75 and 2000 MHz was 31.02%, the value for this parameter between 2000 and 7075 MHz was only 2.75%. The overall average duty cycle over the whole frequency range considered in this study was only 17.78% for location 1, which revealed the existence of significant amounts of unused spectrum, which could potentially be exploited by future cognitive-radio networks. When considering other deployment scenarios, the results were even more promising. The comparison of

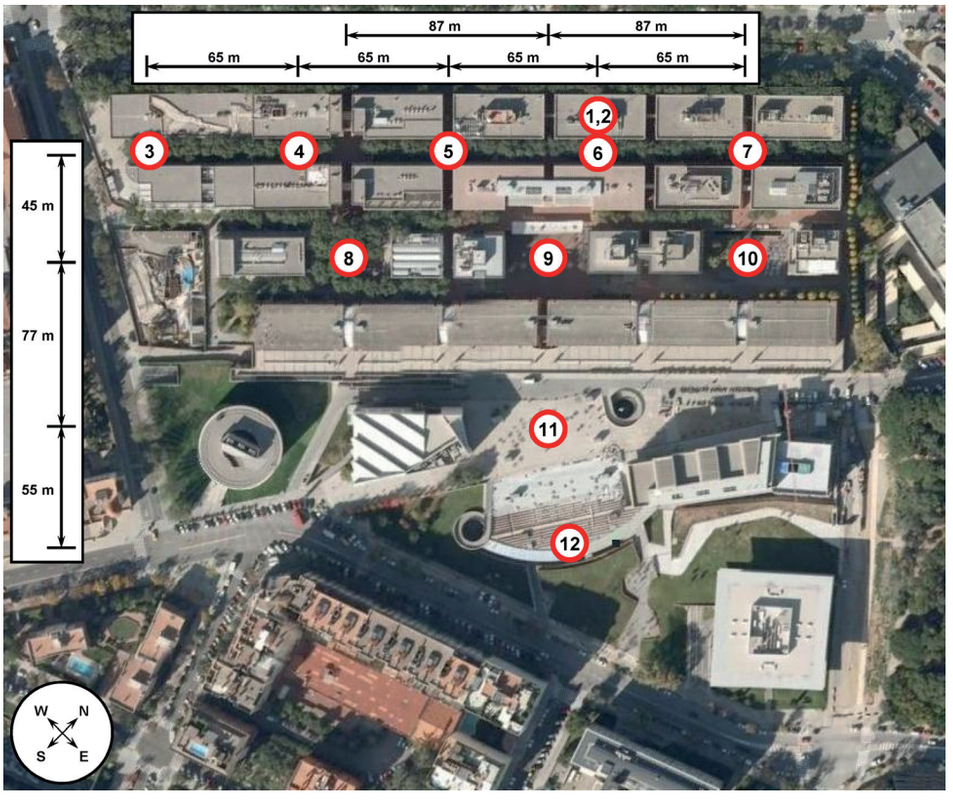

Figure 5. The measurement locations and scenarios in the urban environment.

Frequency Range (MHz)	Average Duty Cycle (%)					
	Loc. 1	Loc. 2	Loc. 1	Loc. 2	Loc. 1	Loc. 2
75 - 1000	42.00	33.70	31.02	21.54	17.78	12.10
1000 - 2000	13.30	1.94				
2000 - 3000	3.73	1.63	2.75	1.39		
3000 - 4000	4.01	1.44				
4000 - 5000	1.63	1.09				
5000 - 6000	1.98	1.34				
6000 - 7075	1.78	1.38				

Table 2. The average duty-cycle statistics in locations 1 and 2.

the results obtained for locations 1 (outdoor) and 2 (indoor) constituted an illustrative example (see Table 2). From a qualitative point of view, the results obtained in location 2 followed the same trend as in location 1, with higher duty cycles at lower frequencies. As a matter of fact, the average spectrum occupancy was moderate below 1 GHz and very low above 1 GHz for location 2. However, significantly lower average occupancy rates were observed for the indoor location, which could be explained by the fact that most of the wireless transmitters were located outdoors, and the propagation loss due to outdoor-to-indoor signal penetration led to lower signal strengths in the indoor scenario, thus resulting in lower occupancy rates. The lower average duty cycles obtained for the indoor case suggested the existence of an even higher amount of free spectrum for cognitive radio in such environments.

The previous results indicated that the amount of spectrum opportunities could be related to the radio-propagation conditions. This could be corroborated by analyzing the spectrum-occupancy level perceived at various locations. In that respect, Figure 6 plots the duty cycle in different locations for the case of TV bands. The duty-cycle values were normalized with respect to the value at location 1. It could be appreciated that this normalized average duty cycle observed at each location was lower than one, meaning that the perceived spectrum occupancy was lower in closed regions. For example, in locations 4 and 6, where radio-propagation blocking caused by buildings was more intense, the normalized duty cycle was lower than in other more open areas, such as locations 3, 5, and 7. Comparing locations 8, 9, and 10, the deepest and most faded region (location 9) exhibited the lowest normalized average duty cycle. Regarding the open areas (locations 11 and 12), the normalized duty cycle was in general higher than in the rest of the outdoor locations at the ground level. In this case, it was interesting to note that a higher spectral-activity level was recorded in location 11 with respect to the open region in location 12, despite the presence of some surrounding buildings. The detection by the measurement equipment of some additional signal components reflected in such buildings could explain the recording of higher activity levels in a less-open region. In any case, it was interesting to observe that the number of spectrum opportunities could be directly related to the radio-propagation conditions of the considered scenario, with lower occupancy rates observed in more-closed regions, and vice versa.

Although the previous results clearly indicated low spectrum-utilization levels, they did not provide a clear picture of how spectrum was used in different frequency bands allocated to different specific services. Figure 7 summarizes the band-by-band average spectrum-occupancy statistics observed at location 1. The results obtained demonstrated that some spectrum bands were subject to intensive usage, while some others showed moderate utilization levels, some were sparsely used, and, in some cases, some were not used at all. The highest occupancy rates were observed for bands allocated to broadcast services (TV as well as analog and digital audio), followed by digital cellular services as PMR/PAMR, paging, and mobile cellular communications (E-GSM 900, DCS 1800, and UMTS), among others. Other services and applications, e.g., aeronautical radio navigation and location or defense systems, showed different occupancy rates, depending on the considered allocated band. In general, the average spectrum occupancy observed in frequency and time in this study was found to be significantly low. This indicated that most of the spectrum offered possibilities for secondary cognitive-radio usage, even in those bands with the highest observed activity levels in terms of average duty cycle.

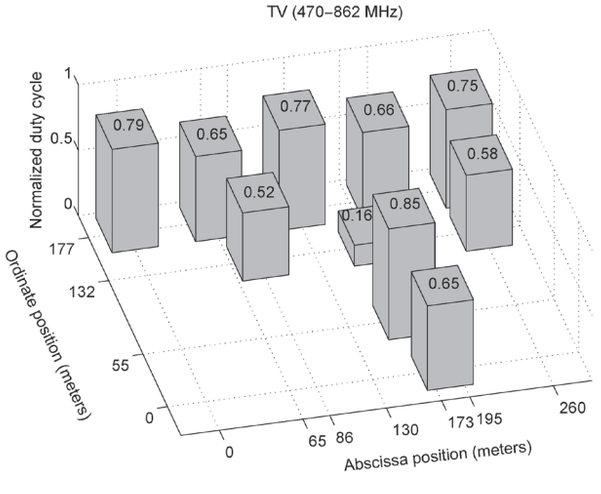

Figure 6. The normalized average duty-cycle statistics in locations 3 to 12 for the TV band (470-862 MHz). From left-to-right and up-to-down, the positions of the bars in each graph correspond to the physical locations of points 3 to 12. The duty cycle at each location was normalized to that of location 1.

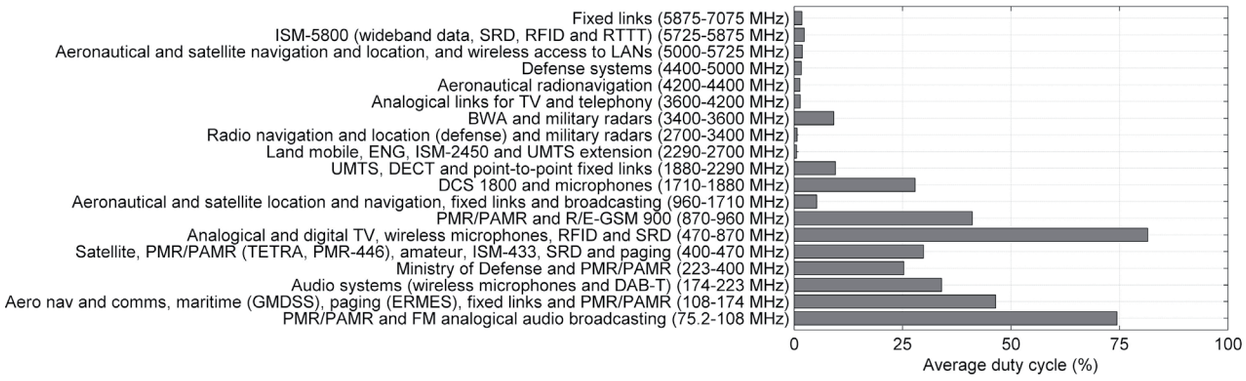

Figure 7. The band-by-band average duty cycle statistics.

6. Conclusions

Dynamic-spectrum-access networks are the topic of one of the current active research areas in the wireless community. They aim at enhancing spectrum efficiency by dynamically allocating underutilized spectrum. Regulation and etiquette implies that dynamic-spectrum-access networks can only operate provided that no harmful interference is caused to the other incumbents. One of the key enabling technologies for this paradigm is cognitive radio, envisaging a radio able to sense and be aware of its operational environment and to accordingly dynamically and autonomously adjust its parameters. Under this framework, this paper has focused on the applicability of measurement-based techniques in the design of cognitive-radio networks. In particular, it has first focused on the spectrum sensing through which secondary users can detect the presence or absence of a primary system in a given band. An overview of the most usual spectrum-sensing techniques, namely matched filter, energy, or power detection, and detection using cyclostationarity properties, has been given. The paper then presented a summary of the main standardization activities that have addressed the cognitive-radio network concept worldwide.

Measurements of the radio environment can provide valuable insights into how the spectrum is used in the different bands and locations. By a proper understanding of the primary-user behavior, it is possible to devise efficient mechanisms for cognitive-radio-network operation, for example by building databases in which different primary-user characteristics are stored and made available to the cognitive-radio users. This information can be combined with the results of real-time spectrum sensing to improve the performance of the different decision-making mechanisms. This paper presented some of the methodological factors for defining a spectrum-occupancy measurement campaign, including the possible equipment, as well as some significant metrics. This was illustrated with a case study corresponding to an urban area, analyzing the primary-user occupation in different bands from 75 MHz to 7 GHz. Measurements revealed that the number of spectrum opportunities can be directly related to the radio-propagation conditions of the scenario considered, with lower occupancy rates observed in more closed regions, and vice versa.

7. Acknowledgements

This work was supported by the European Commission in the framework of the FP7 Network of Excellence in Wireless COMmunications NEWCOM++ (contract no. 216715).

8. References

1. Federal Communications Commission (FCC), "Notice of Proposed Rule Making," ET Docket No. 04-113, May 2004.

2. J. Mitola III and G. Q. Maguire, "Cognitive Radio: Making Software Radios more Personal," *IEEE Personal Communications*, **6**, 4, August, 1999, pp. 13-18.

3. J. Mitola, *Cognitive Radio: An Integrated Agent Architecture for Software Defined Radio*, PhD dissertation, May 2000, Royal Institute of Technology, Sweden.

4. I. F. Akyildiz, W. Y. Lee, M. C. Vuran, and S. Mohanty, "Next Generation/Dynamic Spectrum Access/Cognitive Radio Wireless Networks: A Survey," *Computer Networks*, **50**, 13, September 2006, pp. 2127-2159.

5. J. Pérez-Romero, O. Sallent, R. Agustí, and L. Giupponi, "A Novel On-Demand Cognitive Pilot Channel enabling Dynamic Spectrum Allocation," Proceedings of the IEEE Symposium on New Frontiers in Dynamic Spectrum Access Networks (DySPAN), April 2007, pp. 46-54.

6. I. F. Akyildiz, W. Y. Lee, and K. R. Chowdhury "Spectrum Management in Cognitive Radio Ad Hoc Networks," *IEEE Networks*, **23**, 4, July/August 2009, pp. 6-12.

7. L. Berlemann and S. Mangold, *Cognitive Radio and Dynamic Spectrum Access*, New York, John Wiley and Sons, 2009.

8. A. Sahai and D. Cabric, "A Tutorial on Spectrum Sensing: Fundamental Limits and Practical Challenges," Proceedings of the IEEE Symposium on New Frontiers in Dynamic Spectrum Access Networks (DySPAN), November 2005.

9. D. Noguet (ed.), "Sensing Techniques for Cognitive Radio – State of the Art and Trends," April 2009, available at http://grouper.ieee.org/groups/scc41/6/ documents/white_papers/P1900.6_WhitePaper_Sensing_final.pdf.

10. J. G. Proakis, *Digital Communications, Third Edition*, New York, McGraw-Hill, 1995.

11. D. Cabric, S. M. Mishra, and R. W. Brodersen, "Implementation Issues in Spectrum Sensing for Cognitive Radios," Proceedings of Asilomar Conference on Signals, Systems, and Computers, **1**, November 2004, pp. 772-776.

12. H. Urkowitz, "Energy Detection of Unknown Deterministic Signals," *Proceedings of the IEEE*, **55**, 4, April 1967, pp. 523-531.

13. W. A Gardner, *Statistical Spectral Analysis: A Nonprobabilistic Theory*, Englewood Cliffs, New Jersey, Prentice-Hall, 1988.

14. W. A. Gardner, "Spectral Correlation of Modulated Signals: Part I – Analog Modulation," *IEEE Transactions on Communications*, **35**, 6, June 1987, pp. 584-594.

15. W. A. Gardner, W. Brown, and C. K. Chen, "Spectral Correlation of Modulated Signals: Part II – Digital Modulation," *IEEE Transactions on Communications*, **35**, 6, June 1987, pp. 595-601.

16. V. Turunen, M. Kosunen, S. Kallioinen, A. Pärssinen, and J. Ryynänen, "Spectrum Estimator and Cyclostationary Detector for Cognitive Radio," Proceedings of the European Conference on Circuit Theory and Design (ECCTD), Antalya, Turkey, August 2009.

17. Y. Tachwali, M. Chmeiseh, F. Basma, and H. H. Refai, "A Frequency Agile Implementation for IEEE 802.22 Using Software Defined Radio Platform," Proceedings of the IEEE Global Telecommunications Conference (GLOBECOM), New Orleans, LA, November 2008.

18. J. Lunden, V. Koivunen, A. Huttunen, and H. Vincent Poor, "Spectrum Sensing in Cognitive Radios Based on Multiple Cyclic Frequencies," July 2007, available at http://arxiv.org/abs/0707.0909.

19. P. Jallon, "A Spread Signals Detection Algorithm Based on the Second Order Statistics in Semi-Blind Contexts," Proceedings of the Cognitive Radio Oriented Wireless Networks and Communications (CROWNCOM) Conference, Singapore, May, 2008.

20. D. Noguet, L. Biard, and M. Laugeois, "Cyclostationarity Detectors for Cognitive Radio; Architectural Tradeoffs," EURASIP Journal on Wireless Communications and Networking, July 2010.

21. L. Biard, D. Noguet, T. Gernandt, P. Marques, and A. Gameiro, "A Hardware Demonstrator of an Opportunistic Radio System Using Temporal Opportunities," Proceedings of the Cognitive Radio Oriented Wireless Networks and Communications (CROWNCOM) Conference, Hanover, June 2009.

22. "IEEE 802.15 WPAN Low Rate Alternative PHY Task Group 4a (TG4a)," available at http://www.ieee802.org/15/pub/TG4a.html.

23. C. R. Stevenson, G. Chouinard, Z. Lei, W. Hu, S. J. Shellhammer, and W. Caldwell, "IEEE 802.22: The First Cognitive Radio Wireless Regional Area Network Standard," *IEEE Communications Magazine*, **47**, 1, January 2009, pp. 130-138.

24. "802.22, Wireless Regional Area Networks (WRANs)," available at http://www.ieee802.org/22/.

25. "FCC Adopts Rules for Unlicensed Use of Television White Spaces, Official Announcement of FCC," November 2008, available at http://www.ffc.gov.

26. IEEE Standard Coordinating Committee 41 home page, http://www.scc41.org.

27. "1900.1-2008 IEEE Standard for IEEE Standard Definitions and Concepts for Dynamic Spectrum Access: Terminology Relating to Emerging Wireless Networks, System Functionality, and Spectrum Management," 2008.

28. "1900.2-2008 IEEE Recommended Practice for the Analysis of In-Band and Adjacent Band Interference and Coexistence Between Radio Systems," 2008.

29. "1900.4-2009 IEEE Standard for Architectural Building Blocks Enabling Network-Device Distributed Decision Making for Optimized Radio Resource Usage in Heterogeneous Wireless Access Networks," 2009.

30. "Final Draft Standard ECMA-392 – MAC and PHY for Operation in TV White Space," 2009, available at http://www.ecma-international.org/publications/files/ drafts/tc48-2009-061.doc.

31. http://www.cognea.org.

32. "IEEE P802.11.af," February, 2010, available at IEEE 802.11 Documents, https://mentor.ieee.org/ 802.11/documents?is_group=00af.

33. FCC-10-174, "Unlicensed Operation in the TV Broadcast Bands," Federal Communications Commission (FCC) Second Memorandum Opinion and Order, September 2010, available at http://www.fcc.gov.

34. ETSI TR 102 682 "Functional Architecture for the Management and Control of Reconfigurable Radio Systems."

35. M. Mueck and D. Noguet, "TV White Space Standardization and Regulation in Europe," Proceedings of the 2nd International Conference on Wireless Communications, Vehicular Technology, Information Theory and Aerospace and Electronics Systems Technology (VITAE), Chennai, India, February 2011.

36. D. Noguet, R. Datta, P. H. Lehne, M. Gautier, and G. Fettweis, "TVWS regulation and QoSMOS requirements," Proceedings of the 2nd International Conference on Wireless Communications, Vehicular Technology, Information Theory and Aerospace and Electronics Systems Technology (VITAE), Chennai, India, February 2011.

37. E. Bangeman, "The White Spaces Coalition's Plans for Fast Wireless Broadband: The Technology," *Ars Technica*, April 2007, available at http://arstechnica.com/hardware/news/2007/04/white-space.ars.

38. F. H. Sanders, "Broadband Spectrum Surveys in Denver, CO, San Diego, CA, and Los Angeles, CA: Methodology, Analysis, and Comparative Results," Proceedings of the IEEE International Symposium on Electromagnetic Compatibility, Rome, Italy, August 1998.

39. M. A. McHenry, P. A. Tenhula, D. McCloskey, D. A. Roberson, and C. S. Hood, "Chicago Spectrum Occupancy Measurements & Analysis and a Long-term Studies Proposal," Proceedings of

the 1st International Workshop on Technology and Policy for Accessing Spectrum (TAPAS), Boston, MA, USA, August 2006.

40. A. Petrin and P. G. Steffes, "Analysis and Comparison of Spectrum Measurements Performed in Urban and Rural Areas to Determine the Total Amount of Spectrum Usage," Proceedings of International Symposium on Advanced Radio Technologies (ISART), Boulder, CO, USA, March 2005.

41. R. I. C. Chiang, G. B. Rowe, and K. W. Sowerby, "A Quantitative Analysis of Spectral Occupancy Measurements for Cognitive Radio," Proceedings of the 65th IEEE Vehicular Technology Conference in Spring (VTC'07 Spring), Dublin, Ireland, April 2007.

42. M. Wellens, J. Wu, and P. Mähönen, "Evaluation of Spectrum Occupancy in Indoor and Outdoor Scenario in the Context of Cognitive Radio," Proceedings of the 2nd International Conference on Cognitive Radio Oriented Wireless Networks and Communications (CROWNCOM), Orlando, FL, USA, July 2007.

43. M. López-Benítez, F. Casadevall, A. Umbert, J. Pérez-Romero, R. Hachemani, J. Palicot, and C. Moy, "Spectral Occupation Measurements and Blind Standard Recognition Sensor for Cognitive Radio Networks," Proceedings of the 4th International Conference on Cognitive Radio Oriented Wireless Networks and Communications (CROWNCOM), Hanover, June 2009.

44. P. G. Steffes and A. J. Petrin, "Study of Spectrum Usage and Potential Interference to Passive Remote Sensing Activities in the 4.5 cm and 21 cm Bands," Proceedings of the IEEE International Geoscience and Remote Sensing Symposium (IGARSS 2004), **3**, September 2004, pp. 1679-1682.

45. J. Do, D. M. Akos, and P. K. Enge, "L and S Bands Spectrum Survey in the San Francisco Bay Area," Proceedings of the Position Location and Navigation Symposium (PLANS 2004), April 2004, pp. 566-572.

46. M. Biggs, A. Henley, and T. Clarkson, "Occupancy Analysis of the 2.4 GHz ISM Band," *IEE Proceedings on Communications*, **151**, 5, October 2004, pp. 481-488.

47. S. W. Ellingson, "Spectral Occupancy at VHF: Implications for Frequency-Agile Cognitive Radios," Proceedings of the IEEE 62nd Vehicular Technology Conference (VTC 2005-Fall), **2**, September 2008, pp. 1379-1382.

48. S. D. Jones, E. Jung, X. Liu, N. Merheb, and I. J. Wang, "Characterization of Spectrum Activities in the U.S. Public Safety Band for Opportunistic Spectrum Access," Proceedings of the 2nd IEEE International Symposium on New Frontiers in Dynamic Spectrum Access Networks (DySPAN 2007), April 2007, pp. 137-146.

49. R. J. Matheson, "Strategies for Spectrum Usage Measurements," Proceedings of the IEEE International Symposium on Electromagnetic Compatibility (EMC 1988), August 1988, pp. 235-241.

50. Y. Zhao, B. Le, and J. H. Reed, "Network Support – The Radio Environment Map," *Cognitive Radio Technology*, New York, Elsevier, 2006.

51. Q. Zhao, L. Tong, A. Swami, and Y. Chen, "Decentralized Cognitive MAC for Opportunistic Spectrum Access in Ad Hoc Networks: A POMPD Framework," *IEEE Journal on Selected Areas in Communications*, **25**, 3, April 2007, pp. 580-600.

52. S. Geirhofer, L. Tong, and B. M. Sadler, "Dynamic Spectrum Access in the Time Domain: Modeling and Exploiting White Space," *IEEE Communications Magazine*, **45**, 5, May 2007, pp. 66-72.

53. M. Wellens, J. Riihijärvi, and P. Mähönen, "Empirical Time and Frequency Domain Models of Spectrum Use," *Elsevier Physical Communication*, **2**, 1-2, March 2009, pp. 10-32.

54. S. Pagadarai and A. M. Wyglinski, "A Quantitative Assessment of Wireless Spectrum Measurements for Dynamic Spectrum Access," Proceedings of the 4th International Conference on Cognitive Radio Oriented Wireless Networks and Communications (CROWNCOM 2009), Hanover, June 2009, pp. 1-5.

55. M. Wellens, J. Riihijärvi, and P. Mähönen, "Modelling Primary System Activity in Dynamic Spectrum Access Networks by Aggregated ON/OFF-processes," Proceedings of the IEEE Workshop on Networking Technologies for Software Defined Radio Networks (SDR), June 2009.

56. D. Willkomm, S. Machiraju, J. Bolot, and A. Wolisz, "Primary Users in Cellular Networks: A Large-Scale Measurement Study," Proceedings of the 3rd IEEE Symposium on New Frontiers in Dynamic Spectrum Access Networks (DySPAN 2008), October 2008, pp. 1-11.

57. Z. Wang and S. Salous, "Spectrum Occupancy Statistics and Time Series Models for Cognitive Radio," *Journal of Signal Processing Systems*, March, 2009.

58. M. Wellens, A. de Baynast, and P. Mähönen, "Performance of Dynamic Spectrum Access Based on Spectrum Occupancy Statistics," *IET Communications*, **2**, 6, July, 2008, pp. 772-782.

59. P. J. Laycock, M. Morrell, G. F. Gött, and A. R. Ray, "A Model for HF Spectral Occupancy," Proceedings of the Fourth International Conference on HF Radio Systems and Techniques, 1988.

60. M. Wellens and P. Mähönen, "Lessons Learned from an Extensive Spectrum Occupancy Measurement Campaign and a Stochastic Duty Cycle Model," *Springer Mobile Networks and Applications*, **15**, 3, August 2009, pp.461-474.

61. J. Riihijärvi, P. Mähönen, M. Wellens, and M. Gordziel, "Characterization and Modelling of Spectrum for Dynamic Spectrum Access with Spatial Statistics and Random Fields," Proceedings of the IEEE International Workshop on Cognitive Radios and Networks (CRNETS), September 2008.

62. M. López-Benítez and F. Casadevall, "Methodological Aspects of Spectrum Occupancy Evaluation in the Context of Cognitive Radio," Proceedings of the 15th European Wireless Conference (EW 2009), May 2009, pp. 199-204.

63. Secretaría de Estado de Telecomunicaciones y para la Sociedad de la Información (State Agency for Telecommunications and Information Society), "Cuadro Nacional de Atribución de Frecuencias (Table of National Frequency Allocations)," Spanish Ministry of Industry, Tourism and Commerce, November 2007.

A Review of the Major Developments in Our Understanding of Electric Antennas in Space Plasmas

H. Gordon James

Abstract

Salient ideas in the history of the science of dipoles as an important part of space radio science are reviewed. From the onset of the space age, the study of spontaneous radio emissions in geospace has required accurate measurements of wave electric fields. This review starts with the work done early in the space age on distributed dipole behavior in cold magnetoplasmas. Evidence of the effects of hot-plasma wave modes and of the response of space plasma excited by active antennas led to a broadening of the dipole theory, to include the generation and detection of electrostatic waves. The observations of plasma nonlinearities during the operation of active dipoles required further explanation. Indications of nonlinearity included spectra implying parametric processes and the RF-pumping of ambient ions and electrons, in the dipole near fields. The challenge today of understanding the inherent complexity of dipoles in magnetoplasmas may be met by recourse to particle-in-cell methods to predict classic antenna properties, such as current distribution, impedance, radiated field, and effective length.

Contents

1. Introduction

The development of the theory of electromagnetic (EM) wave propagation in cold magnetoplasmas set the stage in the 1950s and 1960s for solutions of the inhomogeneous wave equation applied to the active distributed dipole. This is an antenna the two aligned arms of which are straight conducting tubes or wires. The historical development was stimulated partly by the start of the space age, where the storable-tubular and wire technologies provided practical means for exploiting the broadband character of distributed-dipole receiving antennas. Figure 1 shows two of the first deployable tubular topside-sounder dipoles under test. The 1960s turned out to be a busy decade for progress of the dipole theory. One development was the inversion of the small-signal wave equation through Fourier transforms, providing Green's functions that were used to derive closed-form expressions for the impedance and radiation field of dipoles [1].

Shortly thereafter, experiments in space on dipole impedance began to explore the accuracy of the cold-plasma impedance theory. This theory has been useful in that a lot of radio-scientific research in geospace has

H. Gordon James is with the Communications Research Centre Canada, Ottawa, ON K2H 8S2 Canada; Tel.: +1 (613) 998-2230; Fax.: +1 (613) 990-6339; E-mail: gordon.james@crc.ca.

This is an invited *Review of Radio Science* from Commission H.

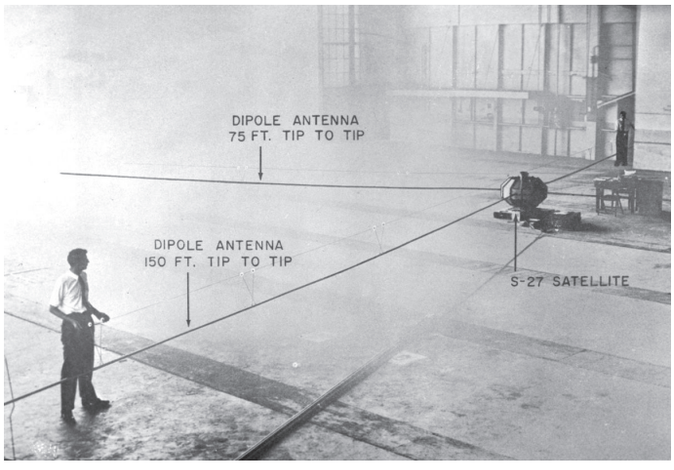

Figure 1. Tests of the storable tubular dipoles for the Alouette-I (S-27) topside sounder spacecraft in 1962.

been concerned with passive-dipole observations of spontaneous EM emissions. A proper interpretation of these observations requires a knowledge of engineering concepts such as the dipole's impedance and effective length. Validations by experiment of the theory of fields radiated by active dipoles have been slower and sparser in coming. Research with active antennas in the laboratory and in space has concentrated on dispersion relations and understanding of plane-wave propagation parameters, such as phase, signal delay, and spectrum; absolute amplitudes have been a secondary consideration. Tests on radiated fields also ideally employ separated synchronized emitting and receiving dipoles, a relatively expensive experiment seldom achieved in space. A limited number of two-point measurements of radiated electric field (E) have indicated that the cold-plasma theory works for EM wave modes, when the refractive index is close to unity.

Dipole theory has been elaborated in response to reports of a number of active- or passive-dipole phenomena. The demonstrated ability of dipoles to emit or detect electrostatic (ES) waves has motivated work on warm- and hot-plasma theory. The complicated form of the dielectric tensor in a hot magnetoplasma expanded the amount of mathematical work needed in the Green's function approach to dipole behavior. In some cases, the theory was simplified by recourse to the electrostatic approximation.

Often in research on space-plasma waves, satisfactory interpretations of received long-wavelength EM waves have been obtained with the hypothesis that the effective length of the distributed dipole is half its physical length, L. However, some evidence has been forthcoming from experiments on electrostatic waves that the dipole's effective length can be significantly larger than $L/2$. Effective length is important, because knowledge of the absolute E-field component amplitudes is required to specify wave-state vectors of ionosphere-magnetosphere emissions.

Given the magnitude of RF voltages that radio sounders place on their emitting dipoles, nonlinear reactions in the near-zone plasma are to be expected. Classifications of the menagerie of electrostatic signals appearing in radio-sounder data at various sum and difference frequencies of the electron plasma and gyrofrequencies attested to the diverse possibilities of plasma physics. The observation of RF-pumped electrons, directly and by their effects, pointed to the richness of the "soup" around an active dipole. The complexities of the nonlinear processes and of the spacecraft-antenna physical structures have spurred interest in particle-in-cell (PIC) and other computer-based methods for understanding waves in space plasmas.

This paper is neither the first nor, hopefully, the last review of dipoles in magnetoplasmas. Already in 1980, reviews of antennas in plasmas had wide ambits, covering the pioneering work in linear and nonlinear aspects of antenna interactions, and related propagation subjects, e.g. [2]. Given the radio-science context of the *Radio Science Bulletin*, the accent in the present update paper is on the physics of distributed dipoles for electron waves in magnetoplasmas. This brief review stresses significant work on capacitively-coupled dipoles, citing gateways to the original literature for any reader needing more detail. The author has lightened his writing burden by citing a number of tutorial papers. References are made to connected topics, such as propagation, spherical double probes, and laboratory plasmas. Some cited references show the relation to the frequency-limit cases of isotropic and uniaxial plasmas. The multifaceted nature of our understanding of dipoles means that given the organization chosen for the present paper, cross-referencing is unavoidable. It is hoped that the "Contents" will help the reader find the way to a desired subject.

2. Active Dipole

2.1 Linear Theory, Wave Equation with External Currents

The physics of electric dipoles at frequencies close to the characteristic electron frequencies – the plasma frequency, f_{pe}, and the cyclotron frequency, f_{ce} – has been a major area of endeavor since research in space plasmas began. This area is attractive conceptually because

the physicist needs only consider the movement of electrons against a background continuum of positive charge supplied by ions that are too massive to respond to EM wave fields. With this simplification, important concepts have been developed, such as the dispersion relation, wave mode, energy flow, heat in plasmas, and instability, to name a few. An important theme throughout this Section 2 is the determination of dipole impedance and radiation. The notions at the beginning are in terms of displacement current and capacitive coupling. Attention will be directed later in the paper to frequencies much lower than the electron plasma frequency, where ion motion enters the picture and where antenna members are electrostatic probes, drawing currently directly from the plasma.

Section 2.1 is devoted exclusively to linear theory. The usefulness of any theory may be judged in its ability to provide elegant engineering models of antennas. The first-order engineering quantities of interest are summarized in Figure 2. In the upper part of Figure 2a, an active dipole located at point $\mathbf{r}'$ is stimulated with a voltage source, V_s . This source has an output impedance, Z_s , and drives a current, I_0 , into the dipole, producing a dipole moment, $\mathbf{p}(\mathbf{r}')$, and a resulting radiation field, **E**, such that $\mathbf{E}(\mathbf{r}) = \mathbf{G}(\mathbf{r}-\mathbf{r}')\bullet\mathbf{p}(\mathbf{r}')$ at some general point $\mathbf{r}$ in the physical space around the dipole. **G** is the Green's function operator. Intimately linked to the nature of **G** is the determination of the driving-point current, I_0 , by the dipole impedance, $R+iX$.

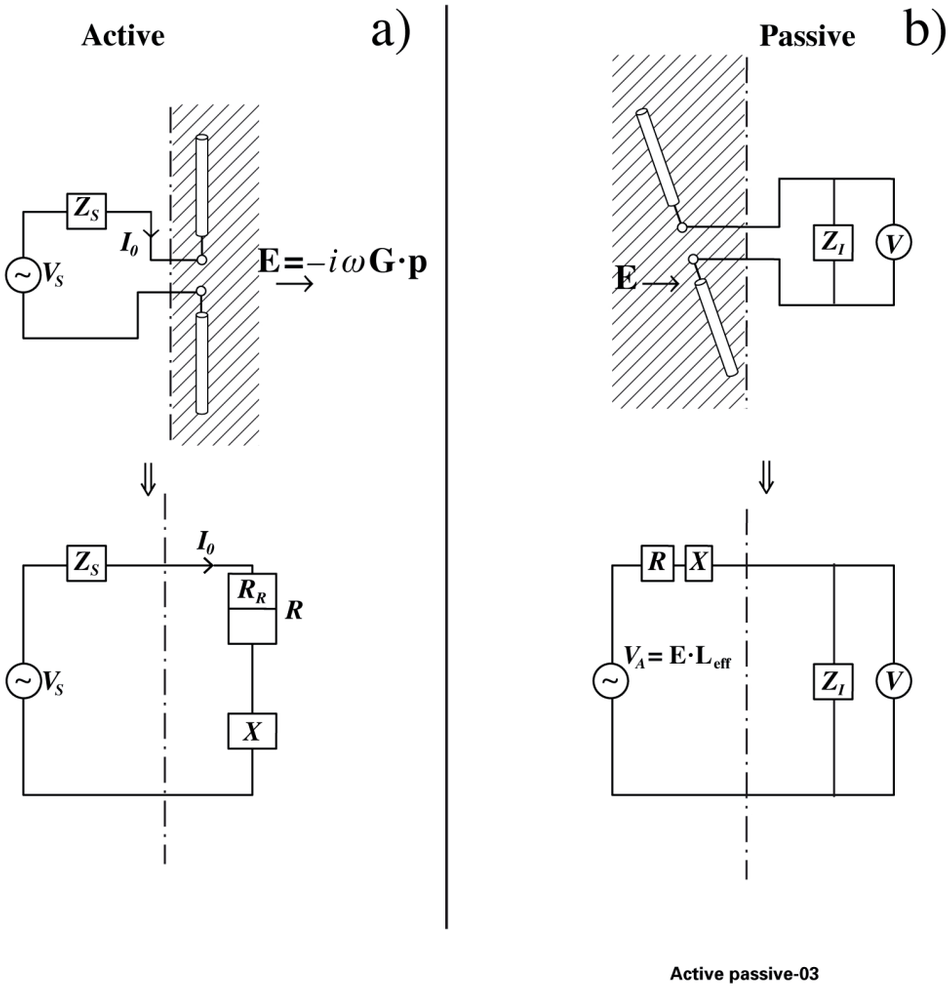

Figure 2. Basic engineering features of (a) an active, emitting dipole on the left, and b) a passive, receiving dipole on the right. The upper diagram on both sides represents the physical arrangement, while the lower part is the corresponding equivalent circuit. On the upper left, a signal source with a voltage, V_S , and an output impedance, Z_S , injects a current, I_0 into a dipole, producing a radiated electric field, **E**, *essentially given by the operation of a Green's function,* **G**, *on the antenna dipole moment,* **p**. ω *is the angular frequency. The dipole impedance, $Z = R + iX$, has a total resistance, R, equal to a radiation resistance plus possibly some other contributions. On the upper right, a radiated field,* **E**, *impinges upon a passive dipole that is connected to a receiver with an input impedance, Z_I , in parallel with a voltmeter that measures the input voltage. The equivalent circuit of the receiving dipole on the lower right consists of a voltage source, V_A , given by the scalar product of the incident electric field and the dipole effective-length vector in series with the dipole impedance.*

2.1.1 Dispersion and Radiation

Derivations of the electromagnetic field of an active antenna have often begun with the inhomogeneous Helmholtz wave equation for plane waves. An external current-density distribution, $\mathbf{J}(\mathbf{r}')$, in real **r** space in a magnetoplasma produces an electric field, $\mathbf{E}(\mathbf{r})$, at a general point **r** obeying the relationship

$$\nabla\times\nabla\times\mathrm{E}-\omega^2\varepsilon_0\mu_0\mathrm{K}\bullet\mathrm{E}=i\omega\mu_0 J \qquad (1)$$

in which ω is the angular frequency, ε_0 is the vacuum permittivity, μ_0 is the vacuum permeability, and **K** is the relative-permittivity tensor of the magnetoplasma [1, 3-5]. When Equation (1) is compared with the wave equation for propagation in a vacuum, it is appreciated that all of the plasma-physical response is bound up in **K**. The role of **K** is to determine how charge is displaced in the dielectric plasma when an electric field is applied to it. Fourier-transformed to wave-vector **k** space, the wave equation becomes

$$\mathrm{k}\times\mathrm{k}\times\tilde{\mathrm{E}}+\frac{\omega^2}{c^2}\mathrm{K}\bullet\tilde{\mathrm{E}}=i\omega\mu_0\tilde{\mathrm{J}}\,, \qquad (2)$$

where $\tilde{\mathbf{E}}$ and $\tilde{\mathbf{J}}$ are the Fourier transforms of **E** and **J**. Equation (2) can be written

$$\left(\mathbf{kk}-k^2\mathbf{I}+\frac{\omega^2}{c^2}\mathbf{K}\right)\bullet\tilde{\mathbf{E}}\equiv\mathbf{T}\bullet\tilde{\mathbf{E}}=i\omega\mu_0\tilde{\mathbf{J}}\,, \qquad (3)$$

in which **kk** is the **k** dyadic, and **I** is the unit matrix. The solution,

$$\tilde{\mathbf{E}}(\mathbf{k})=-i\omega\mu_0\mathbf{T}^{-1}\bullet\tilde{\mathbf{J}}(\mathbf{k})\,, \qquad (4)$$

requires the inverse of the wave matrix,

$$\mathbf{T}^{-1}=\mathbf{T}^a\big/|\mathbf{T}|\,. \qquad (5)$$

Here, $|\mathbf{T}|$ is the determinant of **T**, and $\mathbf{T}^a$ is the adjoint of **T**.

The inverse Fourier transform of Equation (4) is the triple integral

$$\mathbf{E}(\mathbf{r})=-\frac{1}{8\pi^3}\int_{-\infty}^{\infty}\mathbf{T}^{-1}\bullet\tilde{\mathbf{J}}(\mathbf{k})\exp\left[-i\mathbf{k}\bullet(\mathbf{r}-\mathbf{r}')\right]d\mathbf{k}\,, \qquad (6)$$

which is a point of departure often used in linear theories predicting dipole properties of interest, such as impedance and radiated field. This section will cite typical examples.

It was shown [4] that with the current source located at the origin of real space, Equation (6) can be expressed as

$$\mathbf{E}(\mathbf{r})=i\omega\mathbf{G}(\mathbf{r})\bullet\mathbf{p}\,, \qquad (7)$$

where **p** is the vector dipole moment, and the Green's Function operator is

$$\mathbf{G}(\mathbf{r})=-\frac{i\omega\mu_0}{8\pi^3}\int_{-\infty}^{\infty}\frac{\mathbf{T}^a}{|\mathbf{T}|}\exp(-i\mathbf{k}\bullet\mathbf{r})\,d\mathbf{k}\,. \qquad (8)$$

In cases where **p** is known, Equations (7) and (8) provide a simpler solution than Equation (6), in that the inversion is separated into calculations of **G** and **p**. In some cases, authors have preferred to apply current distributions the Fourier transform of which, $\tilde{\mathbf{J}}(\mathbf{k})$, is amenable to the more-fundamental evaluation of Equation (6).

It is important to note in the denominator of Equation (8) the presence of the determinant of the wave matrix, **T**. This same matrix arises in the solution of the homogeneous wave equation, where the statement $|\mathbf{T}|=0$ constitutes the dispersion relation for the waves under consideration. Hence, one sees from Equation (8) that the dispersion of the medium plays a fundamental role in linking radiation and propagation.

An important fact about most dipole-radiation theories is that they start with an assumed current density, $\mathbf{J}(\mathbf{r}')$, as opposed to a unified derivation from the first principles of all antenna variables. Over the last few decades, particle-in-cell (PIC) research has begun to address the absence of a unified theory for active dipoles in plasmas. Some relevant particle-in-cell research will be mentioned in Section 5. Meanwhile, most of what follows is characterized by hypotheses about applied current distributions.

An alternative method of calculating radiation in an anisotropic medium was formulated through the application of waveguide concepts to the antenna [6, 7]. This work provided a timely, independent check on the results of the plane-wave methods described above, in particular, on radiation in a cold plasma, which is the topic of the next subsection.

Let us also recognize at this point the extensive application of the quasistatic (also called quasi-electrostatic, electrostatic) approximation in plasmas, especially in cold plasma. In the quasistatic approximation, **E** is derived from the Maxwell and Poisson equations using a scalar potential. The quasistatic approximation presumes that the size of

the source antenna is small compared with the wavelength of the plasma wave. A fruitful approach of considerable breadth of application is to solve the Poisson equation assuming that the cold-plasma **K** matrix is already known [8]. Such formulation of dipole electrostatics starts with charge distributions rather than currents, but leads to many of the results described below based on a hypothesized current distribution.

2.1.2 Radiation in a Cold Magnetoplasma

Over the last 50 years, there have been many applications of the cold-plasma version of **T** in active-dipole analyses arising from Equation (5) or Equation (7). The relative dielectric tensor [5] is

$$\mathbf{K} = \begin{bmatrix} S & -iD & 0 \\ iD & S & 0 \\ 0 & 0 & P \end{bmatrix}, \qquad (9)$$

where S, D, and P are functions of the wave frequency, f, f_{pe}, f_{ce}, and the collision frequency of each charged-particle species present. In a coordinate system having the Earth's induction field, $\mathbf{B}_0$. along the z axis, and $\mathbf{k}$ in the x-z plane at an angle θ with respect to $\mathbf{B}_0$, the wave matrix corresponding to Equation (9) is

$$\mathbf{T} = \begin{bmatrix} S - n^2\cos^2\theta & -iD & n^2\cos\theta\sin\theta \\ iD & S - n^2 & 0 \\ n^2\cos\theta\sin\theta & 0 & P - n^2\sin^2\theta \end{bmatrix} \qquad (10)$$

where $n = kc/2\pi f$, the refractive index arising from a solution of the dispersion relation $|\mathbf{T}| = 0$. These solutions are graphically organized in the Clemmow-Mullaly-Allis (CMA) diagram, of which an example appears in Figure 3 (see also [5, Chapters 1-2]). References [9-11] are other useful source texts on dispersion relations and concepts of wave-energy transfer needed for the study of EM wave propagation in space magnetoplasmas.

The present text focuses on dipole antennas. References [12-14] are a representative, not-exhaustive additional list of theoretical literature on dipole-radiated fields in the cold-plasma approximation. These are examples of the solution of radiated $\mathbf{E}(\mathbf{r})$ obtained by the application of the matrix of Equation (10) to Equation (6). Among these references, there is a general expression for the dipole-radiated **E** field derived succinctly in covariant tensor notation [12]. Green's functions for small distances from a Hertzian dipole, as well for large values, as is more often the case in dipole theory, were developed [13, 14].

To test the radiation theory, fields radiated by active dipoles have been measured during intra-ionospheric two-

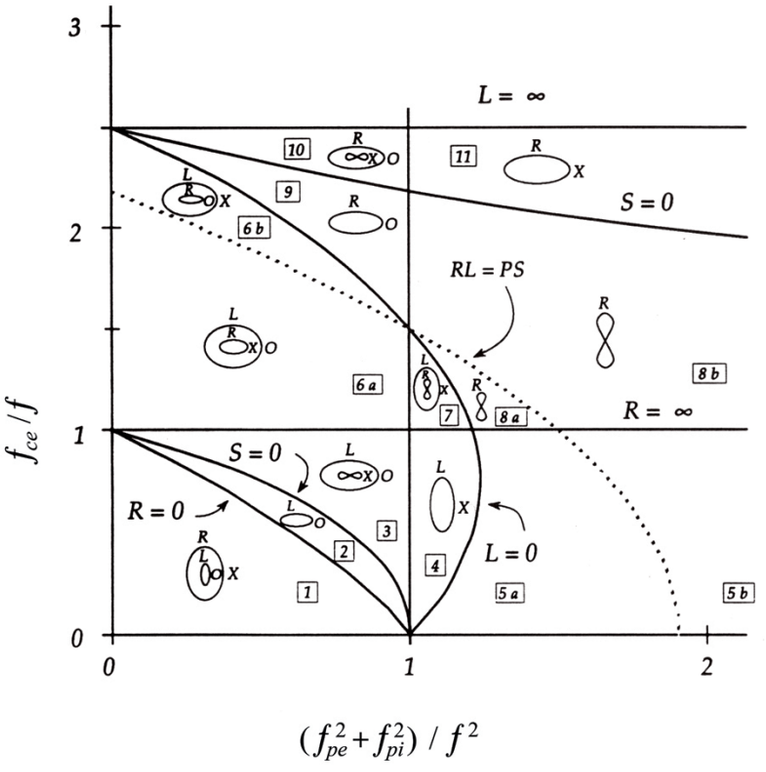

Figure 3. The Clemmow-Mullaly-Allis (CMA) diagram of an electron/single-ion plasma, plotted for the sake of clarity with the unusual ion-to-electron mass ratio of 2.5. The bounding surfaces were determined in terms of plasma parameters defined in [5, Chapter 1-2]. Inside each CMA region are little figures that show how the phase velocities of the propagating cold-plasma wave modes vary as a function of the angle between the wave vector and the magnetic-field axis, which is parallel to the y axis. f_{pi} and f_{ci} are the ion-plasma and ion-cyclotron frequencies, respectively (with kind permission of Springer Science+Business Media).

point propagation studies. The whistler (W) mode of propagation is the right-hand-polarized (R) solution in CMA regions 7 and 8, and is of great interest in spontaneous emissions of space plasmas. The measured power of W-mode, reciprocal, oblique (not resonance-cone) propagation between two sounder spacecraft [15] was compared with predictions of a theory for radiation resistance [16]; agreement was obtained to within an order of magnitude. A tighter test of the W-mode theory was achieved in the rocket double-payload experiment OEDIPUS C (OC), where propagation was close to $\mathbf{B}_0$ -aligned. The closely-

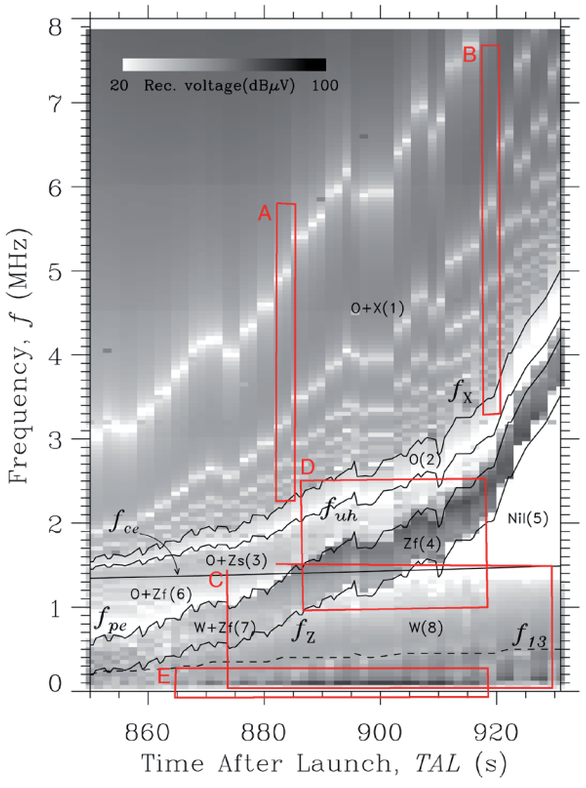

Figure 4. Summary of transmitted signal strengths in OEDIPUS C experiment on dipoles, from the last part of the down-leg trajectory, adapted from [99]. The darkness of the pixels was proportional to the received signal voltage, which can be read from the inserted gray scale. The CMA regions 1-8 are labeled within the frequency domains. The regions designated are also preceded by the cold-plasma wave modes present in that region. The O mode was present in CMA 1, 2, 3, and 6; the X mode in CMA 1; the slow Z mode, Zs, in CMA 3 and CMA 6; the fast Z mode, Zf, in CMA 4 and 7; the W mode in CMA 7 and 8; and no mode was present in CMA 5. The rectangles labeled "A" through "E" identify frequency-time domains the OEDIPUS C data of which were used to test the theory of dipoles, [21, 20, 17, 18, 100], respectively. The line f_{13} separates the frequencies at which there are three separate W-mode **k** *vector solutions the corresponding group-velocity directions of which were parallel to the separation direction connecting the emitting and receiving sub-payloads (below the line) and the frequencies for which there was one* **k** *vector (above the line).*

synchronized frequency sweeps of the separated emitter and receiver permitted exploration of radiating dipole efficiency through various CMA regions, at frequencies between 0.025 and 8 MHz. Good agreement was obtained with the analytic expressions for the radiated $|\mathbf{E}|$ for W-mode frequencies that put the propagation direction well inside the oblique resonance cone [17]. The same theory was the basis of comparison with swept-frequency $|\mathbf{E}|$ values observed in the Z (L-X) mode in CMA4 [18]. Again, agreement was good for most frequencies. Exceptions occurred at the highest frequencies, where the inflected shape of the refractive-index surface has three different **k** vectors with corresponding ray directions parallel to the direction connecting the emitting part of the payload to the receiving part. Relatively strong transmissions were obtained in the Z case because the emitting dipole impedance provided a good match to the output of the transmitter.

Active two-point transmission experiments carried out in CMA region 1 have confirmed that the vacuum dipole theory is adequate for determining E levels radiated by dipoles [19, 20] not far above the cutoff frequencies of the cold-plasma modes. Two-point propagation experiments have verified and exploited the **E** polarization predicted in various CMA regions [21, 22].

Figure 4 shows the strengths of EM waves transmitted between the OEDIPUS C sub-payloads in different CMA regions. For reference to detailed comparisons of the observations with dipole radiation theory, Figure 4 has rectangles labeled "A" through "E," identifying parts of the CMA diagram quantitatively analyzed and quoted in this paper.

In addition to electric field, radiation resistance and radiated power also have been computed with the inverse-transform method [23]. In the context of the energy flux of EM waves in space, it is sometimes preferable to analyze radiated power, even though most space-radio techniques do not directly measure power flux. While a spacecraft can be instrumented to detect both electric and magnetic components of a wave field, conversion of measured EM radiation fields to power flux requires some care. In general, and specifically for inhomogeneous or damped waves, Poynting flux is only part of the power flux [23]. In instances of electrostatic wave propagation, the wave magnetic-component measurement may have a large percentage uncertainty because of its small magnitude. There is also the uncertainty of the effective length of a dipole measuring the electric field of electrostatic waves. For such reasons, the present review emphasizes the measurement and interpretation of radiated electric field, not power flux.

2.1.3 Impedance and Radiation Resistance

Much of the important research about antenna linear response dates from the first 20 years of the space age [2].

As in the formulation of dipole radiation, the development of dipole impedance theory has seen a progressive sophistication of the derivation of the plasma dielectric tensor, **K**. Historical advances from cold- to warm- to hot-plasma paradigms were summarized [24]. The quasistatic approximation allows the driving-point impedance, *Z*, of a dipole to be derived in closed form [25]. *Z* was found using the surface integral

$$Z = \left(-1/I_0^2\right)\int \mathbf{J}\bullet\mathbf{E}ds\,, \qquad (11)$$

where I_0 is the driving-point current magnitude, **J** is the dipole surface-current density, and **E** is the electric field at the surface of the cylindrical dipole. Impedance derivations have almost invariably required an assumption about **J** [26]. Often, a sinusoidal distribution of antenna current as a one-dimensional function of distance along the dipole axis from the driving point has been applied. In the quasistatic limit, the distribution takes on a triangular shape. Consequences of assuming a cylindrically symmetrical three-dimensional current distribution for the magnetically aligned dipole were investigated [27]. Impedances for one-dimensional triangular and three-dimensional exponential current distributions were evaluated, and little difference was found between the resulting values [28]. Other representative work during the 1960s on dipole-impedance theory was given in [29, 30]. The latter reference [30] reported on the importance for impedance of the form of the current distribution along a $\mathbf{B}_0$-aligned cylindrical antenna.

Maxwell's equations have been solved for the dipole impedance using the radiated Poynting flux without recourse to the quasistatic approximation [31]. These authors illustrated the considerable mathematical complexity that ensues when the full inverse Fourier transform is worked out to obtain the Green's function. In a comparison of some experimental results with theory, some differences between the predictions of the quasistatic [25] and full inverse Fourier transform [31] theories were found [32].

An important proviso of the quasistatic approximation is that the wavelength, $2\pi/k$, be much greater than the dipole length. A comparison of the theoretical predictions of the quasistatic impedance theory and those obtained for a finite-length cylindrical antenna oriented parallel to the magnetic field were reported [30]. The challenges of the long-wire-antenna impedance were taken up by representing the wire as a lumped-parameter delay line, in which the capacitances and inductances were transformed so that free-space transmission-line formulas could be applied [33]. This theory was partially successful in predicting measured values of the active dipole impedance modulus [34].

Theoretical impedance predictions were compared with observations in different space experiments. Good agreement was obtained in a swept-frequency rocket experiment on impedance for frequencies above $2f_c$ [35]. The experiment was carried out in the bottomside F region, where f_{pe} was several times greater than f_{ce}. In the EIDI III sounding-rocket experiment at mid-latitude [36], four frequencies between 1.57 and 2.60 MHz were used. The variation of plasma parameters along the trajectory allowed impedance measurements in CMA regions 1 through 5. Agreement was good, except for radiation resistance at frequencies below f_{pe} in CMA region 3, where the upper oblique resonance may play a role.

Much of the just-mentioned work illustrates the relevance of driving-point impedance theory to plasma diagnosis. Depending on what is independently known about the plasma, a measurement of Z can be a measurement of one of the following: plasma frequency, gyrofrequency, or electron temperature.

2.1.4 Oblique Resonance

Great interest has been attached to the oblique resonance conditions inherent in the cold-plasma dispersion relation. The solution $|\mathbf{T}| = 0$ [5] using the **T** of Equation (10) reveals that *n* goes to infinity when

$$\tan^2\theta = -P/S\,. \qquad (12)$$

Since dispersion surfaces are symmetric with respect to the $\mathbf{B}_0$ direction in real and **k** space, the surface shape is said to be a resonance cone. "Lower" and "upper" oblique resonances are found in the W mode in CMA regions 7 and 8, and in the slow Z mode in CMA3, respectively.

Interest in the resonances arises not just from the mathematical challenge of understanding and dealing with the singularity, but also from many observations of different spontaneous radio emissions that owe their existence to a wave-particle interaction involving either oblique resonance. When the papers in the preceding two subsections discussed W-mode propagation, different rationales were proposed for dealing with the infinity in a cold plasma. The "catastrophe" in computed W-mode dipole impedance can be removed by imposing a current distribution that forces both the radiated field and the impedance to be finite near the resonance cone [27]. In the application of the quasistatic theory to the calculation of radiation resistance, it was admitted that so doing effectively excluded accounting for resonance-cone effects [37]. The limitations of the cold-plasma predictions of the radiation resistance of a filamentary current of finite length oriented parallel to $\mathbf{B}_0$ have been pointed out for propagation near the Z, or upper, oblique resonance [29]. The same paper noted that the W-mode infinity can be avoided with the appropriate **k** dependence of the Fourier transform of the current distribution, also discussed in [27].

References to the resonance cones crop up throughout this paper. Exploiting the resonance-cone propagation for diagnostic purposes is mentioned in the next Section 2.1.5.

The same section will refer to warm- and hot-plasma theories that deal with electrostatic-wave **E** fields radiated near the oblique resonances. Section 3.1.2 will cite work on the receiving dipole's effective length under oblique-resonance conditions.

2.1.5 Hot Plasma, Electrostatic Waves, Full EM Theory

The solution of the inhomogeneous wave Equation (3) in a hot plasma, now incorporating a relative permittivity tensor, **K**, which accounts for thermal motion, becomes more challenging than the cold-plasma solution. The mathematical complexity of the problem increases because the dependence of **K** on **k** becomes more complicated. Such is the case in the derivations of hot-plasma plane-wave dispersion relations [38; 5, Equation 10-73 and references on p. 238].

The inclusion of thermal effects in the tensor **K** leads to "warm-" or "hot-plasma" dispersion relations, the solutions for which include electrostatic short-wavelength modes at frequencies associated with f_{pe} and mf_{ce} (m is an integer), and depending on electron temperature. Data from various radio-frequency sounders in space have been the basis of a considerable literature about the propagation of electrostatic waves [39-41].

It is necessary in principle to account for thermal effects in dipole impedance. As an approach to the cylindrical dipole, important magnetoplasma effects can be incorporated exactly for an ellipsoidal antenna [42]. Basic ideas in impedance and noise calculation, albeit mostly about isotropic plasma and frequencies close to f_{pe}, are found in [43].

As in dipole impedance theory, the electrostatic approximation has been applied as a way of getting algebraically tractable expressions for dipole radiation. Based on dispersion relations that include both cold-plasma and thermal-plasma terms, the interference-patterns of the **E** fields in resonance-cone and Bernstein waves in laboratory plasmas have been explained [44-48]. These theories have been able to predict the shape of the interference fringes, but the challenge of a successful explanation of the absolute amplitudes of electrostatic waves persists, and is discussed in Section 3.1.2.

It should be noted that a considerable literature on electrostatic waves, including the just-mentioned references, has been based on the mathematical artifice of the point source. On one hand, this concept has been useful both experimentally and analytically [49], and has been applied to diagnostics of different plasma parameters [50, 51]. On the other hand, there has not been a apparent movement to exploit point-source results for understanding dipole antennas in magnetoplasmas.

The quadripole, or mutual-impedance, probe concept [52] proved to be a useful tool in anisotropic-plasma diagnostics. The quadripole obviates the inherent difficulty of monopole or dipole probes, which perturb the plasma the parameters of which are to be measured. The extraction of plasma parameters from quadripole mutual-impedance measurements has been an important contribution of this work [53]. In addition, a quadripole probe provides a method for detecting relative plasma motion based on the displacement of the oblique-resonance cone structure in the frame of the probe [54]: see [2, 55, 56] for background references.

To date, theoretical use in dipole-antenna analyses of the general **T** matrix without recourse to the quasistatic approximation appears to be limited. Warm-plasma fluid corrections to the dispersion relation were included in a calculation of radiated fields in an isotropic plasma [57].

Some theoretical treatments have incorporated the effect of relative motion of the dipole with respect to the medium. For measurements by receivers on orbital or suborbital vehicles having a velocity **v**, the Doppler shift, $\mathbf{k} \cdot \mathbf{v}$ can be appreciable for electrostatic waves with large $|\mathbf{k}|$. Following a suggestion about Doppler effects on resonance cones [54], change in resonance-cone opening was theoretically predicted [47]. Examples of the way that radiation directivity changes as a function of $|\mathbf{v}|$ have been published [58]. Doppler shifts have been extracted from mutual-impedance probe measurements [59].

2.1.6 Very Low Frequency (VLF), Transition Domain

The impedance measurements reported in Sections 2.1.3 and 2.1.5 are in best agreement with theory at frequencies near and above f_{pe}, and have their largest discrepancy with theory at the lowest frequencies observed. In the Earth's ionosphere-magnetosphere, the VLF range (3-30 kHz) is where the discrepancy begins to be seen as frequency is decreased. The main idea is the increasing importance of the impedance of the thermal-ion sheath and other phenomena in the interaction of spacecraft with plasma. In addition, there is a progression from capacitively-coupled operation at and above f_{pe}, where the induced current is solely displacement current, to direct coupling at and below the ion plasma frequency, where the dipole acts as an electrostatic probe, drawing/injecting current from/into the plasma directly [60]. Also, as frequency is reduced from the electron characteristic frequencies toward their ion counterparts, the theory must account for ion-motion effects in **K**.

Many dipoles flown in space experiments were short compared with the wavelengths of interest, and therefore capacitive. An early theoretical concept developed for dipoles at VLF was to take the capacitance of a cylindrical antenna in vacuum and transform it to cold plasma by the application of magnetoionic relations [61]. To this basic impedance of a VLF dipole on the OV3-3 spacecraft, it was found necessary to add the impedance of the ion sheath

to explain the results [62]. Quasistatic theory for dipole impedance was modified by the addition of a coaxial gap around the arms of the dipole to include ion-sheath effects [63]. The importance of the sheath for models of receiving dipoles is discussed in Section 3.2.

Since about 2000, a return to dipole radiation theory in the USA has been stimulated by proposals to reduce relativistic electron fluxes in the Earth's radiation belts with manmade VLF W-mode waves [64]. Such a reduction would be accomplished using space-borne VLF transmitters using dipoles. It may be that far-field radiation theory for injection of EM W-mode waves from space-borne dipoles with a given current distribution is adequately advanced for VLF mitigation, and that attention should now be directed toward better understanding of the dipole current distribution and associated impedance. The current and impedance for a 100-m dipole parallel to and perpendicular to $\mathbf{B}_0$ was found by applying the integral equations to dipoles [65, 66]. The classical triangular distribution was obtained for parallel orientation with impedance values in good agreement with the theory [25], whereas the situation is different for perpendicular orientation. Finite-difference frequency-domain and "perfectly-matched-layer" concepts have been invoked in a novel approach to a self-consistent derivation of the current and the fields of a dipole [67]. Although this particular work was limited to cold-plasma theory and one dimension along $\mathbf{B}_0$, it hopefully foresees progress towards a unified formulation of dipole EM theory.

2.2 Other Linear Currents in Space Plasmas

The electromagnetics of an electrical current constrained to flow in a metal dipole have been applied to other radiating systems. Radiation into the atmosphere at VLF has been pursued, in part, for its application to communications at wavelengths corresponding to skin depths in sea water of hundreds of meters, thus facilitating communications with submarines. However, this attraction has been offset by the concomitant need at VLF for huge transmitting antennas. Therefore, the idea of modulating the auroral electrojet at VLF over horizontal distances of tens of kilometers has been evaluated in part for its communications interests. This concept was demonstrated using VLF modulation of HF waves from the Tromsø ionospheric heating facility [68]. Radiation was detected on the ground [69] and in space [70]. The variability of successful VLF emission by the modulated electrojet and the modest radiated powers achieved [70, 71] have so far stayed claims for the operational usefulness of the concept. The theory of the current of the radiating "antenna" is more complex than that of a simple dipole [68, 72].

Work cited in Section 2.1.3 above recognized that as the dipole length increases beyond the short or Hertzian dipole case, it may be useful for impedance prediction to treat the long arms of a dipole as a wire or a coaxial cable that supports guided propagation. The cold-plasma EM-wave dispersion relation was solved for a long metal wire in a magnetoplasma aligned along $\mathbf{B}_0$ [73]. In an active experiment on tether-guided waves carried out during the OEDIPUS C rocket flight, good agreement was achieved between the predicted and observed dispersion characteristics of tether waves that were resonant with the varying tether length [74]. The investigation of the effects of a thermal ion sheath arrived at a rigorous representation of the propagating wave modes of an infinitely long wire parallel to $\mathbf{B}_0$ separated from the surrounding plasma by a co-aligned cylindrical insulator [75]. Those authors worked out propagation details specifically for the W-mode frequency domain.

The injection of electrons into the ionosphere to produce electrical current that might radiate waves the way that a wire-carried current might has often been thwarted by beam-plasma instabilities that break up the current over distances of the order of electrostatic wavelengths: see reference [76] as an example. Nevertheless, an "active filament" experiment [77] using a rocket showed some antenna-like properties of a current induced in the ionospheric plasma. Sounder-accelerated electrons also were found to retain some coherence from their causative RF pulse to produce slow-Z radiation [78]. Currents produced in the plasma in the plane of a sounder dipole axis and $\mathbf{B}_0$ also produced fundamental and harmonic Bernstein waves [79, 80].

2.3 Nonlinear Phenomena

2.3.1 Parametric Instabilities

The pulse voltages placed on radio-sounder transmitting dipoles [34] and even the amplitudes of resulting electrostatic echoes measured on radio-sounder receiving dipoles can much exceed the electron thermal kinetic energy divided by electron charge. In other words, active dipoles drive electrons into nonlinear response. Hence, closely connected with the allowed electrostatic-mode frequencies predicted by the linear theory mentioned above in Section 2.1.6 are the observations of electrostatic response at other frequencies systematically depending on, but distinct from, f_{pe} and mf_{ce} [41]. In topside-sounder ionograms, the "diffuse" resonance and its subsidiaries have been discussed in terms of wave-wave interaction in plasma turbulence that follows electron cyclotron absorption [40, 41, 81, 82]. Schemes involving caviton collapse have also been proposed [83].

All evidence considered, the plasma near an active dipole creating near-field amplitudes of hundreds of volts per meter must be a rich "soup." Nonlinear wave-wave processes can organize on larger spatial scales than wavelengths of the primary electrostatic waves near f_{pe} and mf_{ce}. Nonlinear processes also were observed to create O-mode cold-plasma waves at frequencies near 1 MHz linked to f_{ce} [84].

Interest in the importance of sheath physics as a determinant of VLF dipole total impedance has been revived, along with radiation properties, in the VLF mitigation concept already mentioned. At the required frequencies of a few kilohertz, sheaths may dominate the dipole's response. An isotropic electrostatic probe model has been employed in the calculation of an "equivalent" capacitance when large voltages are applied to a dipole [85, 86]. These models were supported by subsequent measurements of nonlinear capacitive "impedance" with the IMAGE Radio Plasma Imager [87]. At higher frequencies, around f_{pe} and f_{ce}, high RF voltages applied to topside sounder dipoles produced RF sheath thicknesses of the order of 1 m [34].

2.3.2 Sounder-Accelerated Particles (SAP)

Shortly after the ISIS-II spacecraft was launched in early 1971, its soft-particle spectrometer gave evidence of sounder-accelerated particles, that is, charged particles accelerated by the dipole RF near electric fields during the sounder pulses. Subsequent observations of energetic particles from the Soviet Interkosmos-19 and Kosmos-1809 sounder spacecraft [88-90] and the ISIS satellites [91] documented the existence of sounder-accelerated-particle electrons at energies up to 15 keV, and concomitant sounder-accelerated-particle ions up to a few hundred electron volts.

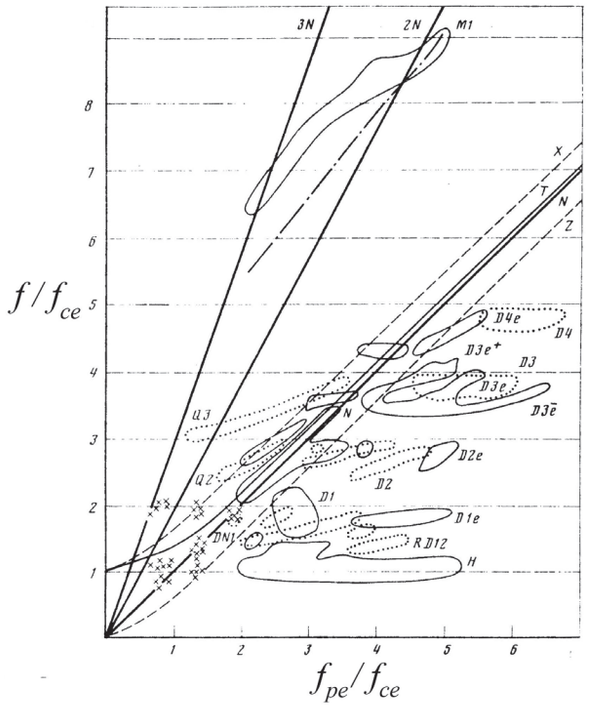

Figure 5. Distribution with respect to frequency of the occurrence of topside-sounder-accelerated electrons (solid thin lines and crosses) and of various "D" and "Q" wave resonances (dotted lines), observed on radio sounder satellites [94]. The other symbols are mN: multiples of the plasma frequency; M1: a parametric resonance in the Mathieu zone; X: cutoff of the X mode, T: upper hybrid resonance frequency; and Z: Z mode cutoff. For details about the D and Q nomenclature, see reference [94].

The OEDIPUS C rocket double payload had a magnetic-field-aligned configuration of a 10 W radio transmitter and a separated energetic-particle instrument. Sounder-accelerated-particle electrons at energies up to 20 keV and flux magnitudes at moderate auroral precipitation levels were produced [92, 93]. Mirrored sounder-accelerated-particle electrons captured on ISIS I and direct, remote sounder-accelerated-particle detection on OEDIPUS C have demonstrated that sounder-accelerated particles are not confined to the near environs of an active antenna, but escape to distances along the $\mathbf{B}_0$ axis of at least hundreds of meters.

In the observations with the Soviet sounders with large f_{pe}/f_{ce}, high fluxes were accelerated at frequencies near f_{pe} and near mf_{ce} [88, 94]. The aggregate evidence about the frequency dependence of sounder-accelerated particles implicates electrostatic waves in their creation. In view of possible parametric instabilities in the intense near field of sounder dipoles, it was proposed that sounder-accelerated-particle electron heating near f_{pe} results from Langmuir caviton collapse and from electron-cyclotron caviton collapse near mf_{ce} [94]. Support for this deduction comes from the similarity of the frequency domains in which sounder-accelerated-particle electrons and the "diffuse" resonances are found in particle-detector and sounder-receiver data, respectively [40, 94]. This similarity is displayed in Figure 5, based on [94].

Resonances other than Langmuir waves may have a role in electron acceleration. In the OEDIPUS C experiment, $f_{pe}/f_{ce} < 1$. Here, the frequencies responsible for sounder-accelerated particles corresponded to CMA regions 3, 7, and 8, and to mf_{ce} [92]. Sounder-accelerated particles were almost entirely absent from the CMA-7, 8 domains in the topside-sounder data. The OEDIPUS C results in CMA-3, 7, 8 turned attention to the role of the oblique resonances in sounder-accelerated-particle production, because in OEDIPUS C data, f_{pe} was well resolved from the upper-hybrid resonance frequency, $f_{uh} = \left(f_{ce}^2 + f_{pe}^2\right)^{1/2}$. In Figure 2 of [92], strong sounder-accelerated particles filled the frequency ranges from 0.1 MHz up to f_{pe} and from f_{ce} to f_{uh}, that is, the lower- and upper-oblique resonance-frequency ranges.

Simple test-particle trajectories through estimated near fields of the OEDIPUS C transmitting dipole resulted in energy enhancements much smaller than the largest observed enhancements [92]. However, the application of particle-in-cell methods to a simplified antenna geometry under OEDIPUS C experimental conditions has furnished some hope for an explanation of the kilo-electron-volt acceleration seen on OEDIPUS C based on collective effects [95].

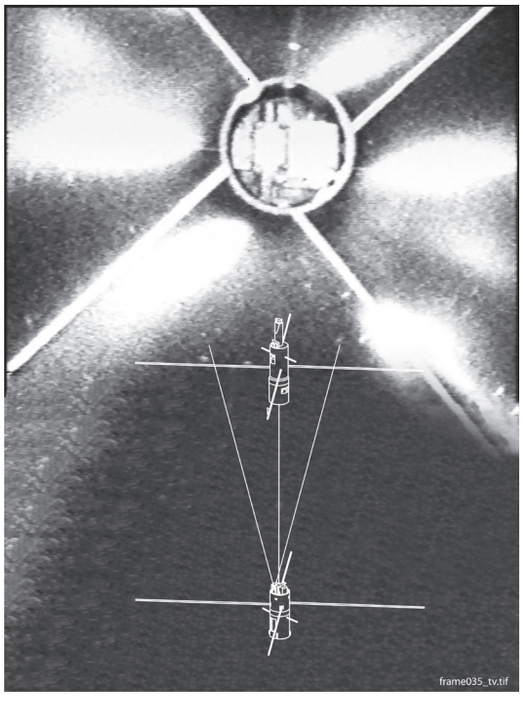

Figure 6. A frame from an image-intensified video camera, on the lower part of the OEDIPUS C payload, showing the luminosity of gases emitted from the upper part of the payload carrying the active RF dipoles. The exposure time was approximately 1/30 s. The arms of the beryllium-copper transmitting dipoles were at about 2, 5, 8, and 11 o'clock, and the arms at 11 and 2 o'clock were connected to form one side of the double-V emitting dipole. Argon gas thrusters were at about 11 and 5 o'clock. The blurred faint line near 12 o'clock was a conducting tether joining the two sub-payloads. The separation direction of the sub-payloads was within 0.3° of the direction of $\mathbf{B}_0$ *. The width of this field of view at the upper sub-payload was about 1.65 m.*

Sounder-accelerated-particle electron fluxes apparently generate secondary radio fields that propagate near the upper-oblique resonance [78]. It was speculated that radio sounders can therefore serve as controlled electron-beam sources with cross-$\mathbf{B}_0$ dimensions of the order of the perpendicular extent of the distributed dipole. Somewhat similar radiation in a laboratory plasma was attributed to cyclotron-pumped electrons [96].

The likelihood of nonlinearities around the OEDIPUS C transmitting sub-payload is supported in Figure 6. This is a single image frame from the visible-white-light video camera mounted on the lower OEDIPUS C sub-payload looking upward and end-on toward the cylindrical transmitting sub-payload. Some 300 such movie frames showed brilliant luminosity like this during the first 15 s after sub-payload separation, when argon-gas jets were providing propulsion to separate the two sub-payloads. The ejected argon apparently became a "fluorescing" volume when the intense fields from the two active crossed dipoles excited the optical emission. Whether the excitation arose directly from the intense electric fields of the dipoles or rather from sounder-accelerated-particle collisions with the argon atoms is yet to be investigated.

3. Passive Dipole

3.1 Distributed Dipole

3.1.1 Equivalent Circuit at High Frequency

Consider the detection of electric fields with a classic dipole as envisaged in Figure 2b. A plane EM wave with an electric field **E** incident from a general direction upon the dipole results in a open-circuit voltage $V_A = \mathbf{E} \bullet \mathbf{L}_{eff}$ being induced in the dipole. The effective length vector, $\mathbf{L}_{eff}$, is aligned along the direction of the dipole's axis.

The receiving-dipole equivalent circuit is the lower part of Figure 2b, comprised of a voltage source, V_A, in series with the dipole impedance, $Z = R + iX$. Without nonlinearities, Z is the same for a dipole, whether active or passive. Hence, there is no separate treatment of the small-signal Z in this section. One should return to Sections 2.1.3 and 2.1.6 for publications dealing with Z. Sometimes, the design goal of a receiver connected to a dipole is to operate it as a voltage probe, i.e., to make the input impedance $|Z_I| \gg |R + iX|$, the antenna plasma impedance. Then the data analyst has $V_A = V$, and can proceed directly to a deduction of **E** without needing to know Z.

3.1.2 Effective Length

The concept of $\mathbf{L}_{eff}$ has been brought over to magnetoplasmas from the vacuum theory, where reciprocity can be applied to show the relationship between V_A of a dipole receiving radiation from an identical transmitting dipole having a known current distribution [97]. Generally, the magnitude of $\mathbf{L}_{eff}$ for a dipole of physical length L is

$$L_{eff} = LF(\theta, \phi, pp), \qquad (13)$$

where the non-normalized electric-field pattern, F, is a function of the dipole-axis direction with respect to $\mathbf{B}_0$ as well as the plasma parameters pp [98]. The derivation of $\mathbf{L}_{eff}$ can be complicated for electrostatic resonances in magnetoplasmas. For cold-plasma propagation with refractive indexes near one, it was found that $\mathbf{L}_{eff} = L/2$ for a simple dipole [99]. This relation and the related assumption of a triangular current distribution along the dipole are typically invoked wherever the quasistatic approximation is deemed applicable. However, this approach to $\mathbf{L}_{eff}$ is hypothetical, and needs examination in particular cases where reciprocity between transmitting

and receiving dipoles in the anisotropic magnetoplasma has to be correctly posed [98]. Note again the success of the conventional view in explaining the two-point EM propagation data for various cold-plasma EM modes described in Section 2.1.2, above.

A valid concept of $\mathbf{L}_{eff}$ for electrostatic waves is another matter. A particular recent example is the calculation of the $\mathbf{L}_{eff}$ of the OEDIPUS C receiving dipole when irradiated by W-mode waves propagating close to the resonance cone. The radiated **E** field at the receiving dipole was considered well-known from two comparable theories [47, 48]. When the receiving dipole voltages, V_A, were calculated using $\mathbf{L}_{eff} = L/2$, they were found to be much below the observed voltage [100]. A novel application of the Nyquist noise theorem to warm magnetoplasma was able to explain the observed $\mathbf{L}_{eff} \approx 30L$ [101]. The same analytical approach was subsequently applied successfully to Langmuir waves observed in the solar wind to explain observed voltages [102].

Figure 7 illustrates older data from the ISIS satellites that are relevant to the question of $\mathbf{L}_{eff}$ for W-mode resonance-cone propagation [15, 99]. The signal delays of these pulses observed during an inter-satellite propagation experiment required resonance-cone propagation. The strength of the received signal-voltage spread over a long range of large delays implied that the receiving dipoles had large $\mathbf{L}_{eff}$ values for the highly delayed components of the pulses.

These results regarding $\mathbf{L}_{eff}$ therefore counseled care in the interpretation of the magnitudes of **E** measured with dipoles. The explanation, in first-principles EM language, of the high $\mathbf{L}_{eff}$ values encountered in the cited cases where electrostatic-wave group velocity was essentially perpendicular to **k** is yet to come. Such an eventual explanation will mark an important step forward in space-plasma metrology, given the fundamental importance of understanding $|\mathbf{E}|$ to our concepts for all aspects of electrostatic-wave generation, propagation, and detection.

A technique has been developed for isotropic plasmas involving tanks of conducting water to measure the performance of spherical double probes [103]. The particle-in-cell technique aided in conceptualizing $\mathbf{L}_{eff}$ of complex dipole shapes [104].

3.2 Other Receiving Electric Dipoles

Because of the comparative simplicity of their mechanical deployment, distributed dipoles have had wide use in wave experiments. Other dipole forms have proven superior for certain space-plasma experiments at frequencies within and below the VLF range. For an introduction to the subject, see [60]. The essential features of receiving dipoles operated at frequencies well below f_{pe} have been reviewed [105]. In the design of passive dipoles for dc and ac field measurements, a variety of considerations require negotiated compromises. Questions of probe length, probe shape, and operating modes enter into the design of passive double probes destined for particular experimental situations [106, 107].

Small metal spheres supported by long shielding arms [60] have had extensive application in the ionosphere-magnetosphere. Such a double-sphere design is superior to the distributed dipole in that it:

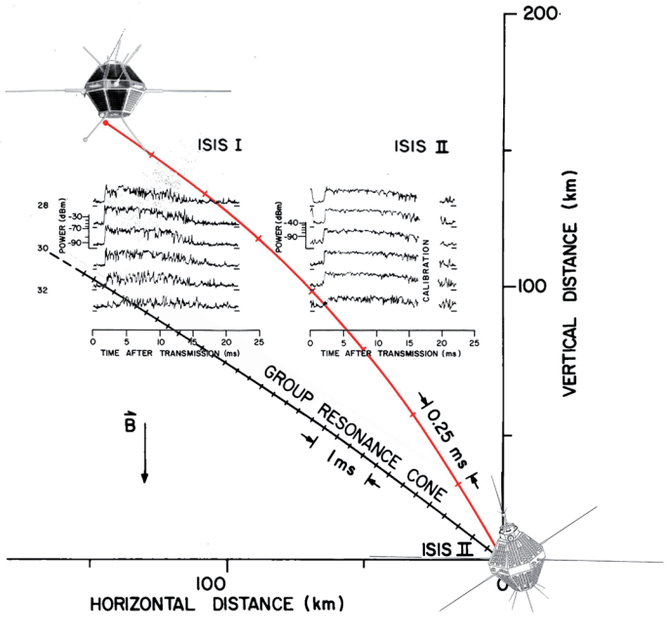

Figure 7. Highly elongated whistler-mode pulses transmitted reciprocally between the ISIS-I and -II sounder spacecraft during a rendezvous on April 14, 1974, at 0432/30 UT [15]. The pulse fixed frequency $f = 0.48$ MHz; $f_{pe} = 0.55$ and 0.65 MHz at ISIS I and ISIS II, respectively; and $f_{ce} = 0.90$ MHz throughout the diagram. The red line is the traced ray that connects the two satellites, corresponding to the 2-ms delay of the sharp leading edge of the pulses. The black oblique line labeled "GROUP RESONANCE CONE" is a ray traced for propagation near the resonance cone.

a. Offers a longer and better-known effective length for a given tip-to-tip length;

b. Avoids ion-sheath non-uniformity induced by motion across the Earth's magnetic field;

c. Permits techniques to minimize antenna impedance to spacecraft ground;

d. Lends itself to electrostatic (Langmuir) probe measurements down to zero frequency.

Here are some further remarks about VLF receiving antennas. The capacitance transformation [61] was applied to a calculation of the impedance of the spherical dipoles of the FR-1 satellite [108]. It was found that the order-of-magnitude agreement obtained between observations and theory could be improved by including thermal effects in the permittivity. The designers of the Plasma-Wave Instrument [109] on the GEOTAIL spacecraft opted for 100-m wire dipoles for measurements from 24 Hz up to 800 kHz, plus the point-sphere technique for near-dc to 1.6 kHz. Their equivalent circuits showed receiver-input arrangements to minimize the complications of stray and sheath capacitances anticipated during visits of the spacecraft to the Earth's magnetospheric tail. In a more-recent design, the Instrument Champ Electrique (ICE, electric-field instrument) on the DEMETER satellite [110] used spherical electrodes with imbedded preamplifiers at 4 m from the spacecraft body, for observations from dc to 3.2 MHz. ICE is an example of the use of polarizing current to reduce sheath-impedance effects in low Earth orbit.

Notwithstanding the listed attractions of directly-coupled antennas, their limitations must be borne in mind. Concerning list point c., pre-amplification for decreasing the sheath-capacitive impedance of dipoles can affect the upper-frequency limit of operations of the antenna [103]. In addition, preamplifiers are potentially unstable when the plasma impedance is inductive, that is, in CMA regions 3, 7, or 8 [111]. The use of a preamplifier between the sphere and a guard cable on the POLAR spacecraft led to instability in spherical dipoles [112].

In regard to point d. in the list, directly-coupled antennas are electrostatic probes, and hence have nonlinear current-voltage characteristics, like solid-state diodes. Nonlinearity can lead to diode-like rectification of strong signals, resulting in confusion about the true spectrum of the waves [113]. An important question in probe design is the electrical bias to be applied, as dictated by the competing measurement objectives of wave fields versus plasma bulk parameters [114].

A general feature of the dc-to-VLF probe metrology is the variety of processes that need to be accounted for in probe-spacecraft models. Equivalent circuits are much more complicated than the lower part of Figure 2b. For instance, in the tenuous magnetosphere, where Debye shielding distances are comparatively large, concerns about photo-electron emission arise [115]. An extensive discussion of all the considerations that must intervene in the design of a probe for interpretable measurements of dc as well as wave **E** fields is beyond the scope of this paper. For further reading on physical models of electrostatic probes, see [116, 117].

Spherical double probes have been usefully employed in multiple-baseline interferometry [118, 119] although the user needs to keep in mind caveats about frequency-time measurements with linear dipoles at short wavelengths [120].

3.3 Thermal Noise, Plasma Diagnostics

The radiation resistance, R_R, shown explicitly in the bottom of Figure 2a, is part of the total antenna plasma resistance, R, which is applicable to the linear dipole whether it plays a transmitting or receiving role. In the latter case, when the constitutive relations underlying a theoretical R encompass thermal characteristics of the medium, R takes the role of a noise generator. The Nyquist noise theorem then states that an antenna in thermal equilibrium with a surrounding thermal plasma will generate noise with an rms voltage of $V_{th} = 2\left(k_B T B R_R\right)^{1/2}$, with k_B being Boltzmann's constant, T being the plasma temperature, and B being the receiver bandwidth.

The effect of plasma thermal noise on total receiver signal-to-noise ratio can be insignificant compared with the effect of front-end thermal noise, spacecraft or distant interference sources, or cosmic noise [97, 105]. However, this is not the case close to electron resonant frequencies of the plasma, particularly the lower-hybrid-resonance, upper-hybrid-resonance and cyclotron-harmonic frequencies. Recalling the adage "one person's noise is another's signal," let us note the development of the important dipole diagnostic technique of thermal noise spectroscopy, and reviews thereon [43, 121]. Measurement of local density, temperature, and drift velocity have been undertaken successfully in the solar wind and at the planets. The history of space research into radio emissions teaches that we need to be careful about distinguishing between instabilities and quasi-thermal noise along the border between equilibrium and nonequilibrium

4. Uniaxial and Isotropic Plasmas

In much of the preceding discussion, the discussion has been kept open with respect to the general case in which the frequency ratio f_{pe}/f_{ce} is not radically different from one. Very-large and very-small extremes of the ratio do occur in regions of geospace and beyond. It is worthwhile to cite some references to work on space plasmas where approximations may be made, in case the reader wants to see how the mathematics of electromagnetics works out in such cases. Some previously-referenced papers that include discussion of limiting f_{pe}/f_{ce} are re-cited here.

In uniaxial plasmas, where $f_{pe} \ll f_{ce}$, the permittivity matrix, **K**, is diagonal, and permits closed-form expressions for electromagnetic fields near a dipole [30]. Anisotropic physical optics [122] may stimulate new understanding in a reader with a background in anisotropic magnetoplasma theory. For instance, dipole impedance calculations might call on the uniaxial approximation in auroral-ionospheric density cavities where auroral kilometric radiation is created.

Considerable mathematical simplification is achieved for plasmas having $f_{pe} \gg f_{ce}$. **K** collapses to a scalar for $f \gg f_{ce}$, and the plasma is said to be isotropic. This occurs in the F region of the Earth's ionosphere, in other planetary ionospheres having low internal magnetic field, and in comets. Derivation of explicit expressions for radiated waves in a warm isotropic plasma [57] is a rather more straightforward exercise than the cold-plasma, anisotropic case [4]. Even at VLF, when nonlinear sheath effects dominate the driving-point response of a dipole, an isotropic approach to "impedance" can be invoked [85-87, 103, 123]. The next section starts with a discussion of a technique for isotropic plasmas called the surface-charge distribution (SCD) method.

5. Computer Modeling

The detailed modeling of spacecraft-plasma interactions can be undertaken when the plasma dielectric is a scalar, as evidenced by the formulation of the surface-charge distribution method [124]. This method offers a general isotropic-plasma solution of the RF **E** field near complicated spacecraft structures including dipoles. Applied to space data, the technique is useful in showing the effects of finite dipole gap and sheath-wave modes, and in evaluating double-probe impedance, effective length, and instability [112, 125-127].

Particle-in-cell (PIC) methods currently appear to be the principal tool for unified self-consistent solutions of the electromagnetic fields of complicated structures in anisotropic plasmas. In contrast to earlier methods for solving spacecraft charging in the steady state, the particle-in-cell technique is needed for following transient effects moderated by electrons, which necessitates inclusion of the full Maxwell's equations [128]. The particle-in-cell tool was applied to a study of the impedance resonance of a dipole antenna, and the role of the ion sheath therein [104]. For all the advantages of its universality, use of the particle-in-cell method entails considerable computing time and care in prescribing configurations. One-dimensional particle-in-cell codes have been applied in research on active antennas for insight into nonlinear processes in dipole near fields, including sheath nonlinearities [86] and RF acceleration of electrons [95].

Some authors have resorted to the finite-difference time-domain technique for solving the dipole response in plasmas that are neither cold nor uniform, on account of the ion sheath. The Maxwell and plasma-fluid equations have been solved in discretized time and space to yield current distributions along dipoles [129]. Based on these distributions, dipole impedances have been calculated and compared with the predictions of analytical cold-plasma theory for different values of f_{pe}/f_{ce}. The alternate use of discretized frequency may be better suited to dipoles in magnetoplasma than discretized time [67], but both approaches incur challenges in the specification of absorbing boundary conditions.

Comparatively little effort has been expended on the questions of how signal energy is injected into active dipoles from power amplifiers, and equivalently of how passive dipoles couple to receiver inputs. Concerns of this sort influence choices of analytical models for active sources [75], and how to build the device that couples signal energy from a feed cable to an antenna [130].

6. Laboratory Research

Large laboratory magnetoplasmas have been employed to investigate plasma-wave propagation theory and to measure dipole variables such as those shown in Figure 2. Laboratory propagation experiments have already been mentioned in connection with the oblique resonance [44, 45]. Laboratory research has contributed to reviews of the unique features of W-mode propagation, particularly features such as the resonance cone and magnetic-field-aligned density troughs that have been of continued interest in space plasmas [131]. The predictions of the dispersion relation for electron cyclotron waves have been found to agree with laboratory measurements of phase patterns [132]. A full treatment of nonlinear laboratory dipole effects is beyond the desired capacity of this paper, but note the reports of sounder-accelerated-particle-like particle acceleration in laboratory magnetoplasmas at the electron gyrofrequency harmonics [96, 133].

Laboratory measurements of the complex impedance at the dipole driving point have been compared with theoretical predictions such as those mentioned above in Section 2.1.3. Work by previously-cited authors [25, 134] was expanded through measurements of the impedance of a monopole oriented at various angles to the ambient dc magnetic field of a magnetoplasma [135]. Under uniaxial and other conditions, fairly good agreement with cold-plasma theory was found. Measurement precision has improved in experiments available recently in large laboratory magnetoplasmas. Observed complex impedances of a short dipole perpendicular and parallel to $\mathbf{B}_0$ were in good agreement [136] with the quasistatic theory. In addition, resonances observed in space dipole experiments reappeared here. There were plasma resonances owing to electrostatic waves and sheath effects. There were also antenna-length resonances, which were the basis of interpretation of double-pulse signatures detected in intersatellite W-mode propagation study [15]. The design of equipment for

laboratory plasma-wave research on dipoles [130] may help builders of space-borne dipoles, who can take advantage of the relatively large physical scale of equipment for space plasma-wave investigation.

7. Concluding Remarks

The purpose of this communication has been to review significant developments since the start of the space age. The references show that there was great progress during the 1960s and 1970s, when useful analytical models for dipoles were developed. These often applied the quasistatic approximation for manageable calculation of the inverse Fourier transform, which the inhomogeneous wave equation required. Research since 1980 has been less plentiful, often responding to needs to understand new data from space experiments.

Continuing attention to the dipole theory for dependable predictions of emitted and detected EM-wave amplitudes remains a worthy objective today for space-plasma physicists. This is a reasonable expectation of space research when multiple-payload projects are being planned, and when data are needed for ionosphere-magnetosphere models that include electron-wave processes. Space-plasma physicists have yet to carry out a definitive experimental investigation wherein all the important variables (current and voltage waveforms) at the dipole terminals are measured at both the emitting and receiving sites. Behind all the foregoing discussion looms one persistent and largely unmet challenge about antenna electromagnetics: we do not possess a unified theory of dipoles. Primary evidence of this lack is that – up until recently – all basic formulations known to the author started with hypotheses about antenna current distribution, in one form or other. New experiments to measure current distributions coupled with simulations – say, with the particle-in-cell technique – might rouse theoretical work on a scale reminiscent of the 1960s heyday of plasma dipoles. In certain situations, it may turn out that the greatest benefit that the particle-in-cell method will be able to confer on dipole understanding will be its ability to help the researcher go back to analytical representations of current or charge distribution and choose a good representation, rather than to provide succinct final answers.

Assumptions like the quasistatic approximation or current distribution point implicitly to an area that has not received as much attention as it might: rigorous accounting for all the wave modes that may be emitted by a dipole at a given frequency at the same time. In spite of the complexity of a Green's function that arises when, say, an expression for impedance sums over all available modes, e.g., [31], there is an engineering objective of understanding the various contributions to the total $Z = R + iX$ in Figure 2. Does the quasistatic approximation automatically select the component of Z that will dominate the series-circuit representation of all available Zs?

Studies of plasma-wave propagation evidently have predominated over antenna research in space electromagnetics. For instance, publications about the W mode, e.g., [131, 137] and references therein, say comparatively little about the details of injection and detection of that mode, even though the existing dipole literature, summarized above, makes clear that there are subtle physical effects to be aware of when analyzing W-mode dipole data. Because of the physical scale of plasma-mode wavelengths in the laboratory, measurements near or along laboratory dipoles require detection on a minute scale. Lab experiments can measure propagation away from point sources, but cannot resolve details of fields near or current distributions along dipoles. A larger and hence more physically manageable physical scale of dipoles in space plasmas makes them potentially more promising, if the challenges listed in the previous paragraph can be taken up. Proponents must find the right language to communicate the need for controlled space-plasma wave experiments in regions of parameter space that are both important for space plasma physics and inaccessible in laboratory experiments.

8. References

1. F. V. Bunkin, "On Radiation in Anisotropic Media," *Soviet Physics JETP*, **5**, 1957, pp. 277-283.

2. K. G. Balmain, "The Properties of Antennas in Plasmas," *Annales des Télécommunications*, **34**, 1979, pp. 273-283.

3. H. Kogelnik, "On Electromagnetic Radiation in Magnetoionic Media," *Journal of Research of the National Bureau of Standards – D. Radio Propagation*, **64D**, 1960, pp. 515-523.

4. H. H. Kuehl, "Electromagnetic Radiation from an Electric Dipole in a Cold Anisotropic Plasma," *Physics of Fluids*, **5**, 1962, pp. 1095-1103.

5. T. H. Stix, *Waves in Plasmas*, New York, American Institute of Physics, 1992.

6. E. Arbel, and L. B. Felsen, "Theory of Radiation from Sources in Anisotropic Media Part I General Sources in Stratified Media," in E. C. Jordan (ed.), *Proceedings of a Symposium on Electromagnetic Theory and Antennas*, New York, Pergamon, 1963, pp. 391-420.

7. L. B. Felsen and N. Marcuvitz, *Radiation and Scattering of Waves*, New York, IEEE Press, 1994.

8. A. A. Andronov, and Yu. V. Chugunov, "Quasisteady-State Electric Fields of Sources in a Dilute Plasma," *Sov. Phys.-Usp.*, **18**, 1975, pp. 343-360.

9. V. L. Ginzburg, *Propagation of Electromagnetic Waves in Plasma*, Oxford, Pergamon Press, 1964.

10. K. G. Budden, *The Propagation of Radio Waves: The Theory of Radio Waves of Low Power in the Ionosphere and Magnetosphere*, Cambridge, Cambridge University Press, 1985.

11. D. Quémada, *Ondes dans les Plasmas*, Paris, Hermann, 1968.

12. V. I. Karpman, "Electromagnetic Field Created by a Dipole Oscillator in an Anisotropic Medium," *Phys. Lett. A*, **121**, 1987, pp. 164-166.

13. M. A. Snyder, and H. Weitzner, "VLF Electromagnetic Radiation in a Magnetoionic Medium," *Radio Science*, **3**, 1968, pp. 943-954.

14. S. S. De, and A. C. Sen, "Field Solution for a Dipole in an Anisotropic Plasma Medium*," Indian Journal of Radio and Space Physics*, **16**, 1987, pp. 207-211.

15. H. G. James, "Wave Propagation Experiments at Medium Frequencies Between Two Ionospheric Satellites, 2, Whistler-Mode Pulses," *Radio Science*, **13**, 1978, pp. 543-558.

16. T. N. C. Wang, "VLF Input Impedance Characteristics of an Electric Antenna in a Magnetoplasma," Rep. no. SU-SEL-70-026, Stanford, Stanford Electronics Laboratories, 1970.

17. H. G. James, "Electromagnetic Whistler-Mode Radiation from a Dipole in the Ionosphere," *Radio Science*, **38**, 2003, doi:10.1029/2003RS002609.

18. R. E. Horita, and H. G. James, "Two-Point Studies of Fast Z-Mode Waves with Dipoles in the Ionosphere," *Radio Science*, **39**, 2004, RS4001, doi:10.1029/2003RS002994.

19. H. G. James, "Wave Propagation Experiments at Medium Frequencies Between Two Ionospheric Satellites, 1, General results," *Radio Science*, **13**, 1978, pp. 531-542.

20. P. Prikryl, H. G. James, D. J. Knudsen, S. C. Franchuk, H. C. Stenbaek-Nielsen, and D. D. Wallis, "OEDIPUS-C Topside Sounding of a Structured Auroral E Region," *Journal of Geophysical Research*, **105**, 2000, pp. 193-204.

21. H. G. James, and W. Calvert, "Interference Fringes Observed on OEDIPUS C," *Radio Science*, **33**, 1998, pp. 617-629.

22. S. A. Cummer, M. J. Reiner, B. W. Reinisch, M. L. Kaiser, J. L. Green, R. F. Benson, R. Manning, and K. Goetz, "A Test of Magnetospheric Radio Tomographic Imaging with IMAGE and WIND," *Geophys. Res. Lett*., **28**, 2001, pp. 1131-1134.

23. T. N. C. Wang, and T. F. Bell, "VLF/ELF Radiation Patterns of Arbitrarily Oriented Electric and Magnetic Dipoles in a Cold Lossless Multicomponent Magnetosplasma," *Journal of Geophysical Research ,* **77**, 1972, 1174-1189.

24. D. T. Nakatani, and H. H. Kuehl, "Input Impedance of a Short Dipole in a Warm Anisotropic Plasma," 1 Kinetic Theory," *Radio Science*, **11**, 1976, pp. 433-444.

25. K. G. Balmain, "The Impedance of a Short Dipole Antenna in a Magnetoplasma," *IEEE Transactions on Antennas and Propagation*, **AP-12**, 1964, pp. 606-617.

26. P. Meyer, and N. Vernet, "Impedance of a Short Antenna in a Warm Magnetoplasma," *Radio Science*, **9**, 1974, pp. 409-416.

27. H. Staras, "The Impedance of an Electric Dipole in a Magneto-Ionic Medium," *IEEE Transactions on Antennas and Propagation*, **AP-12**, 1964, pp. 695-702.

28. P. Nikitin, and C. Swenson, Impedance of a Short Dipole Antenna in a Cold Plasma*," IEEE Transactions on Antennas and Propagation*, **49**, 2001, pp. 1377-1381.

29. S. R. Seshadri, "Radiation Resistance of Elementary Electric-Current Sources in a Magnetoionic Medium," *Proceedings of the Institute of Electrical Engineers, London*, **112**, 1965, pp. 1856-1868.

30. J. Galejs, "Impedance of a Finite Insulated Cylindrical Antenna in a Cold Plasma with a Longitudinal Magnetic Field," *IEEE Transactions on Antennas and Propagation.*, **AP-14**, 1966, pp. 727-736.

31. W. S. Ament, J. C. Katzin, M. Katzin, and B. Y.-C. Koo, Impedance of a Cylindrical Dipole Having a Sinusoidal Current Distribution in a Homogenous Anisotropic Ionosphere, *Radio Science*, **68D**, 1964, pp. 379-405.

32. R. G. Stone, J. K. Alexander, and R. R. Weber, "Measurements of Antenna Impedance in the Ionosphere II. Observing Frequency Greater than the Electron Gyro Frequency," *Planet. Space Sci*., **14**, 1966, pp. 1007-1016.

33. S. Adachi, T. Ishizone, and Y. Mushiake, "Transmission Line Theory of Antenna Impedance in a Magnetoplasma," *Radio Science*, **12**, 1977, pp. 23-31.

34. H. G. James, "Tests of Impedance Theories for a Transmitting Dipole in an Ionospheric Plasma," *IEEE Transactions on Antennas and Propagation*, **AP-28**, 1980, pp. 623-630.

35. E. K. Miller, and H. F. Schulte, Jr., "Antenna Admittance in an Ionospheric-Type Plasma," Scientific Report 05627-18-S, Ann Arbor, University of Michigan, 1968.

36. N. Meyer-Vernet, "Impedance of a Short Antenna in a Warm Magnetoplasma: Experiment and Comparison with Theory," *Radio Science*, **13**, 1978, pp. 1059-1068.

37. T. N. C. Wang and T. F. Bell, "Radiation Resistance of a Short Dipole Immersed in a Cold Magnetoionic Medium," *Radio Science*, **4** , 1969, pp. 167-177.

38. K. Rönnmark, "Computation of the Dielectric Tensor of a Maxwellian Plasma," *Plasma Physics*, **25***,* 1983, pp. 699-701.

39. D. B. Muldrew, "Electron Resonances Observed with Topside Sounders," *Radio Science*, **7**, 1972, pp. 779-789.

40. R. F. Benson, "Stimulated Plasma Instability and Nonlinear Phenomena in the Ionosphere," *Radio Science*, **17**, 1982, pp. 1637-1659.

41. R. F. Benson, "Four Decades of Space-Borne Radio Sounding*, Radio Science Bulletin*, No. 333, 2010, pp. 24-44.

42. Yu. V. Chugunov, "The Reactance of an Antenna in a Magnetoplasma*," Izvestiya VUZ. Radiofizika*, **11**, 1968, pp. 50-55.

43. N. Meyer-Vernet, and C. Perche, "Tool Kit for Antennas and Thermal Noise near the Plasma Frequency," *Journal of Geophysical Research*, **94**, 1989, pp. 2405-2415.

44. R. K. Fisher, and R. W. Gould, "Resonance Cones in the Field Pattern of a Radio Frequency Probe in a Warm Magnetoplasma," *Physics of Fluids*, **14**, 1971, pp. 857-867.

45. A. Gonfalone, and C. Béghin, "Excitation of Quasicylindrical Waves Connected with Bernstein Waves," *Physical Review Letters*, **31**, 1973, pp. 866-870.

46. D. B. Muldrew, "Dispersion Relation and Group Velocity for Inhomogeneous Waves in a Hot Magnetoplasma with Application to an Electron-Bernstein-Wave Propagation Experiment in a Laboratory Plasma," *Radio Science*, **45**, 2010, RS3004, doi: 10.1029/2009RS004254.

47. H. H. Kuehl, "Electric Field and Potential Near the Plasma Resonance Cone," *Physics of Fluids*, **17**, 1974, pp. 1275-1283.

48. E. A. Mareev, and Yu. V. Chugunov, "Excitation of Plasma Resonance in Magnetoactive Plasma by an External Source," *Radio Physics and Quantum Electronics*, **30**, 1987, pp. 713-718.

49. H. C. Koons, D. C. Pridmore-Brown, and D. A. McPherson, "Oblique Resonances Excited in the Near Field of a Satellite-Borne Electric dipole Antenna*," Radio Science*, **9**, 1974, pp. 541-545.

50. E. Michel, C. Béghin, A. Gonfalone, and I. F. Ivanov, "Mesures de Densité et de Température Electroniques sur Fusée dans l'Ionosphère Polaire par l'Etude du Cône de Résonance," Annales de Géophysique, **31**, 1975, pp. 463-471.

51. V. Rohde, A. Piel, H. Thiemann, and K. I. Oyama, "In-Situ Diagnostics of Ionospheric Plasma with the Resonance Cone Technique," *Journal of Geophysical Research*, **98**, 1993, pp. 19,163-19172.

52. L. R. O. Storey, M.P. Aubry, and P. Meyer, "A Quadripole Probe for the Study of Ionospheric Plasma Resonances," in B. J. Landmark and J. O. Thomas (ed.), *Plasma Waves in Space and in the Laboratory*, Edinburgh, Edinburgh University Press, 1969, pp. 303-332.

53. C. Béghin, "Excitation de la Résonance Hybride Basse (LHR) par Sonde Quadripolaire à bord d'une Fusée, *Space Research XI*, Berlin, Akademie-Verlag, 1971, pp. 1071-1078.

54. O. Storey, and R. Pottelette, "Possibilités d'Utiliser la Sonde Quadripolaire pour la Mesure de Courants Electriques dans la Magnétosphère," *Comptes Rendus de l'Academie Française Paris (Sér. B)*, **273**, 1971, pp. 101-104.

55. L. R. O. Storey, "Mutual-Impedance Techniques for Space-Plasma Measurements," in R. F. Pfaff, J. E. Borovsky, and D. T. Young (eds.), *Measurement Techniques in Space Plasmas*, Washington, American Geophysical Union, 1998, pp. 155-160.

56. L. R. O. Storey and L. Cairó, "Measurement of Plasma Resistivity at ELF," in R. F. Pfaff, J. E. Borovsky, and D. T. Young (eds.), *Measurement Techniques in Space Plasmas*, Washington, American Geophysical Union, 1998, pp. 155-160.

57. H. H. Kuehl, "Excitation of Waves in a Warm Plasma by a Current Source," *Physics of Fluids*, **6**, 1963, pp. 1465-1469.

58. S. I. Zaitsev, and G. A. Lupanov, "Wave Radiation by an Oscillating Electric Dipole in a Moving "Warm" Plasma, *Radio Physics and Quantum Electronics*, **22**, 1980, pp. 550-556, doi: 10.1007/BF01033557.

59. C. Béghin, J. F. Karczewski, B. Poirier, R. Debrie, and N. Massevitch, "The ARCAD-3 ISOPROBE Experiment for High Time Resolution Thermal Plasma Measurements," *Annales de Géophysique*, **38**, 1982, pp. 615-629.

60. L. R. O. Storey, "Antenne Electrique Dipole pour Réception TBF dans l'Ionosphère," *L' Onde Électrique*, **45**, 1965, pp. 1427-1435.

61. T. R. Kaiser, "The Admittance of an Electric Dipole in a Magneto-Ionic Environment," *Radio Science*, **9**, 1962, pp. 639-637.

62. H. C. Koons, D. A. McPherson, and W. B. Harbridge, "Dependence of Very-Low-Frequency Electric Field Antenna Impedance on Magnetospheric Plasma Density," *Journal of Geophysical Research*, **75**, 1970, pp. 2490-2502.

63. K. G. Balmain, "Dipole Admittance for Magnetoplasma Diagnostics," *IEEE Transactions on Antennas and Propagation*, **AP-17**, 1969, pp. 389-392.

64. U. S. Inan, T. F. Bell, J. Bortnik, and J. M. Albert, "Controlled Precipitation of Radiation Belt Electrons," *Journal of Geophysical Research*, **108**, 2003, 1186, doi:10.1029/2002JA009580.

65. T. F. Bell, U. S. Inan, and T. Chevalier, "Current Distribution of a VLF Electric Dipole Antenna in the Plasmasphere," *Radio Science*, **41**, RS2009, doi:10.1029/2005RS003260.

66. E. Hallén, "Theoretical Investigations into the Transmitting and Receiving Qualities of Antennae," *Nova Acta Regiae Societatis Scientiarum Upsaliensis-, Ser. IV*, **11**, 1938, pp. 1-44.

67. T. W. Chevalier, U. S. Inan, and T. W. Bell, "Terminal Impedance and Antenna Current Distribution of a VLF Electric Dipole in the Inner Magnetosphere," *IEEE Transactions on Antennas and Propagation*, **56**, 2008, pp. 2454-2468.

68. P. Stubbe, and H. Kopka, "Modulation of Polar Electrojet by Powerful HF Waves," *Journal of Geophysical Research*, **82**, 1977, pp. 2319-2325.

69. R. Barr, P. Stubbe, M. T. Rietveld, and H. Kopka, "ELF and VLF Signals Radiated by the "Polar Electrojet Antenna: Experimental Results," *Journal of Geophysical Research*, **91**, 1986, pp. 4451-4459.

70. H. G. James, U. S. Inan, and M. T. Rietveld, "Observations on the DE 1 Spacecraft of ELF/VLF Waves Generated by an Ionospheric Heater," *Journal of Geophysical Research*, **95**, 1990, pp. 12187-12195.

71. M. Platino, U. S. Inan, T. F. Bell, M. Parrot, and E. J. Kennedy, "DEMETER Observations of ELF Waves Injected with the

HAARP HF Transmitter," *Geophys. Res. Lett*., **33**, L16101, 2006, doi:10.1029/2006GL026462.

72. J. A. Payne, U. S. Inan, F. R. Foust, T. W. Chevalier, and T. F. Bell, "HF Modulated Ionospheric Currents," *Geophys. Res. Lett.*, **34**, L23101, doi: 10129/2007GL 031724.

73. Y. Mushiake, "Electromagnetic Waves Along an Infinitely Long and Thin Conducting Wire in a Magnetoionic Medium," *Radio Science*, **69D**, 1965, pp. 503-510.

74. H. G. James, and K. G. Balmain,, "Guided Electromagnetic Waves Observed on a Conducting Ionospheric Tether," *Radio Science*, **36**, 2001, pp. 1631-1644.

75. A. V. Kudrin, E. Yu. Petrov, G. A. Kyriacou, and T. M. Zaboronkova, "Insulated Cylindrical Antenna in a Cold Magnetoplasma," *Progress in Electromagnetic Research*, **PIER 53**, 2005, pp. 135-166.

76. D. Mourenas, and C. Béghin, "Packets of Cyclotron Waves Induced by Electron Beam Injection from the Space Shuttle. 1. Linear Theory," *Radio Science*, **26**, 1991, pp. 469-479.

77. Yu. V. Chugunov, and G. A. Markov, "Active Plasma Antenna in the Earth's Ionosphere," *J. Atmos. Solar-Terr. Phys.*, **63**, 2001, pp. 1775-1787.

78. H. G. James, "Slow Z-Mode Radiation from Sounder-Accelerated Electrons," *J. Atmos. Solar-Terr. Phys.*, **66**, 2004, pp. 1755-1765.

79. D. B. Muldrew, "Topside Sounder Proton-Cyclotron Echo Generation from a Plasma Memory Process and Electron Bernstein-Wave Propagation," *Radio Science*, **33**, 1998, pp. 1395-1411.

80. D. B. Muldrew, "The Poynting Vector Applied to the Complex Refractive Index in a Hot Plasma near the Electron Cyclotron Frequency and to the Cyclotron Resonance Observed on Topside Ionograms," *Radio Science*, **41**, 2006, RS2006, doi:10.1029/2006RS003496.

81. G. L. Nelms and G. E. K. Lockwood, "Early Results from the Topside Sounder in the Alouette II Satellite," in R. L. Smith-Rose (ed.), *Space Research VII*, Amsterdam, North-Holland Publishing Co., 1967, pp. 604-623.

82. H. Oya, "Sequence of Diffuse Plasma Resonances Observed on Alouette 2 Ionograms," *Journal of Geophysical Research*, **75**, 1970, pp. 4279-4285.

83. S. A. Pulinets, and V. V. Selegey, "Ionospheric Plasma Modification in the Vicinity of a Spacecraft by Powerful Radio Pulses in Topside Sounding," *J. Atmos. Terr. Phys.*, **48**, 1986, pp. 149-157.

84. H. G. James, "Nonlinear Signal Enhancements of Medium-Frequency Electromagnetic Transmissions in the Ionosphere," *Radio Science*, **23**, 1988, pp. 666-684.

85. P. Song, B. W. Reinisch, V. Paznukhov, G. Sales, D. Cooke, J.-N. Tu, X. Huang, K. Bibl, and I. Galkin (2007), "Highvoltage Antenna-Plasma Interaction in Whistler Wave Transmission: Plasma Sheath Effects," *Journal of Geophysical Research.*, **112**, 2007, doi:10.1029/2006JA011683.

86. J. Tu, P. Song, and B. W. Reinisch, "Plasma Sheath Structures around a Radio Frequency Antenna," *Journal of Geophysical Research*, **113**, 2008, doi:10.1029/2008JA013097.

87. V. V. Paznukhov, G. S. Sales, K. Bibl, B. W. Reinisch, P. Song, X. Huang, and I. Galkin, "Impedance Characteristics of an Active Antenna at Whistler-Mode Frequencies," *Journal of Geophysical Research*, **115**, 2010, A09212, doi: 10.1029/2009JA014889.

88. Yu. I. Gal'perin, R. Z. Sagdeev, F. K. Shuiskaya, Y. V. Lisakov, V. V. Migulin, Yu. V. Kushnerevskii, M. D. Fligel, and G. V. Vasil'ev, "Detection of Electron Acceleration in the Ionospheric Plasma under the Influence of High-Power Radio Radiation near the Local Plasma Frequency Aboard the Space Vehicle Interkosmos 19," *Cosmic Research*, **19**, 1981, pp. 22-29.

89. F. K. Shuiskaya, Yu. I. Galperin, A. A. Serov, N. V. Baranets, Yu. V. Kushnerevsky, G. V. Vasil'ev, S. A. Pulinets, M. D. Fligel, and V. V. Selegey, "Resonant Heating of the Ionospheric Plasma by Powerful Radiopulses Aboard the Intercosmos-19 and Cosmos-1809 Satellites," *Planetary and Space Science*, **38**, 1990, pp. 173-180.

90. N. V. Baranets, V. A. Gladyshev, and V. V. Afonin, "Effect of HF Emission of the Topside Sounder Transmitter aboard the Cosmos-1809 Satellite on the Ionospheric Plasma," *Advances in Space Research*, **15**, 1995, pp. (12)95-(12)98.

91. H. G. James, "Sounder-Accelerated Particles Observed on ISIS," *Journal of Geophysical Research*, **88**, 1983, pp. 4027-4040.

92. H. G. James, V. I. Sotnikov, W. J. Burke and C. Y. Huang, "OEDIPUS-C Observations of Electrons Accelerated by Radio Frequency Fields at Whistler-Mode Frequencies," *Physics of Plasmas*, **6**, 1999, pp. 4058-4069.

93. C. Y. Huang, W. J. Burke, D. A. Hardy, M. P. Gough, H. G. James, E. Villalón and L. C. Gentile, Electron Acceleration by Megahertz Waves during OEDIPUS C," *Journal of Geophysical Research*, **106**, 2001, 1835-1847.

94. A. A. Serov, Yu. I. Gal'perin, Yu. V. Lisakov, and F. K. Shuiskaya, "Local Acceleration of Electrons of the Plasma near a Satellite by the Radio Emission of a Powerful on-board Transmitter," *Cosmic Research*, **23**, 1985, pp. 361-372.

95. M. E. Dieckmann, G. Rowlands, B. Eliasson, and P. Shukla, "Particle-in-Cell Simulations of Electron Acceleration by a Simple Capacitative Antenna in Collisionless Plasma," *Journal of Geophysical Research*, **109**, A12304, 2004, doi:10.1029/2004JA010436.

96. M. E. Gushchin, S. V. Korobkov, A. V. Kostrov, D. A. Oderikho, S. E. Priver, and A. V. Strikovskii, "Parametric Generation of Low-Frequency Waves by Plasma Electrons Accelerated under Electron Cyclotron resonance Conditions," *JETP Letters*, **92**, 2010, pp. 85-90.

97. E. C. Jordan, and K. G. Balmain, *Electromagnetic Waves and Radiating Systems*, *Second Edition*, Englewood Cliffs, NJ, Prentice-Hall, 1968.

98. Yu. V. Chugunov, "Receiving Antenna in a Magnetoplasma in the Resonance Frequency Band," *Radiophysics and Quantum Electronics*, **44**, 2001, pp. 151-160.

99. H. G. James, "Dipole Measurements of Waves in the Ionosphere," *Lecture Notes Physics*, **687**, 2006, pp. 191-210.

100. H. G. James, "Electrostatic Resonance-Cone Waves Emitted by a Dipole in the Ionosphere," *IEEE Transactions on Antennas and Propagation*, **AP-48**, 2000, pp. 1340-1348.

101. Yu. V. Chugunov, E.A. Mareev, V. Fiala, and H.G. James, "Transmission of Waves near the Lower Oblique Resonance Using Dipoles in the Ionosphere," *Radio Science*, **38**, 2003, 1022, doi:10.1029/2001RS002531.

102. Y. V. Chugunov, and V. Fiala, "Effective Length of a Receiving Antenna in a Streaming Plasma," *IEEE Transactions on Antennas and Propagation*, **AP-54**, 2006, pp. 2750-2756.

103. R. Manning, "A Simulation of the Behavior of a Spherical Probe Antenna in an AC Field," in R. F. Pfaff, J. E. Borovsky, and D. T. Young (eds.), *Measurement Techniques in Space Plasmas*, Washington, American Geophysical Union, 1998, pp. 181-184.

104. Y. Miyake, H. Usui, H. Kojima, Y. Omura, and H. Matsumoto, "Electromagnetic Particle-in-Cell Simulation on the Impedance of a Dipole Antenna Surrounded by an Ion Sheath," *Radio Science*, **43**, RS3004, doi:10.1029/2007RS003707.

105. D. A. Gurnett, "Principles of Space Plasma Wave Instrument Design," in R. F. Pfaff, J. E. Borovsky, and D. T. Young (eds.), *Measurement Techniques in Space Plasmas*, Washington, American Geophysical Union, 1998, pp. 121-136.

106. F. S. Mozer, "Analysis of Techniques for Measuring DC and AC Electric Fields in the Magnetosphere," *Space Science Reviews*, **14**, 1973, pp. 272-313.

107. N. C. Maynard, "Electric Field Measurements in Moderate to High Density Space Plasmas with Passive Double Probes," in R. F. Pfaff, J. E. Borovsky, and D. T. Young (eds.), *Measurement Techniques in Space Plasmas*, Washington, American Geophysical Union, 1998, pp. 13-27.

108. R. J. L. Grard, and J. K. E. Tunaley, "The Impedance of the Electric Dipole Aerial on the FR-1 Satellite," *Ann. Géophysique*, **24**, 1968, pp. 49-61.

109. H. Matsumoto, I. Nagano, R. R. Anderson, H. Kojima, K. Hashimoto, M. Tsutsui, T. Okada, I Kimura, Y. Omura, and M. Okada, "Plasma Wave Observations with GEOTAIL Spacecraft," *J. Geomag. Geoelectr*., **46**, 1994, pp. 59-95.

110. J.-J. Berthelier, M. Godefroy, F. Leblanc, M. Malingre, M. Menvielle, D. Lagoutte, J. Y. Brochot, F. Colin, F. Elie, C. Legendre, P. Zamora, D. Benoist, Y. Chapuis, J. Artru, and R. Pfaff, "ICE, the Electric Field Experiment on DEMETER," *Planet. Space Sci*., **54**, 2006, 456-471.

111. V. Fiala, "Stabilité des Antennes Electriques du Satellite FR1 dans le Plasma Ionosphérique," *Annales des Télécommunications*, **25**, 1970, pp. 259-264.

112. E. Kolesnikova, C. Béghin, R. Grard and C. P. Escoubet, The Electrical Stability of the Electric Field Antennas in the Plasmasphere," *J. Atmos. Solar-Terr. Phys.*, **63**, 2001, pp. 1217-1224.

113. M. H. Boehm, C. W. Carlson, J. P. McFadden, J. H. Clemmons, R. E. Ergun, and F. S. Mozer, "Wave Rectification in Plasma Sheaths Surrounding Electric Field Antennas," *Journal of Geophysical Research*, **99**, 1944, pp. 21,361-21,374, doi:10.1029/94JA01766.

114. A. I. Eriksson, and R. Boström, "Wave Measurements using Electrostatic Probes: Accuracy Evaluation by Means of a Multiprobe Technique," in R. F. Pfaff, J. E. Borovsky, and D. T. Young (eds.), *Measurement Techniques in Space Plasmas*, Washington, American Geophysical Union, 1998, pp. 149-153.

115. A. Pedersen, C. A. Cattell, C.-G. Fälthammar, V. Formisano, P.-A. Lindqvist, F. Mozer, and R. Torbert, "Quasistatic Electric Field Measurements with Spherical Double Probes on the GEOS and ISEE Satellites," *Space Science Reviews*, **37**, 1984, pp. 269-312.

116. R. Godard, and J. G. Laframboise, "Total Current Flow to Cylindrical Collectors in Collisionless Plasma Flow," *Planetary and Space Science*, **31**, 1983, pp. 275-283.

117. J. G. Laframboise, and L. J. Sonmor, "Current Collection by Probes and Electrodes in Space Magnetoplasmas: a Review," *Journal of Geophysical Research*, **98**, 1993, pp. 337-357.

118. P. M. Kintner, P. W. Schuck, and J. R. Franz, "Space Measurements and Progress in Understanding Space Plasma Waves," *Phys. Plasmas*, **7**, 2000, doi:10.1063/1.874033.

119. R. F. Pfaff, and P. A. Marionni, "Multiple-Baseline Spaced Receivers," in R. F. Pfaff, J. E. Borovsky, and D. T. Young (eds.), *Measurement Techniques in Space Plasmas*, Washington, American Geophysical Union, 1998, pp. 161-167.

120. P. M. Kintner, "Plasma Wave Measurements: Skepticism and Plausibility," in R. F. Pfaff, J. E. Borovsky, and D. T. Young (eds.), *Measurement Techniques in Space Plasmas*, Washington, American Geophysical Union, 1998, pp. 137-145.

121. N. Meyer-Vernet, S. Hoang, K. Issautier, M. Maksimovic, R. Manning, M. Moncuquet, and R. G. Stone, "Measuring Plasma Parameters, with Thermal Noise Spectroscopy," in R. F. Pfaff, J. E. Borovsky, and D. T. Young (eds.), *Measurement Techniques in Space Plasmas*, Washington, American Geophysical Union, 1998, pp. 205-210.

122. J. J. Stamnes, and G. C. Sherman, "Radiation of Electromagnetic Fields in Uniaxially Anisotropic Media," *J. Opt. Soc. Am.*, **66**, 1976, pp. 780-788.

123. D. J. Baker, H. Weil, and L. S. Bearce, "Impedance and Large Signal Excitation of Satellite-Borne Antennas in the Ionosphere," *IEEE Transactions on Antennas and Propagation*, **AP-21**, 1973, pp. 672-679.

124. C. Béghin, and E. Kolesnikova, "Surface-Charge Distribution Approach for Modeling of Quasi-Static Electric Antennas in Isotropic Thermal plasma," *Radio Science*, **33**, 1998, pp. 503-516, doi: 10.1029/97RS03588.

125. E. Kolesnikova, and C. Béghin, "Application of the Surface-Charge Distribution Method to the Interpretation of Impedance Measurements of a Rocket-Borne Dipole Antenna," *Radio Science*, **33**, 1998, pp. 491-502, doi:10.1029/97RS03589.

126. C. Béghin, P. M. E. Décréau, J. Pickett, D. Sundkvist, and B. Lefebvre," Modeling of Cluster's Electric Antennas in Space: Application to Plasma Diagnostics," *Radio Science*, **40**, RS6008, 2005, doi:10.1029/2005RS003264.

127. J. Geiswiller, C. Béghin, E. Kolesnikova, D. Lagoutte, J. L. Michau, and J. G. Trotignon, "Rosetta Spacecraft Influence on the Mutual Impedance Probe Frequency Response in the Long Debye Length Mode," *Planetary and Space Science*, **49**, 2001, pp. 633-644.

128. H. Usui, Y. Miyake, M. Okada, Y. Omura, T. Sugiyama, K. T. Murata, D. Matsuoka, and H. O. Ueda, "Development and Application of Geospace Environment Simulator for the Analysis of Spacecraft-Plasma Interactions, *IEEE Trans. Plasma Sci.*, **34**, 2006, pp. 2094-2102.

129. J. Ward, C. Swenson, and C. Furse, "The Impedance of a Short Dipole Antenna in a Magnetized Plasma via a Finite Difference Time Domain Model," *IEEE Transactions on Antennas and Propagation*, **AP-53**, 2005, pp. 2711-2718.

130. P. Pribyl, W. Gekelman, and A. Gigliotti, "Direct Measurement of the Radiation Resistance of a Dipole Antenna in the Whistler/ Lower Hybrid Wave Regime," *Radio Science*, **45**, 2010, RS4013, doi: 10.1029/2009RS004266.

131. R. L. Stenzel, Whistler Waves in Space and Laboratory Plasma, *Journal of Geophysical Research*, **104**, 1999, pp. 14379-14395.

132. B. Lembège, "Antenna Radiation Pattern of Cyclotron Harmonic Waves in a Hot Magnetoplasma," *Radio Science*, **14**, 1979, pp. 487-502.

133. S. Sasaki, O. Kaneko, and N. Kawashima, "Laboratory Experiment on the Excitation of Electron Cyclotron Harmonic Waves Observed in the Topside RF Sounder Experiment," *Radio Science*, **13**, 1978, pp. 753-762.

134. D. T. Nakatani, and H. H. Kuehl, "Input Impedance of a Short Dipole in a Warm Anisotropic Plasma, 2, Experiment," *Radio Science*, **11**, 1976, pp. 517-529.

135. K. Sawaya, T. Ishizone, and Y. Musiake, "Measurement of the Impedance of a Linear Antenna in a Magnetoplasma," *Radio Science*, **13**, 1978, pp. 21-29.

136. D. D. Blackwell, D. N. Walker, S. J. Messer, and W. E. Amatucci, "Antenna Impedance Measurements in a Magnetized Plasma. II. Dipole Antenna," *Phys. Plasmas*, **14**, 2007, pp. 092106-1- 092106-8.

137. S. Sazhin, *Whistler-Mode Waves in a Hot Plasma*, 1993, Cambridge, Cambridge University Press.

Radio-Frequency Radiation Safety and Health

James C. Lin

ICNIRP and its Role in Setting Guidelines for Radio-Frequency Exposure - The Most Successful Application of Electromagnetics in Biology and Medicine : Magnetic Resonance Imaging

1. Introduction

An overview of the International Non-Ionizing Radiation Protection Commission (ICNIRP) and its role in setting guidelines for radio frequency fields is presented. This article begins with a brief description of the genesis of ICNIRP, and discusses its activities in support of its aims to disseminate information and advice on the potential health hazards from exposure to non-ionizing radiation. It is noted that the products of ICNIRP are published in the form of recommendations for exposure guidelines, scientific reviews and reports, and the proceedings of scientific meetings. ICNIRP also publishes statements providing information and advice on specific topics of non-ionizing-radiation protection and/or radiation-protection issues related to specific devices or exposure situations. Relevant ICNIRP guidelines pertaining to magnetic resonance imaging (MRI) are brief summarized. While exposure guidelines have been promulgated for MRI operations, there are a number of challenges that warrant further consideration.

2. What Is ICNIRP?

The International Non-Ionizing Radiation Protection Commission (ICNIRP) is an independent group of experts with the responsibility for evaluating the state of knowledge about the effects of non-ionizing radiation (NIR) on human health and well being. They also provide science-based advice and recommendations on protection against harmful effects of non-ionizing radiation, including static electric and magnetic fields, radio-frequency waves, visible light, and ultraviolet radiation.

The Commission began as the International Non-Ionizing Radiation Committee, through an initiative of the International Radiation Protection Association (IRPA) in 1977. It was reorganized as an independent commission with a charter adopted by the IRPA General Assembly held in Montreal, Canada, in May 1992.

3. ICNIRP's Role

ICNIRP's scope of activity includes analyzing physical characteristics of non-ionizing radiation and reports of biological effects from exposure to non-ionizing radiation; recommending appropriate terminology, quantities, units, and methods of measurement; developing protection criteria; recommending systems of protection against non-ionizing radiation, including appropriate exposure limits; providing guidance for the protection of workers, members of the public, patients, and the environment; and issuing statements, recommendations, and papers on selected topics as appropriate, including reports on the application of ICNIRP recommendations.

The commission operates through a main commission with 14 members. These include a Chair and a Vice Chair, who are individual experts representing neither their countries nor their institution; four standing committees; and a large group of consulting experts. The Main Commission consists of a Chair, Vice Chair, and up to 12 members. Commission members are individual experts representing neither their countries nor their institution. Current members of the commission come from 11 different countries, and are elected upon nomination by members of the commission, the Executive Council of IRPA, or IRPA Associate Societies. The election takes place every four years at the last Annual General Meeting before the IRPA Congress. The four standing committees are SCI on epidemiology, SCII on biology and medicine, SCIII on physics and engineering, and SCIV on optical radiation. The scientific expertise of ICNIRP members includes medicine, dermatology, ophthalmology, epidemiology, biology, photobiology, physiology, physics, electrical engineering, and metrology.

James C. Lin is with the University of Illinois-Chicago, 851 South Morgan Street, M/C 154, Chicago, IL 60607-7053 USA; Tel: +1 (312) 413-1052 (direct); +1 (312) 996-3423 (main office); Fax: +1 (312) 996-6465; E-mail: lin@ece.uic.edu.

	Exposure Domain	Magnetic Flux Density
Occupational	Head and Trunk	2 T
	Limbs	8 T
General Public	Any Part of the Body	400 mT

Table 1. ICNIRP guidelines on limits of exposure to static magnetic fields (2009).

ICNIRP performs its work in collaboration with a number of regional and international partners and scientific organizations. ICNIRP works closely with the World Health Organization (WHO), through two non-ionizing radiation and health programs: the International EMF Project and the INTERSUN Project. ICNIRP also collaborates closely with the International Labor Organization (ILO) on matters relating to occupational non-ionizing radiation protection. It is officially recognized by WHO and ILO as the international independent advisory body for non-ionizing radiation protection. ICNIRP also collaborates with the European Council (EC), principally DG SANCO (Health), with the European Society for Skin Cancer Prevention (EUROSKIN), the International Commission on Illumination (CIE), and the International Commission for Occupational Hygiene (ICOH), among others.

The products of ICNIRP in fulfilling its aims to disseminate information and advice on the potential health hazards from exposure to non-ionizing radiation are published in the form of scientific reviews and reports and the proceedings of scientific meetings. The reviews, combined with risk assessments conducted in collaboration with WHO, result in the recommendation by ICNIRP of exposure guidelines. Examples of these are guidelines limiting exposure to electromagnetic fields, to lasers and incoherent optical radiation, and to ultraviolet radiation. ICNIRP also publishes statements providing information and advice on specific topics of non-ionizing radiation protection and/or radiation-protection issues related to specific devices or exposure situations.

4. Magnetic Resonance Relevant Exposure Guidelines

Operation of magnetic resonance (MR) equipment for clinical applications involves static, gradient, and radio-frequency magnetic fields. Relevant ICNIRP guidelines are briefly summarized in what follows.

4.1 Guidelines for Exposure to Static Magnetic Fields

There are two very challenging questions when developing guidelines for static fields. These are the transient sensory effects with no known long-term or deleterious consequences, and the concern about lack of knowledge about human exposures higher than those for which there is data. In recommending the exposure limits, ICNIRP considers that there are occupational situations where – with appropriate instruction and guidance – it is realistic for workers voluntarily and knowingly to come across possible momentary sensory effects such as nausea, since they are not deemed to lead to health effects. ICNIRP considers that the exposures allowed under the guidelines should be based on scientific data, and should not go higher than those for which there is information. However, it accepts that for investigational purposes, it might be desirable to explore possible effects at higher levels; such experimental exposures should be a matter for institutional ethics committees.

The limits recommended by ICNIRP for general public and occupational exposures to static magnetic fields are summarized in Table 1 [1], which supersede those published by ICNIRP in 1994 [2]. Based on available scientific data on the direct effects of static fields on humans, acute exposure of the general public should not exceed a spatial peak magnetic-flux density of 400 mT for any part of the body and for all members of the population. However, ICNIRP recognizes that practical policies need to be implemented to avoid potential harmful exposure of persons with implanted electronic medical devices and with implants containing ferromagnetic materials, and injuries due to flying ferromagnetic objects. These considerations can lead to much lower restriction levels, such as 0.5 mT [3]. The exposure limits to be set with regard to these inadvertent effects are beyond the purview of ICNIRP. The exposure limit for the general public represents a reduction

Operating Mode	Exposure Limit (Whole Body)	Comment
Normal (Routine)	4 T	Including fetus and infant
Controlled (Specific)	8 T	Under medical supervision (potential discomfort/adverse effect)
Experimental	> 8 T	Special ethical approval (cardiovascular flow potential)

Threshold for motion-induced vertigo and nausea: 1 T/s for 1 s

Table 2. ICNIRP recommendation for patients in static magnetic fields.

a factor of five with respect to the occupational limit for the head and trunk, which is 2 T. When restricted to the limbs, maximum exposures of up to 8 T are permissible. For work-related circumstances for which exposures above 2 T are deemed necessary, exposure up to 8 T can be accepted if the situation is managed and appropriate work practices are implemented to control movement-induced effects.

4.2 Recommendations for Patients in Static Magnetic Field

An ICNIRP statement on the protection of patients undergoing medical MR procedures was published in 2004 [4]. Since its publication, there have been many studies on the health effects of exposure to the high-strength static magnetic fields used in newer generations of magnetic resonance systems. Although the advice concerning patient exposure to switched-gradient fields remains unchanged, ICNIRP decided to issue an amendment of the statement concerning patient exposure to static magnetic fields in 2009. As in 2004, the statement is intended for use by national and international medical-device regulatory authorities, magnetic resonance users and health professionals, and those involved in the design and manufacture of magnetic resonance equipment for clinical applications.

The recommendation for protection of patients in static magnetic fields is summarized in Table 2 [5]. The three-tiered approach used previously is still considered appropriate, including routine diagnostic imaging. Additionally, it provides flexibility for new investigations and for further development of clinical procedures at higher field strengths. Based on this scheme, a whole-body limit of 4 T is recommended for routine magnetic resonance examinations for all patients under the normal operating mode. It is noted that a knowledge gap remains regarding the effects of static magnetic fields in excess of 4 T on the growth and development of fetuses and infants, and therefore some caution may be warranted regarding their imaging above 4 T. Moreover, caution may be warranted for specific magnetic resonance examinations of all patients outside the normal operating range, where discomfort and/or adverse effects for some patients may occur. A clinical decision must be made to balance perceived medical benefits against the adverse effects, and the exposure must be conducted under direct medical supervision. The upper limit for whole-body exposure is 8 T, in view of uncertainties regarding the effects of higher fields. ICNIRP recognizes the potential risks and the need for providing flexibility in new investigations, and for further development of clinical procedures at field strengths higher than 8 T. It therefore suggests that for experimental magnetic resonance procedures at these levels, a special ethical approval is required.

In addition, it is cautioned that patients should be moved slowly into the magnet's bore, to avoid the possibility of vertigo and nausea. Thresholds for motion-induced vertigo have been estimated to be around 1 T/s for durations greater than 1 s. Avoiding these sensations is likely to afford protection against other effects of induced electric fields and currents that arise as a consequence of motion in a strong static magnetic field.

4.3 Guidelines For Radio-Frequency Dosimetry and Heating: General Public and Occupational Exposures

ICNIRP's "Guidelines for Limiting Exposure to Time-Varying Electric, Magnetic, and Electromagnetic Fields (up to 300 GHz)" was published with the objective of limiting EMF exposure that will provide protection against known adverse health effects [6]. It was mentioned that the guidelines will be periodically revised and updated as advances are made in identifying the adverse health effects of time-varying electric, magnetic, and electromagnetic fields. In view of the time elapsed and the many scientific studies of the effects of such fields that have been published in recent years, ICNIRP currently is in the process of reviewing and assessing the new data with respect to possible health hazards. In the interim, it is the opinion of ICNIRP that the scientific literature published to date do not furnish any compelling data showing adverse effects below the basic restrictions. Thus, it does not necessitate an immediate revision of its guidance on limiting exposure to radio frequency electromagnetic fields [7].

The current ICNIRP guidelines for radio-frequency electromagnetic fields in the magnetic-resonance-pertinent 10 MHz to 10 GHz frequency range are given in Table 3. For example, at 1.5, 3.0, 7.0, 9.4, and 11.7 T, the corresponding frequencies for hydrogen protons are 64, 128, 300, 400,

Exposure Type	Whole-Body Average SAR (W/kg)	Local SAR* (Head and Trunk) (W/kg)	Local SAR (Limbs) (W/kg)
General public	0.08	2	4
Occupational	0.4	10	20

**Local SAR is based on an averaging mass of 10 g of contiguous tissue.*

Table 3. Basic restrictions for time-varying electric and magnetic fields in the 10 MHz to 10 GHz frequency range.

Body Region	Whole-Body SAR (W/kg)	Partial-Body SAR (W/kg)		Local SAR* (W/kg)		
MR Operation	**Whole Body**	**Head**	**Other**	**Head**	**Trunk**	**Extremities**
Normal	2	3	2 - 10	10	10	20
Controlled	4	3	4 -10	10	10	20
Restricted	> 4	> 3	> 4 - 10	> 10	> 10	> 20
Short term SAR**	< 3 times above	< 3 times above	< 3 times above	< 3 times above	< 3 times above	< 3 times above

**Local SAR (averaged over 10 g of contiguous tissue).*
***The SAR limit over any 10 s period should not exceed 3 times*

Table 4. Recommended SAR limits valid at environmental temperatures below 24°C and averaging time of 6 min.

and 500 MHz, respectively. The basic restrictions on the specific absorption rate (SAR) limit for general-public and occupational exposures are provided to avoid whole-body heat stress and excessive localized tissue heating. They are provided specifically to prevent biological and health effects in responses to a body temperature rise of 1°C or more for an averaging time of 6 min. This level of temperature increase results from exposure of individuals under moderate environmental conditions to a whole-body SAR of approximately 4 W/kg for about 30min. A whole-body average SAR of 0.4 W/kg was chosen as the restriction that provides adequate protection for occupational exposure. An additional reduction factor of five was introduced for exposure of the public, giving an average whole-body SAR limit of 0.08 W/kg.

4.4 Patients Undergoing Magnetic Resonance Procedures

In addition to the guidelines on general public and occupational exposure limits promulgated since 1998, ICNIRP has published guidelines on protection of patients undergoing magnetic resonance examinations [4]. The recommended SAR limits for environmental temperatures below 24° C and with averaging time of 6 min are summarized in Table 4 for whole-body and partial-body exposure, and for the head, the trunk, and the extremities. These SAR levels should not be exceeded in order to limit temperature elevation to the values given in Table 5. Whole-body SARs are applicable at environmental temperatures at or below 24° C. At higher temperatures, they should be reduced depending on actual environmental temperature and humidity. The recommended SAR restrictions do not pertain to any individual magnetic resonance sequence, but rather to running SAR averages computed over each 6-min period, which is assumed to be a typical thermal equilibration time for smaller masses of tissue.

Partial-body SARs scale with the ratio between the tissue mass exposed and the total patient mass. For a ratio approaching one, the ratio converges toward the corresponding whole-body values. However, for ratios approaching zero, they converge toward the localized SAR level of 10 W/kg specified by ICNIRP for occupational exposure of the head and trunk (see above).

As mentioned in the previous section, for whole-body exposures, available data suggests that adverse health effects are not expected if the increase in body core temperature does not exceed 1° C. In the case of infants, pregnant women, and persons with cardiovascular impairment, it is desirable to limit body-core temperature increases to 0.5° C. Similarly, local temperature under exposure to the head, trunk, or extremities should be limited to the values given in Table 5 for the three types of magnetic resonance operations.

MR Operation	Elevation of Body-Core Temperature (°C)	Spatially Localized Temperature Limits (°C)		
		Head	**Trunk**	**Extremities**
Normal	0.5	38	39	40
Controlled	1.0	38	39	40
Restricted	> 1.0	> 38	> 39	> 40

Table 5. Basic restrictions for whole-body temperature elevation and localized partial-body temperatures.

5. Remarks on SAR and Temperature

The metric SAR in W/kg is defined as the time rate of change of the incremental energy absorbed by or deposited in an incremental mass contained in a volume of a given density [8]. The total amount of or whole-body energy deposited or absorbed is given by the integral of SAR over a finite interval of time. The whole-body SAR as a metric corresponds to the average value obtained by dividing the mass of the body into the whole-body energy absorption. The whole-body absorption of RF electromagnetic energy by humans and laboratory animals is of interest because it is related to the energy required to alter the thermoregulatory responses of the exposed subject.

Note that in RF exposure, the externally applied electric field induces an electric field inside the biological body. Indeed, the induced electric field is the primary driving force underlying the interaction of electromagnetic energy with biological systems. Once the induced electric field is known, the SAR can be derived from it by a simple conversion formula. Specifically, for an induced electric field, E, in V/m,

$$SAR = \frac{\sigma E^2}{\rho_m}, \qquad (1)$$

where σ is the bulk electrical conductivity (S/m), and ρ_m is the mass density (kg/m^3) of tissue.

However, at present, a small, isotropic, implantable electric-field sensor with sufficient sensitivity is not widely available. Fortunately, at sufficiently high intensity, the induced electric field generates heat in biological tissues with finite electrical conductivity. Consequently, a common practice in experimental dosimetry relies on the use of small field-insensitive temperature probes to measure the temperature elevation produced under a short-duration (~ 30 s), high-intensity exposure condition. The short duration is not enough for significant conductive or convective heat transfer to contribute to tissue temperature rise. In this case, the time rate of initial rise in temperature (the slope of the transient temperature response curve) can be related to SAR through a secondary procedure, i.e.,

$$SAR = \frac{c\Delta T}{\Delta t}, \qquad (2)$$

where c is the specific heat capacity of tissue (J/kg°C), ΔT is the temperature increment (°C), and Δt is the short duration (s) over which ΔT is measured. The rise in tissue temperature during the initial transient period of RF energy absorption is thus linearly proportional to the value of SAR.

It is important to distinguish the use of SAR and its derivation from transient temperature measurements. The derived quantity of SAR is merely a metric for energy deposition or absorption. It should not be construed to imply any mechanism of interaction, thermal or otherwise. Moreover, it is a quantity that pertains to a macroscopic phenomenon by virtue of the use of bulk electrical conductivity and specific heat capacity in its derivation from Equation (1) and Equation (2), respectively [8].

6. Challenges in Setting Guidelines for RF Exposure in MRI

High-magnetic-field-strength magnetic resonance systems are becoming more common. New open designs and interventional and intra-operative procedures increasingly have become routine at many sites. While exposure guidelines have been promulgated for magnetic resonance operations, there are a number of challenges that warrant further consideration. Specifically, these include the following.

6.1 Differences in SAR and Temperature Distributions

The differences in SAR and temperature distributions within heterogeneous human anatomies have been well-documented (see, for example, [9, 10]). Moreover, mammalian thermoregulatory responses can modify tissue-temperature elevations and distributions under high SAR conditions, especially for the whole body and for pregnant women. Given the limitations in measuring in vivo temperature distribution and heating, computational prediction of SAR and temperature over typical magnetic resonance examination periods continues as a challenge in developing safety limits.

6.2 Mass of Averaging Volume for SAR and Temperature

It is significant to note that the use of bulk electrical conductivity, specific heat capacity, and the mass density (kg/m^3) of tissue in the computation and derivation of SAR from electric field strength or from measurement of temperature elevation. Their use in the definition means that a volume of tissue mass must be selected over which SAR is determined. A problem arises when the SAR distribution is highly nonuniform, or when tissues with differing properties and conductivities are within the same volume. In general, a smaller averaging mass or volume would thus allow SAR as a metric to provide a more precise representation of the true values of RF absorption and its variation inside the body or tissue medium. Similarly, the size of the mass of averaging volume will impact temperature predictions.

6.3 Dosimetry and Thermal Models of Pregnant Women

It is important to accurately characterize SAR and heating of tissues during magnetic resonance imaging of pregnant women and fetuses. It should be noted that thermal and dosimetry models of pregnant women and fetuses have only recently become available for SAR and temperature studies. Computer methods for prediction and validation of SAR and temperature distributions will be critical to ensure safe magnetic resonance operation involving this population group.

6.4 Features of SAR and Heating Distributions for High-Field MRI

Many studies have demonstrated SAR and temperature differences from high-field magnetic resonance operations, compared to the current generation of magnetic resonance systems. Comprehensive investigations are needed for safety assurance in high-field magnetic resonance operations.

6.5 Epidemiological Studies of Health Effects in Patients or Magnetic-Resonance Workers

There have been no epidemiological studies performed to assess possible long-term health effects in patients, volunteers, or magnetic resonance workers. It is important that such research be conducted, particularly on individuals with extended and high levels of exposure. There is a paucity of specific information regarding possible long-term health effects, although current understanding suggests that any effects are likely to be acute.

7. References

1. International Commission on Non-Ionizing Radiation Protection, "Guidelines on Limits of Exposure to Static Magnetic Fields," *Health Phys*., **96**, 2009, pp. 504-514.

2. International Commission on Non-Ionizing Radiation Protection, "Guidelines on Limits of Exposure to Static Magnetic Fields," *Health Phys.*, **66**, 1994, pp. 100-106.

3. International Electrotechnical Commission, "Safety of Magnetic Resonance Equipment for Medical Diagnosis," Geneva, Switzerland, 2002, iec 60601-2-33.

4. International Commission on Non-Ionizing Radiation Protection, "Medical Magnetic Resonance (MR) Procedures: Protection of Patients," *Health Phys.*, **87**, 2004, pp. 197-216.

5. International Commission on Non-Ionizing Radiation Protection, "Amendment to the ICNIRP Statement on Medical Magnetic Resonance (MR) Procedures: Protection of Patients," *Health Phys*., **97**, 2009, pp. 259-262.

6. International Commission on Non-Ionizing Radiation Protection, "Guidelines for Limiting Exposure to Time-Varying Electric, Magnetic, and Electromagnetic Fields (up to 300 GHz)," *Health Phys*., **74**, 1998, pp. 494-522.

7. International Commission on Non-Ionizing Radiation Protection, "Statement on the 'Guidelines for Limiting Exposure to Time-Varying Electric, Magnetic, and Electromagnetic Fields (up to 300 GHz)'," *Health Phys*., **97**, 2009, pp. 257-258.

8. J. C. Lin, "Dosimetric Comparison Between Different Possible Quantities for Limiting Exposure in the RF Band: Rationale for the Basic One and Implications for Guidelines," *Health Physics*, **92**, 6, 2007, pp. 547-453.

9. Z. W. Wang, J. C. Lin, W. H. Mao, W. Z. Liu, M. B. Smith, and C. M. Collins, "SAR and Temperature: Simulations and Comparison to Regulatory Limits for MRI," *Journal of Magnetic Resonance Imaging*, **26**, 2, 2007, pp. 437-441.

10. Z. W. Wang, J. C. Lin, J. T. Vaughan, and C. M. Collins, "On Consideration of Physiological Response in Numerical Models of Temperature During MRI of the Human Head," *Journal of Magnetic Resonance Imaging*, **28**, 5, 2008, pp. 1303-1308.

Conferences

CONFERENCE REPORTS

Microwave Signatures 2010

Florence, Italy, October 4 -8, 2010

The URSI Commission F *Specialist Symposium on Microwave Remote Sensing of the Earth, Oceans, and Atmosphere* "Microwave Signatures 2010" was held in Florence, Italy, on the 4 through the 8 October 2010 jointly with the Italian National Workshop on Microwave Remote Sensing. The meeting was chaired by Simonetta Paloscia and co-chaired by Giovanni Macelloni.

The Symposium, co-sponsored by the IEEE GRSS, was organized by the Centro di Telerilevamento a Microonde (CeTeM) and the Institute of Applied Physics of the Italian National Research Council (IFAC-CNR). Financial support was provided by IFAC-CNR and AIT (Italian Society of Remote Sensing),

More than 80 scientists attended the meeting to present and discuss 66 excellent papers organized into 11 oral sessions and 21 posters. The first day of the symposium was devoted to the current and planned satellite microwave missions (SMOS, SMAP, COSMO_SKYMED, COREH2O, Sentinel1) and sensors. The second day opened with a keynote speech delivered by Martti Hallikainen on "Progress and challenges in microwave remote sensing of northern areas" followed by three oral sessions devoted to microwave remote sensing of land with special emphasis of soil and vegetation.

The third day started with a keynote speech on "Electromagnetic models for active and passive microwave remote sensing" delivered by Leung Tsang. This day included also four sessions dedicated to the applications of the Global Navigation Satellite System for the observation of the Earth's surface and for monitoring that the atmosphere. The symposium was concluded on the fourth day by two sessions that addressed the topics of observing planets and terrestrial snow and ice.

Posters on the same topics of the oral sessions remained on display throughout the meeting with an interactive session on Wednesday evening.

The meeting was enlightened by three significant social events: a reception in the old historical Palagio di Parte Guelfa sponsored by ARION spa; a cocktail party offered to the participants during the interactive poster session, and the Award Social Dinner. During the latter event two distinguished scientists Prof. Martti Hallikainen and Prof. Leung Tsang were awarded with the Fiorino d'Oro (Golden Florin). This award, established in 1995 by the Center for Microwave Remote sensing (CeTeM) in recognition for outstanding contributions to research in Microwave Remote Sensing, consists of a gold replica of the old golden florin, the coin first minted by the Florentine Republic in 1252 and acquired, at this time, the role of an international currency..

Most of the presentations have been uploaded on the web page (www.ursif2010.org) with the permission of the authors. A special issue of the Italian Journal of Remote Sensing has been planned for hosting a selection of papers presented at the meeting.

7th European Space WeatherWeek

Bruges, Belgium, November 15 -19, 2010

European Space Weather Week is an annual conference that brings industry, academia, and European agencies together in a lively dialog about space weather. This workshop, began in 2004, has evolved into a leading conference on all issues relating to space weather. The 7th European Space Weather Week(ESWW7) , held in Bruges (Belgium) from 15 to 19 November 2010 has been jointly organized by European Space Agency (ESA), The Solar-Terrestrial Center of Excellence, STCE, COST ESO803, The Belgian Science Policy, The International Space Environment Service, The European Office of Aerospace Research and Development, Air Force Office of Scientific Research, United States Air Force Research Laboratory, Rhea System S.A., The Belgian Presidency of the Council of the European Union, U.R.S.I.

The ESWW7 covered the typical space weather topics divided in the five plenary sessions:

Session 1: SSA Space Weather in Support of European Critical Infrastructure
Session 2: Spacecraft Environments and Effects
Session 3: Tracking Heliospheric Phenomena: New Observing and Analysis Strategies
Session 4: Space Weather Products and Services
Session 5: Space Weather Models: from Research to Applications

A key part of the European Space Weather Weeks are the splinter meetings. These meetings provide the opportunity for interested participants to meet in smaller groups. As the COST083 Management committee meeting, introduced by Beleaki; Validation Procedures for Space Weather Models by Tsagouri, Wintoft and Watermann; Direct Effect of Solar Radio Weather by Messerotti and "SWWT Topical Group: Ionospheric Effects" by Luntama.

This year's event also included a space weather fair, where users and service providers will have the opportunity to interact in an informal working environment. As EISCAT_3D - European volumetric imaging incoherent scatter radar, presented by E. Turunen, the next-generation radar for the high-latitude atmosphere and geospace research, with capabilities going beyond anything currently available in incoherent scatter radars (ISR). Turunen showed an unique 3D movies "Aurora²" by Brian McClave and George Millward, and "Sun 3D", a collaboration with Rutherford Appleton Laboratory using the NASA STEREO mission. In this paper we will focus on the ionospheric papers presented in these sessions. A poster on DIAS Digital Ionospheric Space Service was also presented to illustrate the many ionospheric products given on line by this European project.

In **Session1** we can mention the paper " **CIGALA**: an fp7 Project to tackle Ionospheric Scintillation Threat to GNNS Operations in Latin America" presented by Bougard. The CIGALA project, co-funded by the EC 7th Framwork Program and supervised by the GNSS Supervisory Authority (GSA), aims to develop and test ionospheric scintillation countermeasures to be implemented in professional multi-frequency GNSS receivers. The project and development activities coordinated between European and Brazilian experts, involving a wide scale ionospheric measurement and test campaigns that will be conducted in Brazil.

In **Session 3** A. Mikhailov presented the paper " Prestorm NmF2 Enhancements at low Latitudes: One more Delusion?". Using ground-based ionosonde observations in the American longitudinal sector at the geomagnetic equator and stations located in the vicinity of the Equatorial Ionization Anomaly (EIA) crests cases of NmF2 enhancements were analyzed for their possible relationship with the following magnetic disturbances. It is possible to conclude that there are no convincing arguments that the observed enhancements have a relation with the following magnetic storms.

In **Session 4**, N. Jakowski presented " Operational Products of the Space Weather Application Center Ionosphere (SWACI) and Capabilities of their Use". SWACI operates a powerful data processing system working both in real-time and post-processing modes in order to provide actual information to the registered customers (http://swaciweb.dlr.de). In this talk we will focus on describing transionospheric link related data products offered in near real time for operational use in various applications such as GNSS based navigation and positioning and radar techniques in remote sensing. Then J. Lastovicka presented "Project SX5 - Development of a new Tool for Ionospheric Investigations". SX5 is a project funded by the European Union within the 7th Framework Programme and supervised by the GNSS Supervisory Authority GSA. Its main topic is the scientific exploitation of the Galileo broadband E5 signal. Stanislawska presented "Web - Design of Operational Mapping of the Ionospheric W Index Maps based on EGNOS - TEC Maps of total Electron Content". The European Geostationary Navigation Overlay Service, EGNOS, provides online the regional maps of the vertical total electron content in timely, continuous regime. The W index maps characterizing quiet or stormy state of the ionosphere-plasmasphere plasma are provided online at http://www.cbk.waw.pl/ and archived for comparison with W index maps derived from the global ionospheric maps, GIM. In the paper "Autoscala Output for Ionospheric Station Hornsund", Tomasik explained that Autoscala is a software to automatically scale ionospheric characteristics from an ionogram. Autoscala was applied to ionospheric station Warsaw, proved that ionosondes produced by Space Research Centre PAS and Autoscala software developed by Istituto Nazionale di Geofisica e Vulcanologia, Rome, Italy are complete solution for real time ionosphere monitoring. Haralambous presented "Comparison of foF2 Values extracted from DIAS Maps and Ionosonde Measurements at Nicosia during Low Solar Activity". This paper presents a comparison between values of the critical frequency of the F2-layer (foF2) derived from digital ionosonde measurements at the low-middle latitude operating European station in Nicosia, Cyprus and the DIAS (European Digital Upper Atmosphere system.

In **Session 5,** Beniguel presented "A Global Ionosphere Scintillation Propagation Model **for Equatorial Region".** This paper presents the basis of a multiple phase screen theoretical model allowing reproducing the signal modifications due to propagation through ionosphere and generating time series at receiver level. In the paper" Model and Visualization Software for the Nowcasting of the Middle Atmosphere" Rozanov explained that a climate-chemistry-ionosphere model SOCOL has been developed which is based on a general circulation model and includes complete representation of the chemistry of neutral and ionized species in the atmosphere from the ground up to the mesopause. Pietrella presented "Coerenza: a Software Tool for computing the Maximum Coherence Times of the Ionosphere". This work describes a computer software program (Coerenza) that is able to calculate the maximum

coherence times of the ionosphere from PH data. In the paper "Advanced Thermosphere Modelling for Orbit Prediction (ATMOP)" Menville explained that research project aims at building a new thermosphere model with the potential to spawn an operational version. Tulunay presented "FP7 COST ES0803 I LOVE MY SUN - 3 An Outreach Activity in Europe An exercise on the training of school children of age group 8 - 10 years".

International School on Atmosphere - Ionosphere Radars and Radio Sounding: Science and Applications ISAR - NCU

Jhong-Li, Taiwan, November 15 -24, 2010

Since 2006 the National Central University (NCU) in Jhong-Li (Chung-Li), Taiwan, had conducted International Schools on Atmospheric Radar (ISAR). Due to the great demand, proved by the large number of international applications (there were more than 80 students applying to attend the school in 2009) and the great success, proved by examinations and responses of students, the fifth school ISAR-NCU-2010 was held in November 2010. It was mainly open for students from South-East Asia and all costs for students and lecturers were carried by the NCU.

This school was aiming to graduate and PhD students, young postdoctoral research scientists and engineers having background or work in the fields of atmospheric or ionospheric science, radar and radio system development and experimental applications. In particular methods applying different ground-based lower, middle and upper atmosphere and ionosphere radar and radio methods were addressed.

The ISAR-NCU-2010 was co-directed by Professors Chien-Ming Huang (Graduate Institute of Space Science, NCU, Taiwan) and Jürgen Röttger (Germany), supported by the university under President W.L. Chiang through Prof. Y.H. Chu, Director of the Dept. of Research and Development of NCU, which was the predominant sponsor of this school. The lecturers and presentations were held in the Center for Space and Remote Sensing Research (CSRSR) of the NCU.

Such as earlier schools ISAR-NCU-2010 was performed under the international heading of the SCOSTEP (Scientific Committee on Solar Terrestrial Physics) program CAWSES (Climate and Weather of the Sun-Earth System) and the URSI Working Group GF on Middle Atmosphere (International Union of Radio Science), co-chaired by C.H. Liu and J. Röttger.

The lectures were given by four professors from Taiwan and four foreign ones. They comprised the following topics: J. Röttger (Germany) on basics of radars for scientific research – an overview of atmosphere and ionosphere radars; radar technology, radar control, data acquisition and pre-processing, MST-VHF radars; coherent

and incoherent scatter radars; atmosphere dynamics and ST radar meteorology. Y.C. Liou (NCU) on the introduction of Doppler weather radars and their applications. T.C. Chen Wang (NCU) on the introduction of the principle and the applications of dual-polarization weather radar systems. R.M. Kuong (NCU) on the NCU VHF radar system. T.Y. Yu (USA) on atmospheric radar imaging using multi receivers and multi frequencies. K.K. Reddy (India) on wind profilers for atmospheric research, and natural disasters and implications on Asia. T. Bullett (USA) on HF radars and ionospheric sounding; and L.C. Tsai (NCU) on ionospheric electron density and total electron content measurements and modelling.

The 25 students, attending this international school, were from seven countries: India, Indonesia, Malaysia, Mongolia, Philippines, Vietnam, and Taiwan as well. They enjoyed also visits of the mobile and stationary Doppler dual-polarization radars and the VHF radar of the National Central University. Some special hours were dedicated to questions and answers and introduction to some hands-on data processing and initial interpretation. Each student received a certificate having attended the ISAR-NCU 2010. At the end some students had been invited to give short presentations on their own work, and in the final discussion session remarks were discussed how to continue and further improve future schools. The National Central University has given us very clear signals to support performing future schools. It is planned to hold the next ISAR-NCU in November 2011.

C.M. Huang and J. Röttger

4th IAGA/ICMA/CAWSES-II TG4 Workshop on Vertical Coupling in the Atmosphere-Ionosphere System

Prague, Czech Republic, February 14 -18, 2011

General information

The 4th workshop of 4th IAGA/ICMA/CAWSES-II TG4 Workshop on Vertical Coupling in the Atmosphere/ Ionosphere System took place in Prague, Czech Republic, on 14-18 February, 2011. The workshop was organized by the Institute of Atmospheric Physics, Prague. Financial contributions to the workshop were made by the following organisations: International Association of Geomagnetism and Aeronomy (IAGA), International Commission on the Middle Atmosphere (ICMA), International Union of Geodesy and Geophysics (IUGG), International Union of Radio Science (URSI) and Scientific Committee on Solar-Terrestrial Physics (SCOSTEP).

Scientific committee

Petra Koucká Knížová (chair) - Institute for Atmospheric Physics, Prague, Czech Republic
Dora Pancheva – Geophysical Institute, Sofia, Bulgaria
Werner Singer - Leibniz-Institute of Atmospheric Physics, Kühlungsborn, Germany
Kazuo Shiokawa – STEL, Nagoya University, Japan
Daniel Marsh – ACD/NCAR, USA
Art Richmond – HAO, NCAR. Boulder, USA
Robert Vincent – University of Adelaide, Adelaide, Australia

Local organizing committee

(Institute for Atmospheric Physics, Prague, Czech Republic)

Petra Koucká Knížová (chair), Daniel Kouba, Jan Laštovička, Zbyšek Mošna and Tereza Šindelářová

Topics

1) Coupling processes in the middle atmosphere
   - Coupling through planetary waves, mean flows and temperature variability
   - Gravity wave and tidal forcing of the middle atmosphere
   - The role of dynamics, solar variability and greenhouse gasses on the chemical structure and feedback processes
2) Coupling processes in the atmosphere/ionosphere system
   - Dynamical forcing of the ionosphere from below
   - Electrodynamic coupling and plasma instabilities; the role of electrical processes in the coupling

Abstracts and sessions

79 papers were presented, from which 16 were solicited presentations. Papers are listed online on the workshop website (http://www.ufa.cas.cz/html/conferences/workshop_2011/participants.php).

The workshop program and abstract book can be downloaded: http://www.ufa.cas.cz/html/conferences/workshop_2011/program_coupling.pdf or http://www.ufa.cas.cz/html/conferences/workshop_2011/participants.php

Participants

The workshop attracted 75 participants from 16 countries, including 28 students and young scientists under 35 from 9 countries.

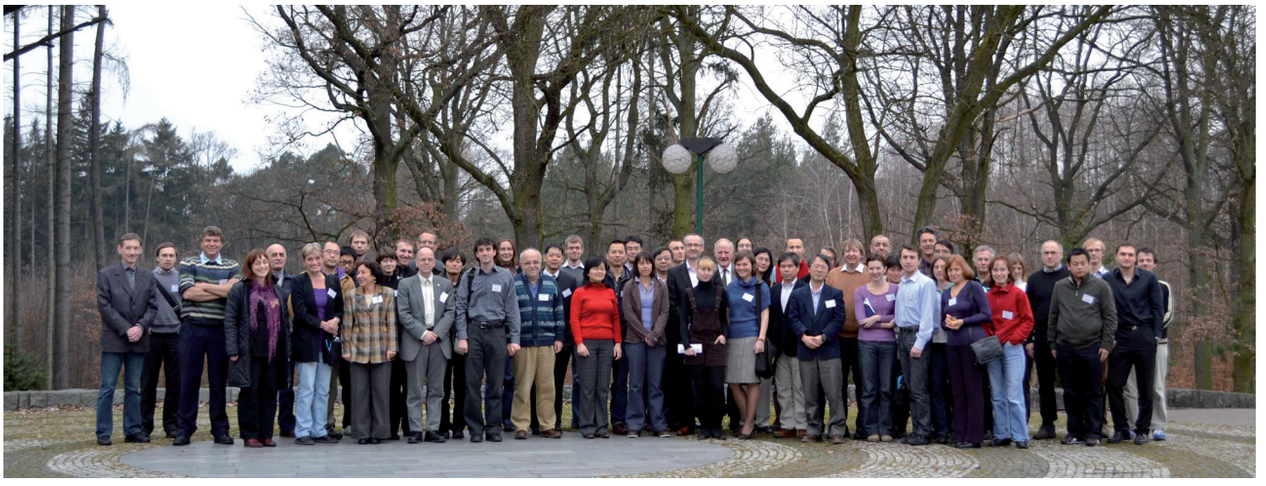

Participants of the 4th IAGA/ICMA/CAWSES-II TG4 Workshop on Vertical Coupling in the Atmosphere/Ionosphere System
Photo taken on 17 February 2011 by D. Kouba

Scientific highlights

The 4th IAGA/ICMA/CAWSES-II TG4 meeting was designed to bring research experts form both the middle and upper neutral atmosphere and ionosphere communities together in order to present their work and assess/debate ongoing issues relating to the theoretical, modelling and observational aspects of all kind of processes which transfer energy and momentum from the lower atmosphere to the upper atmosphere and ionosphere and vice versa. The workshop focussed on the principle mechanisms of the vertical coupling in the atmosphere and addressed the manner in which the coupling takes place. The presented papers reported both theoretical and empirical recent results concerning the coupling mechanisms through dynamics, composition and electrodynamics. This workshop solicited papers dealing with experiments, observations, modelling, and data analyses that describe the effects of atmospheric coupling processes within the atmosphere-ionosphere system. Generally, much progress there has been since the first workshop in 2002. The presentations at this Workshop will be published in a special issue of the Journal of Atmospheric and Solar-Terrestrial Physics.

URSI financial support

Commission G of URSI decided to sponsor the 4th IAGA/ICMA/CAWSES-II TG4 workshop with an amount of EUR 500. The financial support together with other financial grants was used by the local organizing committee of the 4th IAGA/ICMA/CAWSES-II TG4 workshop to partially support 25 participants, they were young scientist and students under 35 years of age at the time of the meeting and other deserving participants judged by the organizing committee of the 4th IAGA/ICMA/CAWSES-II TG4 workshop to be in need of financial support.

Next workshop

It has been widely accepted that following the strengths of our previous IAGA/ICMA workshops, there would be real value in a 5th IAGA/ICMA workshop. At this point it seems sensible to organize this in 2012, as neither IAGA or URSI will meet that year. Organization of the next IAGA/ICMA/CAWSES-II TG4 meeting will be discussed during the XXV IUGG General Assembly in Melbourne.

CONFERENCE ANNOUNCEMENT

9th International Symposium on Electromagnetic Compatibility and Electromagnetic Ecology
EMC 2011

Saint-Petersburg, Russia, September 13 -16, 2011

The main objective of the 9th International Symposium on Electromagnetic Compatibility and Electromagnetic Ecology (EMC&EME) is to give an opportunity to scientists, engineers and students for representation of the advance in their work in the area of EMC and wide discussion of the mutual interesting problems. The venue of the Symposium will be Saint Petersburg Electrotechnical University.

Main topics

- Theoretical problems of EMC & EME
- EMC in radio-electronic systems and equipment
- Spectrum management and monitoring
- EMC in electrical engineering and power systems
- Especial problems EMC & EME in mobile objects (vessels, planes, railways and others)
- Research of natural electromagnetic radiations (GIC, lightning, and others)
- Equipment design with regard to EMC & EME, technology, materials and components
- Electromagnetic monitoring, measurement, certification and test equipment
- EME problems: influence of electromagnetic radiation on biological objects, admissible norms of radiation and ecological protection
- EMC & EME education
- Popov's scientific and educational radio-technical school

The papers of the Symposium will be published in Proceedings of the EMC'2011

Chair

Prof. V. Kutuzov
Saint Petersburg Electrotechnical University
Russia

Vice-Chair

Prof. M. Ianoz
Swiss Federal Institute of Technology (Lausanne)
Switzerland

Contact

Organizing Committee of the EMC'2011
Saint Petersburg Electrotechnical University,
5, Prof. Popov Street, Saint Petersburg,
197376, Russia
Fax: +7 (812) 346-4637
E-mail: irvc@eltech.ru, discone@mail.wplus.net
Web site: http://www.eltech.ru/emc

Deadline for **abstract submission**: May 5, 2011

URSI CONFERENCE CALENDAR

An up-to-date version of this Conference Calendar, with links to various conference web sites can be found at http://www.ursi.org/en/events.asp

June 2011

ISMOT 2011 - 13th International Symposium on Microwave and Optical Technology
Prague, Czech Republic, 20 - 23 June 2011
cf. Announcement in the Radio Science Bulletin of December 2010, p. 59-60.
Contact: Prof. Jan Vrba, Czech Technical University in Prague, Dept. of Electromagnetic Field, CVUT - FEL, K 13117, Technicka 2, 166 27 Prague 6, Czech Republic, Email: vrba@fel.cvut.cz, Website: http://www.ismot2011.com

July 2011

IconSpace 2011: International Conference on Space Science & Communication
Genting Highlands, Pahang, Malaysia, 12-13 July 2011
Contact: Dr. Wayan Suparta, Institute of Space Science (ANGKASA), Level 2, Faculty of Engineering and Built Environment, Universiti Kebangsaan Malaysia, 43600 UKM Bangi, Selangor, Malaysia, E-mail: wayan@ukm.my, w_suparta@yahoo.com, Website: http://www.ukm.my/ispace

August 2011

XXXth URSI General Assembly and Scientific Symposium
Istanbul, Turkey, 13-20 August 2011
Contact: URSI Secretariat, c/o INTEC, Sint-Pietersnieuwstraat 41, B-9000 Gent, Belgium, Fax +32 9 264 4288, E-mail: info@ursi.org and ursigass2011@ursigass2011.org , http://www.ursigass2011.org

3rd International Colloquium on Scientific and Fundamental Aspects of the Galileo Programme
Copenhagen, Denmark, 31 August - 2 September 2011
Contact: ESA Conference Bureau, ESA-ESTEC, PO Box 299, NL-2200 AG Noordwijk, The Netherlands, Tel: +31-71-565 5005, Fax: +31-71-565 5658, E-mail: http://www.congrex.nl/11a12/

September 2011

ISROSES II - International Symposium on Recent Observations and Simulations of the Sun-Earth System
Borovets, Bulgaria, 11-16 September 2011
Contact: Mary Dugan, Los Alamos National Laboratory, Los Alamos, NM, USA, E-mail: isroses@lanl.gov

ICEAA-APWC 2011 - International Conference on Electromagnetics in Advanced Applications
Torino, Italy, 12-17 September 2011
cf. Announcement in the Radio Science Bulletin of September 2010, p. 77-78.
Contact: Prof. P.L.E. Uslenghi, Dept. of ECE (MC 154), University of Illinois at Chicago, 851 S. Morgan Street, CHICAGO, IL 60607-7053, USA, Tel : +1 312 996-6059, Fax : +1 312 996 8664, E-mail : uslenghi@uic.edu , http://www.iceaa.net

EMC 2011 - International Symposium on EMC and EME
Saint-Petersburg, Russia, 13-16 September 2011
cf. Announcement in the Radio Science Bulletin of March 2011, p. 106.
Contact: EMC 2011, St.Petersburg State Electrotechnical University "LETI" , 5, Prof. Popov Street, St. Petersburg, 197376, Russia, Phone/Fax:+7 812 346-46-37, E-mail : http://www.eltech.ru/conference/emc/2011/

EMC Europe 2011
York, United Kingdom, 26-30 September 2011
Contact: Prof. A. C. MARVIN, Department of Electronics, University of York, Heslington, YORK, YO10 5DD, UNITED KINGDOM, Phone : +44 (0)1904 432342, Fax : +44 (0)1904 433224, E-mail : conference@emceurope2011.york.ac.uk, website : http://www.emceurope2011.york.ac.uk/

October 2011

ISAP2011 - 2011 International Symposium on Antennas and Propagation
Jeju, Japan, 25-28 October 2011
cf. Announcement in the Radio Science Bulletin of June 2010, p. 53-54.
Contact: 5F Daehan Bldg., #1018 Dunsan-Dong, Seo-Gu, Daejeon 302-120, Korea, Tel : +82-42-472-7463, Fax : +82-42-472-7459, isap@isap2011.org, *http://*www.isap2011.org

July 2012

EUROEM 2010
Toulouse, France, 2-6 July 2010
Contact: Dr. Jean-Philippe Parmantier, ONERA, DEMR/CDE, BP 4025, Avenue Edouard Belin, 31055 TOULOUSE Cedex 4, FRANCE, Fax : +33 5 62 25 25 77, E-mail: http://www.euroem.org/

COSPAR 2012 - 39th Scientific Assembly of the Committee on Space Research (COSPAR) and Associated Events
Mysore, India, 14 - 22 July 2012
cf. Announcement in the Radio Science Bulletin of September 2010, p. 78-79.
Contact: COSPAR Secretariat, c/o CNES, 2 place Maurice Quentin, 75039 Paris Cedex 01, France, Fax: +33 1 44 76 74 37, cospar@cosparhq.cnes.fr , http://www.cospar-assembly.org/

September 2012

ICEAA 2012
Cape Town, 2-8 September 2012
Contact: Roberto D. Graglia, Corso Duca degli Abruzzi 24, Dip. Elettronica, Politecnico di Torino, Torino 10129, Italy, +39 0115644056, +39 0115644056, +39 0115644099 (fax), E-mail : http://www.iceaa.net/

October 2012

ISAP 2012
Nagoya, Japan, 29 October - 2 November 2012
Contact: Professor Koichi Ito, General Chair of ISAP2012, Chiba University, 1-33 Yayoi-cho, Inage-ku, Chiba-shi, Chiba 263-8522, Japan, Fax: +81-43-290-3327, E-mail : http://www.isap12.org

URSI cannot be held responsible for any errors contained in this list of meetings.

News from the URSI Community

NEWS FROM A MEMBER COMMITTEE

FRANCE
Médaille du CNFRS

The Medal of the Comité National Français de Radioélectricité Scientifique (CNFRS), French national committee of the Union Radio-Scientifique Internationale (URSI), has been awarded to Dr. Eric Gérard on March 29, 2011.

The CNFRS/URSI-France wishes to underline the importance of the Eric Gérard contributions to the development of radio-astronomy in France, the advancement of knowledge on comets and circumstellar envelopes, his involvement in the scientific exploitation of the radio spectrum, as well as his enthusiastic contribution to public outreach. Eric Gérard played an important role in the life of the Radio Science community, especially as a coordinator of the French Radio Astronomy Commission.

The medal is awarded by CNFRS/URSI-France, under the auspices of the French Academy of Sciences, to a leading scientist who has contributed to remarkable advances in Radio Sciences and has participated to the scientific leadership of the French/International community.

Eric Gérard, born in 1939, is a personality of the radio-astronomy world well known for his scientific and instrumental works, for his activity in favour of URSI, for his commitment to the scientific utilization and protection of the Radio spectrum and for his efforts of communication towards large public and schoolchildren.

Young science student in Liège, he was noticed by Professor Pol Swings who sent him for two years in the United States at Harvard University in order to get a training in radio-astronomy and to later participate to the Benelux Cross Antenna, a major project to be built in Belgian Limburg that, much later, became the Westerbork radio-telescope in the Netherlands.

On his return from the United States (1966), he settled in France, obtained his PhD in 1970 and a CNRS research position at the Observatory of Meudon/Nançay. He got interested in instruments (telescopes, receivers, etc.), expanding the limits of their capacities. He participated to the development and refinement of various receivers and associated equipment. He built a parametric amplifier for radio observations at 11 cm of giant planets (in order to study the synchrotron emission in the radiation belts of Jupiter and Saturn). With the large radio decimetric telescope in Nançay, he participated to important discoveries: OH maser emission (18 cm) of comets, HI emission (21 cm) of stars, etc. He became a member of the International Halley Watch, as an "IHW Discipline Scientist" for radio astronomy in Europe. He followed the OH emission of the Halley comet in 1986 in support of space missions (Giotto, etc.), and coordinated the activities of the European radio network. He obtained the first measurement of a comet magnetic field by using the Zeeman Effect, a measurement that was confirmed in situ by the Giotto spacecraft.

In the late 80s, he invested himself in the renovation of the large radio decimetric telescope of Nançay (FORT project) of which he was responsible from 1993 to 2000. The telescope reopened in January 2001, and since provides excellent data in various fields of astrophysics (ranging from the physics of comets to pulsar timing and cosmology). It also serves as a test bed to develop mitigation techniques, and new high dynamic receivers for bands with high levels of

interferences. In particular, Eric Gérard developed a backend adapted to observations in highly disturbed environments that he presented at URSI in 2002.

Since 2001, he has actively participated in the study of the polarization of OH masers in evolved stars, which requires a careful monitoring of the instrumental performances. More recently, he focused his research activity in astrophysics on the two extremes of the life stars by studying the processes associated with star formation, and the processes of mass loss in dying stars. He exploits data produced by the Nançay radio telescope, by the Very Large Array (VLA, USA), by the European VLBI Network (EVN), the 30-meter telescope and the interferometer of IRAM (Pico Veleta and Plateau de Bure). Still very active, he continues to publish regularly. He is the author of well over 218 publications, 85 referred publications. Eric Gérard chaired the French J commission from 1998 to 2004, and participated actively in several General Assemblies of URSI from Ottawa in 1969, to Maastricht in 2002. He is also very active in public outreach, especially at the center "Ciel Ouvert" in Nançay, or at the Astronomy Festival of Haute Maurienne. He is author of many popular science papers (in Pour la Science, La Recherche, Encyclopaedia Universalis, etc.).

BOOKS PUBLISHED FOR URSI RADIOSCIENTISTS

Complex and Dusty Plasmas from Laboratory to Space

edited by Vladimir Fortov and Gregor Morfill, Boca Raton, FL, CRC Press, 2010, 418 pp., ISBN 978-1-4200-8311-8

The fascinating field of complex or "dusty" plasmas has grown into a mature area of research within plasma physics. *Complex and Dusty Plasmas from Laboratory to Space* is a collection of chapters authored by many leading dusty-plasma researchers. It presents a comprehensive overview of the current state of the field and its future directions.

Complex and Dusty Plasmas takes the reader on a carefully guided, detailed tour through many of the major subject areas within the field. Dusty plasmas are systems composed of the usual plasma species – electrons, ions, and neutral particles – along with charged microparticles, which are commonly referred to as "dust." Dusty plasmas are captivating because of the wide variety of effects that highly charged dust grains can have on the dynamics of the system. Dust grains become charged in a plasma by a variety of mechanisms, such as collection of electrons and ions from the plasma, secondary electron emission, and UV ionization. Dusty plasmas can be found in many astrophysical and laboratory settings, and even in industrial-processing plasmas. The size of the microparticles can range from nanometers to several hundred micrometers in diameter, while the scale size of the corresponding dust "clouds" can range from relatively small laboratory systems to vast astrophysical dust clouds.

Readers are first introduced to the numerous types of experimental devices and laboratory environments within which dusty plasmas are investigated through controlled laboratory experiments. Great attention is paid to the particulars of the various devices and to the diagnostic methods used in the experiments. Later, in Chapter 8, dusty-plasma optical-diagnostics methods are revisited in detail.

With knowledge of how the systems can be created and diagnosed, the book proceeds with descriptions of the interactions of charged dust grains with the background plasma. Dust-charging processes are described, as well as the corresponding effects the charged grains have on the local plasma potential distribution. Forces on individual dust grains, such as the drag force produced by the momentum transfer from ions flowing to the charged microparticle, are explained from first principles. In fact, as a general comment regarding the text, the theoretical basis for many of the phenomena described is given in sufficient detail for readers less familiar with the field to follow. The following chapter of the book gives attention to the dynamics of individual dust particles within the plasma.

Among the most interesting aspects of dusty plasmas are the interesting wave modes that a dusty plasma can support. Chapter 4 of the text provides a thorough review of the fundamental wave modes that can exist, along with derivations of the various dispersion relations, and examples from experiment and simulation.

Chapter 5 gives an in-depth overview of kinetic studies of dusty plasmas in the fluid and solid phases. One of the most compelling features of dusty plasmas in the laboratory is the ability to vary the coupling strength between the particles. Laboratory dusty plasmas can be created in a weakly coupled "gaseous" state, yet, by changing the background plasma parameters, strongly coupled "liquid" and "solid" states can be achieved. The ability to observe each of the phases and transitions in systems where individual particles can be followed provides a unique and powerful tool for the investigation of kinetics. In particular, interest is currently very high in the study of plasma crystals, the solid state of

strongly coupled dusty plasmas. This unique new state of matter makes the physics of dusty plasmas relevant to a wide variety of scientific disciplines.

The occurrence of dusty plasmas in nature is the focus of Chapter 6. Dusty plasmas are prevalent in many different space plasmas. This chapter of the book focuses on three solar-system regions in particular, the Earth's mesosphere, planetary rings, and the lunar surface. Noctilucent clouds are dusty plasmas formed by charged ice crystals, which likely condense on nanoscale meteoric dust particles in weakly ionized mesospheric regions. These are among the highest clouds in the Earth's atmosphere, and typically can only be observed when illuminated by sunlight from below the horizon. Planetary rings are another fascinating example of the rich dynamics of dusty plasmas. Here again, there is an excellent first-principles treatment of the effects of charge on the small grains that comprise the faint planetary rings, such as those surrounding Jupiter and Saturn. The text illuminates the complex interactions of the gravitational, electromagnetic, drag, and radiation-pressure forces responsible for shaping the rings and producing structures such as spokes in Saturn's rings. The chapter concludes with an interesting discussion of the formation of dusty plasmas above the surface of airless solar-system bodies, such as the Moon. There, above surfaces exposed to the solar-wind plasma, UV radiation from the sun, and plasma from the Earth's magnetosphere, observations from lunar missions have revealed thin layers of levitating particles.

While a large fraction of *Complex and Dusty Plasmas* focuses on laboratory experiment and space observations, the important contributions of numerical simulation to the advancement of the field are not forgotten. Chapter 7 gives a comprehensive overview of the methods and techniques employed in the computer simulation of complex plasma systems. Examples of investigations looking at transport properties, complex plasmas in narrow channels, and crystallization are discussed.

The last chapter of the book is devoted to applications. Dusty plasmas often form in industrial plasma-processing chambers, and have been present in a number of other industrial applications. This chapter discusses some of the effects, both beneficial and detrimental, on these processes. Charged dust is also known to form in magnetic-confinement fusion reactors, where it can present serious operational safety concerns, as well as influencing the parameters and stability of the fusion plasma.

In summary, *Complex and Dusty Plasmas from Laboratory to Space* is a well written text providing a thorough review of the present state of dusty-plasma physics. The authors and editors have done a good job of covering the major issues in dusty-plasma physics from a fundamental level, and have also discussed the application of those principles to real-world systems. The latest developments in the field are discussed and perspective is given for addressing future issues. New discoveries will continue to fuel excitement about dusty plasmas, attracting new researchers to the field in the future. This text will be a useful tool not only to those new to the field, but will also be a valuable reference for the present community.

Reviewed by:

Bill Amatucci
Plasma Physics Division
Naval Research Laboratory
Washington, DC 20375 USA
Tel: +1 (202) 404-1022;
E-mail: bill.amatucci@nrl.navy.mil

Measurements Using Optic and RF-Waves

edited by Frederique de Fornel and Pierre-Noèl Favennec, New York, Wiley, 2010, ISBN: 978-1-84821-187-2

The book's title, *Measurements Using Optic and RF-Waves*, is indeed appropriate to the heterogeneous nature of the book's content. The book contains a total of 12 chapters, and each chapter is dedicated to a particular topic. In this manner, the book covers topical measurement methods and techniques employed in diverse areas of the optical and RF domains.

The various topics covered in this book include an introduction to the electromagnetic environment; near-field scanning optical microscopy; optical measurements of visibility and range in meteorological media; low-coherence interferometry for measurements of fiber properties; passive remote sensing at sub-millimeter wavelengths and in the THz range; exposimetry (measurement of the ambient RF electromagnetic fields in and around the human body with reference to different electromagnetic sources and surroundings); ambient RF electromagnetic measurements in rural environments; measurement techniques for mobile radio; dosimetry of interactions between EM waves and human tissues using a hybrid approach of metrology; measurement and evaluation of electromagnetic compatibility; high-precision pulsar tuning in centimetric radio astronomy; and long-baseline decameter interferometry under the deployment of LOFAR (Low Frequency Array).

One might well ask how such a heterogeneous mixture of topics could be kept together, that too, in one book! In my view, the editors, Frederic de Fornel and Pierre-Noèl

Favennec, and the various chapter authors, successfully addressed this challenge. The editors and authors accomplish this by carefully structuring and styling the chapters. A key feature of the "unification strategy" is that all chapters firstly emphasize the basic physics of measurement involved in the particular applications (a fine thing to do!), and then go on to the state-of-the-art of the measurement technique and results. The editors and authors back up this strategy by including a list of pertinent references for further reading. Under this approach, each chapter, though self-contained, is yet unified with the rest of the book and provides amenable reading. I believe both the system engineers and the end-user scientists will find that the contents swiftly launch the reader into the subject matter covered by the individual chapters. The chapters generally include adequate and befitting diagrams and figures that an interested reader might expect.

The book possesses a well-thought-of framework of chapters that might be expected from a book of this kind. I expect that other readers will also find this book to be a useful contribution – as I did. The diversity of topics did not – as I first feared – deprive the book of a coherent approach to the different topics. If anything, I found the diversity of topics to be an enriching reading experience. In many ways, the book reflects the ever-expanding interdisciplinary nature of the emerging developments in radio science. I have no hesitation in welcoming and recommending this new book, edited by Frederique de Fornel and Pierre-Noèl Favennec.

Reviewed by

Madhu Chandra
Chair, URSI Commission F
Chemnitz University of Technology, Chemnitz, Germany
E-mail: madhu.chandra@etit.tu-chemnitz.de

Information for authors

Content

The *Radio Science Bulletin* is published four times per year by the Radio Science Press on behalf of URSI, the International Union of Radio Science. The content of the *Bulletin* falls into three categories: peer-reviewed scientific papers, correspondence items (short technical notes, letters to the editor, reports on meetings, and reviews), and general and administrative information issued by the URSI Secretariat. Scientific papers may be invited (such as papers in the *Reviews of Radio Science* series, from the Commissions of URSI) or contributed. Papers may include original contributions, but should preferably also be of a sufficiently tutorial or review nature to be of interest to a wide range of radio scientists. The *Radio Science Bulletin* is indexed and abstracted by INSPEC.

Scientific papers are subjected to peer review. The content should be original and should not duplicate information or material that has been previously published (if use is made of previously published material, this must be identified to the Editor at the time of submission). Submission of a manuscript constitutes an implicit statement by the author(s) that it has not been submitted, accepted for publication, published, or copyrighted elsewhere, unless stated differently by the author(s) at time of submission. Accepted material will not be returned unless requested by the author(s) at time of submission.

Submissions

Material submitted for publication in the scientific section of the *Bulletin* should be addressed to the Editor, whereas administrative material is handled directly with the Secretariat. Submission in electronic format according to the instructions below is preferred. There are typically no page charges for contributions following the guidelines. No free reprints are provided.

Style and Format

There are no set limits on the length of papers, but they typically range from three to 15 published pages including figures. The official languages of URSI are French and English: contributions in either language are acceptable. No specific style for the manuscript is required as the final layout of the material is done by the URSI Secretariat. Manuscripts should generally be prepared in one column for printing on one side of the paper, with as little use of automatic formatting features of word processors as possible. A complete style guide for the *Reviews of Radio Science* can be downloaded from http://www.ips.gov.au/IPSHosted/NCRS/reviews/. The style instructions in this can be followed for all other *Bulletin* contributions, as well. The name, affiliation, address, telephone and fax numbers, and e-mail address for all authors must be included with

All papers accepted for publication are subject to editing to provide uniformity of style and clarity of language. The publication schedule does not usually permit providing galleys to the author.

Figure captions should be on a separate page in proper style; see the above guide or any issue for examples. All lettering on figures must be of sufficient size to be at least 9 pt in size after reduction to column width. Each illustration should be identified on the back or at the bottom of the sheet with the figure number and name of author(s). If possible, the figures should also be provided in electronic format. TIF is preferred, although other formats are possible as well: please contact the Editor. Electronic versions of figures *must* be of sufficient resolution to permit good quality in print. As a rough guideline, when sized to column width, line art should have a minimum resolution of 300 dpi; color photographs should have a minimum resolution of 150 dpi with a color depth of 24 bits. 72 dpi images intended for the Web are generally *not* acceptable. Contact the Editor for further information.

Electronic Submission

A version of Microsoft *Word* is the preferred format for submissions. Submissions in versions of T_EX can be accepted in some circumstances: please contact the Editor before submitting. *A paper copy of all electronic submissions must be mailed to the Editor, including originals of all figures.* Please do *not* include figures in the same file as the text of a contribution. Electronic files can be send to the Editor in three ways: (1) By sending a floppy diskette or CD-R; (2) By attachment to an e-mail message to the Editor (the maximum size for attachments *after* MIME encoding is about 7 MB); (3) By e-mailing the Editor instructions for downloading the material from an ftp site.

Review Process

The review process usually requires about three months. Authors may be asked to modify the manuscript if it is not accepted in its original form. The elapsed time between receipt of a manuscript and publication is usually less than twelve months.

Copyright

Submission of a contribution to the *Radio Science Bulletin* will be interpreted as assignment and release of copyright and any and all other rights to the Radio Science Press, acting as agent and trustee for URSI. Submission for publication implicitly indicates the author(s) agreement with such assignment, and certification that publication will not violate any other copyrights or other rights associated with the submitted material.

APPLICATION FOR AN URSI RADIOSCIENTIST

I have not attended the last URSI General Assembly, and I wish to remain/become an URSI Radioscientist in the 2009-2011 triennium. Subscription to *The Radio Science Bulletin* is included in the fee.

(please type or print in BLOCK LETTERS)

Name : Prof./Dr./Mr./Mrs./Ms. _____
Family Name First Name Middle Initials

Present job title: _____

Years of professional experience: _____

Professional affiliation: _____

I request that all information be sent to my ☐ home ☐ business address, i.e.:

Company name: _____

Department: _____

Street address: _____

City and postal/zip code: _____

Province/State: _____ Country: _____

Phone: _____ ext._____ Fax: _____

E-mail: _____

Areas of interest (Please tick)

☐ A Electromagnetic Metrology
☐ B Fields and Waves
☐ C Radio-Communication Systems & Signal Processing
☐ D Electronics and Photonics
☐ E Electromagnetic Environment & Interference
☐ F Wave Propagation & Remote Sensing
☐ G Ionospheric Radio and Propagation
☐ H Waves in Plasmas
☐ J Radio Astronomy
☐ K Electromagnetics in Biology & Medicine

I prefer (Please tick)

☐ An electronic version of the RSB downloadable from the URSI web site
(The URSI Board of Officers will consider waiving the fee if a case is made to them in writing.) 40 Euro

☐ A hard copy of the RSB sent to the above address 100 Euro

Method of payment : VISA / MASTERCARD (we do not accept cheques)

Credit card No ☐☐☐☐ ☐☐☐☐ ☐☐☐☐ ☐☐☐☐ Exp. date _____

CVC Code: _____ Date : _____ Signed _____

Please return this signed form to :

The URSI Secretariat
c/o Ghent University / INTEC
Sint-Pietersnieuwstraat 41
B-9000 GHENT, BELGIUM
fax (32) 9-264.42.88